Photoluminescent Lanthanide-based Materials for Probing Temperature and Pressure for Further Tribological Applications

Yujiao Zhou

N° d'ordre NNT : 2023LYO10189

THESE de DOCTORAT DE

L'UNIVERSITE CLAUDE BERNARD LYON 1
Et
Institut National des Sciences Appliquées de Lyon

Ecole Doctorale N° 206
Chimie de Lyon
Spécialité de doctorat : Chimie
Discipline : Chimie Physique

Soutenance prévue le 06 octobre 2023, par :

Yujiao ZHOU

Photoluminescent Lanthanide-based Materials for Probing Temperature and Pressure for Further Tribological Applications

---

Devant le jury composé de :

POTDEVIN Audrey	Maître de Conférences, HDR, ICCF Clermont Auvergne	Rapportrice
RABU Pierre	Directeur de Recherche, CNRS Strasbourg	Rapporteur
BESSIERE Aurélie	Chargée de Recherche, HDR, CNRS Montpellier	Examinatrice
LUNEAU Dominique	Professeur des Universités, Université Lyon 1	Examinateur
MOLIMARD Jérôme	Professeur, Ecole des Mines de Saint-Etienne	Examinateur
JOURNET Catherine	Professeure des Universités, Université Lyon 1	Directrice de thèse
BOIS Laurence	Chargée de Recherche, CNRS Lyon	Co-encadrante de thèse
PHILIPPON David	Maître de Conférences, INSA de Lyon	Co-encadrant de thèse
DESCARTES Sylvie	Ingénieure de Recherche, HDR, INSA de Lyon	Invitée
LEDOUX Gilles	Directeur de Recherche, CNRS Lyon	Invité

致姥姥
愿她在她最想去的地方过得开心
我永远想念她

This thesis was supported by the LABEX MANUTECH-SISE (ANR-10-LABX-0075) of Université de Lyon, within the Plan France 2030 operated by the French National Research Agency (ANR)

Remerciements

Merci à toutes les personnes qui ont contribué de près ou de loin à ma thèse au cours de ces trois dernières années. Réaliser une thèse est déjà un défi en soi, mais le faire à l'étranger rend l'expérience encore plus complexe. C'est grâce à votre soutien inestimable que j'ai pu surmonter les obstacles et avancer dans mes travaux de recherche.

Tout d'abord, je souhaite adresser mes remerciements les plus sincères au Dr. Audrey Potdevin et Dr. Pierre Rabu pour avoir accepté d'être les rapporteurs de ma thèse, ainsi qu'aux Dr. Aurélie Bessière, Prof. Dominique Luneau et Prof. Jérôme Molimard qui m'ont fait l'honneur d'être les examinateurs.

Je tiens à exprimer ma profonde gratitude à la professeure Mme Catherine Journet, ma directrice de thèse, ainsi qu'à mes co-encadrants : le Dr. Laurence Bois, le Dr. Sylvie Descartes et le Dr. David Philippon. Je vous suis reconnaissante pour ce sujet de thèse formidable que vous m'avez proposé et pour m'avoir choisie pour le réaliser. Je tiens également à vous remercier d'avoir cru en moi, de m'avoir soutenue et accordé votre confiance tout au long de ces trois années de thèse. J'ai eu la chance d'avoir des encadrants aussi exceptionnels non seulement dans ma vie académique, mais aussi dans ma vie personnelle. Votre présence et vos conseils ont été précieux pour moi.

Je souhaiterais remercier aussi Dr. Gilles Ledoux de m'avoir accueillie dans son laboratoire l'ILM pour les caractérisations spectroscopiques. Merci aussi pour toute son aide pendant mes manipulations et le travail de rédaction. Merci de m'avoir soutenue comme un encadrant. Je remercie aussi le Prof. Jean-Marie Bluet pour son aide dans les mesures spectroscopiques au début de ma thèse. Un grand merci à eux pour avoir bien voulu faire partie du comité de suivi de thèse.

Je remercie également Dr. Nathalie Bouscharain pour toute son aide dans les mesures rhéologiques, et pour avoir rendu le temps d'attente super agréable. Merci à Dr. Lionel Lafarge pour les montages expérimentaux, sans lesquels aucune mesure à haute pression n'aurait pu être réalisée aussi efficacement. Merci aussi à Dr. Matteo Martini pour son aide dans les mesures de DLS et son inspiration dans l'avancement de mon sujet. Merci à Dr. Mishra Shashank et Dr. Bhagyesh Purohit pour leur accueil au laboratoire IRCELYON et pour m'avoir aidée à faire les synthèses et les caractérisations de nanoparticules. Je remercie Dr. Guillaume Pilet pour les études sur les complexes de Lanthanide et son aide dans les caractérisations et traitements de données. Merci également à Laurent Mollet pour les moules des matériaux, j'ai apprécié nos discussions autour des technologies d'impression 3D. Je voudrais aussi remercier Dr. Cédric Desroches, Dr. Bruno Gardiola, Dr. Nina Attik, Dr. Fernand Chassagneux, Didier Fournier, Dr. Erwann Jeanneau, Dr. Ruben Vera, Dr. Nicolas Devaux et Dr. Rodica Chiriac pour leurs aides dans les synthèses et les caractérisations pendant ces trois années.

Je souhaite remercier tous les membres du LMI et LaMCoS pour leur gentillesse et leur aide à m'intégrer facilement dans l'équipe au sein de ces laboratoires. Merci à Dr. Bérangère Toury et au Prof. Dominique Luneau de m'avoir accueillie dans leur équipe « Chimie Inorganique Moléculaire et Précurseurs » au LMI. Merci aussi au Prof. Benyebka Bou-saïd pour son accueil dans l'équipe « Tribologie et Mécanique des Interfaces » au LaMCoS.

Je tiens à remercier chaleureusement mes collègues et amis rencontrés au cours de ces trois années de thèse. Une mention spéciale va à Camille et Yamina pour leur gentillesse, leur patience et leur précieuse aide dans mes recherches. Un grand merci également à Sabrina et Yamaldi pour leur contribution précieuse à mon projet et leur soutien pendant le moment difficile de ma rédaction. Je souhaite également exprimer ma gratitude envers Zhijian et Margherita pour leur aide dans le traitement des données. Je ne peux pas oublier de remercier Neil, Ali, Hyewon, Loïs, Izabel, Axel, Fangbing et tous les autres amis et collègues qui ont partagé de bons moments avec moi. Votre soutien et la bonne ambiance ont rendu cette expérience de thèse encore plus agréable.

J'aimerais également exprimer ma sincère gratitude envers le LABEX MANUTECH-SISE de l'Université de Lyon pour son soutien dans le cadre de ce projet. Je tiens particulièrement à remercier Aurélie Guillarme pour son travail administratif remarquable. Son dévouement et son professionnalisme sont exemplaires, et elle a toujours été là pour m'apporter son aide et ses conseils.

Evidemment, je ne peux pas oublier de remercier mes collègues exceptionnels qui ont joué un rôle clé dans mon activité complémentaire d'enseignement. Tout d'abord, un grand merci à Dr. Alexandra Fateeva, Prof. Dominique Luneau et Dr. Caroline Felix pour m'avoir confié des missions d'enseignement. Leur confiance en moi et leur soutien constant ont été une source d'inspiration et de motivation. Je tiens également à exprimer ma gratitude envers Fabrice, Matteo, Shashank, Bérangère, Guillaume, Sabrina et tous les autres collègues qui m'ont accompagnée tout au long de mes enseignements. Leur aide précieuse et leur soutien inconditionnel ont contribué de manière significative à mon développement professionnel.

Je tiens à exprimer ma profonde gratitude envers mes parents pour leur soutien inconditionnel, leur amour et leurs encouragements constants depuis ma naissance. Je souhaite également remercier mon chouchou pour son aide inconditionnelle et son accompagnement précieux. Il a toujours été là pour me soutenir et m'encourager, et je suis extrêmement reconnaissante de l'avoir à mes côtés. Un grand merci à tous mes amis, en particulier à mes besties, pour leur présence chaleureuse dans ma vie. Je tiens également à exprimer ma gratitude à mon dance crew UNI-K. Merci pour les moments de danse, de rires et d'aventures partagés ensemble.

Contents

Abstract

Photoluminescent Lanthanide-based Materials for Probing Temperature and Pressure for Further Tribological Applications

Accurate measurement of local temperature and pressure in tribological contacts has long been a challenge. The development of non-contact photoluminescent nanosensors has offered new possibilities for precise and non-intrusive measurements in tribology. This thesis develops rare-earth-based photoluminescent sensors for the local temperature and pressure measurement in frictional contacts. Gadolinium orthovanadate upconversion nanoparticles (NPs) doped with Yb^{3+} and Er^{3+} are synthesized and exhibit reversible sensitivity to temperature (20-300°C) thanks to the luminescent intensity ratio (LIR) of the Er^{3+} emission. The uncertainty in temperature calibration caused by laser-induced heating is corrected. The independence of temperature calibration from pressure is verified in a fluid suspension subjected to a hydrostatic pressure up to 1GPa. In addition, a new method of pressure sensing is proposed using LIR of Tb^{3+}/Eu^{3+} emission from a β-diketonate complex. Under hydrostatic below 700 MPa, the Ln complex exhibits excellent sensitivity and reversibility. A prior temperature calibration is required to correct the sensitivity of the LIR of this complex to the temperature for pressure sensing. These sensors have potential applications for accurate measurement of temperature and pressure in tribological systems.

Keywords: Photoluminescence, Nanomaterials, Thermometry, Manometry, Lanthanide-complexes, Tribology.

Résumé

Matériaux Photoluminescents à Base de Lanthanides pour Mesurer la Température et la Pression en vue d'Applications en Tribologie

La mesure précise de la température et de la pression locales dans les contacts tribologiques est un défi de longue date. Le développement de nanosondes photoluminescentes a offert de nouvelles possibilités de mesures précises, et non intrusives en tribologie. Cette thèse développe des sondes photoluminescentes à base de terres rares pour la mesure locale de la température et de la pression dans des contacts tribologiques. Des nanoparticules à conversion ascendante d'orthovanadate de gadolinium $GdVO_4$ dopées Yb^{3+} et Er^{3+} sont synthétisées ; elles présentent une sensibilité réversible à la température (20-300°C) grâce au rapport d'intensité luminescente (LIR) de l'émission des ions Er^{3+}. L'incertitude de la détection de température causée par le chauffage induit par laser est corrigée. L'indépendance de la calibration de la température par rapport à la pression est vérifiée dans une suspension fluide soumise à une pression hydrostatique allant jusqu'à 1 GPa. En outre, une nouvelle méthode de détection de la pression est proposée en utilisant le LIR de l'émission de Tb^{3+}/Eu^{3+} dans un complexe de β-dikétonate. Sous une pression hydrostatique inférieure à 700 MPa, le complexe de Tb^{3+}/Eu^{3+} présente une excellente sensibilité sans hystérésis. Un étalonnage préalable de la température est nécessaire pour corriger la sensibilité du LIR de ce complexe à la température pour la détection de pression. Ces sondes photoluminescentes présentent un potentiel d'application pour la mesure précise de la température et de la pression dans des systèmes tribologiques.

Mots-clés: Photoluminescence, Nanomatériaux, Thermométrie, Manométrie, Complexes de lanthanide, Tribologie.

Extended Abstract

This thesis focuses on the development and characterizations of rare-earth-based photoluminescent sensors for the local measurement of temperature and pressure in a friction contact, with a view to subsequent tribological applications. To overcome the limitations of traditional electrical devices for surface characterization in tribology, optical nano-sensors for temperature and pressure measurement are investigated. The use of light as an information transmission offers advantages such as non-contact, high penetrability, and real-time monitoring, enabling substantial temporal and spatial resolution.

Among the various types of photoluminescent sensors, rare-earth compounds are chosen because of their desirable spectral properties. The long lifetime and narrow peak of Ln^{3+} emission allow high accuracy and simple data processing. Furthermore, the chemical characteristics of Ln-based materials make them suitable for sensing applications. In addition to their low toxicity, high chemical stability, and excellent functionalizability, their versatility allows for the customization and adaptation of the materials to meet the specific requirements of different tribological systems and applications.

This thesis demonstrates the successful synthesis of gadolinium orthovanadate $GdVO_4$: Yb^{3+}/Er^{3+} upconversion nanoparticles (NPs) through a co-precipitation method. These NPs exhibit accurate and reversible temperature sensitivity between 20 to 300°C, as indicated by the luminescent intensity ratio (LIR) of Er^{3+} emission under near-infrared excitation. Laser-induced heating effects are observed both in the NPs powder and in the high-concentration dispersed medium at high irradiation intensity, but a correction method has been developed to address this issue. NPs, dispersed in solid and fluid lubricants at low concentration, enable precise temperature measurements while preserving the initial properties of the material. Temperature calibration under varying hydrostatic pressure (up to 1.1 GPa) confirms the negligible impact of pressure on thermometry, establishing the applicability of $GdVO_4$: Yb^{3+}/Er^{3+} nanosensors for temperature measurement under varying pressure conditions.

In the second part of this thesis, a novel self-monitoring pressure sensor is developed by Tb^{3+}/Eu^{3+} β-diketonate complexes. Ln complexes exhibit different nuclearities depending on the coordinated ligands, leading to different structures and thus different interionic distances. Three types of Ln complexes are studied in this part. Using Tb^{3+} as the Eu^{3+}sensitizer, the rate of Tb^{3+}-Eu^{3+} energy transfer is strongly impacted by the distance between them. Based on FRET theory, this process is applied to pressure sensing. Using Tb/Eu LIR under excitation at 405 nm, the Tb^{3+}/Eu^{3+} mononuclear complex demonstrates self-calibrated, reliable, and reversible pressure sensitivity (up to 700 MPa). Since the Tb/Eu LIR is also influenced by temperature variations up to 60°C, temperature calibration is required for accurate pressure measurement. The emission of a complex suspension has also been studied under different shear rates. The results show that the reliability of pressure sensing is limited at low shear rates ($< 500\ s^{-1}$) in the complex suspension.

The rare-earth-based photoluminescent sensors studied in this work show promising potential for tribological applications. $GdVO_4$: Yb^{3+}/Er^{3+} upconversion nanoparticles exhibit pressure-independent thermometry, and laser-induced heating effects are negligible at low NP concentrations. In addition, a Tb^{3+}/Eu^{3+} β-diketonate complex exhibits high sensitivity to

pressure due to variations in the energy transfer process resulting from structural changes. These sensors are further analyzed under frictional conditions using solid and fluid lubricants, showing excellent applicability for future tribological measurements.

List of Abbreviations

acac	Acetylacetone
APTE	Addition de Photons par Transfert d'Energie
APTES	3-aminopropyltriethoxysilane
arb. units	Arbitrary units
atm	Atmosphere
BET	Back energy transfer
CCD	Charge coupled device
CCDC	The Cambridge crystallographic data center
CET	Cooperative energy transfer
CIF	Crystallographic Information File
CTS	Charge transfer state
DAC	Diamond anvil cell
DLS	Dynamic Light Scattering
DS	Down-shifting
ED	Electric dipole
EDX	Energy Dispersive X-ray (EDX)
EHL	Elastohydrodynamic Lubrication
EM	Energy migration
ESA	Excited state excitation
ET	Energy transfer
ETU	Energy transfer upconversion
Ex	Excitation
FRET	Förster resonant energy transfer
FWHM	Full width at half maximum
GSA	Ground-state absorption
hfa	Hexafluoroacetylacetone
HR TEM	High-resolution transmission electron microscopy

Int.	Intensity
IR	Infrared
ISC	Intersystem crossing
JCPDS	Joint committee on powder diffraction standards
LIR	Luminescence intensity ratio
MD	Magnetic dipole
MTEOS	Methyltriethoxysilane
MTPS	Modified Transient Plane Source
NIR	Near infrared
NP(s)	Nanoparticle(s)
NR	Nonradiative process
Nycobase	Nycobase 5750
PA	Photons avalanche
PDMS	Polydimethylsiloxane
phen	1,10-phenanthroline
PL	Photoluminescence
PM	Photo-multiplicator
QDs	Quantum dots
RS	Russell-Saunders
SEM	Scanning electron microscopy
SNR	Signal-to-noise ratio
TCL(s)	Thermally coupled level(s)
TEM	Transmission electron microscopy
TEOS	Tetraethyl orthosilicate
tfa	Trifluoro-acetylacetone
TFTC	Thin film thermocouple
UC	Upconversion
UV	Ultra-violet

XRD	X-ray diffraction
[Ln$_1$]	Mononuclear lanthanide (complex)
[Ln$_2$]	Binuclear lanthanide (complex)
[Ln$_9$]	Nonanuclear lanthanide (complex)

List of Nomenclatures

Symbol	Units	Definition
B	/	Pre-exponential constant of Boltzmann distribution
d	mm	Diameter
ε_e	/	Deformation level
F	N	Normal force
g	/	Degeneracy
I	arb.units	Intensity
I_{laser}	W/cm²	Laser intensity (or Laser power density)
J	/	Total moment
k	W/mK	Thermal conductivity
k_B	/	The Boltzmann constant
L	/	Total orbital moment
N (or n)	/	Population of electrons
P	MPa (or GPa)	Pressure
P_{atm}	/	Atmospheric pressure or Ambient pressure)
θ	°	Diffraction angle
R_0	nm (or Å)	Critical distance in the FRET theory
S (In Chapter 1)	/	Total spin moment
S (In Chapter 1)	mm²	Surface
S_r or S_R	% K^{-1}	Relative thermal sensitivity
T	K (or °C)	Temperature
t	ms (or s)	Time
τ	ms (or s)	Decay time
t (In Chapter 2)	mm	Thickness
x	/	Molar composition
ΔE	cm^{-1}	Energy gap
λ	nm (or Å)	Wavelength
σ	/	Emission cross section
ω	rad/s	Angular frequency

General Introduction

Photoluminescent (PL) sensors have received increasing attention in a variety of applications in recent decades. When light is used as an information carrier for a measurement device sensor, advantages such as noncontact, high penetrability, and fast response allow substantial temporal and spatial resolution. Depending on the physicochemical characteristics of the materials, their photoluminescence can be sensitive to various physical variables.

This thesis aims to develop PL sensors for the local measurement of temperature and pressure adapted for tribological tests. In this context, PL sensors should provide high sensitivity to temperature or pressure variations. This sensitivity must be as far as possible, independent of any other varying parameters in the contact. In addition, optimization of detectability, accuracy, reliability, and reproducibility compared with traditional techniques such as Raman spectroscopy, infrared thermography and electric resistivity should be considered. For further *in situ* tribological measurement, PL sensors are inserted into different media (fluid or solid), and the collaboration of matrix and the sensor is evaluated by the optical and mechanical properties of the mixture, which is called the composite PL material. Among the many PL sensors, Lanthanides (Ln)-based PL materials will be further studied in the present work. Thanks to their spectral features, such as long emission lifetime, sharp emission peak, leading to the simplicity of data collections and processing, thus resulting in high resolution and accuracy in measurement.

The emission characteristics of Ln-based materials, specifically Ln^{3+} ions, are highly sensitive to the surrounding environment. The radiative emission of the f-f transitions is initially forbidden by the Laporte selection rules. However, these selection rules can be relaxed by alterations in local crystal symmetry or through interactions with the surrounding environment. Changes in temperature or pressure can influence crystal symmetry or alter the local environment around Ln^{3+} ions, thus affecting luminescence. This sensitivity to temperature and pressure variations allows Ln-based materials to be utilized as sensors for these parameters.

The long emission lifetimes of Ln-based materials, resulting from the restrictions imposed by Laporte selection rules, offer several advantages for sensing applications. One of these advantages is the manipulation of nonradiative pathways, particularly through energy transfer (ET) processes. Based on the Förster resonant ET (FRET) theory, the interionic distance between the Ln^{3+} sensitizer and the Ln^{3+} acceptor has a significant impact on the ET rate. Pressure-induced structural contraction can thus lead to enhancement in the ET rate, resulting in a variation in emission characteristics. The emission can be expected to be manometric to exploit an Ln-based potential pressure sensor.

Temperature sensing by Ln-based sensors following the principles of the Boltzmann distribution, is typically achieved through the Luminescence Intensity Ratio (LIR) method. The LIR method relies on the temperature-dependent populations of different energy levels within the Ln-based material. The LIR method involves measuring the ratio of luminescence intensities emitted from two thermally coupled energy levels within the Ln-based material. By monitoring the ratio of luminescence intensities, it is possible to determine the temperature of the system based on the Boltzmann distribution. Compared with other temperature sensing

methods, the LIR method is self-monitoring as the measurement is not limited to external spectral references. By selecting appropriate energy levels within the Ln-based material, temperature sensing by the LIR method can be highly accurate and simply processing. Those advantages make LIR-based thermometry well-suited for non-contact and non-intrusive temperature sensing in dynamic tribological systems.

Compared to Ln-based thermometers, Ln-based pressure sensors have received less attention and are relatively less studied. This indicates a research gap in the field, highlighting the potential for further investigation and development of Ln-based materials as pressure sensors in the context of tribology. Exciting pressure sensors of Ln-based materials are mostly based on the peak-shift method. However, requiring wavelength reference during measurement by peak-shift method will be difficult for dynamic sensing applications. In addition, the development of a reliable PL pressure sensor capable of measuring in the 0-1 GPa range for tribological tests, with the desired sensitivity, accuracy, and reliability, is an ongoing research area. In this work, the challenge is thus to develop a novel method based on the self-monitoring LIR method and incorporating a FRET system, for pressure sensing in the range up to 1 GPa. This approach involves ET between two Ln^{3+} ions, where the ET rate is sensitive to the structural contraction induced by pressure.

Focusing on Ln-based PL materials and exploring their temperature and pressure sensing capabilities for tribological applications, this work presents Yb^{3+}/Er^{3+}-doped $GdVO_4$ nanoparticles (NPs) as PL thermometer, and the Tb^{3+}/Eu^{3+}-based β-diketonate complexes as PL manometer. The thesis is structured as follows:

- Chapter 1: This chapter provides an overview of the project context and the theoretical aspects of rare-earth trivalent ions photoluminescence. It discusses the mechanisms and characteristics of various methods for temperature and pressure sensing by photoluminescence of Ln^{3+}-based materials.
- Chapter 2: The second chapter focuses on the chemical synthesis of the PL sensors and their structural and mechanical characterizations. It also explores the incorporation of PL sensors into fluid or solid matrices and evaluates the mechanical properties of the resulting mixtures.
- Chapter 3: This chapter is dedicated to the PL thermometer using Yb^{3+}/Er^{3+}-doped $GdVO_4$ nanoparticles (NPs). It presents the PL properties and temperature calibration of the NPs and their incorporation into matrices. The reliability of these NPs as thermos-sensors in *in situ* tribological measurements is discussed, considering their thermometric properties under pressure-coupling environments and laser-induced heating.
- Chapter 4: The fourth chapter focuses on the pressure-sensitivity of PL β-diketonate complexes based on Tb^{3+} and Eu^{3+}. It discusses the peak-shift-based and LIR-based sensing methods for measuring hydrostatic pressure up to 1 GPa. The applicability of the Tb^{3+}/Eu^{3+} β-diketonate complex as a LIR-based pressure sensor in dynamic measurements is explored, considering the pressure sensitivity at different temperatures and shear rates.

Chapter 1:

State of art

1. State of art

1.1 Context

1.1.1 The tribological contact

The term 'Tribology' became widely used after being reported for the first time in "The Jost Report" published in 1966.[1] This report highlighted the huge cost of friction, wear and corrosion to the UK economy. Tribology is defined as the science of friction, lubrication and wear.[2–4] Friction is the force generated between the two contacting and sliding surfaces, resisting to the relative motion of these two surfaces, which is ubiquitous in our daily life. The history of human using friction to simplify life can be dated back more than 100 000 years ago. Nowadays, tribology has become an important part of mechanical engineering in many fields such as aeronautics and automotive industries or bio-medical field. Since the first construction of the tribological mechanism, the way to control wear and friction has been studied.

To describe the tribological contact, including fluid and solid lubricated contact, as well as dry contact, Godet introduced the third body concept.[5] The so-called third body includes all the interfacial elements between the contacting surfaces (called first bodies), Figure 1.1. It includes fluid or solid lubricant, generated debris, oxide layers, ...

The dimension of the third body depends, among other parameters, on the surface geometry and the mechanical properties of properties of the first body. Its characteristic dimensions range between thickness of few nanometers up to several microns. The third body separates the two first bodies while accommodating most of their difference in speed. The tribological contact size might be lower than 500 µm in diameter. The surface contact velocities may reach values higher than 10 m/s). Based on these extreme values the transient time of the third body in the contact may range between 10^{-5}-10^{-3} seconds. This implies important difficulties to have access to the contact and perform local measurements of parameter that can vary importantly.

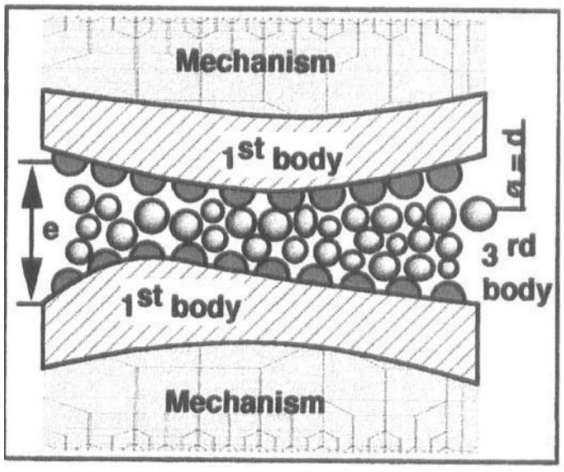

Figure 1.1: Schematic presentation of the third body in tribological contact. (Figures from ref.[6], Y. Berthier. 1996. Copyright @ Tribology Series)

Friction and wear are not intrinsic initial material properties but are controlled by the tribo-system parameters. It is convenient to consider that the parameters affecting friction and wear are interacting with each other. These factors among others include normal load, local temperature, relative surface motion and sliding speed, surface roughness, surface material nature, lubrication, stiffness of the device containing the contact, environment (gaz, partial pressure…) of the contact zone …

In general, an increase of applied load leads to an increase of friction and wear, attributed to the effect of load on asperities interaction. Hence, an increase of friction results in a temperature rise which may affect the surface (mechanical properties such as hardness, oxidation, contaminating film formation, …) and alter, as the consequence, the wear resistance of the surface. Variation of the sliding velocity leads to a variation of the shear stress, altering the mechanical properties of the contacting material. Furthermore, the effect of sliding speed might also increase the surface temperature locally. Regarding lubricated contact, temperature and pressure variations between two contacting surfaces affect the rheological properties of the interface. The shear stress may also affect the rheological properties of the lubricant. The viscosity directly influences the lubricant film thickness, and consequently, wear and friction that control the life and performance of the tribological system.[7,8]

Among the previously mentioned factors, local temperature and pressure are two relevant parameters in tribology to understand and predict the behavior of the interface between solids in contact. The tribological contact is complex since the combination of the applied load, the surface geometry, roughness, sliding speeds and the lubricant characteristics leads to local pressure and temperature gradients in the whole area of contact. Therefore, local temperature and pressure measurement with high accuracy and efficiency has become a major topic in tribology research.

1.1.2 Review of experimental techniques to measure P&T in tribological contact

In the literature various techniques for measuring temperature or pressure in a tribological contact are detailed in dedicated review paper considering dry contact[9] or lubricated contact.[10] The next sections aim to give an overview of the main developed methods to measure pressure and temperature in the tribological contact.

1) Thermocouple.

Inserted thermocouple in the material is one of the earliest traditional temperature measurement technologies, in particular for cutting tool application. The thermocouple is embedded in near-surface material, several millimeters away from the contact surface to protect the thermocouple from frictional damage.[11–13] First, the introduction of the thermocouple in the solid/close to the surface alters heat transfer and thus temperature distribution in the solid. Second, direct measurement of the temperature is not possible due to the distance from the surface. Consequently, the accuracy of the measurement is limited. Moreover, the insertion of thermocouple in the material with accurate localization is

considered as a difficult manipulation due to the size of current thermocouple that is small (about 70 µm for a typical chrome-nickel thermocouple[14]). Moreover, the limited transient response of thermocouple due to their thermal inertia limits this technique to punctual measurements. For sliding surfaces, thin film thermocouple (TFTC), having better response time (~1s) and smaller measuring spatial resolution, were also developed.[15]

2) Electric resistivity for pressure and temperature measurement

The sensibility to temperature and pressure of certain materials is shown by their change in electric resistance. Thin film of a few micrometers of thickness made from these kinds of materials is used in temperature and pressure sensing in friction contacts. For temperature sensing, the thin film in platinum and titanium is widely used.[16] Moreover, manganese-based thin film (Cu - Mn - Ni) is used as a pressure sensor since its electric resistance is highly pressure-sensitive but slightly sensitive to temperature.[17] Thin film sensors are required to be deposited on electrically insulating materials such as ceramic substrates[18] (sapphire, zirconia, silicon nitrite, etc.) or on protective insulating coatings (usually aluminum oxide or silicon oxide) when used on metal surfaces. However, the deposition of an additional film, even with 0.1 µm of coating thickness is intrusive. Indeed, the response could be disturbed by their different thermal or mechanical properties to the substrate. In elastohydrodynamic lubrication (EHL) where the lubricant film thickness ranges between few nanometers and hundreds of nanometers, the thickness of sensor is not negligible. Moreover, reduced lifetime of deposited film sensor is another issue due to the severity of the contact conditions. Small variations of the sensor dimensions and/or mechanical properties during the fabrication will affect the thin film sensor response to pressure or temperature, which require individual calibrations for each sensor.

3) Infrared thermography for temperature measurement.

Based on the theory that heat induces infrared (IR) radiation, IR thermography is a technique currently used to measure temperature. The first application of IR thermography in temperature measurement was performed by Winer *et al.* in 1970s in lubricated contact.[19] This technology requires an IR radiometric detector and corresponding filters, and also the pre-calibration of experimental temperatures to distinguish various sources of radiation.[20] This technique was also used to measure temperature in dry contact.[21,22] The experimental approach is considered intrusive since it might require the use of infrared reflective materials, for example a chromium coating or to know the local emissivity of the surfaces involved. Moreover, different sources (solid surfaces and bodies, lubricant film or the interface and the environment) contribute to the overall IR radiation, and they must be separated by applying appropriate coatings on the transparent disc and/or using different filters. However, IR thermography can be used as a complementary technology to others temperature measurements to optimize accuracy.

4) Raman micro-spectroscopy

Raman spectroscopy is a non-destructive analytical technique based on Raman scattering. It provides chemical and structural information. It is based upon the interaction of light with the chemical bonds within a material. A Raman spectrum represents the vibrational movement of chemical bond in a molecule. The impact of temperature or/ and pressure on molecular structure can be thus observed by variation of its vibrational energy in Raman spectral shift. The resolution of this technology in temperature measurement can reach 5 K in Rassat's work.[23] The application of Raman spectroscopy for pressure sensing has first been applied in lubricated contact by Gardiner et al.[24] Later, local pressure contribution mapping in tribological measurements has been determined by Jubault *et al*. [25,26] and Yagi *et al*.[27] in the case of lubricated contact. In such experiments, this technique provides a precise and accurate measurement of pressure with a higher spatial and temporary resolution than other temperature measurement techniques. However, this technology is limited by requiring the lubricant as strong Raman scatter, and that is not the case for most of the lubricant for tribological measurement.

5) Photoluminescence

Recently, photoluminescence has been considered as a potential technique to measure pressure and temperature. CdSe/CdS/ZnS core/shell/shell quantum dots (QDs) were dispersed in a lubricant (squalane) to map pressure and temperature in an EHL contact.[28,29] These nanosensors were previously calibrated for temperature and pressure in diamond anvil cell (from 0.2 to 1.3 GPa between 20 to 80 °C). Their emission energy shift was found to be linearly dependent on pressure and temperature (Figure 1.2). As the optical techniques previously mentioned, the measurement by PL sensor is contactless, has a fast response and high spatial resolution (~5 - 10 μm). The very small size of QDs (7 nm) was adapted to the lubricant film thickness (~200 nm) to be considered as non-intrusive and the PL intensity is much higher than Raman scattering. The main drawback of this technique was the coupled dependence of the emission energy to pressure and temperature, while these two parameters generally vary independently in the tribological contact.

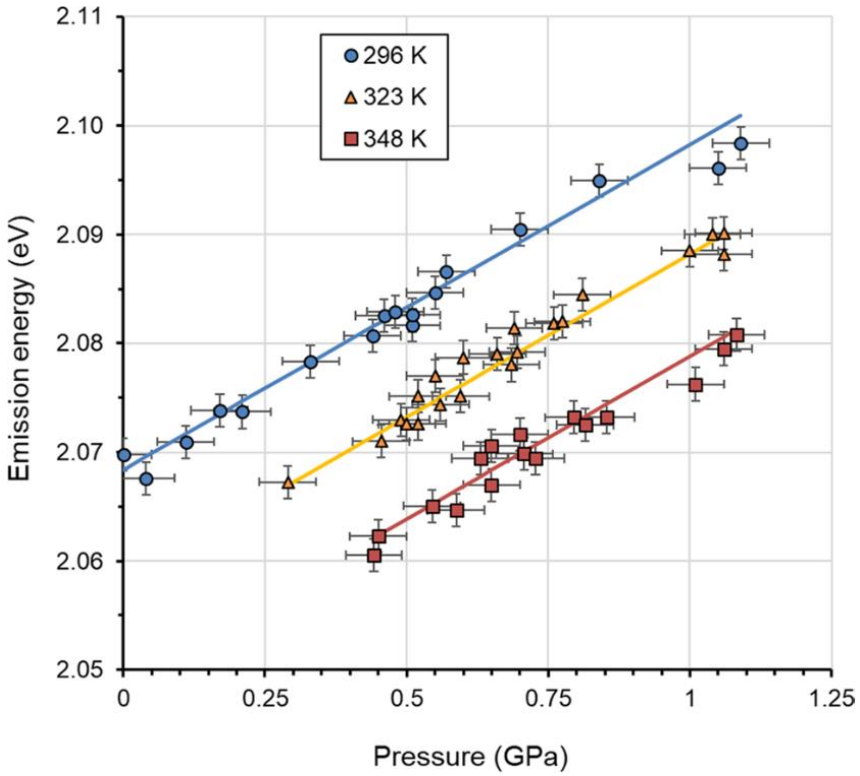

Figure 1.2: Calibration of the squalane-CdSe/CdS/ZnS QDs suspension of 0.125 mg/mL concentration versus pressure on the 0–1.2 GPa range at 3 temperatures. (Figures on the bottom from ref.[29], T. Seoudi *et al.* 2020. Copyright© Tribology Letters)

1.1.3 Further challenges in using PL for P and T measurements

1) Conception of PL sensing system for tribological contact

The previous results demonstrated the potential of PL to probe P and T in lubricated contacts. The main challenge is the development of nanosensors sensitive to one factor in order to be able to uncouple pressure and temperature measurements. High sensitivity to temperature (up to the flash temperature of materials) or to pressure (up to 5 GPa) should be required to investigate a wide range of tribological applications. However, here we focus on conditions classically encountered in lubricated contact, in particular in elastohydrodynamic lubrication, as well as in dry contact under moderate conditions. Thus, the required specifications of the PL sensor can thus be summarized as:

- High sensitivity in required measurement range:
  - Temperature measurement range: 20 – 200 °C
  - Pressure measurement range: 0 – 1 GPa
- Not affected by influence quantities
- Nano-scale size
- Chemical-physical stability in dispersed medium
- Low toxicity (for other applications in lifescience, foodscience, …)

Another challenge is the development of PL nanosensors suitable not only for measurement in lubricated contacts but also in dry contacts. Then, those synthesized photoluminescent sensors should be inserted into a solid matrix, where the matrix should be:

- Resisting to friction test: high stability to temperature and pressure
- Non-toxic
- Optically transparent
- Easy-to-make

Using the third body concept detailed previously, for *in situ* tribological measurements, the PL nanosensors may be:

- dispersed in a fluid third body (lubricant/grease). In that case, as demonstrated in the previous works,[28,29] the sensors in suspension in the fluid is continuously entering and exiting the contact, thus making possible the continuous measurement.

- mixed in the solid third body (solid lubricants as graphite, MoS_2), however the stability of the mixture is not guaranteed.

- encapsulated in the first bodies. In that case, the advantage is the local measurement at the extreme surface layer of the first body surface (within the first 100µm) becomes possible. But the possible subsequent wear of the surface may lead to the "dispersion" of the sensor in the dry third body and thus outside of the contact if the third body is ejected.

In the following, only the encapsulation of the PL nano-sensors in the first body or dispersion in the fluid third body will be considered. Regarding the first bodies, sensors may be located at the top surface or in the bulk as shown in Figure 1.3. In that later case, during the friction test, the sensors in 1st body could be rubbed out and then become the 3rd body. Minimizing the production of debris during the friction test by changing the loading pressure and the speed of friction, should be considered in further measurement to better control the PL sensing system.

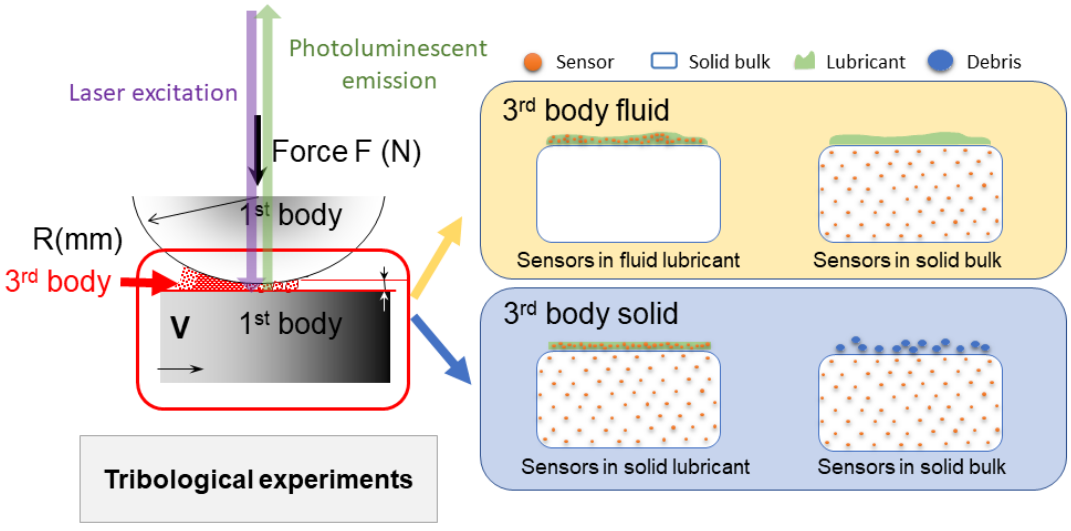

Figure 1.3: Conception of PL temperature and pressure sensing materials and their application in tribological contact.

2) Incorporative matrices for PL nanosensors

Based on our previous works,[28–31] two commercially available fluid lubricants to disperse the PL sensors are chosen to be:

- Nycobase 5750: commercial polyol-ester-based oil used for aero spatial applications.
- Squalane: A characteristic model lubricant.

In the case where PL nanosensors are incorporated in a solid matrix, two potential options for the incorporative solid matrix are hybrid silica (sol-gel glass) and PDMS polymer (Polydimethylsiloxane). Here are some key characteristics of each matrix:

- Mechanical properties adapted for tribological test: PDMS is a widely used elastic siloxane polymer known for its excellent mechanical properties, including flexibility and durability.[32,33] Incorporating PL nanosensors within a PDMS matrix provides a resilient and deformable structure that can withstand mechanical stresses and adapt to tribological contact conditions. Compared to PDMS, hybrid silica provides less flexibility and deformability, whereas it exhibits good mechanical strength. In addition, hybrid silica and PDMS[34] can exhibit good adhesion to various substrates providing a stable and reliable interface for the nanosensors during tribological measurements.
- Optical transparency: Hybrid silica matrices prepared via sol-gel processes can offer optical transparency, allowing the transmitted light to reach the PL nanosensors without significant absorption in the near UV to NIR (near-ultraviolet to near-infrared) range, [35–37]as well as the PDMS.[38] This property is beneficial for efficient excitation and detection of the emitted light from the nanosensors and thus facilitates accurate measurement of the emitted light and reliable sensing performance.
- Low-temperature elaboration: Sol-gel processes and PDMS polymerizations typically involve low-temperature synthesis, making it compatible with the incorporation of temperature-sensitive PL nanosensors. Such conditions prevent any degradation or loss of sensing properties during the matrix fabrication process.
- Large degree of functionalization: Various functional groups, organic molecules, or nanoparticles can be incorporated into the silica matrix and PDMS during its synthesis, allowing for additional functionalities or tailored interactions with the surrounding environment. This flexibility enables the customization of the matrix to enhance sensor performance and adapt to specific tribological contact requirements.

Both hybrid silica and PDMS polymer offer advantages for incorporating PL nanosensors in tribological contacts. The choice between the two would depend on the specific requirements of the application, such as mechanical properties, fabrication conditions, and desired functionalization options.

3) Lanthanide-based PL sensors

Lanthanide-based materials have been explored and employed as effective PL sensors for temperature and pressure. Compared to other thermo-or mano-sensitive PL materials, such as quantum dots, organic dye and metallic halide complex, Ln-based PL materials possess unique spectral features that make them suitable for high-accurate sensing applications.

One significant advantage of lanthanide-based materials is their long emission lifetime due to initially forbidden f–f transitions of lanthanide ion Ln^{3+}.[39] This property allows for accurate time-resolved measurement and for implementation of time-gated detection techniques. In addition, the long lifetime facilitates the manipulation of nonradiative pathways (for example ET processes) which can be introduced or modified by incorporating an external luminescent species. Through ET, the lanthanide-based material interacts with the external species, altering its emission properties in response to changes in temperature or pressure.

Another beneficial characteristic of lanthanide-based materials is their narrow emission peaks. This feature simplifies data collection and processing, as it enables easy identification and analysis of emitted light, leading to enhanced measurement accuracy.

Besides these spectral features, lanthanide-based materials offer several advantages as sensors due to their chemical properties. Ln-doped inorganic nanoparticles, such as lanthanide-doped oxides[40] or phosphates[41], are known for their excellent thermal stability. In addition, Ln elements are generally considered to be non-toxic, it ensures the safety of using Ln-based materials in various environments, including biomedical or biological applications. Non-toxicity is especially crucial for *in situ* measurement in tribology as the measurement is often conducted in contact with lubricants, components, or even human operators.[42] Other advantages of Ln-based sensors such as the versatile sensing mechanisms, variety of Ln ions and their incorporations, possibility of functionalization of Ln-based sensing systems, make the Ln-based materials highly adaptable and customizable for various sensing applications.[43,44]

1.2 Rare-earth ions and their photoluminescence

1.2.1 Rare-earth: 'Missing' block of periodic table

In the 18th century, the lanthanides were studied as they were previously considered as the hidden elements in the 'missing block' of the periodic table.[39] The term "rare-earth" is commonly used to refer to a group of elements known as the lanthanides, which include elements with atomic number between 57 (Lanthanum) to 71 (Lutetium) on the periodic table. These elements are called rare-earth because they were initially discovered in rare minerals and were difficult to extract. On the other hand, Yttrium and Scandium are not lanthanides but they are often included in discussions about rare-earth elements because of their similar chemical properties and their occurrence in the same minerals.[39]

Unlike other elements on the periodic table, rare-earth ions progressively occupy the inner 4f layer after filling the outermost 5s, 5p, and 6s layers. Having similar outer layers, these atoms have comparable chemical properties, as the outer layers participate in the chemical bond in the same way. Such properties allow rare earths to be easily substituted with one another in a given chemical composition. The spectral properties of rare-earth trivalent ions are closely associated with transitions occurring within the 4f electronic level, shielded by the 5s and 5p solid layers from external influences. The [Xe] $4f^n$ (n = 0–14) configuration represents the ground state electronic configuration of lanthanide (Ln) ions. The 4f-orbitals of Ln ions are well shielded by the outer 5s and 5p electrons. The $5s^25p^6$ subshells, exhibiting a larger radial expansion, lead to the important shielding to make the valence 4f orbitals of Ln

ions are referred to as "inner orbitals". The more stable state of Ln ions is trivalent (Ln^{3+}) due to their electronic configurations, from the first element Cerium to the last element Lutetium in the f-block of the periodic table. The electronic configuration of Ln^{3+} is characterized by a significant energy separation from the [Xe] $4f^{n-1}5d^1$ configuration, with an energy difference (ΔE) exceeding 32,000 cm^{-1}. The radial distribution probability densities for 4f, 5s, 5p, 5d, 6s and 6p orbital of Nd ([Xe] $4f^46s^2$) is shown in Figure 1.4.[45] That specific electronic configuration significantly influences the chemical and spectroscopic properties of Ln^{3+} ions.

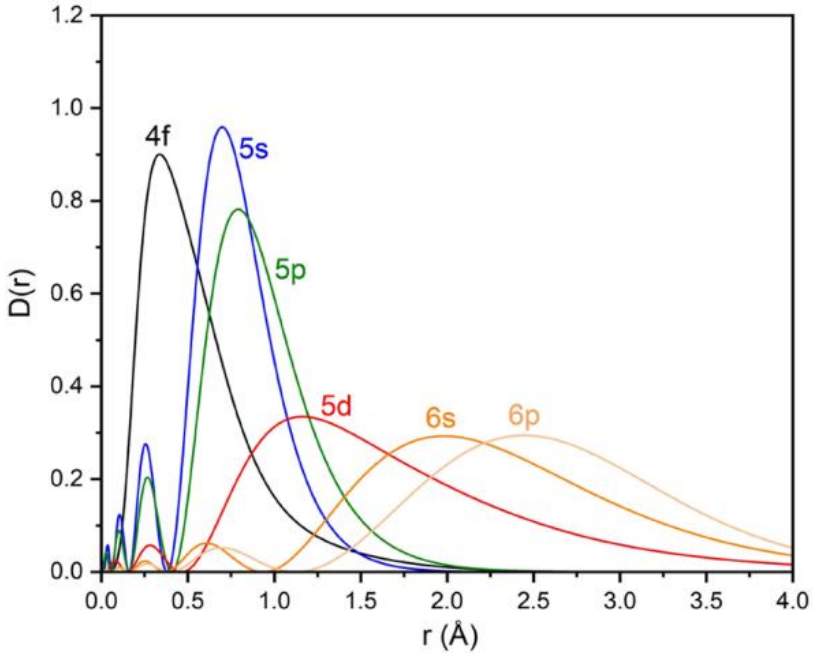

Figure 1.4: Radial distribution probability densities $D(r) = r^2R(r)^2$ for 4f, 5s, 5p, 5d, 6s, and 6p orbitals of Nd atoms. R(r) is the radial wave- function. (Scheme from ref.[45], J. Lu *et al.*, 2023. Copyright© Journal of Chemical Theory and Computation)

Studies of the electronic levels of lanthanide were first developed by Slater, then completed by Condon and Shortley.[46] Later, they were summarized and systematized by other scientists. The complexity of analyzing the energy levels of lanthanides ions is due to the degeneracy of the electronic configurations of the valence 4f-electrons: the $4f^n$ configuration allows for the association of each of the n electrons with one of the seven 4f wavefunctions, and to consider the spin of ±½ for each electron.[39] This association can occur in numerous ways, resulting in a lot of different possible arrangements of electrons within the 4f orbitals. Based on the atomic physics theory, the electronic levels can be described using the Russell-Saunders (RS) coupling scheme.[47] The individual orbital moments of the electrons are combined to form a total orbital moment L. Similarly, the spins of the electrons are coupled to give a total spin moment S. As presented in Equation 1.1, the total moment J is obtained by summing these moments. This RS coupling approach provides a theoretical framework for understanding and describing the energy levels of atoms, including rare earth ions.

$$\vec{J} = \vec{L} + \vec{S}$$

Thus,

$$|L - S| \leq J \leq |L + S|$$

Equation 1. 1

In an approximated representation, the energy levels of 4f ions can be approximated using the fine structure levels of a free ion, denoted as $^{2S+1}L_J$. It is important to note that the L and S quantum numbers are only approximately valid for the first excited levels of rare-earth ions, the intermediate coupling levels are determined by the same J but different L and S. The energy levels of free rare-earth ions can exhibit a degeneracy of (2J + 1). This means that (2J + 1) levels have exactly the same energy, emphasizing the multiplicity and degeneracy of the energy states associated with a specific value of J. As presented in Figure 1.5, the partial energy diagram for an trivalent rare-earth ion, taking an example of Eu^{3+}, with the spin-orbit interactions of $4f^6$ electrons.[48]

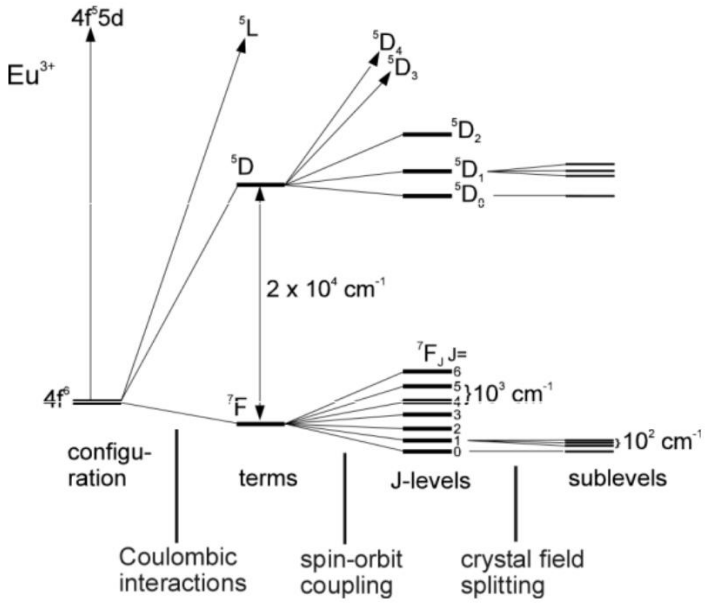

Figure 1.5: Partial energy diagram for Eu^{3+}, $4f^6$ ions show the related magnitude of the interelectronic repulsion, spin-orbit coupling and ligand field effects. (Scheme from ref. [48], M. Werts, 2005. Copyright© Science progress)

Lanthanide-based materials have become more and more developed in different ways, in an inorganic or an organic host, nanoparticles, complexes, hybrid materials and polymers. Besides their PL properties, their interesting features are also widely used in magnetics,[49,50] optoelectronics,[51] energy conversions.[52,53] In this work, we are mainly interested in the photoluminescence of lanthanide ions, which will be discussed below.

1.2.2 Lanthanide photoluminescence

1) Photoluminescence

The term luminescence was introduced in literature at the first time in 1888, by Wiedemann,[54] as the excess emission over and above the thermal emission background. Later, Vavilov (1952) proposed to complement this term: the luminescence is the excess emission over and above the thermal emission with a consideration emitting duration.[55] And this definition is continuously used until now.[56,57]

Luminescence is generally used to describe the light emitted from relaxation of excited electrons. As shown in Figure 1.6, this phenomenon in a solid crystal consists of a) Absorption of energy from an external source; b.) Promotion of electrons to the upper energy; c) Relaxation of excited electrons to the lower level. The released energy can be transformed to non-radiative relaxation or radiative relaxation by light emitting and can also be accepted by its surroundings following ET process. To distinguish various excitation sources of luminescence, different prefixes have been added to clarify the luminescence phenomena, as illustrated in Figure 1.6. When electrons absorb the energy that comes from high energetic wavelengths, the emission of light is called photoluminescence. Others excitation source such as thermoluminescence, defined by the emission following an absorption of energy from heating radiation; or the chemiluminescence, meaning the emission after a chemical action.

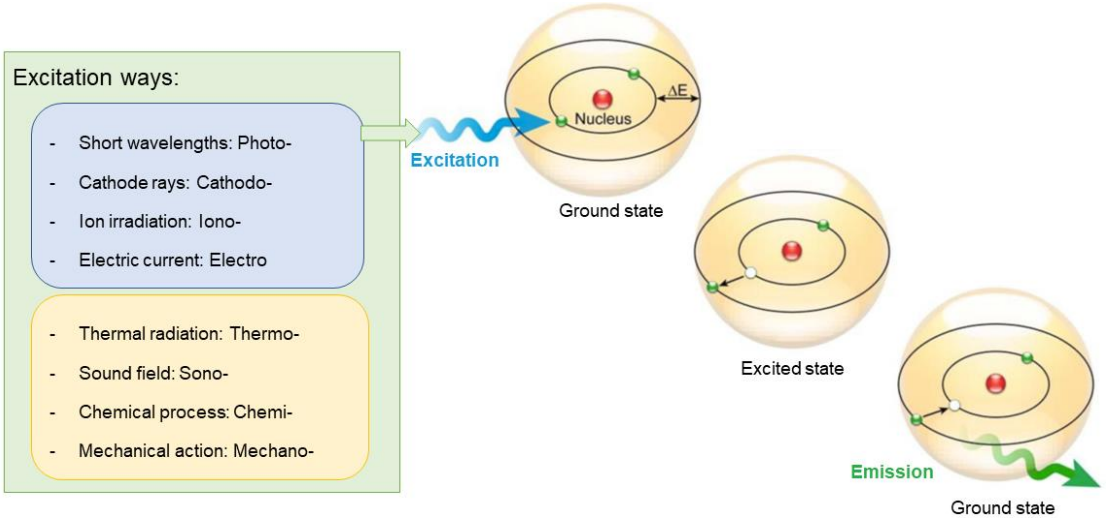

Figure 1.6: Scheme of simplified luminescent mechanism and the major classifications of luminescence.

The excitation-emission process can be impacted by external parameters, typically temperature. After photon-irradiation, vibrational levels in the excited states can be activated by increasing temperature, the probability of excited electrons in the upper vibrational levels rises exponentially to the temperature, described by Boltzmann's distribution, which will be more deeply discussed in section 1.3.1. Additionally, the lattice parameter is a critical variable in the luminescence process. For example, the nature of constituents, and their concentrations, positions; lattice size, types of symmetry, as well as the external change can induce structural variation. Early in 1960s, the impact of stress-induced structural change on the photoluminescence was studied by Kaplyanskii[58] and Runciman[59] groups to resolve the

symmetry of anisotropic centers in cubic crystals. These sensitivities to temperature or to pressure of photoluminescence can be interesting for further studies on sensing applications.

Thermoluminescent and mechanoluminescent materials are also studied, respectively, as temperature or pressure sensor.[60–62] But we only focus on the photoluminescence of materials in this thesis.

2) Energy transition between levels of lanthanide ions

Lanthanide optical spectroscopy has been introduced in 1936 by van Vleck,[63] however the interest of lanthanide material in optics can date back to the 1880s. Later, lanthanide optical properties started to be widely applied in optical devices. The first lanthanide-based sensor was proposed by Soini and Hemmilä in 1979,[64] for time-resolved immunoassays, which has inspired numerous studies on bio-applications. Nowadays, lanthanide-based sensors have become more and more developed in other areas of fundamental scientific technology and engineering. The emitted light of lanthanide ions corresponds to the energy released from the inter-configurational electronic transition. The generally allowed transitions between the electronic levels of rare-earth ions are the $4f^{n-1}$-5d transitions, whereas the 4f-4f transitions are forbidden as the decay time is relatively long. Moreover, the emissive transition can also be the transfer of charge via a delocalized electron from a neighboring ligand ion to rare-earth ions.

- **$4f^{n-1}$-5d transitions**

The 5d orbitals of rare-earth ions are more influenced by the surrounding crystal environment compared to the 4f orbitals. Consequently, the energy of the $4f^{n-1}5d$ configuration of rare-earth ions exhibits significant variations depending on the specific crystal host material. While most $4f^n$ to $4f^{n-1}$-5d transitions occur in the ultraviolet or even x-ray spectrum, there are exceptions such as Ce^{3+} and Pr^{3+}, where their $4f^n$ to $4f^{n-1}5d$ transitions have been observed in the visible range.[47]

In many cases, the $4f^{n-1}5d$ states can exhibit strong fluorescence due to the electric dipole allowed nature of the 4f-5d transitions. These transitions are approximately 10000 times stronger than the strongest transitions within the $4f^n$ configuration. On the other hand, the weak oscillator strengths of 4f-4f transitions result in long-lived states with lifetimes in the microsecond to millisecond range.[65] In contrast, the lifetimes of 4f-5d transitions are generally in the range of dozens to hundreds of nanoseconds.

- **Transition via charge transfer state**

Luminescence due to charge transfer transition of the lanthanide ions Yb^{3+} has first been observed by Nakazawa in 1977.[66] Under high energy light excitation of UV light or X-ray, the electrons promote to a charge transfer state (CTS). Emission from CTS can rarely be observed as the relaxation to ^5D_J state is fast. After fast non-radiative relaxation to lower 4f levels, emission in the visible range can be observed. Lanthanide ions, such as Eu^{3+} and Yb^{3+} are typically used in charge transfer luminescent materials.[67–69] The charge transfer luminescent material are mainly applied for X-Ray detection and neutrino capture.[69,70]

- **4f-4f transitions in rare-earth ions: Judd-Ofelt Theory**

The narrow, long-lived emission due to 4f-4f transition of rare-earth ions exhibit in wide wavelength range from UV to infrared (IR). Initially, the 4f-4f through electric dipole (ED) transitions are forbidden by the Laporte selection rule as the parity of the initial and final states remains unchanged. However, when the Ln ions are in a special medium, the selection rule can be relaxed due to the mixing of opposite parity states into the $4f^n$ levels.

The spectral properties of a rare-earth ion in a given structure are usually characterized by the 4f-4f transitions peaks. Judd-Ofelt theory describes a simplified model for explaining the intensities of f-f transitions in both solids and solutions.[39,71] This theory only considers the $4f^n$ electronic configuration and does not account for inter-configurational $4f^n$-$4f^{n-1}$ $5d^1$ interactions. However, the effects of spin-orbit coupling are taken into consideration in this model. Judd-Ofelt theory has been used to understand and predict the spectral properties of lanthanide, mostly in inorganic host, but less in lanthanide complexes.[72]

The multiplicity (2J+1) of the electronic configuration depends on the association of the electrons with each 4f wavefunctions. The complete $4f^n$ energy level diagram of trivalent lanthanide ions has been reported in 2005, the energy levels can extend to 190 000 cm^{-1}.[71] However, for many luminescent systems, a partial energy level diagram that covers an energy range up to 50 000 cm^{-1} can provide sufficient information. The partial diagram has been published by Carnall for trivalent lanthanide family (Ln^{3+}) from $Ce^{3+}(4f^1)$ to $Yb^{3+}(4f^{13})$ by using $LaCl_3$ as the host lattice,[73] as plotted in Figure 1.7.

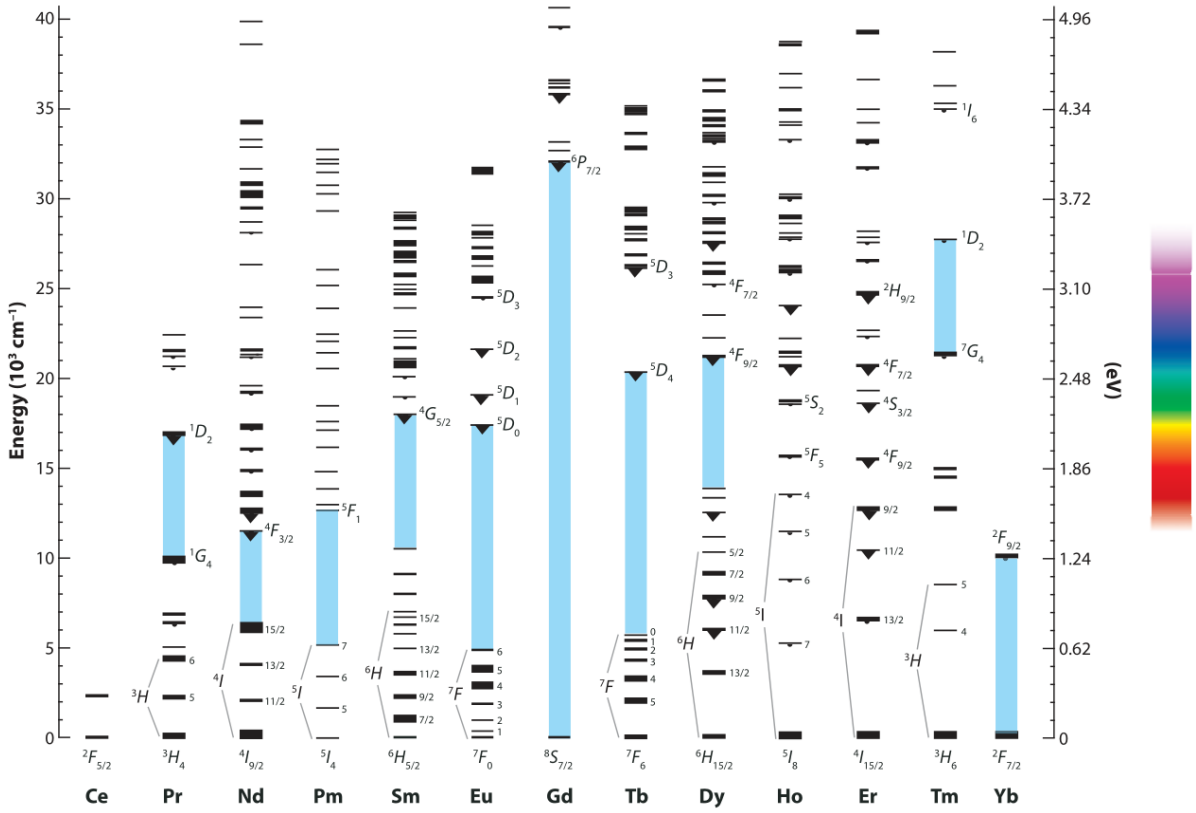

Figure 1.7: Dieke energy diagram for trivalent lanthanide ions, the largest energy gaps are shaded in blue. (Scheme from ref.[74], M.D. Chambers and D. R. Clarke, 2009. Copyright© Annual Review of Materials Research)

The energy levels diagrams are very important in lanthanide luminescence characteristics studies, by precisely proposing the energy offset of each possible transition. Nonetheless, the energy levels of Ln^{3+} can vary slightly with the crystal lattice, emission peak shift can thus be observed with same Ln^{3+} in different host. To excite the electrons from the ground state, precise monochromic light is always required. However, alternative excitation by an external sensitizer can also be considered. Due to the complexity of electrons transitions mechanism, the Ln^{3+} can emit light in a wide region, from ultra-violet (UV) to near infrared (NIR). The ET process can be also observed in Ln^{3+} luminescent system.

1) Radiative relaxation

The emission of luminescence from an excited state of lanthanide ions is called the radiative transitions (Figure 1.8a&b), which can occur through electric dipole (ED) and magnetic dipole (MD) mechanisms in lanthanide ions.[75,76] MD transitions result from the interaction between the lanthanide ion and the oscillating magnetic field component of light. These transitions are allowed by the Laporte selection rule,[47] but they have a low transition probability, and their intensity is independent from the local environment.

On the other hand, ED transitions arise from the interaction between the lanthanide ion and the oscillating electric field component of light. These 4f-4f ED transitions are forbidden by the Laporte selection and thus strongly depend on the medium with the mixing of opposite parity states into the $4f^n$ levels. The degree of mixing is influenced by the lanthanide ion's placement on a site with stronger deviation from inversion symmetry and a reduced energy difference between opposite parity states. This enhanced mixing degree leads to higher probabilities of electric dipole transitions. Consequently, the intensity of electric dipole transitions is strongly dependent on the local environment surrounding the lanthanide ion. For example, the transition $^5D_0 \rightarrow {}^7F_2$ of Eu^{3+} has been reported as a hypersensitive ED transition emission to environment.

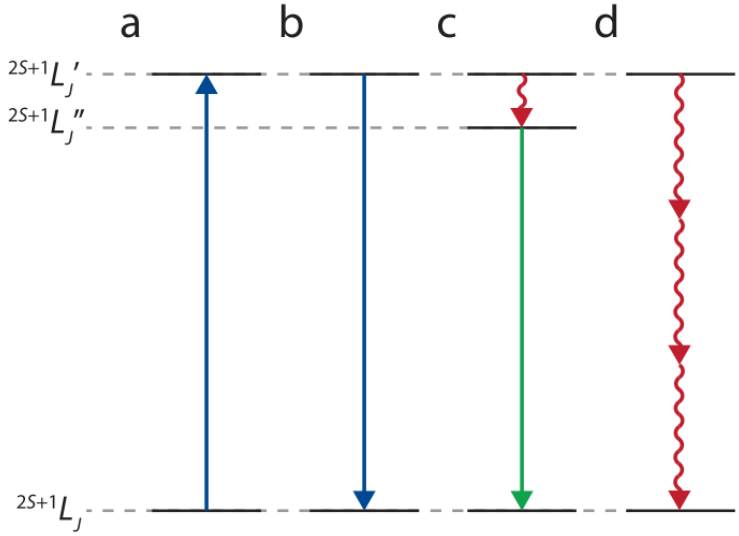

Figure 1.8: Luminescent mechanism in rare-earth ions: a.) excitation to the upper level; b.) Radiative relaxation to the ground state; c.) One-photon non-radiative relaxation followed by radiative relaxation to the ground state; d.) Multiple-photons non-radiative relaxation to the ground state. (Scheme from ref.[76], J. Hest, Thesis in 2018. Copyright© ProefschriftMaken)

2) Non-radiative relaxation

Non radiative energy relaxation in lanthanide ions can be followed by an ET to another site, or occur through the release of non-emissive phonons, which are the quantized vibrations of the surrounding lattice. The relaxation of one phonon is usually observed between two energy levels with small offset, and the emission from lower energy level to the ground state can occur next (Figure 1.8c). In cases where the energy gap between two levels exceeds the energy of a single phonon, multiple phonons can be simultaneously released. This process is referred to as multi-phonon relaxation (Figure 1.8d). The efficiency of multi-phonon relaxation increases when the energy gap can be bridged by a smaller number of phonons.

The proportion of non-radiative relaxation will be influenced by the temperature. When the energy gap between two levels can be bridged by less than 4 or 5 times the phonon energy, multi-phonon relaxation becomes dominant over radiative relaxation.[77] The increase in temperature induces greater non-radiative relaxation, called thermal quenching. Additionally, other interactions among Ln^{3+} ions or between Ln^{3+} ions and other species can also interfere with the probability of non-radiative transition.

1.2.3 Characterizations of Ln-photoluminescence

1) Absorption and emission spectrum

Photoluminescence spectrum presents luminescence intensity in the function of wavelength, frequency, or energy of radiation. Excitation and emission spectra are the two main types of luminescent spectra, which show the dependence of photoluminescence intensity on the wavelength or frequency of the exciting or emitting light, respectively (Figure 1.9). In addition, absorption spectrum is also a classical tool to characterize the absorption of materials.

The absorption spectrum is often represented as a plot of absorbance or transmittance as a function of wavelength or energy. The absorbance is calculated by the ratio of the amount of absorbed light to the amount of excited light of source. Quantitative analysis can be performed using the Beer-Lambert law[78], which relates the absorbance of a substance to its concentration and the path length of light through the sample. By measuring the absorbance at a known concentration, a calibration curve can be constructed, allowing the determination of the concentration of an unknown sample based on its absorbance. In addition, the absorbance peak position allows determine the wavelength at which the substance absorbs light most strongly. The absorption spectrum provides valuable insights into the energy levels and electronic transitions occurring within the sample, which can help in understanding its optical and chemical properties.

The excitation spectrum measures the number of emitted photons at assigned wavelength under varied wavelengths of radiation at constant intensity, shows a general distribution of emission in the function of exciting wavelength. Since only the radiative emission is taken into account by excitation spectrum, excitation spectrum cannot be considered equally as absorption spectrum, which describes the dependence of number of absorbed photons on wavelength of exciting light. Therefore, absorption spectrum is generally used for completing

excitation spectrum to analyze simultaneously the non-radiative process. Experimentally, the excitation spectrum is an essential characterization, allowing to determine the excitation pathway of the substance.

Emission spectrum or also called photoluminescence spectrum, shows the number of emitted photons as the function of emission wavelength or frequency, Under exciting source, emission spectrum allows to quantify the number of emitted photons by their emission intensity. However, the absolute emission intensity usually depends on many external conditions, such as sample preparation (quantity, surface aspect, physical forms…) or excitation source (light power, focus status…), and also internal parameters within spectrometer. Therefore, when measuring using emission intensity as a variable, the external variables must be carefully controlled. In addition, a reference emission peak is usually used to calibrate the change in emission intensity from the internal variables. The ratio of the reference intensity to the variable intensity is usually called the relative emission intensity, or the luminescence intensity ratio (LIR). The reference emission can be collected from an additional device such as a monochromatic lamp, or from an internal emitter. The position of emission, or centroid wavelength (λ) of emission peak is also used as a parameter to characterize the photoluminescence. The shift in the emission peak (Δλ) shows the energy of the emission, thus reflects the change in the energy levels of the emitter. The wavelength of emission band can also be impacted by internal parameters of spectrometer, a reference position must be used to correct the uncertain shift caused by the spectrometer.

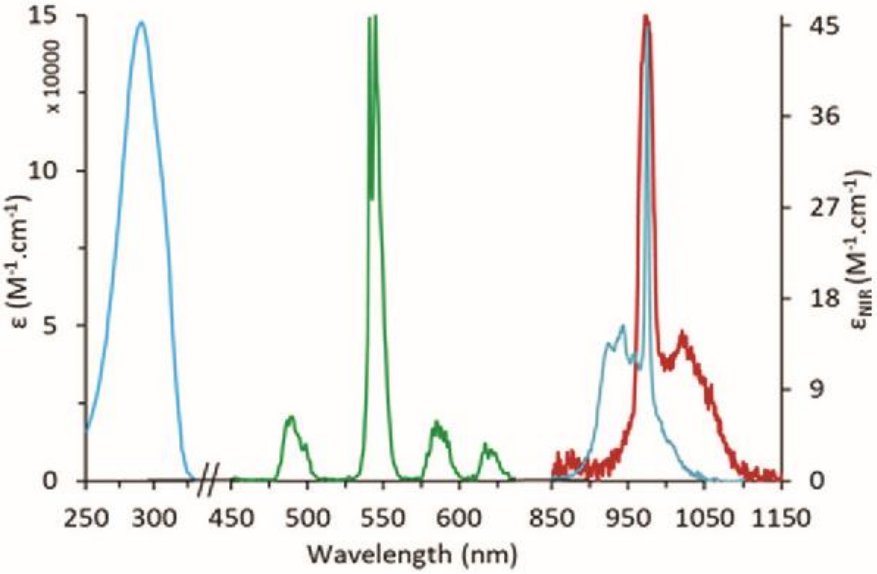

Figure 1.9: UV-Vis-NIR absorption spectrum (blue) and normalized emission spectra (λexc = 292 nm) in the visible (green) and NIR (red) domains for the Tb^{3+}/Yb^{3+} complex in CH_3OH. (Scheme from ref.[79], R. C. Knighton *et al*. 2021. Copyright© Chemical Communications)

2) Quantum and energy yield

Upon photoexcitation, the quantum yield of substance is defined by the ratio of the number of emitted photons to the number of absorbed photons. The measurement of quantum yield simultaneously requires the absorption spectrum and the emission spectrum, and a no-emitting substance with same physical properties as reference to correct the uncertainty caused by diffusion or reflection of matter. For anti-Stokes photoluminescence, as the emitted

photon is more energetic than the absorbed photon, the energy yield is more often used to quantify the energy conversion. The concept of energy yield was first introduced in Vavilov's works in 1924,[56,80] showing that substance with high energy yield has more luminescence. Quantum and energy yield are always considered as reliable characterizations to quantify the capacity of radiative emission upon photoexcitation for a PL material.

3) Luminescence rise and decay

In photoexcitation processes, any variation in the excitation source results in changes in the intensity of the emission. Depending on time (t), the variation in emission intensity is not instantaneous. The relation between the decrease or increase in emission intensity in the function of time was resumed by Stepanov and Gribkovskii in 1963,[81] as shows in Equation 1.2:

$$I(t) = I_1(t_1)\exp\left[-(t - t_1)/\tau\right]$$

Equation 1. 2

I is the emission intensity as a function of time $t = 0$ and $t = t_1$, which are the time of the beginning and the end of excitaiton process; τ determines the mean time of emission rise or decay (Figure 1.10).

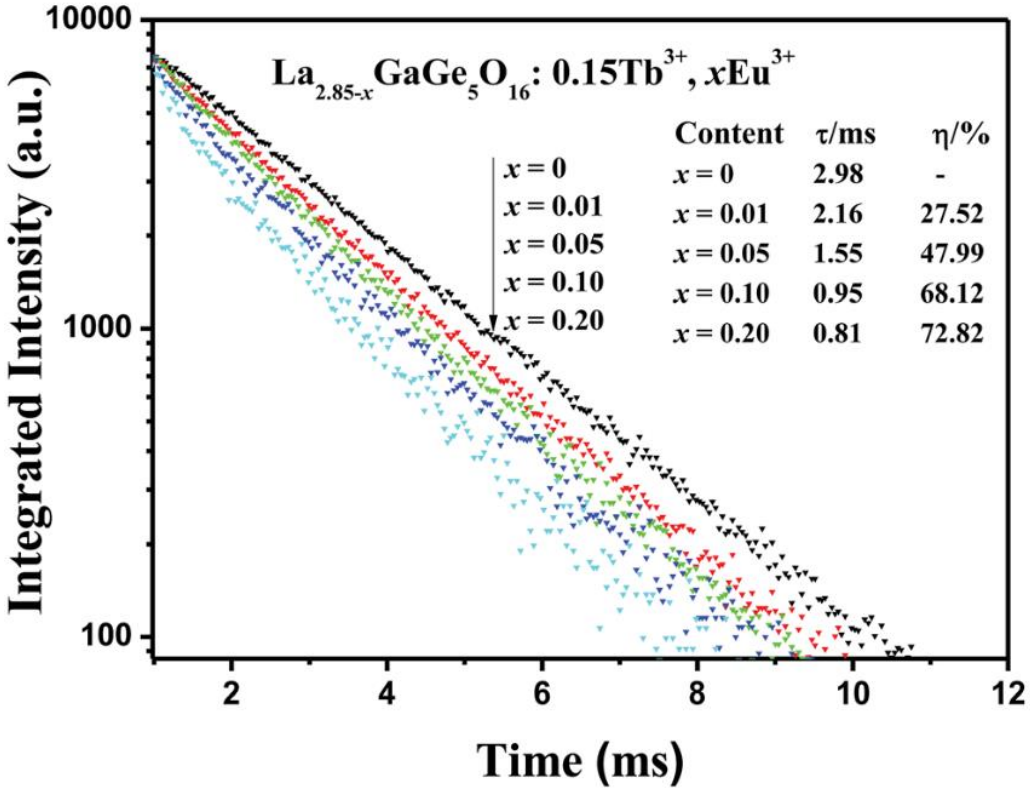

Figure 1.10: Typical Tb^{3+} luminescence decay profiles observed for $Ln_3GaGe_5O_{16}$ in the solid state at room temperature, with excitation at 377 nm. (Scheme from ref.[82], J. Zhou and Z. Xia 2014. Copyright© Journal of Materials Chemistry C)

The measurement of rise or decay time, or generally called the lifetime of substance, requires pulsed excitation and time-resolved photon detection. The wavelength of excitation source is selected to match the maximal absorption. The frequency of the excitation pulse must be low enough to adapt to the lifetime of the emission, especially for long-lifetime compounds like lanthanide-based phosphor, which provide lifetimes up to milliseconds.[39,56] Lifetime measurement is particularly important in complex quantum mechanisms, such as ET or emission quenching processes. By varying the excitation and emission wavelength, it becomes possible to distinguish different PL pathways. However, it should be noted that even for the same emitter, the lifetime can be very different depending on their environment.[39]

1.3 Energy transfer in rare-earth ions

1.3.1 Förster resonant energy transfer (FRET)

In 1948, Förster studied the rate of ET between dipoles,[83] and then the critical distance (R_0) has been defined when the probability of ET and spontaneous deactivation of ion donor starts to become equal (Figure 1.11a).[84,85] This theory has later been extended by Dexter to complete with other interaction types.[85–88] It has been clarified that ET can only occur if there is a spectral overlap of the emission of the donor and the absorption of the acceptor and if the interaction of two participants is suitable (Figure 1.11b). The interaction can be electric or magnetic multipolar or be an exchange interaction with wave function overlap. According to the theory of Förster resonant ET (FRET) for electric multipolar interaction, a R^{-n} dependence of the ET rate on the intersystem distance can be found, with n = 6, 8, 10… for dipole-dipole, quadrupole-dipole and quadrupole-quadrupole, respectively. Therefore, the FRET rate can be easily influenced by contraction or distortion of crystal lattices.

When the concentration of rare earth ions is increased in a host matrix, whether it is for the same type of ion or different types through co-doping, ion-ion interactions start to emerge. The interactions are mainly ET in the 4f-4f transitions of Ln^{3+} ions. In addition, in a ligand-Ln^{3+} systems, FRET can occur if a donor ligand is suitable to the Ln^{3+}, which will act as an acceptor. Excitation of Ln^{3+} by an activated ligand sensitizer with a large absorption band is usually called ‘Luminescence sensitization’ or ‘Antenna effect’.

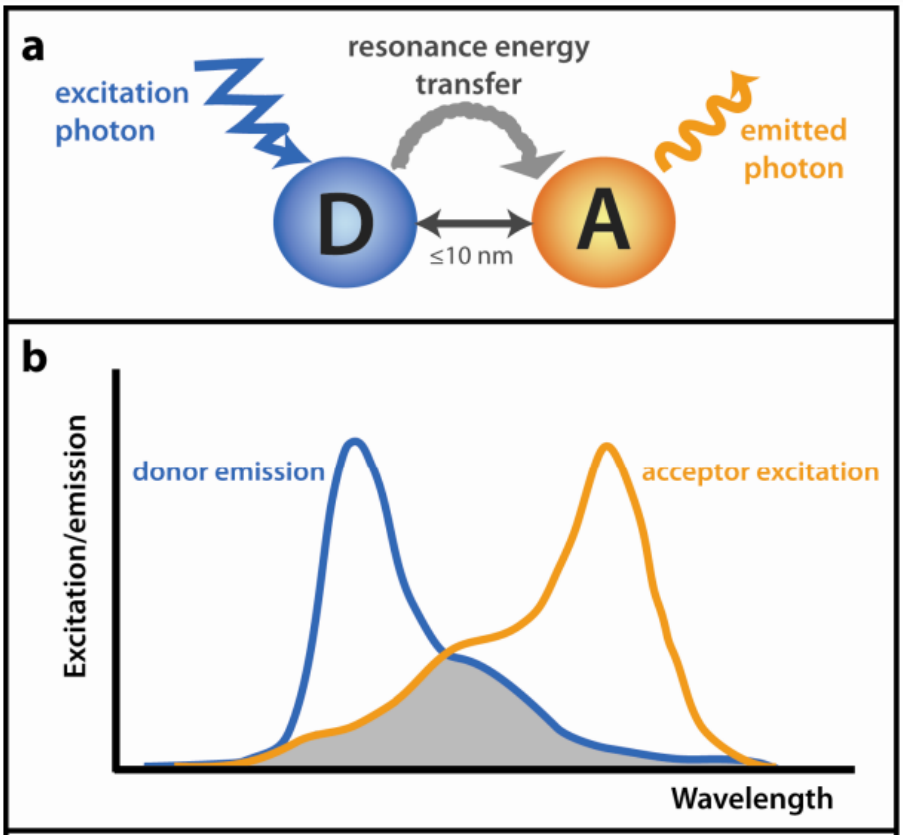

Figure 1.11: Förster resonance energy transfer (FRET) fundamentals: (a) Schematic representation of FRET. Excited donor (D) transfers its energy by a non-radiative process to the nearby acceptor (A), causing it to emit fluorescence. The distance between fluorophores should not exceed 10 nm; (b) The donor emission peak must overlap with the acceptor excitation spectrum. The grey area corresponds to the overlap region. (Scheme from ref.[89], E. Šimková and D. Staněk, 2012. Copyright© International Journal of Molecular Sciences)

1.3.2 Luminescent sensitizer to rare-earth ions

Luminescent sensitization has been developed as an alternative to enhance the Ln^{3+} emission intensity, as the f-f transitions probabilities in Ln^{3+} electrons are usually too low to provide a strong density of Ln electrons population in f-orbital to upper levels. An additional light absorbent is used to transfer energy to the Ln^{3+} emitter, improving the absorption efficiency. The additional species could be transition metal groups (such as tungstates, molybdates, vanadates, etc..)[72], another strong absorbent Ln^{3+} ion [85,90] or organic ligands[91]. Owing to the multiplicity of energy levels of lanthanide ions, interaction between lanthanides and other species is usually easy to occur.

1) The Antenna Effect

The antenna effect has briefly been described by De Andrade *et al.*, [92] as shown in Figure 1.12). Enhanced absorption of UV radiation by the sensitizer; 2). Non-radiative relaxation from the excited singlet state (S_1) to their lowest triplet state (T_1): 3). ET to the emitter; 4). Emission from relaxation of the excited emitter. The sensitizer can be the anionic group in an

inorganic compound (like vanadate, oxides) or an organic ligand[92–98] (like acetylacetonate, phenanthroline). In the case where the organic ligand is the sensitizer, the interaction between the ligands may further improve the efficiency of the antenna effect. [92–95] Aromatic (π-π*) and/or (n-π*) transitions between unsaturated ligands, occurring mostly for ligands with large cross sections, allow to enhance the antenna effect and result in more efficient ET.

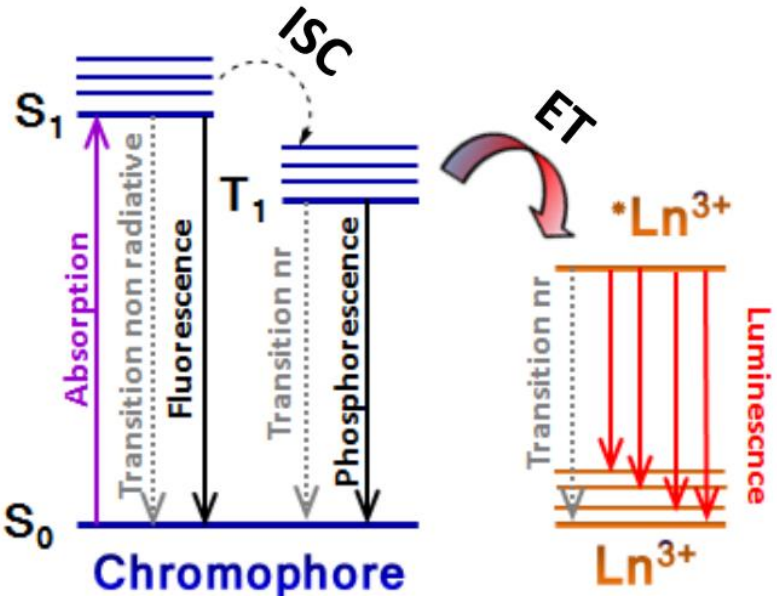

Figure 1.12: Energy transfer process between organic chromophore to lanthanide ions (Transition nr: Non-radiative transition; ISC: Intersystem crossing; ET: Energy transfer; Scheme from ref.[99], K. Nchimi nono. Thesis in 2014. Copyright© Hal. Université de Strasbourg)

2) Quenching in Ligand-Ln energy transfer process

The overall ET pathway between ligand and metal (ligand-ligand, ligand-metal and metal-metal) can be strongly influenced by crystal lattice parameters (distance donor-acceptor[83,84,86]), ligand orientations[100] and parallelism[101], and quenching sites (surface defect[56,85,102,103], oxygen presence[104,105,114,115,106–113]). The oxygen-quenching can occur with the presence of oxygen site in OH[114,115] or O_2.[107]. The presence of oxygen in the OH quenches the emission of the luminescent center by its efficient absorption from the O-H vibration. Meanwhile, O_2 molecules in solution or air shorten the triplet lifetime of organic ligand and thus reduce the quantum yield of the triplet (T_1) emission of the ligand. This O_2-quenching effect is mostly observed in organic complexes when the ligand acts as a sensitizer for the Ln^{3+} emitter (Figure 1.13). [107,116]

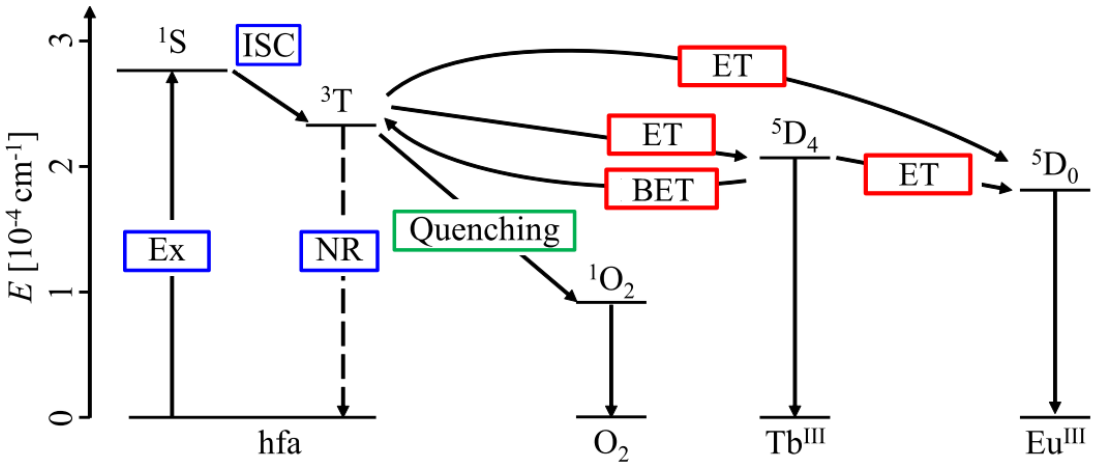

Figure 1.13: Proposed mechanism for energy transfer between ligand and Ln^{3+} when O_2-quenching occurs (Ex: excitation, ISC: intersystem crossing, NR: nonradiative process, ET: energy transfer, BET: back energy transfer, hfa: hexafluoroacetylacetone) (Scheme from ref. [116], M. Kasai *et al*. 2020. Copyright© Sensors)

Once the quenching effect occurs, the traps absorb the energy of the emitter and result in a substantial decrease in emission intensity. The quenching site can also absorb directly from the ligand, making ligand-Ln^{3+} ET much less efficient. Furthermore, it has been recently clarified that the intramolecular ET rate between ligand-metal (Eu) cannot be simply described by the distance-dependent Förster or Dexter theory.[94,117,118] The ET rate between L-M should be carefully modelized with the other competitive deactivation processes, lattice symmetry, uncontrolled vibrational quenching. Wu *et al.*[118] has demonstrated that the crossing-controlled ET model is predominant over FRET theory in ET L-M mechanism.

Additionally, the ET or energy migration (EM) between the emitters can enhance the quenching, leading to an overall luminescence quenching. Considering FRET theory, when the concentration of emitters is high, the interionic distance is shortened, and the ET is thus optimized. The impact of the emitter concentration on the quenching effect is called concentration quenching.[39,57,87] Such phenomena are usually observed in lanthanide-based compounds. Consequently, the dose of Ln^{3+} ions is always low, known as Ln-doping.

1.3.3 Energy transfer among rare-earth ions

The ET between two Ln^{3+} occurs when the emission band of the donor and the absorption band of the acceptor overlap. However, as the 4f-4f transition of Ln^{3+} exhibit narrow emission and absorption bands, ET is only allowed between two Ln^{3+} with highly matched of the energy transition.

The 'Stokes' rule' was first formulated in 1852, to describe the phenomenon that the wavelength of excitation is less than the wavelength of emission, the difference being called the Stokes' shift. Due to the unique features of 4f-4f transitions, the Stokes' shift of the Ln^{3+} emitter is generally smaller than others, such as transition metal ions, or organic dyes. Therefore, ET between two identical Ln^{3+} centers is considerably efficient, which is usually called energy migration (EM).[93] Like classical Ln^{3+}-Ln^{3+} ET, the efficiency of EM highly

depends on the interionic distance.[83] Ln^{3+}-Ln^{3+} EM is widely applied in optics materials. In a classic ET process, the EM between the Ln^{3+} sensitizers allow the energy to be spread in the crystal lattice, thus enhancing the probability of ET. This process is often used to optimize the efficiency of multi-photon assisted ET, such as in the Yb^{3+}/Er^{3+} system. The concentration of Yb^{3+} is often higher than needed to activate Yb^{3+}-Yb^{3+} EM.[119,120] However, efficient EM facilities surface quenching, especially in small material like the Ln-doped nanoparticles, which induces significant decrease in emission efficiency.[121] Consequently, the concentration of the Ln^{3+} sensitizer is often between 10 mol% to 20 mol% to reduce surface quenching as well as to activate ET.

1.3.4 Multi-photons excitation via energy transfer

According to Stokes' rule, a higher excitation energy is indeed required to activate a lower emission energy. However, multi-photons assisted excitation allows an emission energy higher than the absorption energy to be obtained. This process is also considered as anti-Stokes emission, which requires upon multi-photons pulsed excitation with femtosecond frequency.[39] Conversion of low-energy photons into higher-energy photons is allowed, which is known as upconversion.

1) Upconversion

The theory of upconversion luminescence was first proposed in 1962,[122] and then widely developed in next 20 years.[123–125] The advance in upconversion optics of nanomaterials has been first reported for biological applications by Heer *et al.*[126] in 2003. The synthesis and characterizations of upconverting phosphates nanoparticles (doped Yb^{3+} with Tm^{3+} or Er^{3+}) has been published. In the next year, Auzel has introduced the physical fundamentals of upconversion phosphors.[52] In the theory of Auzel, six types of sensitizations in upconversion luminescence were clarified. Later, the classifications have been simplified as shown in Figure 1.14.[127]

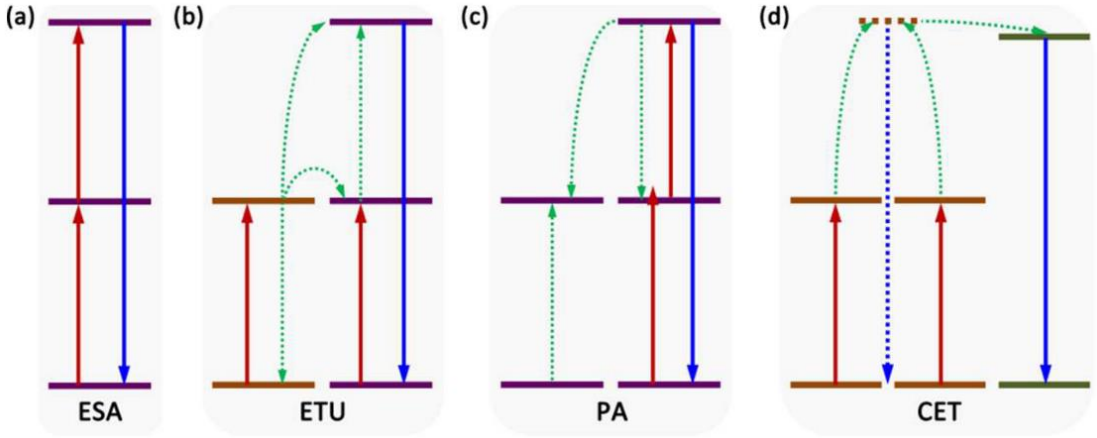

Figure 1.14: Scheme of two-photons upconversion processes: Full arrows in red and in blue are the excitation and radiative emission, respectively. Dashed arrows in green stand for energy transfer processes. Non-radiative relaxations are not presented in Figure for clarity. a.) ESA (Excited state excitation); b.) ETU (Energy transfer upconversion); c.) PA (Photons

avalanche); d.) CET (Cooperative energy transfer). (Scheme from ref.[127], H. Dong *et al.* 2015. Copyright© Chemical Society Reviews)

1) ESA or Two-step absorption (Auzel): one electron of S absorbs two times of energy to promote to its upper levels.
2) ETU or Addition de Photons par Transfers d'Energie (APTE) effect (Auzel): excited electrons of S transfer subsequently energy to ion A, and then A emit from the upper levels.
3) PA: promotion of electron to intermediate state by one-photon excitation, following by other absorption to the excited state, from cross-relaxation of a neighboring ion.
4) CET or Cooperative sensitization (Auzel): same as the APTE effect except the A has no intermediate energy level.

2) Upconversion energy transfer

ET between a sensitizer and an acceptor can occur through the classic process where the sensitizer transfers energy from its higher energy excited states to the ground state of the acceptor. Besides the ET following the Stokes' rule, multi-photons assisted ET allow a higher emission energy than absorption energy.

APTE process or also called ETU occurs usually in Er^{3+} (for NIR to green) or Tm^{3+} (NIR to blue) doped luminescent materials, with Yb^{3+} as the sensitizer. To reach the emitted level of Er^{3+} or Tm^{3+}, two-equivalent or three-equivalent Yb^{3+} photons are required (Figure 1.15).[126,128] The inorganic host is mostly used for Yb^{3+}; Er^{3+} or Tm^{3+} doped materials. Depending on the synthesis, the size of particles can vary from micron-scale to nanoscale. Oxide,[129] fluoride, [130–132] molybdate,[133] tungstate,[134] phosphate[126,134] and vanadate[135–137] are the current host for those nanoparticles. Upconverting nanoparticles can be produced in many synthesis methods such as sol-gel,[138] co-precipitation,[139–141] hydro-and solvo-thermal,[142–144] thermal decomposition[128,145] and combustion.[146,147] Recently, multi core-shells Ln-doped nanoparticles are studied to optimize the efficiency of ETU for diverse applications. [121,148,149]

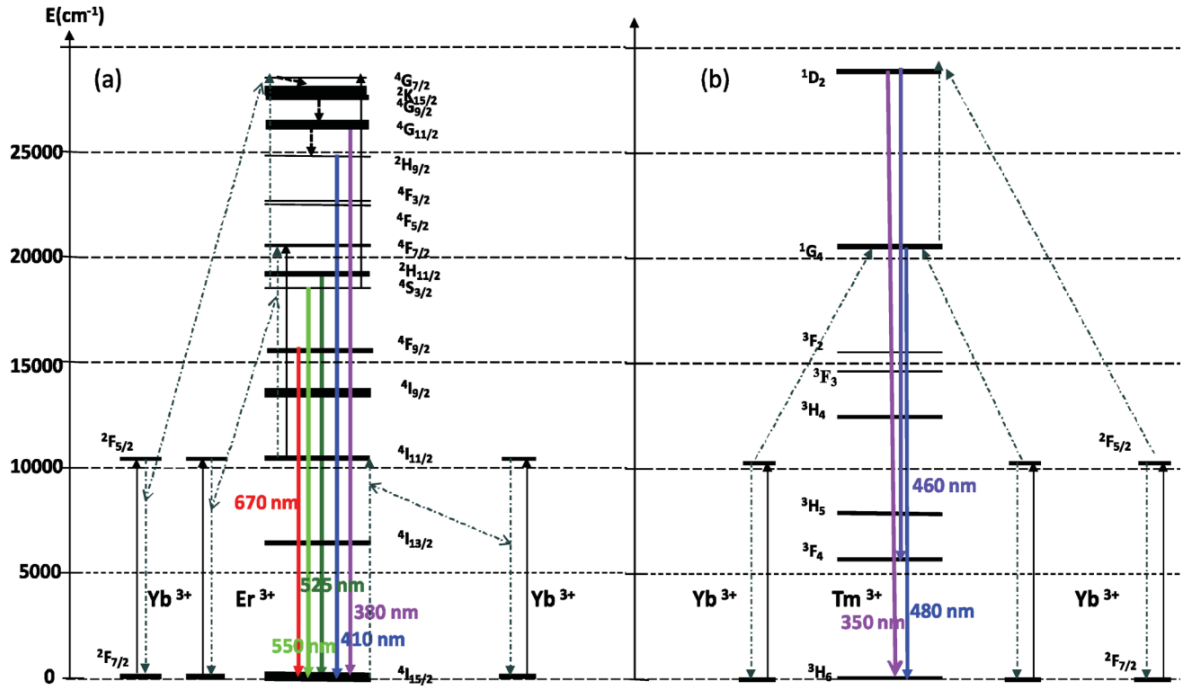

Figure 1.15: Schematic energy level diagrams showing cooperative sensitization and energy transfer up-conversion for the Yb^{3+}/Er^{3+} and Yb^{3+}/Tm^{3+} systems. (Scheme from ref.[128], S. Mishra *et al.* 2012. Copyright© Dalton Transactions)

The advantages of upconverting luminescence are that it converts low-energetic light into emission in the visible or UV range. The interest of NIR excitation over direct excitation by UV light is to eliminate possible perturbed emission from the utilization medium and to minimize the degradation of host materials induced by photoionization.[52,44] Moreover, NIR light provides more penetration than UV light, thus more efficiency and accuracy in sensing applications. Scientific research and industrial engineering in diverse fields like biology, mechanics, chemistry, optics can take lots of advantages of upconversion material. However, with ions having several equal energy gaps, the ET between these levels can result in the de-excitation of the highest level. This de-excitation process leads to the simultaneous excitation of two lower energy levels, specifically the intermediate level. Such behavior is known as cross relaxation, which is the main cause of the concentration quenching of lanthanide ions.[47]

3) Non-radiative relaxations in upconversion excitation

Several effects brought by the general ET process can also interfere with the UC process. For example, emission quenching due to the concentration,[150] the surface defects of the nanoparticles,[151] the thermal effects[152] or the presence of OH,[114] can significantly reduce the intensity of UC emission. In multi-photons excitation process, increasing concentration of sensitizers optimizes the rate of ET. Thus, the compromise between the concentration quenching of sensitizers and the efficiency of multi-photons excitations should be considered.

Besides, the laser-induced heating phenomenon should be carefully considered in upconversion system. Compared to one-photon assisted excitation, multi-photons assisted excitation has lower quantum yield.[84,91,153,154] the proportion of non-radiative relaxation is important.[115] The laser-induced heating can be impacted by the laser power density, which affects significantly the intensity of the luminescence by interfering with the population of

electrons in the excited state of the emitter ions.[155–158] Moreover, the influence of the particle morphology on non-radiative process[132] was also studied: a higher non-radiative process associated with a higher red/green emission was more evidenced in smaller nanoparticles. Recently, an increase in temperature leading to an increase in the laser-induced heating effect has also been reported.[159] This laser heating effect could be beneficial because Ln^{3+} doped NPs are used as nano-heaters in the field of photothermal energy.[129,132,137,160] Precise and selective heating on a nanometric scale could be used for cancer treatment, data storage[161–164] or microflow control.[165] However, laser heating can lead to substantial uncertainty in temperature measurement for the upconversion thermometer.[137,159]

1.3.5 Conclusion

Excitation of Ln^{3+} ions by the ET process is nowadays more and more developed as an efficient excitation method. A large amount of advantage in ET has been briefly presented above, although there are some disadvantages like possible quenching, important non-radiative relaxation, studies on the Ln ET process remains very interesting. Besides the general benefits of the ET process, the interaction between the sensitizer and the emitter can inspire many sensing applications. Thanks to their high sensitivity to the environment, slight changes in structure (crystal lattice, interionic distance), in temperature and in pressure (O_2 presence, structure change induced by compression) have an impact on the ET process and therefore on luminescence.

1.4 Rare-earth based photoluminescence for T/P sensing

The sensitivity of emitted light to the environment is now being used to develop PL sensing processes. The advantages of PL sensing processes include non-contact detection, high sensitivity, versatility, multiplexing capability, and real-time monitoring. Temperature and pressure sensing are hot topics in the study of PL sensing applications in diverse area.[166,167] Luminescent temperature sensing properties have been discovered in various materials such as organic dyes,[168–170] metallic complexes,[171,172] nano[173] or micro[174] diamond, quantum dots[175–177] and nanoparticles. Meanwhile, well-known PL pressure sensor are quantum dots, [178,179] perovskite semiconductors,[179] ZnS: Mn particles,[180] Mn-based complexes. [113] Among the various PL sensor families, lanthanides-based phosphors are widely studied in temperature and pressure sensing.[42,166,167,181] In the following parts, the main mechanism of thermo-sensitive and pressure-sensitive PL will be generally discussed.

1.4.1 Ln-based thermometer

1) Photoluminescent thermometer

Temperature is one of the fundamental physical variables determining dynamic and performance in overall scale measurement. Based on the temperature-induced change in the intrinsic energy of molecules or atoms, the optical properties of luminescent materials varies with the temperature.[42] Luminescent thermometry has long been known as a non-invasive

temperature-sensing technology with high sensitivity and accuracy.[182] Since the first introduction by Neubert in 1930s,[183] the luminescent thermometer has developed rapidly and has been widely applied in many fields such as biology, mechanics, and optics. Compared to traditional thermometers requiring contact with the objective, the luminescent thermometer provides greater spatial resolution by non-contact measurement, especially for small systems (nano or micro scale).

- **The Boltzmann distribution**

The thermo-sensitivity of luminescent materials is mostly based on the Boltzmann distribution, named after the physicist Ludwig Boltzmann,[184] which describes the distribution of particles among the different energy states of a system in thermal equilibrium. Following the Boltzmann distribution, more energy states become populated at higher temperatures, and the probability of a thermal population of electrons to the upper levels depends exponentially on the temperature. As shown in Figure 1.16, energy levels 3 and 2 are in thermal equilibrium, or "Thermally coupled levels (TCL)", the relationship between the promoted electrons population in level 3 N_3 and that in level 2 N_2 can be expressed as:

$$N_3 = N_2 B\, exp(-\frac{\Delta E}{k_B T}) = \frac{g_3 \sigma_3 \omega_3}{g_2 \sigma_2 \omega_2} exp(-\frac{\Delta E}{k_B T})$$

Equation 1. 3

where the pre-exponential constant B includes the g_i , σ_i , ω_i, which are the degeneracy, the emission cross section, and the angular frequency of transitions for a given level i, respectively. ΔE is the energy gap between the two TCLs, k is the Boltzmann constant, and T is the absolute temperature.[185]

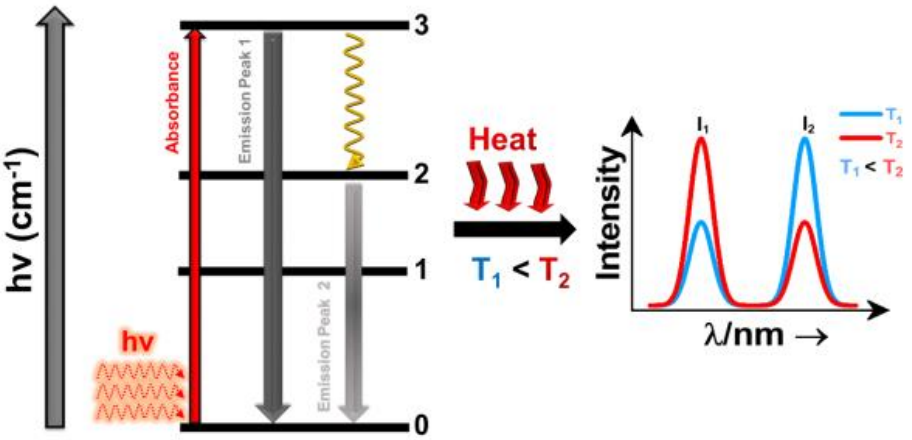

Figure 1.16: Temperature-induced photons promotion according to the Boltzmann distribution (Scheme from ref.[186], A. Nexha. Thesis in 2020. Copyright© Hal. Universitat Rovira I Virgli)

It is important to note that the energy level gap ΔE should range from 200 – 2000 cm^{-1} to allow the thermal photons promotions, otherwise they cannot be considered as "thermally-coupled".[42] Emissions from the TCLs with a given ΔE, vary with temperature, so emission intensity or lifetime can be a tool to monitor the variation of temperature. Lifetime-based thermometry using a Boltzmann distribution can be found in micro-diamonds. Ni-based

defects center in the diamond provide TCLs with ΔE = 920 cm^{-1}, suitable for the temperature measurement range from 200 to 700 K.[174]

Compared with the method using emission lifetime, emission intensities are more widely studied.[166,182] Since, the absolute emission intensity is proportional to the number of emitted photons, the variation of the absolute intensity as a function of temperature can be used in thermo-sensing. However, the intensity reference is always required to determine the absolute intensity, which increases the complexity in sensing application. On the other hand, using the relative emission intensity from the TCLs to monitor the variation in temperature can solve the problem. Ratiometric thermometry is generally considered as a reliable approach because of advantages such as self-monitoring and high-accurate measurement. Based on the Boltzmann distribution (Equation 1.3), the relative intensity or luminescent intensity ratio (LIR) varies with temperature with a given energy gap ΔE. ΔE can be determined by the calibration curve of Ln(LIR) versus 1/T. Compared to the theoretical value, this experimental value can be used to check the accuracy of the temperature value (Equation 1.4).

$$\frac{N_{L3}}{N_{L2}} = \frac{I_{L3}}{I_{L2}} = LIR = B\ exp(-\frac{\Delta E}{k_B T})$$

Equation 1. 4

where N_i denotes the population of excited ions, and I_i is the average of the total emitted intensities for a given level i, which is calculated by integrated emission band areas.[187]

An important indicator of the temperature measurement reliability by LIR method, the relative thermal sensitivity S_R, is defined by equation (Equation 1.5).[188]

$$S_R = \frac{1}{LIR} \times \frac{d(LIR)}{dT} = \frac{\Delta E}{k_B T^2}$$

Equation 1. 5

- **Temperature-dependent non-radiative rate: The Mott-Seitz model**

The time-resolved measurement for thermal sensing relies on the change in the non-radiative relaxation rate of the emitter as a function of temperature. The Mott-Seitz model proposed in the 1940s [189,190] describes the competition between non-radiative and radiative transitions by the transition probability of an emitting levels, which was evaluated by the inverse of the lifetime τ. The non-radiative lifetime depends on temperature based on the Arrhenius dependence (Equation 1.6):

$$\tau_{NR} = \frac{\tau_{NR}(T = 0K)}{\exp\left(-\Delta E / k_B T\right)}$$

Equation 1. 6

where the $\tau_{NR}(T = 0K)$ is the non-radiative lifetime at T = 0K, ΔE is the activation energy of thermal quenching process and k_B is the Boltzmann constant. Thus, the temperature is linearly proportional to the lifetime of emitting levels. Following the Arrhenius dependence, the non-radiative transition rate increases with increasing temperature. When the temperature is high enough, the non-radiative transition becomes more important than the radiative relaxation, the emission is totally quenched, which is known as the thermal quenching phenomenon. Numerous life-time based temperature sensor have been developed in recent years.[74,191,192] Er^{3+}-based optical fiber was first demonstrated as lifetime thermal sensors by Kewell *et al.* in 1998[193] with the decay time of emission at 1540 nm using the Mott-Seitz model.

- **Temperature-induced energy level shifts**

Temperature-induced change in the energy of electronic levels results in variations in the energy of photons emitted during energy transitions, manifesting changes in the emission band wavelength or band shape in PL systems. [166,182,194] Temperature-dependent peak shifts can always be observed in organic dye[195] and metallic complex.[113] Depending on the accuracy of the spectrometer, the measurement by peak shift can be considerably sensitive. Due to the low thermal stability of the sensor (coordination complex), the thermo-sensing based on peak-shift is usually applied for low temperature measurements (< 373 K). However, the shift in spectral position is usually related parameters other than the temperature such as refractive index and inter-atomic distances.[194] For some materials, concentration can also influence peak position.[196] Therefore, in temperature measurement, it is necessary to accurately determine the peak position by using a spectral reference. Studies have been developed to investigate multi-centers for the purpose of self-monitoring temperature sensors.[170]

In conclusion, among the spectral variables used for thermometry (Figure 1.17), temperature sensing technologies based on lifetime and LIR variation are not limited by the reference required. However, depending on the emission efficiency, lifetime measurement may need longer acquisition times and complementary equipment (pulsed excitation source). Moreover, early in 1926, Perrin reported the dependence of the radiative lifetime on the refractive index.[197] Compared to the lifetime-based measurement, the LIR-based method is more studied and developed. The relatively ease of experimental set-up and data processing means that LIR thermometry can be adapted to most situations. Nonetheless, an accurate temperature calibration is always required before measurement for all types of thermometry approaches.

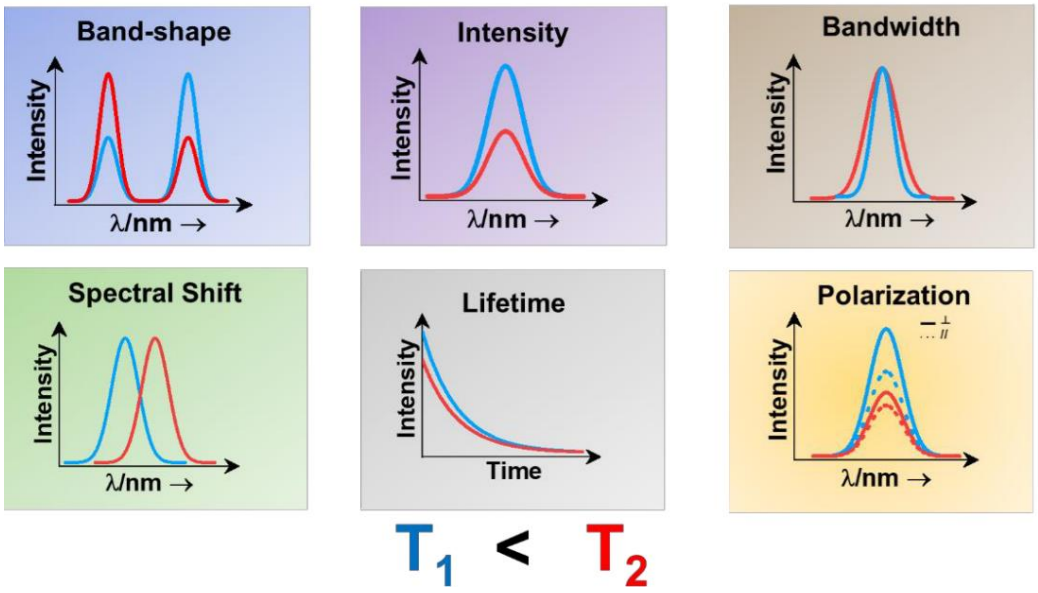

Figure 1.17: Temperature-induced spectral variations (Scheme from ref.[186], A. Nexha. Thesis in 2020. Copyright© Hal. Universitat Rovira I Virgli)

2) Ln-based phosphors in LIR-thermometry

The emission of Ln^{3+} provides the narrow emission band and long lifetime, making the LIR-based temperature sensing method that relies on the emission from 4f-4f transitions a simple and accurate thermometer. More importantly, the wide range of TCLs transitions in Ln^{3+} ions ensures that it is always possible to find a suitable sensing temperature range for various applications. Lanthanide based LIR thermometers are divided into two parts: single-center and dual center as shown in Figure 1.18.

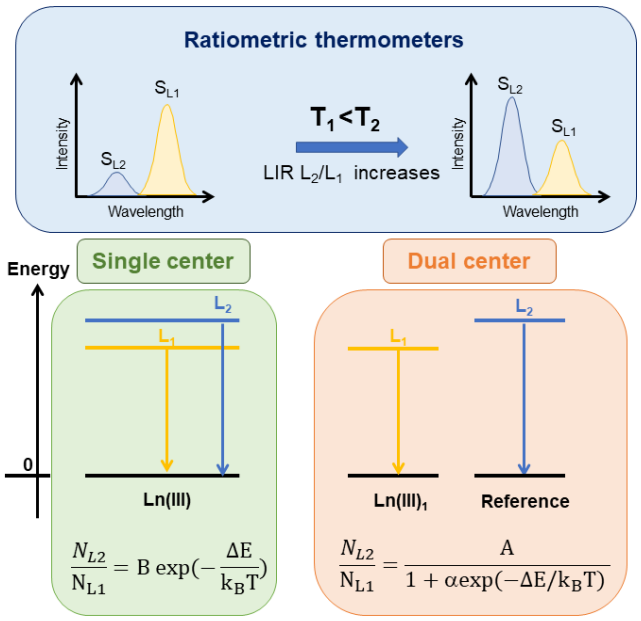

Figure 1.18: Schematic presentation of ratiometric luminescence thermometry in single and dual-center emissions. (Reproduced from ref. [42]).

- **Single center LIR-based thermometer**

In a single-center thermometer, two distinct transitions from the same emitting center can be considered as TCLs. The increase in temperature causes a promotion of electrons from L_1 to L_2 following the Boltzmann distribution, which leads to an increase in the emission intensity of the L_2 transition and decrease in that of L_1. Single-center thermometry was first introduced by Kusama et al. in a seminal presentation in 1976. Later, Collins (1998) and Wade (2003) described the thermometric approach using the ratio of two energy-close emission intensities based on Boltzmann distribution. Common example of single-center thermometer has individual suitable measurement range depending on the energy level gap ΔE. Several well-known single-center thermometers are reported in Table 1.1.

Table 1.1: Example of single-center thermometers.

Host	Ln^{3+}	Transitions	Temperature range (K)	$S_{r\,MAX}$ (% K^{-1})	Reference
SrF_2	Nd^{3+}	$^4F_{5/2}$, $^4F_{3/2}$	298-573	1.68	[198]
YF_3	Pr^{3+}	$^3P_1$, $^3P_0$	293-421	1.24	[199]
$NaYF_4$: Yb^{3+}	Ho^{3+}	$^5F_5$, $^5F_4$	300-500	1.53	[200]
$NaYF_4$: Yb^{3+}/Silica	Er^{3+}	$^2H_{11/2}$, $^4S_{3/2}$	300-900	1.02	[148]

- **Dual center LIR-based thermometer**

A dual-center thermometer involves two transitions of two distinct emitters, which could be divided into:

a. A Ln^{3+} as the probe and an organic dye as the reference.[201–204]
b. A Ln^{3+} as the reference and quantum dots as the probe.[205]
c. A Ln^{3+} as the probe and another as the reference without interaction (energy transfer).[206]
d. A Ln^{3+} as the probe and another as the reference with interaction inducing change in the intensity ratio.[41,207]
e. Two Ln^{3+} incorporating into organic or hybrid host, with thermally sensitive interaction Ln^{3+} – host.[208–212]

Similarly to single-center thermometry, the Boltzmann distribution can also applied on dual-center ones. Based on Mott-Seitz model (Equation 1.6), Cooke *et al.* derived a model for dual-center thermometry.[213,214] However, compared to single-center thermometry, dual-center thermometry could sometimes be limited. For example, in upconverting nanoparticles Y_2O_3: Yb^{3+}; Ho^{3+}; Tm^{3+}, Pandey and Rai[215] have observed an overlap between the transitions of ion Ho^{3+} ($^1G_4 \rightarrow {}^3H_6$) and ion Tm^{3+} ($^5F_3 \rightarrow {}^5I_8$) due to their close energy levels ($\Delta E \sim 470$ cm^{-1}). Such behavior certainly decreases the measurement accuracy even if the authors tried to replace the integrated areas with peak intensity maximum to calculate the LIR.

3) Erbium-based thermometry: Upconversion system thermometer

Among numerous single-center thermometers, Er^{3+} is one of the most used emitters for ratiometric thermometry owing to its large temperature range of measurement.[182,216–218] The energy gap between Er^{3+} TCLs ($^4S_{3/2}$ and $^2H_{11/2}$ levels; ~ 700 cm^{-1}) allows high thermometric sensitivity over a suitable temperature range (300 - 600 K, Figure 1.19a) for most temperature measurement applications,[148] as well as for our further tribological measurements. Moreover, as mentioned previously, Er^{3+} can be easily excited by two Yb^{3+} via an upconversion process due to their highly matched energy gaps (Figure 1.19b). In the coupled Er^{3+}-Yb^{3+} FRET system, the Yb^{3+} ion is used as a sensitizer to transfer energy to the Er^{3+}; this process is referred to as the ETU. The use of a NIR laser as an excitation source in an ETU system is very attractive for tribological temperature measurements, because the current laser excitation of Er^{3+} under blue light can cause interfering emission from the scattered medium. In addition, the ETU system is very popular in biological applications because of the high spatial and temporal resolution thanks to the large penetration depth of NIR light.[44,52,166]

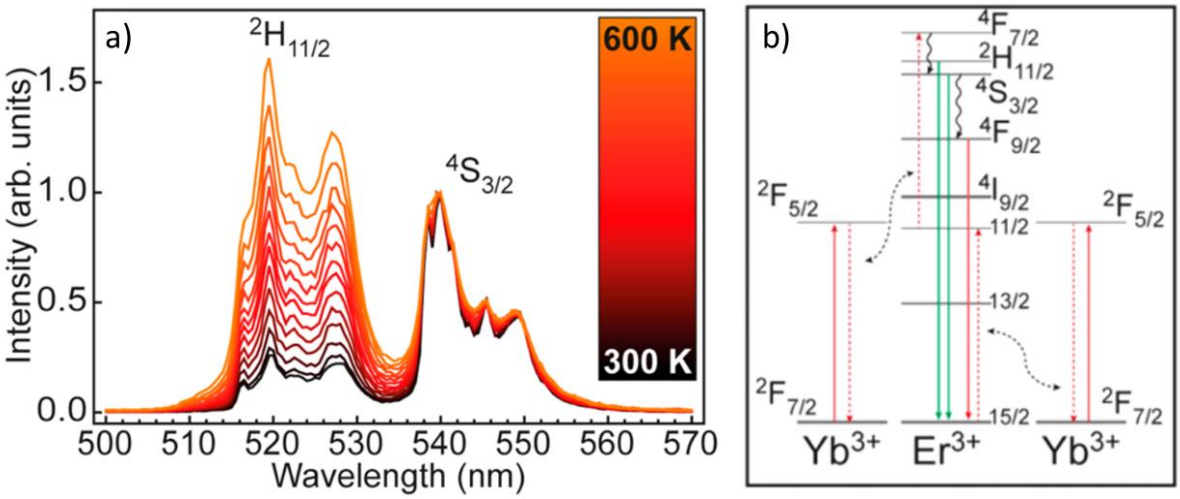

Figure 1.19: a.) Emission spectra of $NaYF_4$ nanoparticles upon excitation at 980 nm for temperatures ranging from 300 to 600 K recorded with steps of 25 K; b.) Energy diagrams of Er^{3+} and Yb^{3+}, including the transitions involved in the UC process (Scheme from ref.[148], R.G. Geitenbeek *et al*. 2017. Copyright© Journal of Physical Chemistry C)

4) Tb/Eu thermometer for low-range temperature sensing

One of the most common dual-center thermometers is Tb^{3+}/Eu^{3+}, which is mainly developed for lower-range temperature sensing. Two different slopes of temperature calibration curve by using Eu^{3+}/Tb^{3+}-doped APTES/TEOS nanoparticles as thermometer has been reported by Brites et al.,[208] in which the two regimes switch around 175 – 200 K. Moreover, as the efficiency of ET from Tb^{3+} to Eu^{3+} can be influenced by temperature, more than by intrinsic thermo-sensitivity, the ET process also provides a temperature-induced variation in LIR.[219–223] In the work of Carneiro Neto *et al.*,[223] thermally activation of Tb-Eu ET in the $[Ln(bpy)_2(NO_3)_3]$ (Ln = Tb, Eu) complex has been observed at T > 175 K, and the

rate of ET increased with increasing temperature. As shown in Figure 1.20 by Carneiro Neto *et al.*, at 330 nm excitation, the emission intensity of Tb^{3+} decreases with increasing temperature while the emission intensity of Eu^{3+} is the opposite.[223] Dual-center thermometry is very interesting for low temperature sensing. For example, the Eu^{3+}/Tb^{3+} complex provides high sensitivity for temperature measurement in the range 0 - 330 K.[223]

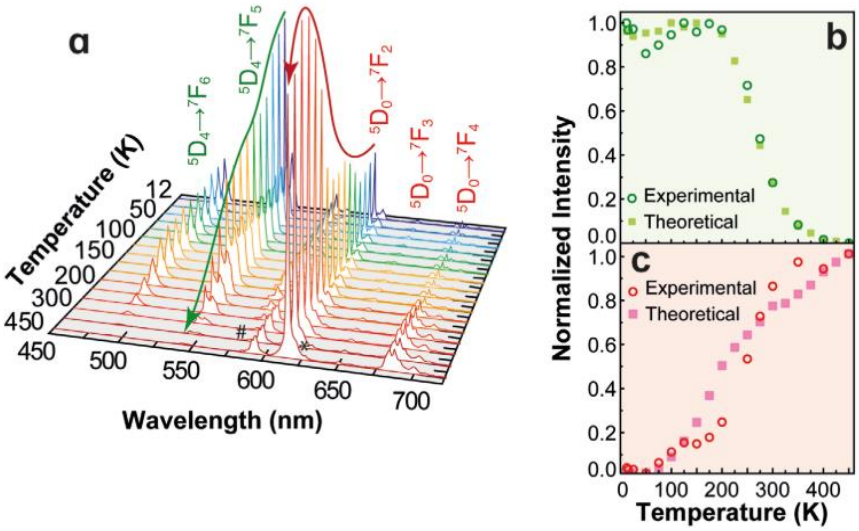

Figure 1.20: a.) Emission spectra of $[Tb_{0.94}Eu_{0.06}(bpy)_2(NO_3)_3]$ (11–450 K) excited at 330 nm. Normalized emission intensity of b.) Tb^{3+} and c.) Eu^{3+} as a function of temperature. (Figure 1.from ref.[223], A.N. Carneiro Neto *et al.* 2022. Copyright© Advanced Optical Materials).

1.4.2 Ln-based pressure sensitivity

1) Photoluminescent manometry

Luminescent manometer has been extensively required for numerous new technologies owing to their unique feature: contactless pressure measurement.[28,29,224,225] Nonetheless, compared to the widely developed PL thermometry, PL manometry is so far poorly studied. Lanthanide-based materials are the most popular topic because of their long emission lifetime and narrow emission peak hence high measurement accuracy. Quantitative pressure sensitivity arises from the structural variation of phosphor, which is characterized by the spectral variable. Commonly used parameters include luminescent lifetime, emission wavelength shift, and recently the ratio between two emission intensities. The pression range measurable by PL sensors is by far quite wide, from a hundred kPa to hundred GPa.[116,167,226] In the following part, pressure-sensing process will be discussed in terms of their origins and measurement methods.

- **Structural-variation-induced energy levels offset**

Compression leading to structural variation generally manifests in a decrease in the distance between species, thus in contraction and distortion of crystalline lattice even more in crystalline phase transitions. The shortening distances between species induced by

environmental change induces stronger covalent interactions between the emitter and its surrounding, and also decreases in the Coulomb and spin-orbit interactions, considered as the nephelauxetic effect.[227] Additionally, the lattice contraction leads to an increase in the strength of the crystal field and thus of the Stokes' splitting, which manifests in a spectral shift of the Stark sublevels (Figure 1.21).[228,229] Thus, the shift of the emission peak and the variation in the emission bandwidth are the most common spectral variable for pressure sensing.

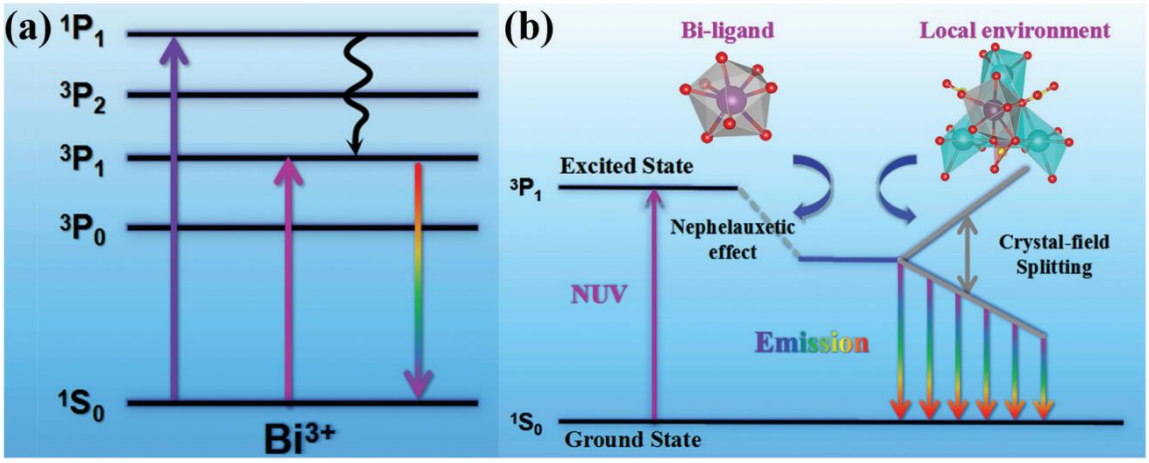

Figure 1.21: a.) Energy level scheme of $Na_2Y_2B_2O_7$: Bi^{3+} ions. (b) Both the nephelauxetic effect and crystal-field splitting control the Bi^{3+} emission. (Figure from ref.[229], S. Wu, *et al.* 2020. Copyright© Journal of Materials Chemistry C)

- **Energy transfer in pressure sensing**

In a solid system, the interaction between species can also be strongly influenced by structural variations. The FRET theory claims that the ET rate increases exponentially with decreasing interionic distance, with order of R^{-n} (n = 6, 8, 10… for dipole-dipole, quadrupole-dipole and quadrupole-quadrupole, respectively).[84–88] The interionic distance can be easily influenced by the contraction or distortion of crystal lattices under the effect of increased pressure. This methodology is so far mostly applied for ET process between lanthanide ions. However, the pressure required to induce a structural variation can vary depending on the hardness of the crystal lattice, which determines the sensitivity and sensing limit. For an inorganic host, a relative high pressure is usually needed, so that the sensing range can reach a high pressure while reducing the sensitivity.

Besides, the pressure sensing under compression in air has been discovered.[107] In a ligand-activated system, quenching sites such as O_2 can absorb the energy transferred by the sensitizers. Therefore, in the presence of O_2, the emitter cannot be excited by the sensitizer, resulting in a reduction in emission intensity. O_2-sensitive properties are usually observed in complex where the ligand is the sensitizer.[96,107,110,113,116,230,231] Such O_2-quenching effect is very sensitive to O_2 concentration, so pressure can be measured indirectly by changes in luminescence in the presence of O_2. This mechanism provides high sensitivity in a smaller pressure sensing range (140 kPa). [116]

Among those PL temperature or pressure sensors, lanthanide-based materials will be further studied in this work. Advantages such as long emission lifetime, narrow emission peak

provide a more measurable spectral change, resulting in high sensitivity, greater accuracy, and reliability. Moreover, the low toxicity, and a large possibility of functionalization make the lanthanide-based PL sensor easy to apply in *in situ* or *in vivo* measurement. In the following paragraphs, lanthanide-based PL sensors will be presented.

2) Ln-based phosphors in manometry

- **Peak-shift-based manometry**

The PL properties of the Ln^{3+} emitter due to the 4f-4f transition are highly dependent on the crystal structure. Variables such as structural symmetry, crystal lattice, interionic distance influence the emission of Ln-based materials, which can be manifested by shift in emission peak, variation in peak shape and in emission intensity or lifetime. [232–234] Pressure sensing relying on spectral peak shift is more commonly studied. In Y_2O_3:Eu^{3+}, Zhang *et al.* found out that the crystalline phase transformed under compression, from cubic to monoclinic then to hexagonal, under about 11 GPa and 20 GPa, respectively.[235] The transformation of the crystalline phases leads to the appearance of new Eu^{3+} emission peaks. Meanwhile, during the structural change, a slight shift of the red peak (0.098 nm/GPa) has been observed as an indicator for the detection of pressure. The pressure-driven emission peak shift has later been reported by Wang et al. in Eu(II)-Doped $BaLi_2Al_2Si_2N_6$.[225] Under high pressure (> 10 GPa), compression leads to lattice contraction and distortion, resulting in crystal field splitting and then in an increase in the Stokes shift, characterized by a significant shift in the emission peak (1.58 nm/GPa). Similar studies on the impacts of structural symmetry of Eu^{3+} in a β-diketone complex have been reported by Wong et al.[236] Coordination environments including ligand orientations, symmetry of Eu^{3+} sites and interionic distances have considerable impacts on PL performance. Under a compression of less than 6 GPa, a peak shift has also been observed up to 0.38 nm/GPa.

Other lanthanide ions like Sm(II), Nd^{3+} and Ce^{3+} are also reported as band-shift-based pressure sensors for decades. The emission peak of Nd^{3+} doped $YAlO_3$ from transition $^4F_{9/2} \rightarrow {}^4I_{9/2}$ presented the shift of 0.47 nm/GPa up to 10 GPa.[228] Furthermore, under higher-range pressure, the emission band (5d → 4f) of Ce^{3+} in $Y_6Ba_4(SiO_4)_6F_2$ shifted 0.63 nm/GPa up to 30 GPa,[237] while the Sm(II) doped SrB_4O_7 has been confirmed to be sensitive up to 40.9 GPa by peak shift ($^5D_0 \rightarrow {}^7F_0$) of 0.321 nm/GPa.[238]

- **Energy transfer in pressure sensing**

a) Ln-Ln

According to the theory of FRET, the d^{-6}-dependent dipole-dipole mechanism can be easily influenced by contraction or distortion of crystal lattices under increasing pressure. This methodology is so far mostly applied to Ln-Ln ET in an inorganic host as pressure-sensitive phosphors for various applications.[223,224,239] The upconversion nanoparticles $LaPO_4$ and YPO_4 doped Yb^{3+} and Tm^{3+} were developed as pressure sensors by Runowski et al.[240] The Yb^{3+} to Tm^{3+} ET pathway change caused by Yb-Tm distance decreasing with applied pressure, resulting in the relative intensity ($^3H_4 \rightarrow {}^3H_6/{}^1G_4 \rightarrow {}^3H_6$), lifetime, peak position and FWHM

peak of Tm^{3+} varying with pressure up to 26 GPa. At lower range of pressure (up to 10 GPa), the pressure-sensing properties of upconversion Yb^{3+}/Er^{3+} doped nanoparticles have also been discovered with the lifetime and brightness of Er^{3+} varying with pressure.[181,241] At lower-range pressure (up to 6 GPa), the pressure sensitivity on SrF_2: Yb^{3+}/Er^{3+} has been reported in Runowski's works, with variations in lifetime, emission intensity and peak centroid observed under compression up to 5.5 GPa (Figure 1.22).[242] Moreover, the pressure-sensing properties of Yb^{3+}/Er^{3+} upconversion doped fluoride nanoparticles have also been discovered with the variation of the red-to-green ratio, lifetime and brightness of Er^{3+} with pressure up to 5.4 GPa by McLellan *et al.*[241]

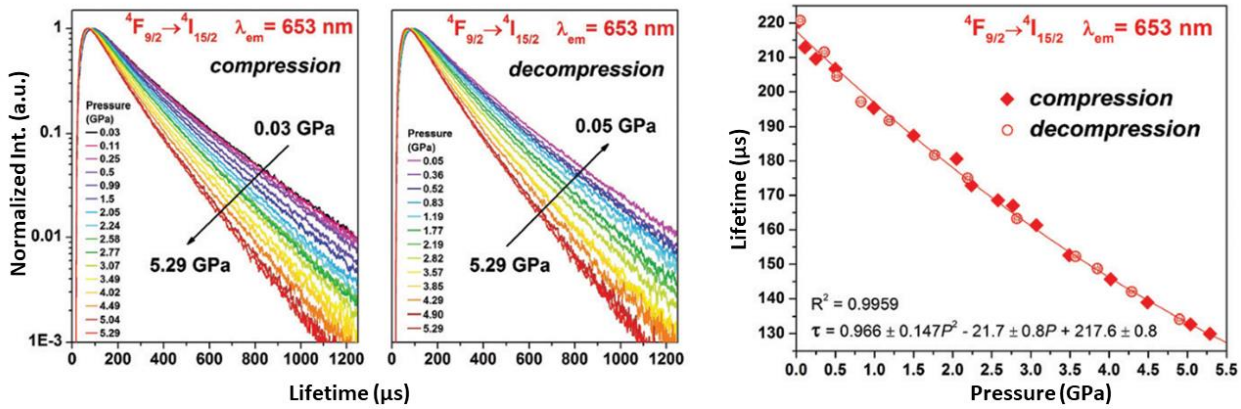

Figure 1.22: Luminescence decay curves (left) and determined emission lifetimes (right) for the SrF_2:Yb^{3+}/Er^{3+} sample under high pressure; λ_{ex} = 980 nm, λem = 653 nm for $^4F_{9/2} \rightarrow {}^4I_{15/2}$ transitions. (Figure from ref.[242] , M. Runowski *et al.* 2017. Copyright© Nanoscale)

b) Ln-Ligand

In a ligand-sensitized Ln^{3+} system, the overall ligand-Ln ET pathway can be strongly influenced by crystal lattice parameters (distance donor-acceptor[83,84,86]), ligand parallelism[101] and quenching sites (surface defect[56,85,102,103], oxygen[104–112]). Under hydrostatic pressure, the 'Antenna effect' of the organic ligand can be restricted by shortening the intermolecular distance. Such phenomena have been observed in halogen-substituted Eu^{3+} β-diketonate complexes by Wong *et al.* in 2022[108]: the emission intensity of Eu^{3+} in the complex decreases under hydrostatic pressure up to 6 GPa, with a peak shift measurement (maximum at 0.331 nm/GPa), and the Eu^{3+} decay time slumps under 4 GPa (Figure 1.23). At higher pressure, Eu^{3+} and Tb^{3+} complexes with pyridine- and quinoline- based ligands show their pressure-sensitivity below 160 kbar (16 GPa), based on the decrease in their decay time.[243]

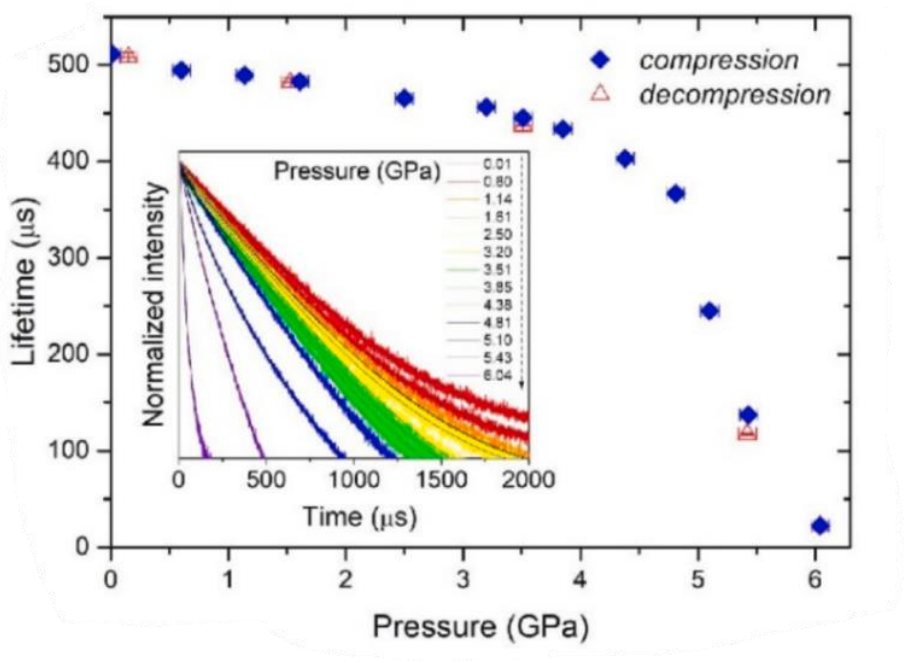

Figure 1.23: Determined luminescence lifetimes as a function of pressure, for Eu^{3+} in β-diketonate halogen-substituted complexes (λex = 355 nm, λem = 613 nm.). Inset shows the luminescence decay curves recorded at different pressure values. (Scheme from ref.[108], H. Wong *et al.* 2022. Copyright© Chemical Engineering Journal Advances)

On the other hand, other pressure-sensitive mechanism for lower-range pressure (< 140 kPa) has been discovered relying on the O_2-quenching effect. With the presence of O_2, pressure-sensing by an Ln-based complex has been developed. The pressure-sensitive Eu^{3+} complex with the trifluoro-acetylacetonate ligands was first proposed by Amao *et al* in 2000,[107] in which the pressure can be indirectly measured by luminescence changes in the presence of oxygen, where the presence of O_2 promotes the luminescence quenching of the T_1 state of these materials. Recently, Hasegawa *et al.* discovered a pressure-sensitive Eu^{3+} coordination polymer, a decrease on Eu^{3+} lifetime has been observed under pressure induced by the rise of the O_2 concentration.[110] Meanwhile, the O_2-quenched Ln^{3+} intensity reaction has also been found in a mixed Eu^{3+} and Tb^{3+} coordination polymer as both Eu^{3+} and Tb^{3+} emissions decreased with increasing pressure up to 140 kPa (Figure 1.24).[116]

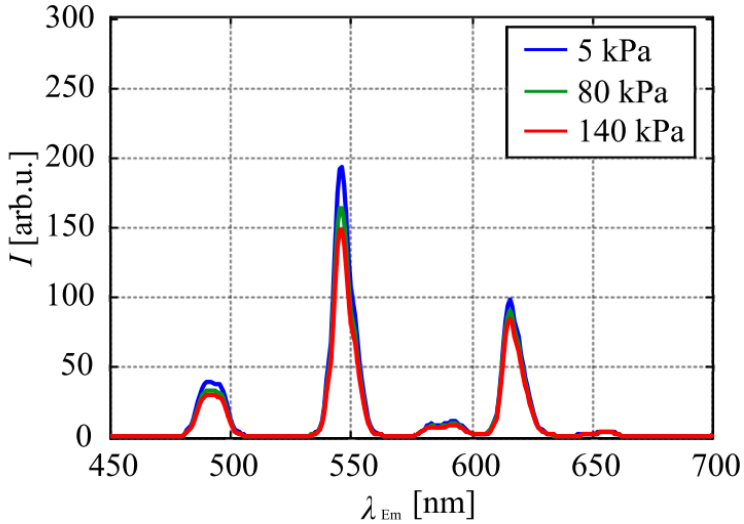

Figure 1.24: Effect of pressure on the emission spectrum of $[Tb_{0.99}Eu_{0.01}(hfa)_3(dpbp)]_n$ (hfa: hexafluoroacetylacetone, dpbp: 4,4'-bis(biphenylphosphoryl)biphenyl), respectively, excited at 320 nm) in the polymer. (Scheme from ref. [116], M. Kasai *et al*. 2020. Copyright© Sensors)

3) Future: Ln-Ln ET in complex for pressure sensing

The pressure sensing mechanism based on the ET process is by far limited to Ln^{3+}-Ln^{3+} ET in an inorganic host and Ln^{3+}-ligand ET in lanthanide complex. The evolution of photoluminescence under pressure in a complex relying on Ln^{3+}-Ln^{3+} ET has not been developed to our knowledge. In Table 1.2, several examples of Ln^{3+}-based manometers are shown. Compared to the pure inorganic host, the lanthanide complex provides a softer structure,[244] with greater structural variation to be expected under the same pressure, leading to higher sensitivity over a lower range of pressure. By applying a dual-emitters Ln-based complex within occurring Ln^{3+}-Ln^{3+} ET process, changing the interionic distance can lead to a variation in emission intensities. Like PL thermometry, the intensity-based pressure sensing process can take advantage of the simplicity of data collection and processing for potential applications. Intensity-based manometry is not as mature as thermometry so far, many studies are required to improve the sensitivity, accuracy, and reliability of the sensor for pressure detection. The application of Ln^{3+}-Ln^{3+} ET in a complex for P-sensing is an interesting approach to develop.

Table 1.2: Example of Ln-ions-based manometers.

Pressure range	5 - 140 kPa	0 – 5.4 GPa (Hydrostatic)	0 - 10 GPa (Hydrostatic)	0 -10 GPa (Hydrostatic)
Host	Diketonate complex	UCNPs SrF_2	$NaBiF_4$	YF_3
Ln ions	Tb^{3+} and Eu^{3+}	Yb^{3+} and Er^{3+}		
Mechanism	O_2-quenching	Structural-contraction-induced variation in FRET Yb^{3+}-Er^{3+}		
Variance	Emission intensity	Emission ratio (green/red), lifetime (Er^{3+})	NIR peak shift (Er^{3+})	Red peak shift (Er^{3+})
Ref	116	241	181	245

1.5 Aims and challenges of the thesis

Over the past decade, there has been more and more research on Ln-based materials PL for temperature and pressure sensing. These sensors offer advantages such as considerable reliability, contactless operation, and high accuracy. The sensor in nanoscale size made them also as non-intrusive in a number application. Ln materials are known for their non-toxic nature, making them suitable for applications in biology and biomedicine. However, their potential application in tribological measurements remains relatively unexplored.

This work aims to bridge the gap by applying Ln-based materials in tribological measurements. By incorporating the PL sensor into mechanical contacts (lubricated or not), it becomes possible to measure local temperature and pressure in real-time. This approach enables the monitoring of temperature and pressure variations at the extremes of the contact interface, providing valuable insights on the tribological behavior of the system.

The main challenge addressed in this thesis is to develop a PL sensing system able to operate in a multivariable environment. In tribological interface, various factors such as temperature, pressure, and shearing forces continuously vary, challenging for accurate and reliable sensing. The sensor is needed to exhibit high sensitivity and selectivity to each variable, allowing their individual quantification in real-time.

Due to the unique characteristics of Ln-based PL materials, including their long emission lifetime, sharp emission peak, and ease of data collection and processing, they hold significant potential for applications as sensors in tribological contact. In time-dependent measurements where system parameters continuously change, self-monitoring sensing methods play a crucial role in maintaining accurate and reliable measurements. LIR-based method is one of self-monitoring methods, which has been widely used in Ln-based temperature sensing. However, application of this method is relatively limited in the field of pressure sensing. To develop a LIR-based pressure sensitivity method, the focus would be on the pressure-induced

structural contraction and its impact on the ET process between two Ln^{3+} ions, following the FRET theory. By addressing the research gap in LIR-based pressure sensitivity, this work aims to expand the capabilities of Ln-based sensors in time-dependent measurements for further tribological applications.

References

(1) Jost, P. Lubrication (Tribology)-A Report on the Present Position and the Industry's Needs. *Dep. Educ. Sci. HM Station. Off. London, UK* **1966**.

(2) Dowson, D. *History of Tribology*; 1979. https://doi.org/10.2474/trol.6.ii.

(3) Bartz, W. J. Tribology, Lubricants and Lubrication Engineering - a Review. *Wear* **1978**, *49* (1), 1–18. https://doi.org/10.1016/0043-1648(78)90019-4.

(4) Cameron, A.; Gohar, R. Theoretical and Experimental Studies of the Oil Film in Lubricated Point Contact. *Proc. R. Soc. London. Ser. A. Math. Phys. Sci.* **1966**, *291* (1427), 520–536. https://doi.org/10.1098/rspa.1966.0112.

(5) Godet, M. The Third-Body Approach: A Mechanical View of Wear. *Wear* **1984**, *100* (1–3), 437–452. https://doi.org/10.1016/0043-1648(84)90025-5.

(6) Berthier, Y. Maurice Godets Third Body. *Tribol. Ser.* **1996**, *31*, 21–30. https://doi.org/10.1016/s0167-8922(08)70766-1.

(7) Semenov, A. P. Tribology at High Temperatures. *Tribol. Int.* **1995**, *28* (1), 45–50. https://doi.org/10.1016/0301-679X(95)99493-5.

(8) Meng, Y.; Xu, J.; Jin, Z.; Prakash, B.; Hu, Y. *A Review of Recent Advances in Tribology*; 2020; Vol. 8. https://doi.org/10.1007/s40544-020-0367-2.

(9) Komanduri, R.; Hou, Z. B. A Review of the Experimental Techniques for the Measurement of Heat and Temperatures Generated in Some Manufacturing Processes and Tribology. *Tribol. Int.* **2001**, *34* (10), 653–682. https://doi.org/10.1016/S0301-679X(01)00068-8.

(10) Albahrani, S. M. B.; Philippon, D.; Vergne, P.; Bluet, J. M. A Review of in Situ Methodologies for Studying Elastohydrodynamic Lubrication. *Proc. Inst. Mech. Eng. Part J J. Eng. Tribol.* **2016**, *230* (1), 86–110. https://doi.org/10.1177/1350650115590428.

(11) El-Wardany, T. I.; Mohammed, E.; Elbestawi, M. A. Cutting Temperature of Ceramic Tools in High Speed Machining of Difficult-to-Cut Materials. *Int. J. Mach. Tools Manuf.* **1996**, *36* (5), 611–634. https://doi.org/10.1016/0890-6955(95)00043-7.

(12) STEPHENSON, D. A. Tool-Work Thermocouple Temperature Measurements—Theory and Implementation Issues. *Trans. ASME J. Eng. Ind.* **1993**, *115*, 432–437.

(13) Kitagawa, T.; Kubo, A.; Maekawa, K. Temperature and Wear of Cutting Tools in High-Speed Machining of Inconel 718 and Ti-6Al-6V-2Sn. *Wear* **1997**, *202* (2), 142–148. https://doi.org/10.1016/S0043-1648(96)07255-9.

(14) K-J, K. Das Temperaturfeld in Drehmeissel (The Temperatue Field in the Cutting Edge of a Cutting Tool). *Essen, Ger. Verlag W. Girardet*, **1954**, 1954.

(15) Kennedy, F. E.; Frusescu, D.; Li, J. Thin Film Thermocouplearrays for Sliding Surface Temperaturemeasurement. *Wear* **1997**, *207*, 46–54.

(16) Safa, M. M. A.; Anderson, J. C.; Leather, J. A. Transducers for Pressure, Temperature and Oil Film Thickness Measurement in Bearings. *Sensors and Actuators* **1982**, *3* (C), 119–128. https://doi.org/10.1016/0250-6874(82)80013-9.

(17) Mokhtar, M. O. A.; Abdel Ghany, A. A. Elastohydrodynamic Behavior of Rolling Elliptical Contacts: PartI: Pressure and Temperature Distributions. **1984**, *107* (July), 343–348.

(18) Ebner, M.; Ziegltrum, A.; Lohner, T.; Michaelis, K.; Stahl, K. Measurement of EHL Temperature by Thin Film Sensors – Thermal Insulation Effects. *Tribol. Int.* **2020**, *149* (December 2018), 105515. https://doi.org/10.1016/j.triboint.2018.12.015.

(19) Turchina, V.; Sanborn, D.; Winer, W. Temperature Measurements in in Sliding Sling Elastohydrodynamic Point Contacts. *J. Lubr. Tech* **1974**, 464–469.

(20) Spikes, H. A.; Anghel, V.; Glovnea, R. Measurement of the Rheology of Lubricant Films within Elastohydrodynamic Contacts. *Tribol. Lett.* **2004**, *17* (3), 593–605.

https://doi.org/10.1023/B:TRIL.0000044509.82345.16.

(21) Sutter, G.; Ranc, N. Flash Temperature Measurement during Dry Friction Process at High Sliding Speed. *Wear* **2010**, *268* (11–12), 1237–1242. https://doi.org/10.1016/j.wear.2010.01.019.

(22) Briatte, M.; Mege-Revil, A.; Desplanques, Y.; Parrens, C.; Santacreu, P. O. Relationships between Third Body Flows, Load-Bearing Mechanisms and Particle Emissions in Automotive Braking. *Wear* **2023**, *524–525* (September 2022), 204855. https://doi.org/10.1016/j.wear.2023.204855.

(23) Rassat, S. D.; James Davis, E. Temperature Measurement of Single Levitated Microparticles Using Stokes / Anti-Stokes Raman Intensity Ratios. *Appl. Spectrosc.* **1994**, *48* (12).

(24) Gardiner, D. J.; Baird, E. M.; Craggs, C. Raman Microspectroscopy of a Working Elastohydrodynamic Contact. *Lubr. Sci.* **1989**, *1* (4), 301–313.

(25) Jubault, I.; Mansot, J. L.; Vergne, P.; Lubrecht, A. A.; Molimard, J. In Situ Pressure Measurements in an Elastohydrodynamically Lubricated Point Contact Using Raman Microspectrometry. Comparison with Numerical Calculations. *Tribol. Ser.* **2003**, *41* (September), 663–673. https://doi.org/10.1016/s0167-8922(03)80179-7.

(26) Jubault, I.; Molimard, J.; Lubrecht, A. A.; Mansot, J. L.; Vergne, P. In Situ Pressure and Film Thickness Measurements in Rolling/Sliding Lubricated Point Contacts. *Tribol. Lett.* **2003**, *15* (4), 421–429. https://doi.org/10.1023/B:TRIL.0000003068.07650.2e.

(27) Yagi, K.; Vergne, P.; Nakahara, T. In Situ Pressure Measurements in Dimpled Elastohydrodynamic Sliding Contacts by Raman Microspectroscopy. *Tribol. Int.* **2009**, *42* (5), 724–730. https://doi.org/10.1016/j.triboint.2008.10.005.

(28) Albahrani, S. M. B.; Seoudi, T.; Philippon, D.; Lafarge, L.; Reiss, P.; Hajjaji, H.; Guillot, G.; Querry, M.; Bluet, J. M.; Vergne, P. Quantum Dots to Probe Temperature and Pressure in Highly Confined Liquids. *RSC Adv.* **2018**, *8* (41), 22897–22908. https://doi.org/10.1039/C8RA03652G.

(29) Seoudi, T.; Philippon, D.; Fillot, N.; Lafarge, L.; Devaux, N.; Mondelin, A.; Vergne, P. CdSe-Based Quantum Dots as In Situ Pressure and Temperature Non-Intrusive Sensors in Elastohydrodynamic Contacts. *Tribol. Lett.* **2020**, *68* (3). https://doi.org/10.1007/s11249-020-01312-x.

(30) Seoudi, T. Non-Intrusive CdSe-Based Quantum Dots for Sensing Pressure and Temperature in Lubricated Contacts, Thesis in Université Claude Bernard Lyon 1, 2020.

(31) Mohamed Baqer Albahrani Sayed. Photoluminescent CdSe/CdS/ZnS Quantum Dots for Temperature and Pressure Sensing in Elastohydrodynamic Contacts, Thesis in Université Claude Bernard Lyon 1, 2017.

(32) Johnston, I. D.; McCluskey, D. K.; Tan, C. K. L.; Tracey, M. C. Mechanical Characterization of Bulk Sylgard 184 for Microfluidics and Microengineering. *J. Micromechanics Microengineering* **2014**, *24* (3). https://doi.org/10.1088/0960-1317/24/3/035017.

(33) Section, S. P.; Railways, B.; Centre, T.; Physics, S. Surface Energy and the Contact of Elastic Solids. *Proc. R. Soc. London. A. Math. Phys. Sci.* **1971**, *324* (1558), 301–313. https://doi.org/10.1098/rspa.1971.0141.

(34) Barthel, E. Adhesive Elastic Contacts – JKR and More. *J. Phys. D. Appl. Phys.* **2008**.

(35) Sanchez, C.; Lebeau, B.; Chaput, F.; Boilot, J. P. Optical Properties of Functional Hybrid Organic-Inorganic Nanocomposites. *Adv. Mater.* **2003**, *15* (23), 1969–1994. https://doi.org/10.1002/adma.200300389.

(36) Desroches, C.; Lopes, C.; Kessler, V.; Parola, S. Design and Synthesis of Multifunctional Thiacalixarenes and Related Metal Derivatives for the Preparation of Sol-Gel Hybrid Materials with Non-Linear Optical Properties. *Dalt. Trans.* **2003**, No. 10, 2085–2092. https://doi.org/10.1039/b210252h.

(37) Chateau, D.; Chaput, F.; Lopes, C.; Lindgren, M.; Brännlund, C.; Öhgren, J.; Djourelov, N.; Nedelec, P.; Desroches, C.; Eliasson, B.; Kindahl, T.; Lerouge, F.; Andraud, C.; Parola, S. Silica Hybrid Sol-Gel Materials with Unusually High Concentration of Ptorganic Molecular Guests: Studies of Luminescence and Nonlinear Absorption of Light. *ACS Appl. Mater. Interfaces* **2012**, *4* (5), 2369–2377. https://doi.org/10.1021/am2015537.

(38) Li, F.; Wang, X.; Xia, Z.; Pan, C.; Liu, Q. Photoluminescence Tuning in Stretchable PDMS Film Grafted Doped Core/Multishell Quantum Dots for Anticounterfeiting. *Adv. Funct. Mater.* **2017**, *27* (17). https://doi.org/10.1002/adfm.201700051.

(39) Bünzli, J.-C. G.; Eliseeva, S. V. *Lanthanide Luminescence*; 2010; Vol. 7.

(40) Dramićanin, M. D. Sensing Temperature via Downshifting Emissions of Lanthanide-Doped Metal Oxides and Salts. A Review. *Methods Appl. Fluoresc.* **2016**, *4* (4). https://doi.org/10.1088/2050-6120/4/4/042001.

(41) Marciniak, L.; Bednarkiewicz, A.; Stefanski, M.; Tomala, R.; Hreniak, D.; Strek, W. Near Infrared Absorbing near Infrared Emitting Highly-Sensitive Luminescent Nanothermometer Based on Nd3+ to Yb3+ Energy Transfer. *Phys. Chem. Chem. Phys.* **2015**, *17* (37), 24315–24321. https://doi.org/10.1039/c5cp03861h.

(42) Brites, C. D. S.; Millán, A.; Carlos, L. D. *Lanthanides in Luminescent Thermometry*; 2016; Vol. 49. https://doi.org/10.1016/bs.hpcre.2016.03.005.

(43) Casar, J. R.; McLellan, C. A.; Siefe, C.; Dionne, J. A. Lanthanide-Based Nanosensors: Refining Nanoparticle Responsiveness for Single Particle Imaging of Stimuli. *ACS Photonics* **2021**, *8* (1), 3–17. https://doi.org/10.1021/acsphotonics.0c00894.

(44) Himmelstoß, S. F.; Hirsch, T. A Critical Comparison of Lanthanide Based Upconversion Nanoparticles to Fluorescent Proteins, Semiconductor Quantum Dots, and Carbon Dots for Use in Optical Sensing and Imaging. *Methods Appl. Fluoresc.* **2019**, *7* (2). https://doi.org/10.1088/2050-6120/ab0bfa.

(45) Lu, J. B.; Jiang, X. L.; Hu, H. S.; Li, J. Norm-Conserving 4f-in-Core Pseudopotentials and Basis Sets Optimized for Trivalent Lanthanides (Ln = Ce-Lu). *J. Chem. Theory Comput.* **2023**, *19* (1), 82–96. https://doi.org/10.1021/acs.jctc.2c00922.

(46) CONDON, E. U.; SHORTLEY, G. H. *The Theory of Atomic Spectra*; Cambridge University Press, 1951.

(47) AUZEL, F.; MONCORGÉ, R. *Engineering Techniques: Optical Properties of Rare Earths [In French]*; 2017.

(48) Werts, M. H. V. Making Sense of Lanthanide Luminescence. *Sci. Prog.* **2005**, *88* (Pt 2), 101–131. https://doi.org/10.3184/003685005783238435.

(49) Habib, F.; Murugesu, M. Lessons Learned from Dinuclear Lanthanide Nano-Magnets. *Chem. Soc. Rev.* **2013**, *42* (8), 3278–3288. https://doi.org/10.1039/c2cs35361j.

(50) Zhang, P.; Zhang, L.; Tang, J. Lanthanide Single Molecule Magnets: Progress and Perspective. *Dalt. Trans.* **2015**, *44* (9), 3923–3929. https://doi.org/10.1039/b000000x.

(51) Kenyon, A. J. Recent Developments in Rare-Earthdoped Materials for Optoelectronics. *Prog. Quantum Electron.* **2002**, *26*, 225–284.

(52) Auzel, F. Upconversion and Anti-Stokes Processes with f and d Ions in Solids. *Chem. Rev.* **2004**, *104* (1), 139–173. https://doi.org/10.1021/cr020357g.

(53) Reisfeld, R. New Developments in Luminescence for Solar Energy Utilization. *Opt. Mater. (Amst).* **2010**, *32* (9), 850–856. https://doi.org/10.1016/j.optmat.2010.04.034.

(54) E. Wiedemann. Ueber Fluorescenz Und Phosphorescenz i. Abhandlung. *Ann. Phys.* **1888**, 446–463.

(55) Vavilov, S.-J. The Duration of Luminescence. *A.S. USSR [In Russ.* **1952**, *2*, 293.

(56) Vij, D.-R. *Luminescence of Solids*; 1998. https://doi.org/10.1007/978-1-4615-5361-8.

(57) Lakowicz, J. R. *Principles of Fluorescence Spectroscopy*; 2006. https://doi.org/10.1007/978-0-387-46312-4.

(58) Kaplyanskii, A. A.; Feofilov, P. P. Low-Temperature Spectra of Divalent Samarium in Alkali Halide Single Crystals. *Opt. Spectrosc.* **1964**, *16*, 144.

(59) Runciman, W. A. Stress Spectra of Defects in Diamond. *Proc. Phys. Soc.* **1965**, *86* (3), 629–636. https://doi.org/10.1088/0370-1328/86/3/322.

(60) Xu, C. N.; Zheng, X. G.; Watanabe, T.; Akiyama, M.; Usui, I. Enhancement of Adhesion and Triboluminescence of ZnS:Mn Films by Annealing Technique. *Thin Solid Films* **1999**, *352* (1–2), 273–277. https://doi.org/10.1016/S0040-6090(99)00327-2.

(61) Chandra, V. K.; Chandra, B. P.; Jha, P. Mechanoluminescence of ZnS:Mn Phosphors Excited by Hydrostatic Pressure Steps and Pressure Pulses. *Phys. B Condens. Matter* **2014**, *452*, 23–30. https://doi.org/10.1016/j.physb.2014.06.038.

(62) Xu, H.; Wang, F.; Wang, Z.; Zhou, H.; Zhang, G.; Zhang, J.; Wang, J.; Yang, S. Intelligent Solid Lubricant Materials with Failure Early-Warning Based on Triboluminescence. *Tribol. Lett.* **2019**, *67* (1), 1–10. https://doi.org/10.1007/s11249-018-1120-0.

(63) J. H. VAN VLECK. THE PUZZLE OF RARE-EARTH SPECTRA IN SOLIDS; 1936; pp 67–79. https://doi.org/10.1063/1.45424.

(64) Soini, E.; Hemmila, I. Fluoroimmunoassay: Present Status and Key Problems. *Clin. Chem.* **1979**, *25* (3), 353–361. https://doi.org/10.1093/clinchem/25.3.353.

(65) LIU, G. *Spectroscopic Properties of Rare Earths in Optical Materials*; JACQUIER, B., Ed.; Springer Science & Business Media, 2005.

(66) Eiichiro Nakazawa. Charge-Transfer Type Luminescence of Yb3+ Ions in LuPO4 and YPO4. *Chem. Phys. Lett.* **1978**, *56* (1), 161–163.

(67) Van Pieterson, L.; Heeroma, M.; De Heer, E.; Meijerink, A. Charge Transfer Luminescence of Yb3+. *J. Lumin.* **2000**, *91* (3), 177–193. https://doi.org/10.1016/S0022-2313(00)00214-3.

(68) Guerassimova, N.; Garnier, N.; Dujardin, C.; Petrosyan, A. G.; Pedrini, C. X-Ray Excited Charge Transfer Luminescence of Ytterbium-Containing Aluminium Garnets. *Chem. Phys. Lett.* **2001**, *339* (3–4), 197–202. https://doi.org/10.1016/S0009-2614(01)00331-1.

(69) Kamenskikh, I. A.; Guerassimova, N.; Dujardin, C.; Garnier, N.; Ledoux, G.; Pedrini, C.; Kirm, M.; Petrosyan, A.; Spassky, D. Charge Transfer Fluorescence and F-f Luminescence in Ytterbium Compounds. *Opt. Mater. (Amst).* **2003**, *24* (1–2), 267–274. https://doi.org/10.1016/S0925-3467(03)00133-2.

(70) Kornoukhov, V. N. Detector Lens as a New Tool for Solar Neutrino Spectroscopy. *Phys. At. Nucl.* **2002**, *65* (12), 2161–2164. https://doi.org/10.1134/1.1530294.

(71) Peijzel, P. S.; Meijerink, A.; Wegh, R. T.; Reid, M. F.; Burdick, G. W. A Complete 4fn Energy Level Diagram for All Trivalent Lanthanide Ions. *J. Solid State Chem.* **2005**, *178* (2 SPEC. ISS.), 448–453. https://doi.org/10.1016/j.jssc.2004.07.046.

(72) Reisfeld, R. Optical Properties of Lanthanides in Condensed Phase, Theory and Applications. *AIMS Mater. Sci.* **2015**, *2* (2), 37–60. https://doi.org/10.3934/matersci.2015.2.37.

(73) W. T. Carnall; Goodman, G. L.; Rajnak, K.; Rana, R. S. A Systematic Analysis of the Spectra of the Lanthanides Doped into Single Crystal LaF3. *J. Chem. Phys.* **1989**, *90* (7), 3443. https://doi.org/https://doi.org/10.1063/1.455853.

(74) Chambers, M. D.; Clarke, D. R. Doped Oxides for High-Temperature Luminescence and Lifetime Thermometry. *Annu. Rev. Mater. Res.* **2009**, *39*, 325–359. https://doi.org/10.1146/annurev-matsci-112408-125237.

(75) Binnemans, K. Interpretation of Europium (III) Spectra. *Coord. Chem. Rev.* **2015**, *45*, 1–45.

(76) Hest, J. J. H. A. van. Luminescence Properties of Lanthanide-Doped Nanocrystal Labels, 2018.

(77) WEBER, M. Radiative and Multiphonon Relaxation of Rare-Earth Ions in Y 2 O 3. *Phys. Rev.* **1968**, *171* (2), 283.

(78) Swinehart, D. F. The Beer-Lambert Law. *J. Chem. Educ.* **1962**, *39* (7), 333–335. https://doi.org/10.1021/ed039p333.

(79) Knighton, R. C.; Soro, L. K.; Lecointre, A.; Pilet, G.; Fateeva, A.; Pontille, L.; Francés-Soriano, L.; Hildebrandt, N.; Charbonnière, L. J. Upconversion in Molecular Hetero-Nonanuclear Lanthanide

Complexes in Solution. *Chem. Commun.* **2021**, *57* (1), 53–56. https://doi.org/10.1039/d0cc07337g.

(80) Vavilov, S.-J. The Fluorescence Efficiency of Dye Solutions. *Z. Phys* **1924**, *22*, 266.

(81) Stepanov, B.; Gribkovskii, V. Introduction to the Theory of Luminescence [in Russian]/Translation: Theory of Luminescence (1968) (ILIFFE Books, London). *Izd. AN BSSR Minsk* **1963**.

(82) Zhou, J.; Xia, Z. Multi-Color Emission Evolution and Energy Transfer Behavior of La 3GaGe5O16:Tb3+,Eu3+ Phosphors. *J. Mater. Chem. C* **2014**, *2* (34), 6978–6984. https://doi.org/10.1039/c4tc01091d.

(83) Förster, T. Zwischenmolekulare Energiewanderung Und Konzentrationsdepolarisation Der Fluoreszenz [German]. *Ann. Phys.* **1948**, *6* (2), 55–75. https://doi.org/10.1002/andp.19614630112.

(84) Förster, T. Transfer Mechanisms of Electronic Excitation. *Discuss. Faraday Soc.* **1959**, *27*, 7–17. https://doi.org/10.1039/DF9592700007.

(85) Edgar, A. *Luminescent Materials*; 2007. https://doi.org/10.1007/978-0-387-29185-7_40.

(86) Dexter, D. L. A Theory of Sensitized Luminescence in Solids. *J. Chem. Phys.* **1953**, *21* (5), 836–850. https://doi.org/10.1063/1.1699044.

(87) Dexter, D. L.; Schulman, J. H. Theory of Concentration Quenching in Inorganic Phosphors. *J. Chem. Phys.* **1954**, *22* (6), 1063–1070. https://doi.org/10.1063/1.1740265.

(88) Speiser, S. Photophysics and Mechanisms of Intramolecular Electronic Energy Transfer in Bichromophoric Molecular Systems: Solution and Supersonic Jet Studies. *Chem. Rev.* **1996**, *96* (6), 1953–1976. https://doi.org/10.1021/cr941193+.

(89) Šimková, E.; Staněk, D. Probing Nucleic Acid Interactions and Pre-MRNA Splicing by Förster Resonance Energy Transfer (FRET) Microscopy. *Int. J. Mol. Sci.* **2012**, *13* (11), 14929–14945. https://doi.org/10.3390/ijms131114929.

(90) Carneiro Neto, A. N.; Moura, R. T.; Shyichuk, A.; Paterlini, V.; Piccinelli, F.; Bettinelli, M.; Malta, O. L. Theoretical and Experimental Investigation of the Tb3+ → Eu3+ Energy Transfer Mechanisms in Cubic A3Tb0.90Eu0.10(PO4)3 (A = Sr, Ba) Materials. *J. Phys. Chem. C* **2020**, *124* (18), 10105–10116. https://doi.org/10.1021/acs.jpcc.0c00759.

(91) Weissman, S. I. Intramolecular Energy Transfer the Fluorescence of Complexes of Europium. *J. Chem. Phys.* **1942**, *10* (4), 214–217. https://doi.org/10.1063/1.1723709.

(92) De Andrade, A. V. M.; Longo, R. L.; Simas, A. M.; De Sá, G. F. Theoretical Model for the Prediction of Electronic Spectra of Lanthanide Complexes. *J. Chem. Soc. - Faraday Trans.* **1996**, *92* (11), 1835–1839. https://doi.org/10.1039/FT9969201835.

(93) Kleinerman, M. Energy Migration in Lanthanide Chelates. *J. Chem. Phys.* **1969**, *51* (6), 2370–2381. https://doi.org/10.1063/1.1672355.

(94) Zahariev, T.; Shandurkov, D.; Gutzov, S.; Trendafilova, N.; Enseling, D.; Jüstel, T.; Georgieva, I. Phenanthroline Chromophore as Efficient Antenna for Tb 3 + Green Luminescence : A Theoretical Study. *Dye. Pigment.* **2021**, *185* (PA), 108890. https://doi.org/10.1016/j.dyepig.2020.108890.

(95) Bünzli, J. C. G.; Piguet, C. Taking Advantage of Luminescent Lanthanide Ions. *Chem. Soc. Rev.* **2005**, *34* (12), 1048–1077. https://doi.org/10.1039/b406082m.

(96) Kitagawa, Y.; Ferreira Da Rosa, P. P.; Hasegawa, Y. Charge-Transfer Excited States of π- And 4f-Orbitals for Development of Luminescent Eu(Iii) Complexes. *Dalt. Trans.* **2021**, *50* (42), 14978–14984. https://doi.org/10.1039/d1dt03019a.

(97) Kitagawa, Y.; Kumagai, M.; Nakanishi, T.; Fushimi, K.; Hasegawa, Y. The Role of π-f Orbital Interactions in Eu(III) Complexes for an Effective Molecular Luminescent Thermometer. *Inorg. Chem.* **2020**, *59* (9), 5865–5871. https://doi.org/10.1021/acs.inorgchem.9b03492.

(98) Yamamoto, M.; Kitagawa, Y.; Nakanishi, T.; Fushimi, K.; Hasegawa, Y. Ligand-Assisted Back Energy Transfer in Luminescent TbIII Complexes for Thermosensing Properties. *Chem. - A Eur. J.* **2018**, *24* (67), 17719–17726. https://doi.org/10.1002/chem.201804392.

(99) NCHIMI NONO, K. SYNTHESIS OF LUMINESCENT COMPLEXES BASED ON LANTHANIDE IONS FOR BIOMOLECULE LABELLING Application to the Diagnosis of Alzheimer's Disease [In French]. **2014**.

(100) Alexander, O. T.; Kroon, R. E.; Brink, A.; Visser, H. G. Symmetry Correlations between Crystallographic and Photoluminescence Study of Ternary β-Diketone Europium(III) Based Complexes Using 1,10-Phenanthroline as the Ancillary Ligand. *Dalt. Trans.* **2019**, 16074–16082. https://doi.org/10.1039/c9dt02580d.

(101) Blais, C.; Daiguebonne, C.; Suffren, Y.; Bernot, K.; Calvez, G.; Le Pollès, L.; Roiland, C.; Freslon, S.; Guillou, O. Investigation of Intermetallic Energy Transfers in Lanthanide Coordination Polymers Molecular Alloys: Case Study of Trimesate-Based Compounds. *Inorg. Chem.* **2022**, *61* (30), 11897–11915. https://doi.org/10.1021/acs.inorgchem.2c01650.

(102) Wisser, M. D.; Chea, M.; Lin, Y.; Wu, D. M.; Mao, W. L.; Salleo, A.; Dionne, J. A. Strain-Induced Modification of Optical Selection Rules in Lanthanide-Based Upconverting Nanoparticles. *Nano Lett.* **2015**, *15* (3), 1891–1897. https://doi.org/10.1021/nl504738k.

(103) Wang, Y.; Zhou, J.; Gao, J.; Zhang, K.; Gao, C.; Xie, X.; Huang, L. Physical Manipulation of Lanthanide-Activated Photoluminescence. *Ann. Phys.* **2019**, *531* (9), 1–12. https://doi.org/10.1002/andp.201900026.

(104) Neal Watkins, A.; Peak, S. M. Addition of Silica-Coated Ag Nanoparticles to Enhance Luminescence Intensity of Pressure-Sensitive Paints. *ACS Appl. Nano Mater.* **2020**, *3* (10), 9813–9821. https://doi.org/10.1021/acsanm.0c01898.

(105) Pilch, M.; Ortyl, J.; Chachaj-Brekiesz, A.; Galek, M.; Popielarz, R. Europium-Based Luminescent Sensors for Mapping Pressure Distribution on Surfaces. *Sensors Actuators, B Chem.* **2020**, *305* (August 2019), 127409. https://doi.org/10.1016/j.snb.2019.127409.

(106) Sano, S.; Yuuki, T.; Hyakutake, T.; Morita, K.; Sakaue, H.; Arai, S.; Matsumoto, H.; Michinobu, T. Temperature Compensation of Pressure-Sensitive Luminescent Polymer Sensors. *Sensors Actuators, B Chem.* **2018**, *255*, 1960–1966. https://doi.org/10.1016/j.snb.2017.08.221.

(107) Amao, Y.; Okura, I.; Miyashita, T. Optical Oxygen Sensing Based on the Luminescence Quenching of Europium(III) Complex Immobilized in Fluoropolymer Film. *Bull. Chem. Soc. Jpn.* **2000**, *73*, 2663–2668.

(108) Wong, H. Y.; Zhou, X. Le; Yeung, C. T.; Man, W. L.; Woźny, P.; Półrolniczak, A.; Katrusiak, A.; Runowski, M.; Law, G. L. Stress to Distress: Triboluminescence and Pressure Luminescence of Lanthanide Diketonates. *Chem. Eng. J. Adv.* **2022**, *11* (May). https://doi.org/10.1016/j.ceja.2022.100326.

(109) Hasegawa, Y.; Kitagawa, Y. Luminescent Lanthanide Coordination Polymers with Transformative Energy Transfer Processes for Physical and Chemical Sensing Applications. *J. Photochem. Photobiol. C Photochem. Rev.* **2022**, *51* (June 2021), 100485. https://doi.org/10.1016/j.jphotochemrev.2022.100485.

(110) Hasegawa, Y.; Sawanobori, T.; Kitagawa, Y.; Shoji, S.; Fushimi, K.; Nakasaka, Y.; Masuda, T.; Hisaki, I. An Europium (III) Luminophore with Pressure-Sensing Units: Effective Back Energy Transfer in Coordination Polymers with Hexadentate Porous Stable Networks. *Chempluschem* **2020**, *85* (9), 1989–1993. https://doi.org/10.1002/cplu.202000513.

(111) Parker, D.; Kanthi Senanayake, P.; Gareth Williams, J. A. Luminescent Sensors for PH, PO2, Halide and Hydroxide Ions Using Phenanthridine as a Photosensitiser in Macrocyclic Europium and Terbium Complexes. *J. Chem. Soc. Perkin Trans. 2* **1998**, No. 10, 2129–2139. https://doi.org/10.1039/a801270i.

(112) Mei, E.; Vinogradov, S.; Hochstrasser, R. M. Direct Observation of Triplet State Emission of Single Molecules : Single Molecule Phosphorescence Quenching of Metalloporphyrin and Organometallic Complexes by Molecular Oxygen and Their Quenching Rate Distributions. *J. Am. Chem. Soc.* **2003**, No. 125, 13198–13204.

(113) Suffren, Y.; O'Toole, N.; Hauser, A.; Jeanneau, E.; Brioude, A.; Desroches, C. Discrete Polynuclear Manganese(Ii) Complexes with Thiacalixarene Ligands: Synthesis, Structures and Photophysical Properties. *Dalt. Trans.* **2015**, *44* (17), 7991–8000. https://doi.org/10.1039/c5dt00827a.

(114) Yingchao Yan; Anne Jans Faber; Waal, H. de. Luminescence Quenching by OH Groups in Highly Er-

Dopedphosphate Glasses. *J. Non. Cryst. Solids* **1995**, *181*, 283–290.

(115) Purohit, B.; Amans, D.; Guyot, Y.; Mahler, B.; Joubert, M. F.; Dujardin, C.; Daniele, S.; Ledoux, G.; Mishra, S. Quest to Enhance Up-Conversion Efficiency: A Comparison of Anhydrous vs. Hydrous Synthesis of NaGdF4: Yb3+ and Tm3+ Nanoparticles. *Mater. Today Chem.* **2020**, *17*. https://doi.org/10.1016/j.mtchem.2020.100326.

(116) Kasai, M.; Sugioka, Y.; Yamamoto, M.; Nagata, T.; Nonomura, T.; Asia, K.; Hasegawa, Y. Characteristic Evaluation of Chameleon Luminophore Dispersed in Polymer. *sensors* **2020**, *20* (2623), 1–15. https://doi.org/10.3390/s20092623.

(117) Zhang, Q.; Wu, L.; Cao, X.; Chen, X.; Fang, W.; Dolg, M. Energy Resonance Crossing Controls the Photoluminescence of Europium Antenna Probes. *Angew. Chemie Int. Ed.* **2017**, *56*, 7986–7990.

(118) Wu, L.; Fang, Y.; Zuo, W.; Wang, J.; Wang, J.; Wang, S.; Cui, Z.; Fang, W.; Sun, H. L.; Li, Y.; Chen, X. Excited-State Dynamics of Crossing-Controlled Energy Transfer in Europium Complexes. *JACS Au* **2022**, *2* (4), 853–864. https://doi.org/10.1021/jacsau.1c00584.

(119) Grzyb, T.; Gruszeczka, A.; Lis, S. Up-Conversion Luminescence of Yb3+ and Er3+ Doped YPO4, LaPO4 and GdPO4 Nanocrystals. *J. Lumin.* **2016**, *175*, 21–27. https://doi.org/10.1016/j.jlumin.2016.02.021.

(120) Nie, Z.; Ke, X.; Li, D.; Zhao, Y.; Zhu, L.; Qiao, R.; Zhang, X. L. NaYF4:Yb,Er,Nd@NaYF4:Nd Upconversion Nanocrystals Capped with Mn:TiO2 for 808 Nm NIR-Triggered Photocatalytic Applications. *J. Phys. Chem. C* **2019**, *123* (37), 22959–22970. https://doi.org/10.1021/acs.jpcc.9b05234.

(121) Cui, X.; Cheng, Y.; Lin, H.; Huang, F.; Wu, Q.; Wang, Y. Size-Dependent Abnormal Thermo-Enhanced Luminescence of Ytterbium-Doped Nanoparticles. *Nanoscale* **2017**, *9* (36), 13794–13799. https://doi.org/10.1039/c7nr04575a.

(122) ENGELBRECHT, R. Parametric Energy Conversion by Nonlinear Admittances. *Proc. IRE* **1962**, *50* (3), 312–321.

(123) MIDWINTER, J. E.; WARNER, J. Up-conversion of near Infrared to Visible Radiation in Lithium-meta-Niobate. *J. Appl. Phys.* **1967**, *38* (2), 519–5263.

(124) TANG, C. L. Spontaneous Emission in the Frequency Up-Conversion Process in Nonlinear Optics. *Phys. Rev.* **1969**, *182* (2), 367.

(125) ANDREWS, R. IR Image Parametric Up-Conversion. *IEEE J. Quantum Electron.* **1970**, *6* (1), 68–80.

(126) Heer, S.; Lehmann, O.; Haase, M.; Güdel*, H.-U. Blue, Green, and Red Upconversion Emission from Lanthanide-Doped LuPO 4 and YbPO 4 Nanocrystals in a Solution. **2003**, 3179–3182. https://doi.org/10.1002/anie.200351091.

(127) Dong, H.; Sun, L.-D.; Yan, C.-H. Energy Transfer in Lanthanide Upconverting Studies for Extended Optical Applications. *Chem. Soc. Rev.* **2015**, *44* (6), 1608–1634. https://doi.org/10.1039/x0xx00000x.

(128) Mishra, S.; Ledoux, G.; Jeanneau, E.; Daniele, S.; Joubert, M. F. Novel Heterometal-Organic Complexes as First Single Source Precursors for up-Converting NaY(Ln)F 4 (Ln = Yb, Er, Tm) Nanomaterials. *Dalt. Trans.* **2012**, *41* (5), 1490–1502. https://doi.org/10.1039/c1dt11070e.

(129) Zhang, Z.; Suo, H.; Zhao, X.; Sun, D.; Fan, L.; Guo, C. NIR-to-NIR Deep Penetrating Nanoplatforms Y2O3:Nd3+/Yb3+@SiO2@Cu2S toward Highly Efficient Photothermal Ablation. *ACS Appl. Mater. Interfaces* **2018**, *10* (17), 14570–14576. https://doi.org/10.1021/acsami.8b03239.

(130) Du, P.; Luo, L.; Huang, X.; Yu, J. S. Ultrafast Synthesis of Bifunctional Er 3+ /Yb 3+ -Codoped NaBiF 4 Upconverting Nanoparticles for Nanothermometer and Optical Heater. *J. Colloid Interface Sci.* **2018**, *514*, 172–181. https://doi.org/10.1016/j.jcis.2017.12.027.

(131) Suo, H.; Zhao, X.; Zhang, Z.; Guo, C. 808 Nm Light-Triggered Thermometer-Heater Upconverting Platform Based on Nd3+-Sensitized Yolk-Shell GdOF@SiO2. *ACS Appl. Mater. Interfaces* **2017**, *9* (50), 43438–43448. https://doi.org/10.1021/acsami.7b12753.

(132) Suo, H.; Zhao, X.; Zhang, Z.; Li, T.; Goldys, E. M.; Guo, C. Constructing Multiform Morphologies of YF: Er3+/Yb3+up-Conversion Nano/Micro-Crystals towards Sub-Tissue Thermometry. *Chem. Eng. J.*

2017, *313*, 65–73. https://doi.org/10.1016/j.cej.2016.12.064.

(133) Wei, Y.; Su, C.; Zhang, H.; Shao, J.; Fu, Z. Thermal Sensor and Optical Heater of Upconversion Phosphor: Yb3+/Er3+ Co-Doped KY(MoO4)2. *Phys. B Condens. Matter* **2017**, *525* (May), 149–153. https://doi.org/10.1016/j.physb.2017.06.046.

(134) Savchuk, O. A.; Carvajal, J. J.; Brites, C. D. S.; Carlos, L. D.; Aguilo, M.; Diaz, F. Upconversion Thermometry: A New Tool to Measure the Thermal Resistance of Nanoparticles. *Nanoscale* **2018**, *10* (14), 6602–6610. https://doi.org/10.1039/c7nr08758f.

(135) Mahata, M. K.; Kumar, K.; Rai, V. K. Er3+–Yb3+ Doped Vanadate Nanocrystals: A Highly Sensitive Thermographic Phosphor and Its Optical Nanoheater Behavior. *Sensors Actuators B Chem.* **2015**, *209*, 775–780. https://doi.org/10.1016/j.snb.2014.12.039.

(136) Suo, H.; Zhao, X.; Zhang, Z.; Wu, Y.; Guo, C. Upconverting LuVO4:Nd3+/Yb3+/Er3+@SiO2@Cu2S Hollow Nanoplatforms for Self-Monitored Photothermal Ablation. *ACS Appl. Mater. Interfaces* **2018**, *10* (46), 39912–39920. https://doi.org/10.1021/acsami.8b18184.

(137) Sun, J.; Zhang, Z.; Suo, H.; Chen, Y.; Xiang, J.; Guo, C. Temperature Self-Monitoring Photothermal Nano-Particles of Er3+/Yb3+ Co-Doped Zircon-Tetragonal BiVO4. *Ceram. Int.* **2021**, *47* (1), 409–415. https://doi.org/10.1016/j.ceramint.2020.08.147.

(138) Guo, H.; Dong, N.; Yin, M.; Zhang, W.; Lou, L.; Xia, S. Visible Upconversion in Rare Earth Ion-Doped Gd2O3 Nanocrystals. *J. Phys. Chem. B* **2004**, *108* (50), 19205–19209. https://doi.org/10.1021/jp048072q.

(139) Buissette, V.; Huignard, A.; Gacoin, T.; Boilot, J. P.; Aschehoug, P.; Viana, B. Luminescence Properties of YVO4:Ln (Ln = Nd, Yb, and Yb-Er) Nanoparticles. *Surf. Sci.* **2003**, *532–535*, 444–449. https://doi.org/10.1016/S0039-6028(03)00203-6.

(140) Mialon, G.; Gohin, M.; Gacoin, T.; Boilot, J. P. High Temperature Strategy for Oxide Nanoparticle Synthesis. *ACS Nano* **2008**, *2* (12), 2505–2512. https://doi.org/10.1021/nn8005784.

(141) Fischer, L. H.; Harms, G. S.; Wolfbeis, O. S. Upconverting Nanoparticles for Nanoscale Thermometry. *Angew. Chemie - Int. Ed.* **2011**, *50* (20), 4546–4551. https://doi.org/10.1002/anie.201006835.

(142) Li, A. H.; Sun, Z. J.; Lü, Q. Laser Heating Effect on the Power Dependence of Upconversion Luminescence in Er3+-Doped Nanopowders. *J. Nanoparticle Res.* **2013**, *15* (1). https://doi.org/10.1007/s11051-012-1377-4.

(143) Chunxia, L.; Cuimiao, Z.; Zhiyao, H.; Lili, W.; Zewei, Q.; Hongzhou, L.; Jun, L. β-NaYF4 and β-NaYF4:Eu3+ Microstructures: Morphology Control and Tunable Luminescence Properties. *J. Phys. Chem. C* **2009**, *113* (6), 2332–2339. https://doi.org/10.1021/jp8101628.

(144) Savchuk, O. A.; Carvajal, J. J.; Cesteros, Y.; Salagre, P.; Nguyen, H. D.; Rodenas, A.; Massons, J.; Aguiló, M.; Díaz, F. Mapping Temperature Distribution Generated by Photothermal Conversion in Graphene Film Using Er,Yb:NaYF4 Nanoparticles Prepared by Microwave-Assisted Solvothermal Method. *Front. Chem.* **2019**, *7* (FEB), 1–11. https://doi.org/10.3389/fchem.2019.00088.

(145) Mai, H. X.; Zhang, Y. W.; Si, R.; Yan, Z. G.; Sun, L. D.; You, L. P.; Yan, C. H. High-Quality Sodium Rare-Earth Fluoride Nanocrystals: Controlled Synthesis and Optical Properties. *J. Am. Chem. Soc.* **2006**, *128* (19), 6426–6436. https://doi.org/10.1021/ja060212h.

(146) Capobianco, J. A.; Vetrone, F.; D'Alesio, T.; Tessari, G.; Speghini, A.; Bettinelli, M. Optical Spectroscopy of Nanocrystalline Cubic Y2O3: Er3+ Obtained by Combustion Synthesis. *Phys. Chem. Chem. Phys.* **2000**, *2* (14), 3203–3207. https://doi.org/10.1039/b003031g.

(147) Capobianco, J. A.; Vetrone, F.; Boyer, J. C.; Speghini, A.; Bettinelli, M. Visible Upconversion of Er3þ Doped Nanocrystalline and Bulk Lu2O3. *Opt. Mater. (Amst).* **2002**, *19*, 259–268.

(148) Geitenbeek, R. G.; Prins, P. T.; Albrecht, W.; Van Blaaderen, A.; Weckhuysen, B. M.; Meijerink, A. NaYF4:Er3+,Yb3+/SiO2 Core/Shell Upconverting Nanocrystals for Luminescence Thermometry up to 900 K. *J. Phys. Chem. C* **2017**, *121* (6), 3503–3510. https://doi.org/10.1021/acs.jpcc.6b10279.

(149) Lay, A.; Siefe, C.; Fischer, S.; Mehlenbacher, R. D.; Ke, F.; Mao, W. L.; Alivisatos, A. P.; Goodman, M. B.; Dionne, J. A. Bright, Mechanosensitive Upconversion with Cubic-Phase Heteroepitaxial Core − Shell Nanoparticles. *Nano Lett.* **2018**, *18*, 4454–4459. https://doi.org/10.1021/acs.nanolett.8b01535.

(150) Chen, B.; Wang, F. Combating Concentration Quenching in Upconversion Nanoparticles. *Acc. Chem. Res.* **2019**. https://doi.org/10.1021/acs.accounts.9b00453.

(151) Wang, F.; Wang, J.; Liu, X. Direct Evidence of a Surface Quenching Effect on Size-Dependent Luminescence of Upconversion Nanoparticles. *Angew. Chemie - Int. Ed.* **2010**, *49* (41), 7456–7460. https://doi.org/10.1002/anie.201003959.

(152) Zhao, J.; Li, H.; Zeng, Q.; Song, K.; Wang, X.; Kong, X. Temperature-Dependent Upconversion Luminescence of NaYF 4 :Yb 3+ ,Er 3+ Nanoparticles . *Chem. Lett.* **2013**, *42* (3), 310–312. https://doi.org/10.1246/cl.2013.310.

(153) Binnemans, K. Lanthanide-Based Luminescent Hybrid Materials. *Chem. Rev.* **2009**, *109* (9), 4283–4374. https://doi.org/10.1021/cr8003983.

(154) Pichaandi, J.; Boyer, J. C.; Delaney, K. R.; Van Veggel, F. C. J. M. Two-Photon Upconversion Laser (Scanning and Wide-Field) Microscopy Using Ln3+-Doped NaYF4 Upconverting Nanocrystals: A Critical Evaluation of Their Performance and Potential in Bioimaging. *J. Phys. Chem. C* **2011**, *115* (39), 19054–19064. https://doi.org/10.1021/jp206345j.

(155) Wang, H.; Yin, X.; Xing, M.; Fu, Y.; Tian, Y.; Feng, X.; Jiang, T.; Luo, X. Thermal Effects of Er3+/Yb3+-Doped NaYF4 Phosphor Induced by 980/1510 Nm Laser Diode Irradiation. *J. Am. Ceram. Soc.* **2018**, *101* (2), 865–873. https://doi.org/10.1111/jace.15246.

(156) Joseph, R. E.; Busko, D.; Hudry, D.; Gao, G.; Biner, D.; Krämer, K.; Turshatov, A.; Richards, B. S.; Howard, I. A. A Method for Correcting the Excitation Power Density Dependence of Upconversion Emission Due to Laser-Induced Heating. *Opt. Mater. (Amst).* **2018**, *82* (February), 65–70. https://doi.org/10.1016/j.optmat.2018.05.025.

(157) Zhang, W. W.; Gao, Y. Q.; He, X. D.; Li, S. Monitoring of Laser Heating Temperature in Laser Spectroscopic Measurements. *Opt. Commun.* **2012**, *285* (9), 2414–2417. https://doi.org/10.1016/j.optcom.2012.01.009.

(158) Dey, R.; Pandey, A.; Rai, V. K. Er3+-Yb3+ and Eu3+-Er3+-Yb 3+ Codoped Y2O3 Phosphors as Optical Heater. *Sensors Actuators, B Chem.* **2014**, *190*, 512–515. https://doi.org/10.1016/j.snb.2013.09.025.

(159) Zhou, Y.; Ledoux, G.; Philippon, D.; Descartes, S.; Martini, M.; He, S.; Desroches, C.; Fournier, D.; Journet, C.; Bois, L. Laser-Induced Heating in GdVO 4 : Yb 3 + / Er 3 + Nanocrystals for Thermometry. *ACS Appl. Nano Mater.* **2022**, *5*, 16388–16401. https://doi.org/10.1021/acsanm.2c03466.

(160) Carrasco, E.; Del Rosal, B.; Sanz-Rodríguez, F.; De La Fuente, Á. J.; Gonzalez, P. H.; Rocha, U.; Kumar, K. U.; Jacinto, C.; Solé, J. G.; Jaque, D. Intratumoral Thermal Reading during Photo-Thermal Therapy by Multifunctional Fluorescent Nanoparticles. *Adv. Funct. Mater.* **2015**, *25* (4), 615–626. https://doi.org/10.1002/adfm.201403653.

(161) Zhu, J.; Wang, S.; Yang, Z.; Liao, S.; Lin, J.; Yao, H.; Huang, F.; Zheng, Y.; Chen, D. A Single-Beam NIR Laser-Triggered Full-Color Upconversion Tuning of a Er/Tm:CsYb2F7@glass Photothermal Nanocomposite for Optical Security. **2022**, 3407–3415. https://doi.org/10.1039/d1nr08535b.

(162) Wang, S.; Lin, J.; Li, X.; Chen, J.; Yang, C.; Huang, P.; Cheng, Y.; Chen, D. Glass-Limited Yb/Er:NaLuF4nanocrystals: Reversible Hexagonal-to-Cubic Phase Transition and Anti-Counterfeiting. *J. Mater. Chem. C* **2020**, *8* (45), 16151–16159. https://doi.org/10.1039/d0tc03775c.

(163) Wang, S.; Lin, J.; He, Y.; Chen, J.; Yang, C.; Huang, F.; Chen, D. Remarkable Laser-Driven Upconverting Photothermal Effect of Cs3LnF6@glass Nanocomposites for Anti-Counterfeiting. *Chem. Eng. J.* **2020**, *394* (January), 124889. https://doi.org/10.1016/j.cej.2020.124889.

(164) Erol, E.; Kibrisli, O.; Vahedigharehchopogh, N.; Çelikbilek Ersundu, M.; Ersundu, A. E. The Synergistic Effect of Er3+and Ho3+on Temporal Color Tuning of Upconversion Emission in a Glass Host: Via a Facile Excitation Modulation Technique for Anti-Counterfeiting Applications. *Phys. Chem. Chem. Phys.* **2020**, *22* (44), 25963–25972. https://doi.org/10.1039/d0cp04809g.

(165) Bednarkiewicz, A.; Wawrzynczyk, D.; Gagor, A.; Kepinski, L.; Kurnatowska, M.; Krajczyk, L.; Nyk, M.; Samoc, M.; Strek, W. Giant Enhancement of Upconversion in Ultra-Small Er 3+/Yb 3+:NaYF 4 Nanoparticles via Laser Annealing. *Nanotechnology* **2012**, *23* (14). https://doi.org/10.1088/0957-4484/23/14/145705.

(166) Quintanilla, M.; Henriksen-Lacey, M.; Renero-Lecuna, C.; Liz-Marzán, L. M. Challenges for Optical Nanothermometry in Biological Environments. *Chem. Soc. Rev.* **2022**, *51* (11), 4223–4242. https://doi.org/10.1039/d2cs00069e.

(167) Pieprz, M.; Runowski, M.; Ledwa, K.; Carvajal, J. J.; Bednarkiewicz, A.; Marciniak, L. Improving Accuracy and Sensitivity of Lanthanide-Based Luminescent Manometers by Augmented Spectral Shift Method. *ACS Appl. Mater. Interfaces* **2023**. https://doi.org/10.1021/acsaom.2c00198.

(168) Sutton, J. A.; Fisher, B. T.; Fleming, J. W. A Laser-Induced Fluorescence Measurement for Aqueous Fluid Flows with Improved Temperature Sensitivity. *Exp. Fluids* **2008**, *45* (5), 869–881. https://doi.org/10.1007/s00348-008-0506-4.

(169) Ano, T.; Kishimoto, F.; Sasaki, R.; Tsubaki, S.; Maitani, M. M.; Suzuki, E.; Wada, Y. In Situ Temperature Measurements of Reaction Spaces under Microwave Irradiation Using Photoluminescent Probes. *Phys. Chem. Chem. Phys.* **2016**, *18* (19), 13173–13179. https://doi.org/10.1039/c6cp02034h.

(170) Mishra, Y. N.; Yoganantham, A.; Koegl, M.; Zigan, L. Investigation of Five Organic Dyes in Ethanol and Butanol for Two-Color Laser-Induced Fluorescence Ratio Thermometry. *Optics* **2019**, *1* (1), 1–17. https://doi.org/10.3390/opt1010001.

(171) Veselska, O.; Podbevšek, D.; Ledoux, G.; Fateeva, A.; Demessence, A. Intrinsic Triple-Emitting 2D Copper Thiolate Coordination Polymer as a Ratiometric Thermometer Working over 400 K Range. *Chem. Commun.* **2017**, *53* (90), 12225–12228. https://doi.org/10.1039/c7cc06815h.

(172) Veselska, O.; Guillou, N.; Ledoux, G.; Huang, C. C.; Newell, K. D.; Elkaïm, E.; Fateeva, A.; Demessence, A. A New Lamellar Gold Thiolate Coordination Polymer, [Au(M-SPhCO2H)]n, for the Formation of Luminescent Polymer Composites. *Nanomaterials* **2019**, *9* (10). https://doi.org/10.3390/nano9101408.

(173) Kucsko, G.; Maurer, P. C.; Yao, N. Y.; Kubo, M.; Noh, H. J.; Lo, P. K.; Park, H.; Lukin, M. D. Nanometre-Scale Thermometry in a Living Cell. *Nature* **2013**, *500* (7460), 54–58. https://doi.org/10.1038/nature12373.

(174) Homeyer, E.; Pailhès, S.; Debord, R.; Jary, V.; Dujardin, C.; Ledoux, G. Diamond Contact-Less Micrometric Temperature Sensors. *Appl. Phys. Lett.* **2015**, *106* (24). https://doi.org/10.1063/1.4921177.

(175) Brites, C. D. S.; Lima, P. P.; Silva, N. J. O.; Millán, A.; Amaral, V. S.; Palacio, F.; Carlos, L. D. Thermometry at the Nanoscale. *Nanoscale* **2012**, *4* (16), 4799–4829. https://doi.org/10.1039/c2nr30663h.

(176) Yang, Q.; Zhao, L.; Fang, Z.; Yang, Z.; Cao, J.; Cai, Y.; Zhou, D.; Yu, X.; Qiu, J.; Xu, X. Transparent Perovskite Glass-Ceramics for Visual Optical Thermometry. *J. Rare Earths* **2021**, *39* (6), 712–717. https://doi.org/10.1016/j.jre.2020.05.009.

(177) Han, B.; Hanson, W. L.; Bensalah, K.; Tuncel, A.; Stern, J. M.; Cadeddu, J. A. Development of Quantum Dot-Mediated Fluorescence Thermometry for Thermal Therapies. *Ann. Biomed. Eng.* **2009**, *37* (6), 1230–1239. https://doi.org/10.1007/s10439-009-9681-6.

(178) Dai, G.; Wang, L.; Cheng, S.; Chen, Y.; Liu, X.; Deng, L.; Zhong, H. Perovskite Quantum Dots Based Optical Fabry-Pérot Pressure Sensor. *ACS Photonics* **2020**, *7* (9), 2390–2394. https://doi.org/10.1021/acsphotonics.0c01109.

(179) Feng, G.; Qin, Y.; Ran, C.; Ji, L.; Dong, L.; Li, W. Structural Evolution and Photoluminescence Properties of a 2D Hybrid Perovskite under Pressure. *APL Mater.* **2018**, *6* (11), 2–9. https://doi.org/10.1063/1.5042645.

(180) Chen, W.; Li, G.; Malm, J. O.; Huang, Y.; Wallenberg, R.; Han, H.; Wang, Z.; Bovin, J. O. Pressure Dependence of Mn2+ Fluorescence in ZnS:Mn2+ Nanoparticles. *J. Lumin.* **2000**, *91* (3), 139–145. https://doi.org/10.1016/S0022-2313(00)00222-2.

(181) Antoniak, M. A.; Zelewski, S. J.; Oliva, R.; Żak, A.; Kudrawiec, R.; Nyk, M. Combined Temperature and Pressure Sensing Using Luminescent NaBiF4:Yb,Er Nanoparticles. *ACS Appl. Nano Mater.* **2020**, *3* (5), 4209–4217. https://doi.org/10.1021/acsanm.0c00403.

(182) Dramićanin, M. D. Trends in Luminescence Thermometry. *J. Appl. Phys.* **2020**, *128* (4). https://doi.org/10.1063/5.0014825.

(183) Neubert, P. Method and Apparatus for Recording Temperatures of Hot Bodies. *US Pat.* **1937**, No. June.

(184) CERCIGNANI, C. Ludwig Boltzmann. *Phys. World* **2006**, *19* (9), 34. https://doi.org/10.1021/ed029p298.

(185) Wade, S. A.; Collins, S. F.; Baxter, G. W. Fluorescence Intensity Ratio Technique for Optical Fiber Point Temperature Sensing. *J. Appl. Phys.* **2003**, *94* (8), 4743–4756. https://doi.org/10.1063/1.1606526.

(186) Nexha, A. Synthesis and Characterizations of Multifunctional Luminescent Lanthanide Doped Materials, 2020.

(187) Rakov, N.; Maciel, G. S.; Xiao, M. Upconversion Fluorescence and Its Thermometric Sensitivity of Er3+:Yb3+ Co-Doped SrF2 Powders Prepared by Combustion Synthesis. *Electron. Mater. Lett.* **2014**, *10* (5), 985–989. https://doi.org/10.1007/s13391-014-4030-9.

(188) Li, L.; Qin, F.; Zhou, Y.; Zheng, Y.; Zhao, H.; Zhang, Z. Approximate Energy Gaps, Dissimilar Relative Thermal Sensitivities. *Sensors Actuators, B Chem.* **2018**, *269*, 203–209. https://doi.org/10.1016/j.snb.2018.04.158.

(189) Mott, N. F. On the Absorption of Light by Crystals. *Proc. R. Soc. Lond. A Math. Phy. Sci.* **1938**, 384–391.

(190) Seitz, F. An Interpretation of Crystal Luminescence. *Trans. Faraday Soc.* **1939**, *35*, 74–85. https://doi.org/10.1039/tf9393500074.

(191) Yu, J.; Sun, L.; Peng, H.; Stich, M. I. J. Luminescent Terbium and Europium Probes for Lifetime Based Sensing of Temperature between 0 and 70 C †. *J. Mater. Chem.* **2010**, *20*, 6975–6981. https://doi.org/10.1039/c0jm01069c.

(192) Galyametdinov, Y. G.; Krupin, A. S.; Knyazev, A. A. Temperature-Sensitive Chameleon Luminescent Films Based on PMMA Doped with Europium(III) and Terbium(III) Anisometric Complexes. *Inorganics* **2022**, *10* (7). https://doi.org/10.3390/inorganics10070094.

(193) Kewell, A. K.; Reed, G. T.; Namavar, F. Integrated Temperature Sensor in Er-Doped Silicon. *Sensors Actuators, A Phys.* **1998**, *65* (2–3), 160–164. https://doi.org/10.1016/S0924-4247(97)01699-3.

(194) Jaque, D.; Vetrone, F. Luminescence Nanothermometry. *Nanoscale* **2012**, *4* (15), 4301–4326. https://doi.org/10.1039/c2nr30764b.

(195) Ayela, F.; Medrano-Muñoz, M.; Amans, D.; Dujardin, C.; Brichart, T.; Martini, M.; Tillement, O.; Ledoux, G. Experimental Evidence of Temperature Gradients in Cavitating Microflows Seeded with Thermosensitive Nanoprobes. *Phys. Rev. E - Stat. Nonlinear, Soft Matter Phys.* **2013**, *88* (4). https://doi.org/10.1103/PhysRevE.88.043016.

(196) Perrin, L.; Castanet, G.; Lemoine, F.; Perrin, L.; Castanet, G.; Lemoine, F.; Perrin, L.; Castanet, G.; Lemoine, F. Characterization of the Evaporation of Interacting Droplets Using Combined Optical Techniques. *Exp. Fluids* **2015**, *56*, 1–16.

(197) Perrin, F. Polarisation of Fluorescent Light. Average Life of Molecules in the Excited State [In French]. *J. Phys. le Radium* **1926**, *7* (12), 390–401. https://doi.org/10.1051/jphysrad:01926007012039000.

(198) Rakov, N.; Maciel, G. S. Near-Infrared Emission and Optical Temperature Sensing Performance of Nd3+:SrF2 Crystal Powder Prepared by Combustion Synthesis. *J. Appl. Phys.* **2017**, *121* (11). https://doi.org/10.1063/1.4978380.

(199) Runowski, M.; Woźny, P.; Martín, I. R.; Lavín, V.; Lis, S. Praseodymium Doped YF3:Pr3+ Nanoparticles as Optical Thermometer Based on Luminescence Intensity Ratio (LIR) – Studies in Visible and NIR Range. *J. Lumin.* **2019**, *214* (June). https://doi.org/10.1016/j.jlumin.2019.116571.

(200) Li, H.; Zhang, Y.; Shao, L.; Htwe, Z.; Yuan, P. Luminescence Probe for Temperature Sensor Based on Fluorescence Intensity Ratio. *Opt. Mater. Express* **2017**, *7* (3), 1077. https://doi.org/10.1364/ome.7.001077.

(201) Peng, H. S.; Huang, S. H.; Wolfbeis, O. S. Ratiometric Fluorescent Nanoparticles for Sensing Temperature. *J. Nanoparticle Res.* **2010**, *12* (8), 2729–2733. https://doi.org/10.1007/s11051-010-0046-8.

(202) Gorris, H. H.; Ali, R.; Saleh, S. M.; Wolfbeis, O. S. Tuning the Dual Emission of Photon-Upconverting

Nanoparticles for Ratiometric Multiplexed Encoding. *Adv. Mater.* **2011**, *23* (14), 1652–1655. https://doi.org/10.1002/adma.201004697.

(203) Cui, Y.; Song, R.; Yu, J.; Liu, M.; Wang, Z.; Wu, C.; Yang, Y.; Wang, Z.; Chen, B.; Qian, G. Dual-Emitting MOF⊃dye Composite for Ratiometric Temperature Sensing. *Adv. Mater.* **2015**, *27* (8), 1420–1425. https://doi.org/10.1002/adma.201404700.

(204) D'Vries, R. F.; Álvarez-García, S.; Snejko, N.; Bausá, L. E.; Gutiérrez-Puebla, E.; De Andrés, A.; Monge, M. Á. Multimetal Rare Earth MOFs for Lighting and Thermometry: Tailoring Color and Optimal Temperature Range through Enhanced Disulfobenzoic Triplet Phosphorescence. *J. Mater. Chem. C* **2013**, *1* (39), 6316–6324. https://doi.org/10.1039/c3tc30858h.

(205) Cerõn, E. N.; Ortgies, D. H.; Del Rosal, B.; Ren, F.; Benayas, A.; Vetrone, F.; Ma, D.; Sanz-Rodríguez, F.; Solé, J. G.; Jaque, D.; Rodríguez, E. M. Hybrid Nanostructures for High-Sensitivity Luminescence Nanothermometry in the Second Biological Window. *Adv. Mater.* **2015**, *27* (32), 4781–4787. https://doi.org/10.1002/adma.201501014.

(206) Ishiwada, N.; Fujioka, S.; Ueda, T.; Yokomori, T. Co-Doped Y 2 O 3 : Tb 3+= Tm 3+multicolor Emitting Phosphors for Thermometry. *Opt. Lett.* **2011**, *36* (5), 760–762.

(207) Liu, Y.; Qian, G.; Wang, Z.; Wang, M. Temperature-Dependent Luminescent Properties of Eu-Tb Complexes Synthesized in Situ in Gel Glass. *Appl. Phys. Lett.* **2005**, *86* (7), 1–3. https://doi.org/10.1063/1.1864233.

(208) Brites, C. D. S.; Lima, P. P.; Silva, N. J. O.; Millán, A.; Amaral, V. S.; Palacio, F.; Carlos, L. D. Ratiometric Highly Sensitive Luminescent Nanothermometers Working in the Room Temperature Range. Applications to Heat Propagation in Nanofluids. *Nanoscale* **2013**, *5* (16), 7572–7580. https://doi.org/10.1039/c3nr02335d.

(209) Wang, T.; Li, P.; Li, H. Color-Tunable Luminescence of Organoclay-Based Hybrid Materials Showing Potential Applications in White LED and Thermosensors. *ACS Appl. Mater. Interfaces* **2014**, *6* (15), 12915–12921. https://doi.org/10.1021/am5028555.

(210) Wang, Z.; Ananias, D.; Carné-Sánchez, A.; Brites, C. D. S.; Imaz, I.; Maspoch, D.; Rocha, J.; Carlos, L. D. Lanthanide-Organic Framework Nanothermometers Prepared by Spray-Drying. *Adv. Funct. Mater.* **2015**, *25* (19), 2824–2830. https://doi.org/10.1002/adfm.201500518.

(211) Brites, C. D. S.; Lima, P. P.; Silva, N. J. O.; Millán, A.; Amaral, V. S.; Palacio, F.; Carlos, L. D. Thermometry at the Nanoscale Using Lanthanide-Containing Organic-Inorganic Hybrid Materials. *J. Lumin.* **2013**, *133*, 230–232. https://doi.org/10.1016/j.jlumin.2011.12.050.

(212) Brites, C. D. S.; Lima, P. P.; Silva, N. J. O.; Millán, A.; Amaral, V. S.; Palacio, F.; Carlos, L. D. A Luminescent Molecular Thermometer for Long-Term Absolute Temperature Measurements at the Nanoscale. *Adv. Mater.* **2010**, *22* (40), 4499–4504. https://doi.org/10.1002/adma.201001780.

(213) Cooke, D. W.; Bennett, B. L.; Muenchausen, R. E.; Lee, J. K.; Nastasi, M. A. Intrinsic Ultraviolet Luminescence from Lu2O3, Lu2SiO5 and Lu2SiO5:Ce3+. *J. Lumin.* **2004**, *106* (2), 125–132. https://doi.org/10.1016/j.jlumin.2003.09.001.

(214) Cooke, D. W.; Muenchausen, R. E.; Bennett, B. L.; McClellan, K. J.; Portis, A. M. Temperature-Dependent Luminescence of Cerium-Doped Ytterbium Oxyorthosilicate. *J. Lumin.* **1998**, *79* (3), 185–190. https://doi.org/10.1016/S0022-2313(98)00042-8.

(215) Pandey, A.; Rai, V. K. Optical Thermometry Using FIR of Two Close Lying Levels of Different Ions in Y2O3:Ho3+-Tm3+-Yb3+ Phosphor. *Appl. Phys. B Lasers Opt.* **2013**, *113* (2), 221–225. https://doi.org/10.1007/s00340-013-5460-z.

(216) Ćirić, A.; Gavrilović, T.; Dramićanin, M. D. Luminescence Intensity Ratio Thermometry with Er3+: Performance Overview. *Crystals* **2021**, *11* (2), 1–19. https://doi.org/10.3390/cryst11020189.

(217) Goderski, S.; Runowski, M.; Woźny, P.; Lavín, V.; Lis, S. Lanthanide Upconverted Luminescence for Simultaneous Contactless Optical Thermometry and Manometry-Sensing under Extreme Conditions of Pressure and Temperature. *ACS Appl. Mater. Interfaces* **2020**, *12* (36), 40475–40485. https://doi.org/10.1021/acsami.0c09882.

(218) Runowski, M.; Stopikowska, N.; Szeremeta, D.; Goderski, S.; Skwierczyńska, M.; Lis, S. Upconverting Lanthanide Fluoride Core@Shell Nanorods for Luminescent Thermometry in the First and Second Biological Windows: β-NaYF 4 :Yb 3+ - Er 3+ @SiO 2 Temperature Sensor. *ACS Appl. Mater. Interfaces* **2019**, *11* (14), 13389–13396. https://doi.org/10.1021/acsami.9b00445.

(219) Lin, L.; Li, Z.; Wang, Z.; Feng, Z.; Huang, F.; Dai, Q.; Zheng, Z. Hypersensitive and Color-Tunable Temperature Sensing Properties of (Eu,Tb)(AcAc)3phen via Phonon-Assisted Energy Transfer. *Opt. Mater. (Amst).* **2020**, *110* (August), 110532. https://doi.org/10.1016/j.optmat.2020.110532.

(220) Rodrigues, M. O.; Dutra, J. D. L.; Nunes, L. A. O.; De Sá, G. F.; De Azevedo, W. M.; Silva, P.; Paz, F. A. A.; Freire, R. O.; Júnior, S. A. Tb 3+→Eu 3+ Energy Transfer in Mixed-Lanthanide-Organic Frameworks. *J. Phys. Chem. C* **2012**, *116* (37), 19951–19957. https://doi.org/10.1021/jp3054789.

(221) Trannoy, V.; Carneiro Neto, A. N.; Brites, C. D. S.; Carlos, L. D.; Serier-Brault, H. Engineering of Mixed Eu3+/Tb3+ Metal-Organic Frameworks Luminescent Thermometers with Tunable Sensitivity. *Adv. Opt. Mater.* **2021**, *9* (6), 1–12. https://doi.org/10.1002/adom.202001938.

(222) Viravaux, C.; Oms, O.; Dolbecq, A.; Nassar, E.; Busson, L.; Mellot-Draznieks, C.; Dessapt, R.; Serier-Brault, H.; Mialane, P. Temperature Sensors Based on Europium Polyoxometalate and Mesoporous Terbium Metal-Organic Framework. *J. Mater. Chem. C* **2021**, *9* (26), 8323–8328. https://doi.org/10.1039/d1tc01532j.

(223) Carneiro Neto, A. N.; Mamontova, E.; Botas, A. M. P.; Brites, C. D. S.; Ferreira, R. A. S.; Rouquette, J.; Guari, Y.; Larionova, J.; Long, J.; Carlos, L. D. Rationalizing the Thermal Response of Dual-Center Molecular Thermometers: The Example of an Eu/Tb Coordination Complex. *Adv. Opt. Mater.* **2022**, *10* (5), 1–12. https://doi.org/10.1002/adom.202101870.

(224) Mehlenbacher, R. D.; Kolbl, R.; Lay, A.; Dionne, J. A. Nanomaterials for in Vivo Imaging of Mechanical Forces and Electrical Fields. *Nat. Rev. Mater.* **2017**, *3*, 1–17. https://doi.org/10.1038/natrevmats.2017.80.

(225) Wang, Y.; Seto, T.; Ishigaki, K.; Uwatoko, Y.; Xiao, G.; Zou, B.; Li, G.; Tang, Z.; Li, Z.; Wang, Y. Pressure-Driven Eu2+-Doped BaLi2Al2Si2N6: A New Color Tunable Narrow-Band Emission Phosphor for Spectroscopy and Pressure Sensor Applications. *Adv. Funct. Mater.* **2020**, *30* (34), 1–10. https://doi.org/10.1002/adfm.202001384.

(226) Zheng, T.; Sójka, M.; Woźny, P.; Martín, I. R.; Lavín, V.; Zych, E.; Lis, S.; Du, P.; Luo, L.; Runowski, M. Supersensitive Ratiometric Thermometry and Manometry Based on Dual-Emitting Centers in Eu2+/Sm2+-Doped Strontium Tetraborate Phosphors. *Adv. Opt. Mater.* **2022**, *10* (20), 1–10. https://doi.org/10.1002/adom.202201055.

(227) Runowski, M.; Shyichuk, A.; Tymiński, A.; Grzyb, T.; Lavín, V.; Lis, S. Multifunctional Optical Sensors for Nanomanometry and Nanothermometry: High-Pressure and High-Temperature Upconversion Luminescence of Lanthanide-Doped Phosphates - LaPO4/YPO4:Yb3+-Tm3+. *ACS Appl. Mater. Interfaces* **2018**, *10* (20), 17269–17279. https://doi.org/10.1021/acsami.8b02853.

(228) Muñoz, A.; Venkatramu, V.; Martín, I. R.; Rodríguez-, U. R. High Pressure Luminescence of Nd 3 + in YAlO 3 Perovskite Nanocrystals : A Crystal-Field Analysis High Pressure Luminescence of Nd Field Analysis in YAlO3 Perovskite Nanocrystals : A Crystal. *J. Chem. Phys.* **2018**, *044201* (January).

(229) Wu, S.; Xiong, P.; Liu, X.; Fu, Y.; Liu, Q.; Peng, M.; Chen, Y.; Ma, Z. Bismuth Activated High Thermal Stability Blue-Emitting Phosphor Na2Y2B2O7:Bi Used for near-UV White-Light LEDs. *J. Mater. Chem. C* **2020**, *8* (46), 16584–16592. https://doi.org/10.1039/d0tc04148c.

(230) Piccinelli, F.; Rosa, C. De; Lazarowska, A.; Mahlik, S.; Grinberg, M.; Nakanishi, T.; Omagari, S.; Bettinelli, M. Optical Properties of Eu (III) and Tb (III) Complexes with Pyridine- and Quinoline-Based Ligands under High Hydrostatic Pressure. *Inorganica Chim. Acta* **2020**, *499* (July 2019), 119179. https://doi.org/10.1016/j.ica.2019.119179.

(231) Kitagawa, Y.; Tsurui, M.; Hasegawa, Y. Bright Red Emission with High Color Purity from Eu(Iii) Complexes with π-Conjugated Polycyclic Aromatic Ligands and Their Sensing Applications. *RSC Adv.* **2022**, *12* (2), 810–821. https://doi.org/10.1039/d1ra08233g.

(232) B.R., J. OPTICAL ABSORPTION INTENSITIES OF RARE-EARTH IONS. *Phys. Rev.* **1962**, *127* (750). https://doi.org/10.1021/i650564a772.

(233) Opelt, G. S. Intensities of Crystal Spectra of Rare-Earth Ions. *J. Chem. Phys.* **1962**, *37* (3), 511–520. https://doi.org/10.1063/1.1701366.

(234) Forest, H.; Ban, G. Evidence for Eu+3 Emission from Two Symmetry Sites in Y2O3: Eu+3. *J. Electrochem. Soc.* **1969**, *116* (4), 474. https://doi.org/10.1149/1.2411909.

(235) Zhang, J.; Cui, H.; Zhu, P.; Ma, C.; Wu, X.; Zhu, H.; Ma, Y.; Cui, Q. Photoluminescence Studies of Y2O3:Eu3 under High Pressure. *J. Appl. Phys.* **2014**, *115* (2), 3–8. https://doi.org/10.1063/1.4861386.

(236) Wong, H. Y.; Zhou, X. Le; Yeung, C. T.; Man, W. L.; Woźny, P.; Półrolniczak, A.; Katrusiak, A.; Runowski, M.; Law, G. L. Stress to Distress: Triboluminescence and Pressure Luminescence of Lanthanide Diketonates. *Chem. Eng. J. Adv.* **2022**, *11* (May). https://doi.org/10.1016/j.ceja.2022.100326.

(237) Stopikowska, N.; Guo, Q.; Lis, S.; Runowski, M. Optical Pressure Sensor Based on the Emission and Excitation Band Width (Fwhm) and Luminescence Shift of Ce 3+ -Doped Fluorapatite High-Pressure Sensinǵ. *ACS Appl. Mater. Interfaces* **2019**, *11*, 4131–4138. https://doi.org/10.1021/acsami.8b19500.

(238) Datchi, F.; Letoullec, R.; Loubeyre, P. Improved Calibration of the SrB4O7 Sm2+ : Optical Pressure Gauge: Advantages at Very High Pressures and High Temperatures. *J. Appl. Phys.* **1997**, *81* (8), 3333–3339.

(239) Dasari, S.; Singh, S.; Sivakumar, S.; Patra, A. K. Dual-Sensitized Luminescent Europium(III) and Terbium(III) Complexes as Bioimaging and Light-Responsive Therapeutic Agents. *Chem. - A Eur. J.* **2016**, *22* (48), 17387–17396. https://doi.org/10.1002/chem.201603453.

(240) Runowski, M.; Shyichuk, A.; Tymiński, A.; Grzyb, T.; Lavín, V.; Lis, S. Multifunctional Optical Sensors for Nanomanometry and Nanothermometry: High-Pressure and High-Temperature Upconversion Luminescence of Lanthanide-Doped Phosphates - LaPO4/YPO4:Yb3+-Tm3+. *ACS Appl. Mater. Interfaces* **2018**, *10* (20), 17269–17279. https://doi.org/10.1021/acsami.8b02853.

(241) McLellan, C. A.; Siefe, C.; Casar, J. R.; Peng, C. S.; Fischer, S.; Lay, A.; Parakh, A.; Ke, F.; Gu, X. W.; Mao, W.; Chu, S.; Goodman, M. B.; Dionne, J. A. Engineering Bright and Mechanosensitive Alkaline-Earth Rare-Earth Upconverting Nanoparticles. *J. Phys. Chem. Lett.* **2022**, *13* (6), 1547–1553. https://doi.org/10.1021/acs.jpclett.1c03841.

(242) Runowski, M.; Marciniak, J.; Grzyb, T.; Przybylska, D.; Shyichuk, A.; Barszcz, B.; Katrusiak, A.; Lis, S. Lifetime Nanomanometry-High-Pressure Luminescence of up-Converting Lanthanide Nanocrystals-SrF2:Yb3+,Er3+. *Nanoscale* **2017**, *9* (41), 16030–16037. https://doi.org/10.1039/c7nr04353h.

(243) Piccinelli, F.; Rosa, C. De; Lazarowska, A.; Mahlik, S.; Grinberg, M.; Nakanishi, T.; Omagari, S.; Bettinelli, M. Optical Properties of Eu(III) and Tb(III) Complexes with Pyridine- and Quinoline- Based Ligands under High Hydrostatic Pressure. *Inorganica Chim. Acta* **2020**, *499* (September 2019). https://doi.org/10.1016/j.ica.2019.119179.

(244) Kato, M.; Ishii, K. *Soft Crystals*; 2023. https://doi.org/10.1007/978-981-99-0260-6.

(245) Goderski, S.; Kanno, S.; Yoshihara, K.; Komiya, H.; Goto, K.; Tanaka, T.; Kawaguchi, S.; Ishii, A.; Shimoyama, J. I.; Hasegawa, M.; Lis, S. Lanthanide Luminescence Enhancement of Core-Shell Magnetite-SiO2Nanoparticles Covered with Chain-Structured Helical Eu/Tb Complexes. *ACS Omega* **2020**, *5* (51), 32930–32938. https://doi.org/10.1021/acsomega.0c03746.

Chapter 2:

Synthesis and structural analysis

The work presented in this chapter has been published in the following papers:

A. Zhou, Y.; Ledoux, G.; Bois, L.; Descartes, S.; Bouscharain, N.; Chassagneux, F.; Martini, M.; Midiladji Bakary, Y.; Journet, C.; Philippon, D. Er3+ Doped Nanoparticles as Upconversion Thermometer Probe in Confined Fluids. *Phys. Chem. Chem. Phys.* **2023**. https://doi.org/10.1039/D3CP02218H.

B. Zhou, Y.; Ledoux, G.; Philippon, D.; Descartes, S.; Martini, M.; He, S.; Desroches, C.; Fournier, D.; Journet, C.; Bois, L. Laser-Induced Heating in GdVO 4 : Yb 3 + / Er 3 + Nanocrystals for Thermometry. *ACS Appl. Nano Mater.* **2022**, *5*, 16388–16401. https://doi.org/10.1021/acsanm.2c03466

2 Synthesis and structural analysis

2.1 Introduction

In the science of PL solid-state materials, structural characterization plays a crucial role in understanding the optical properties and behavior of various materials. The PL properties of lanthanide compounds can be strongly influenced by crystal structure and symmetry. In addition, the mechanical analysis of PL sensors dispersed in materials, fluid lubricants or solids should be carried out for further tribological applications.

This chapter aims to provide an overview of the essential methods and techniques employed for the synthesis of PL sensors and their structural characterization. To forecast the applicability of materials in further friction testing, it is essential to determine the mechanical properties of PL sensor hosting materials (fluid and solid).

This chapter is divided into two parts: the first part is dedicated to the PL $GdVO_4$ nanoparticles (NPs) for temperature measurement and the second to the PL Ln complex for pressure measurement. The crystal structure and lattice parameters will be presented for each compound, followed by electronic microscopy images to determine their size. The incorporation of the PL sensor into matrices will also be discussed, as will their mechanical characterization.

2.2 Matrices for PL sensor incorporation

2.2.1 Fluid matrices

Based on our previous works,[1–4] two commercially available fluid lubricants to disperse the photoluminescent sensors are chosen to be (Figure 2.1):

1) Nycobase 5750: commercial polyol-ester-based oil used in aerospace applications.
2) Squalane: a well-characterized reference lubricant made of branched alkane.

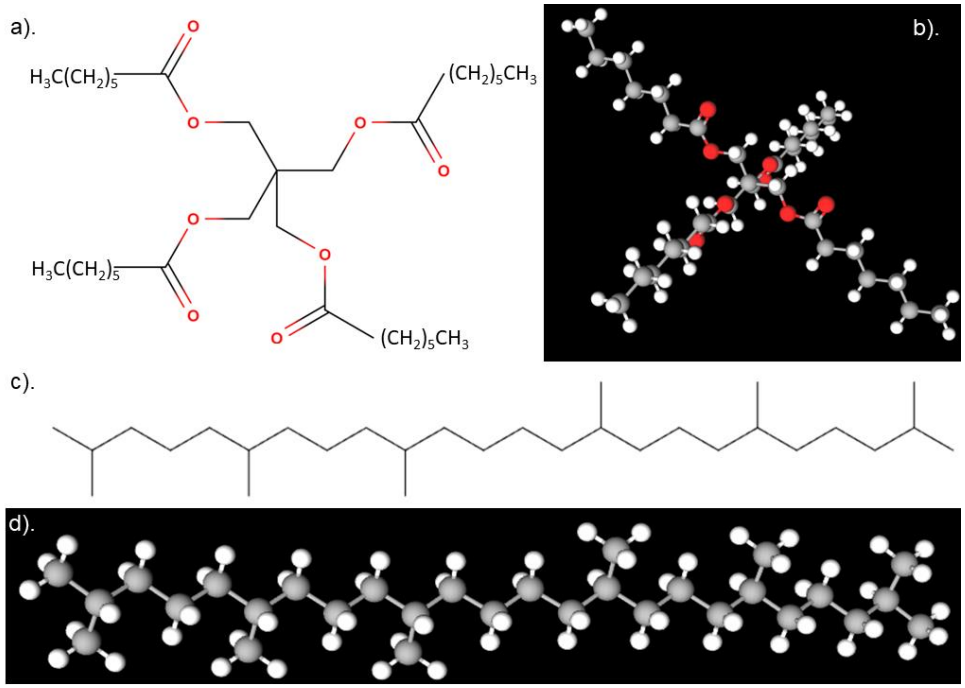

Figure 2.1: Chemistry formula a) of Nycobase 5750 and b) its chemistry structure presentation; Chemistry formula c) of Squalane 5750 and d) its chemistry structure presentation (red ball stands for oxygen, grey for carbon and white for hydrogen).

As shown in Figure 2.1, Nycobase 5750 has the chemical formula of monopentaerythritol tetrahexane, making Nycobase 5750 more hydrophilic in nature due to the presence of an ester group in its chemical composition. On the other hand, Squalane is composed of a long alkane chain and is therefore more hydrophobic. Hydrophobicity refers to the lack of affinity or interaction with water.

Nycobase 5750 and Squalane are well-characterized lubricant in literature and commonly used in the field of tribology.[1,2,5,6] Both substances possess characteristics such as being Newtonian fluids, high thermal resistance, chemical stability, and non-toxicity.

2.2.2 Solid matrices

The solid matrices to incorporate PL sensor are:

1) Hybrid silica: sol-gel glass
2) PDMS polymer (Polydimethylsiloxane): elastic siloxane polymer

Both hybrid silica and PDMS exhibit improved mechanical strength, thermal stability, optical transparency, and chemical resistance (Figure 2.2a and 2.2c).[7–10]

In the context of sol-gel glass, the elaboration process involves converting a liquid sol, consisting of the silica precursor methyltriethoxysilane (MTEOS, Figure 2.2b), into a solid gel or glass through controlled hydrolysis in an acid medium and condensation reactions. On the other hand, PDMS is a type of silicone polymer (Figure 2.2d) that can be produced in bulk or film form through polymerization of commercial precursors at room temperature.

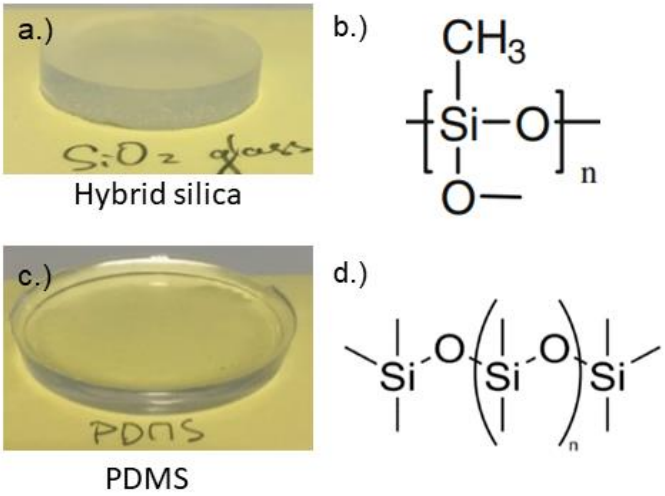

Figure 2.2: a) Photo of pure hybrid silica bulk and b) chemical formula of MTEOS-based silica; c) Photo of pure PDMS bulk and d) chemical formula of PDMS.

The incorporation of PL sensors occurs before the gelation or polymerization of the solid material, the mixture is stirred using mechanical or ultrasonic methods for homogeneity. Compared to hybrid silica, which is adapted to low loading rate (0.5-5 wt.%), PDMS is easier to support high concentrations (ex. 50 wt.%) of PL sensors. The homogeneity of dispersed PL sensors is then analyzed by electronic microscope (SEM image in Figure 2.12).

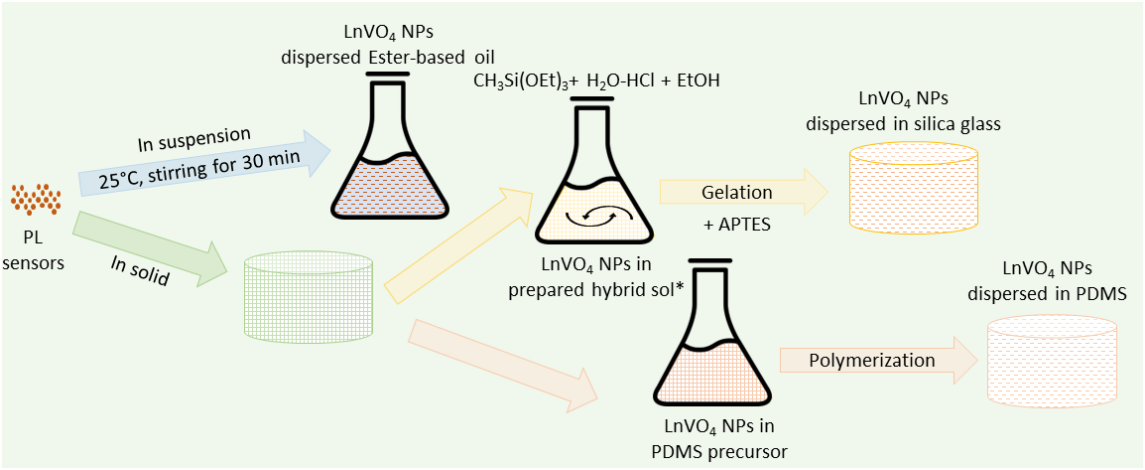

Scheme 2.1: Overview of process used for the preparation of the PL sensor incorporated materials. *Prepared hybrid sol: Hybrid silica sol after hydrolysis, condensation, and evaporation process.

2.3 Nanoparticles $GdVO_4$: Er^{3+}/Yb^{3+}

2.3.1 Synthesis of PL $GdVO_4$ nanoparticles

Lanthanide orthovanadates exhibit a wide range of physical and chemical properties, including excellent thermal stability, chemical durability, and interesting optical and magnetic properties. The PL lanthanide vanadates can be easily synthesized through soft chemistry under ambient pressure and at low temperature, such as coprecipitation. Following by thermal

treatment, the material provides highly efficient PL. Vanadates are crystallized in the form of NPs of the order of 50 nm using a co-precipitation method. For temperature sensing applications, the vanadate matrix provides very good sensitivity for Er^{3+}/Yb^{3+} thermometry.[11,12] It has the disadvantage of having a fairly high phonon energy,[13] which is carefully considered in the PL characterizations in this work. Besides, the mechanical stability of the sensor is also required in further tribological measurements. $GdVO_4$ is known to exhibit a phase transition from a zircon-like to a scheelite-like structure at 6.8 GPa,[14] which exceeds the pressure typically encountered in tribological tests (up to 5 GPa), and we focus on a pressure range of less than 1 GPa in this work.

In 2000, Huignard et al. reported the synthesis of europium(III)-doped yttrium(III) orthovanadate NPs by coprecipitation from soluble yttrium(III) and europium(III) salts in a basic solution; they obtained a colloidal solution of PL YVO_4: Eu^{3+} NPs.[15] The first step of this reaction is the precipitation of the kinetically favored hydroxide $Ln(OH)_3$

$$Ln^{3+} + 3OH^- \rightarrow Ln(OH)_3\searrow$$

Then, the lanthanide hydroxide reacts with orthovanadate ions to obtain thermodynamically stable precipitation: $LnVO_4$

$$Ln(OH)_3 + VO_4^{3-} \rightarrow LnVO_4\searrow + 3OH^-$$

In a later report from Huignard et al.,[16] the authors demonstrated that this reaction strongly relies on the pH, with yttrium orthovanadate only being obtained within a narrow pH range of 12.2 to 12.8. When the pH is above 12.8, the reaction does not occur, the yttrium hydroxide precipitating instead of yttrium orthovanadates. When the pH is below 12.2, they observed that the colloidal solution turned yellow, indicating the formation of polyvanadate species.[17] The authors claimed that the optimum pH should be 12.5.

While Huignard et al.[15,16] focused only on the properties of aqueous Y^{3+} and Eu^{3+} ions, Chang and Mao reported in 2007 that they obtained $Gd(OH)_3$ using a colloidal hydrothermal method with dissolved Gd^{3+} salt and NaOH at pH 13.[18] Later, $GdVO_4$ NPs were successfully synthesized by coprecipitation at pH 12.[19,20] Doped ions, such as Yb^{3+} and Er^{3+}, have also been reported to modify the PL properties of NPs.[21]

To optimize the PL properties of Ln-doped vanadates NPs formed by coprecipitation, further thermal treatment should be followed for better crystallization. The upconversion emission intensity of Er^{3+} in $GdVO_4$: Er^{3+}/Yb^{3+} NPs at annealed 1000°C increased more than 2 times compared to those at annealed 800 °C. However, the size of the NPs increased significantly with the increasing annealed temperature.[19] The size the NPs is less than 100 nm when annealed at 600 °C whereas the size reaches 1 µm when annealed at 1000 °C.

In this work, $GdVO_4$: Er^{3+}/Yb^{3+} NPs are synthesized using a co-precipitation method described by Huignard et al.[15,16] The doping concentration de Er^{3+} and Yb^{3+} are fixed at 2 and 10 mol.% respectively to obtain a better upconversion efficacity as reported. The NPs are annealed maximum at 600°C to prevent their size from increasing.

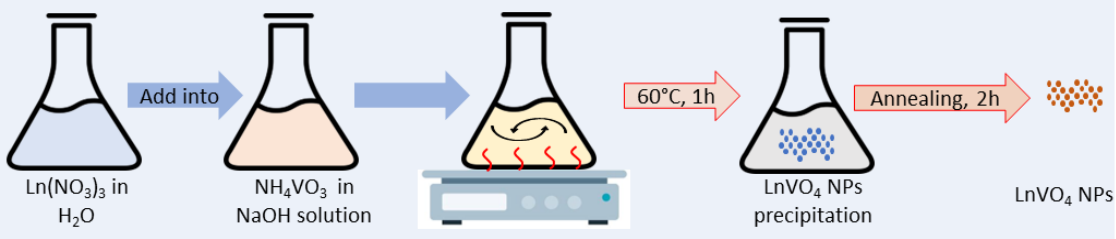

Scheme 2.2: Overview of the co-precipitation synthesis of $LnVO_4$ nanoparticles.

2.3.2 Materials and Methods

1) Materials

The chemicals were used as follows: $Gd(NO_3)_3$ hydrated (Alfa Aesar 99.9%), $Yb(NO_3)_3$ hydrated (Sigma-Aldrich 99.9%), $Er(NO_3)_3$ hydrated (Alfa Aesar 99.9%), NH_4VO_3 (min. 99.0%, Alfa Aesar), NaOH (Sodium hydroxide pellets, min. 99%, MERCK). A conventional mono-pentaerythritol lubricating oil (Nycobase 5750, supplied by NYCO, Paris, France) was chosen as the solvent to study the effect of the environment on the thermometric performance of the probes. The solids were obtained by soft chemistry processes using the chemicals: NPs $GdVO_4$: Yb^{3+}/Er^{3+} ground powder, MTEOS (Methyltriethoxysilane 98%, abcr), EtOH (Ethanol anhydrous, Carlo Erba Reagents), Hydrochloric acid (HCl 37%, Carlo Erba Reagents), 3-aminopropyltrimethoxysilane (APTES, 95%, ACROS Organics), SYLGARD® 184 Silicone Elastomer (PDMS Polydimethylsiloxane, DOW).

2) Synthesis methods

- **Synthesis of $GdVO_4$: Yb^{3+}/Er^{3+} NPs**

A chemical co-precipitation technique was used to prepare $GdVO_4$: 10% Yb^{3+}; 2% Er^{3+} NPs.[20,22,23] Solution 1: 0.05 M $NaVO_3$ aqueous solution at pH 12, prepared by adding NH_4VO_3 in 0.15 M NaOH solution; Solution 2: Solutions in distilled water of 0.05 M $Ln(NO_3)_3$ in stoichiometric ratio (Gd^{3+}: 88% mol.; Yb^{3+}: 10% mol.; Er^{3+}: 2% mol.). For greater precision in the composition of the synthesis, we need to take into account the hydration of the precursor salts. Solution 2 was slowly added to solution 1 (dropwise), the mixture became turbid with a white precipitate. After heating under stirring at 60°C for 1 h, the precipitate was separated by centrifugation, and washed with distilled water 3 times. The powder was dried at 80°C in an oven overnight, as the product without annealing. The other product was then annealed in air at 600°C or at 800°C for 2 h. Noted that the unannealed product was not observed with emission under upconversion excitation.

- **Preparation of a suspension of $GdVO_4$: Yb^{3+}/Er^{3+} NPs in a lubricant**

The suspension of $GdVO_4$: Yb^{3+}/Er^{3+} NPs was prepared by adding the ground powder in an ester-based oil (Nycobase 5750) at mass concentrations of 0.1, 0.5, 0.75, 1 and 50 wt.%, followed by mechanical stirring and by ultrasound at room temperature for 30 minutes, respectively (Scheme 2.1).

- **Solid preparation of $GdVO_4$: Yb^{3+}/Er^{3+} in a hybrid glass or PDMS polymer**

a) In Glass: 5 wt.% of NPs

The NPs hybrid glass was prepared by a sol-gel procedure via hydrolysis and condensation of the MTEOS precursor in acid water (HCl pH =2.4, 1:0.3 by mass) and ethanol (1:0.8 by mass).[8] After 18 h of stirring at room temperature, the solvent was removed by evaporation under vacuum. A quantity of NPs powder was then dispersed in the concentrated sol and stirred ultrasonically for 10 minutes. To accelerate condensation, 2 vol.% of APTES was added to the mixture under stirring. Then, the NPs suspension in the sol was placed in an oven at 50°C for gelation and subsequent drying to a solid glass. In our case, 5 wt.% of NPs powder in the sol is the maximum amount that can be dispersed to obtain a transparent glass (Scheme 2.1).

b) In PDMS: 5 wt.%; 50 wt.% of NPs

PDMS polymer with 5 wt.% or 50 wt.% NPs was prepared by polymerization at room temperature. The NPs powder was first mixed with the PDMS silicone precursor under mechanical stirring, the initiator (1:10) was added to start the polymerization (Scheme 2.1).

3) Characterizations and methods

The crystalline phase of the synthesized NPs was characterized by an X-ray diffractometer (Bruker D8 Advance diffractometer) with Cu Kα radiation (λ = 1.54060 Å) operating at 45 kV and 30 mA at room temperature. Diffractograms were collected at 2θ between 5 and 70° with steps of 0.016° (Centre de Diffractométrie Henri Longchambon, Univ Lyon 1).

The morphology of the NPs was analyzed by transmission electron microscopy (TEM, JEOL 2100F 200 kV). Scanning electron microscopy SEM images were obtained using a Zeiss Merlin Compact SEM with a secondary electron detector at a low accelerating voltage up to 5 kV and backscattered images at 20 kV (Centre de Microstructures CTμ, Univ Lyon 1. The solid sample was cut into a thin slice, and then metallized by copper vapor on the surface for the analysis.

The hydrodynamic size of the NPs in the suspension was calculated by the Dynamic Light Scattering (DLS, Malvern-Zetasizer) at different concentrations.

The viscosity of the colloidal suspension was determined by a rheometer (Physica MCR301, Anton Paar) with a parallel-plate geometry (PP40), at different temperatures (293—373K, ± 0.03K) and imposing a shear rate (range between 1 to 10^4 s^{-1}). During the measurement, a steel plate is rotating against a glass plate, the gap between the two parallel plates was fixed at 0.2 mm. Transparent glass plate will be used for further optical measurement. The uncertainty on viscosity measurement is about 5%.

The mechanical resistance of solids matrices is determined in compression using a custom-built High Pression Torsion test rig, capable of compression and/or torsion.[24–26] A schematic of the rig is included in Fig. 2.12. The test rig is placed on a servo-hydraulic machine, consisting of hydraulic actuators operated by electrohydraulic servo valves. In our case we use the system in compression only. The monoliths were placed between two anvils made from cobalt-tungsten carbide (WC-Co) composite of diameter d (Figure 2.3). Prior to HPT tests, the disks and anvils were bathed in acetone and alcohol, respectively, for 10 min

using ultrasonic cleaning. Applied normal load F measurement was accomplished using a static torque sensor. Vertical displacement, to monitor the change in sample thickness t, was measured using 3 inductive sensors (positioned at 120° intervals).

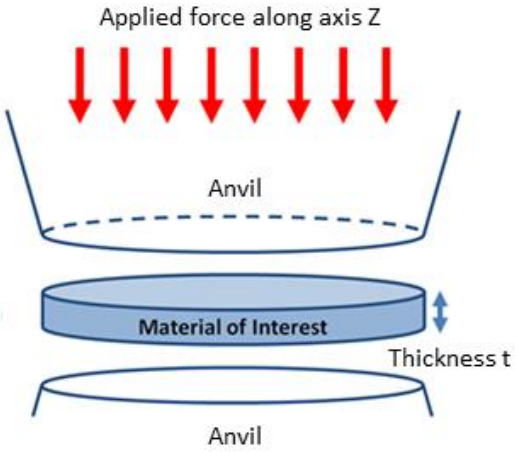

Figure 2.3: Schematic presentation of the High Pression Torsion test rig.

Then, the mean compressive pressure or the normal stress P is calculated by the equation $P = \frac{F}{S}$, with their surface S determined as $S = \pi \left(\frac{d}{2}\right)^2$.

Thermal conductivity was studied using MTPS (Modified Transient Plane Source) method with a TCi thermal conductivity analyzer (C-Therm, TCi-3-A) (Hervé Pabiou, CETHIL). The fluid sample is placed into a liquid cell and the solid sample is deposited on the solid support, as shown in Figure 2.4. The precision of measurements is better than 1%, and the accuracy is better than 5%.

Figure 2.4: Photos of sample supports of TCi thermal conductivity analyzer.

2.3.3 Structural characterizations of NPs powder

1) Crystal phases determinations: XRD

The X-Ray powder diffraction of $GdVO_4$: Yb^{3+}/Er^{3+} NPs are determined for the products after coprecipitation (without annealing), annealed at 600°C for 2 h and annealed at 800 °C for 2 h. As shown in Figure 2.5, the XRD patterns of all the $GdVO_4$: Yb^{3+}/Er^{3+} synthesized match well with the theoretical planes of the tetragonal phase (JCPDS 17-0260) whatever the annealing temperature. The product is a pure gadolinium vanadate with an $I4_1/amd$ space group. The crystal quality can also be inferred from the XRD diagram: the XRD pattern of the NPs without annealing is considerably noisy, the crystallization is thus not good. Consequently, the NPs without annealing do not show luminescence under excitation. Annealing at 600°C optimizes crystallization, the XRD pattern is thus clearer and the hkl peaks are narrower than those of NPs without annealing. The crystallization of $GdVO_4$: Yb^{3+}/Er^{3+} NPs is even better at 800°C. Both annealed NPs exhibit significant green light under excitation.

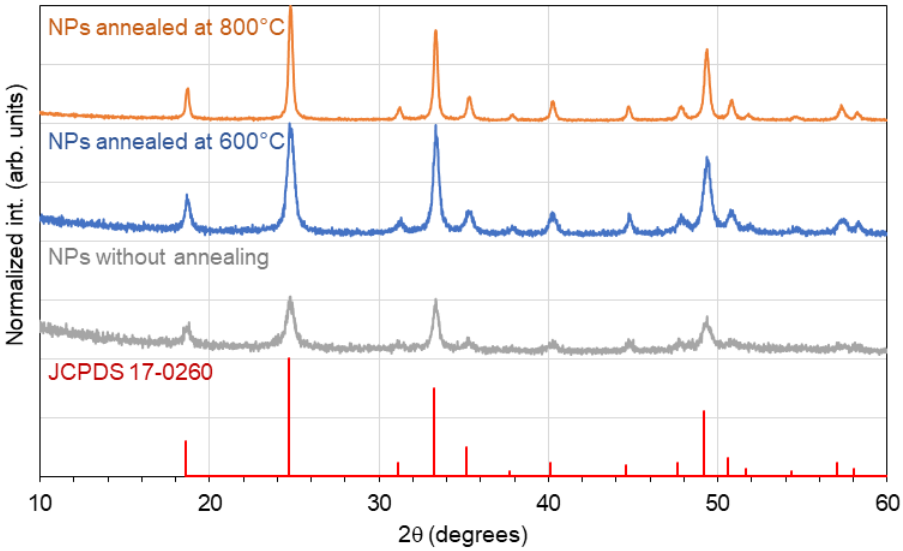

Figure 2.5: X-ray powder diffraction patterns of NPs $GdVO_4$: Yb^{3+}/Er^{3+} without annealing (in grey), annealed at 600°C (in blue) and at 800°C (in orange), reference in red line from JCPDS 17-0260.

The crystalline structure of $GdVO_4$: Yb^{3+}/Er^{3+} NPs is similar to that of YVO_4, with four molecules occupying a unit cell (Figure 2.6).[27] Along the c-axis, the crystalline structure exhibits an organized arrangement. It consists of alternating $[VO_4]$ tetrahedra, which contain the vanadium atom at their center, and $[YO_8]$ polyhedral, which are composed of a central yttrium atom and oxygen atoms at their corners. The Y^{3+} in polyhedral $[YO_8]$ is non-centrosymmetric and has D_{2d} symmetry. When Yb^{3+} and Er^{3+} are introduced into the structure as dopants for PL properties, they replace the Y^{3+} site.

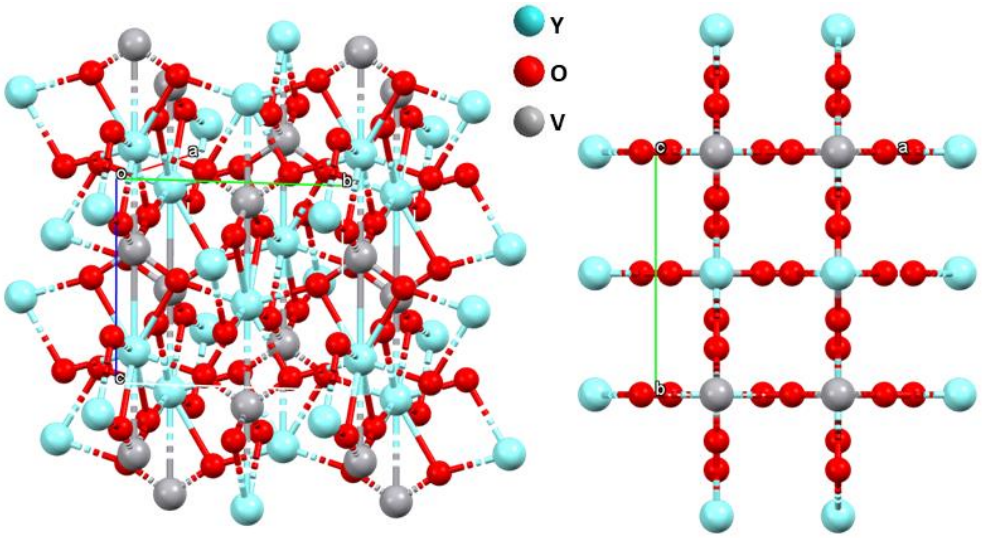

Figure 2.6: Crystalline structure of YVO_4, from Broch[28] (CIF 1011156), the file can be found in the Crystallography Open database.[29]

2) Nanoparticle size analysis: TEM and SEM

SEM images of $GdVO_4$: Yb^{3+}/Er^{3+} NPs annealed at 600°C and 800 °C are shown in Figure 2.7. The size of the NPs annealed at 600°C is homogenous, around 30 nm diameter whereas the size of those annealed at 800°C is not uniform, some reaching 100 nm. Some aggregated NPs are recrystallized together to form large-size particles during high temperature annealing, which agrees with the observation of Gavrilović et al.[19] The NPs annealed at 600°C are chosen for further characterization as the monodispersed size of NPs is preferable for better special resolution of measurements.

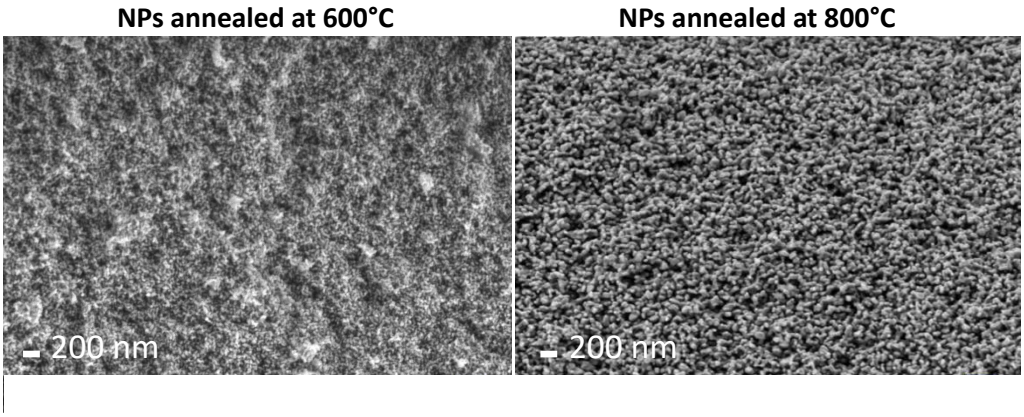

Figure 2.7: SEM images of NPs $GdVO_4$: Yb^{3+}/Er^{3+} powder annealed at 600°C and 800°C.

The $GdVO_4$: Yb^{3+}/Er^{3+} NPs are elongated ellipsoidal crystallites 30 nm long and the clusters formed have a size of 300 nm.[30] The TEM image (Figure 2.8a) confirms that the particle size is of the order of 30 nm and shows the porosity of the particles induced by atomic diffusion during heat treatment.[30,31] The HR TEM image (Figure 2.8b) shows reticular planes 0.47 nm apart, which is consistent with the plane distance (101) of $GdVO_4$ (JCPDS-17-0260). The electron diffraction pattern (Figure 2.8c) confirms the presence of crystalline $GdVO_4$

(JCPDS-17-0260). Finally, the EDX spectrum (Figure 2.8d) confirms the chemical composition of the probes, which contain Gd (28.9 at%), V (28.5 at%), Yb (4 at%) and Er (low content). This analysis leads to a Yb/Gd ratio of 0.14, consistent with the theoretical one (Yb/Gd=0.10). The agglomerates formed by NPs have a size of around 300 nm, which has been confirmed by a TEM image,[32] this result has also been observed in other's work.[30] This size of aggregation will be a problem for our application, solutions should be considered to limit it.[16,33,34] A solution to avoid an increase in size after annealing has been proposed by Mialon et al.[35] A silica coating on the NPs formed by the Stöber method can be applied before heat treatment. The silica coating protects the NPs from coalescence. This method will be considered in our further synthesis but not in this work.

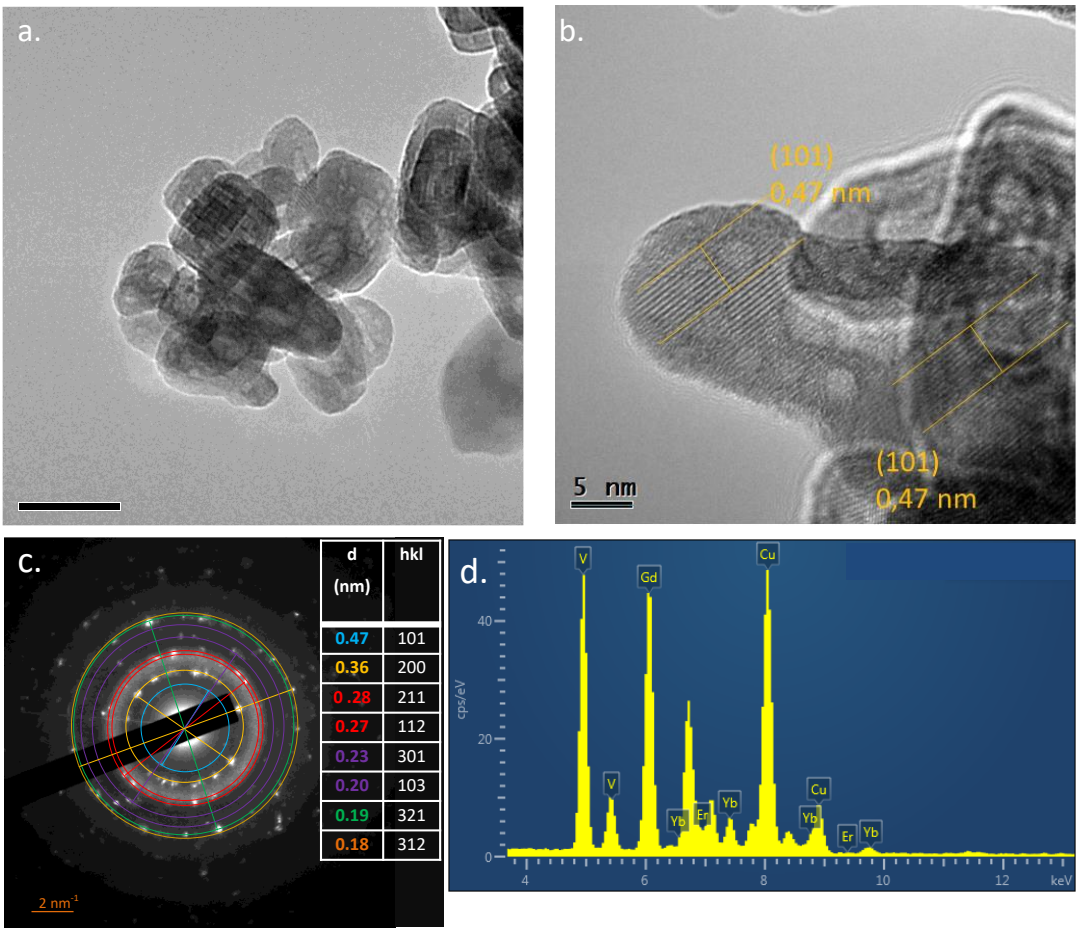

Figure 2.8: a.) TEM picture; b.) HRTEM picture; c.) Electron diffraction pattern d.) and EDX spectrum of $GdVO_4$: Yb^{3+}/Er^{3+} NPs powder.

2.3.4 Dispersion of NPs in a fluid matrix

The Nycobase 5750, namely Nycobase for clarity in the following, was chosen as a fluid medium to apply $GdVO_4$: Yb^{3+}/Er^{3+} nanoprobes for tribological temperature measurement.[2]

1) Hydrodynamic size of NPs

The NPs suspensions are prepared at different and relatively low concentrations: 0.1, 0.5, 0.75 and 1 wt.% for DLS analysis. As shown in Figure 2.9, the measured hydrodynamic size

of the NPs suspension after one week of settling. The hydrodynamic size of the NPs aggregate is about 400 nm, which corresponds to the previous result observed in the TEM image.[32] However, although in the 0.1 wt.% suspension, the hydrodynamic size is the smallest among all, around 100 nm, the second peak at 5000 nm shows that the suspension is not homogeneous. The hydrodynamic size of NPs aggregation increases with dispersion concentration, with the largest size among all concentrations centered at 459 nm in the 1 wt.% suspension.

In lubricated tribological measurements, the NPs suspension passes through the interface of the two first bodies. The thickness of the fluid interface, depending on the mean speed of the surfaces and the viscosity of the fluid, may range between few nm and 10 µm. Compared to the interface thickness, the NP size should be at least 10 times smaller. Consequently, the smaller the NPs size, the better for application in any tribological measurement. Moreover, it is important to note that when spatial resolution is not limited to the size of the laser beam, monodispersity and the small size of nanoprobes are required for tribological applications to improve spatial resolution. . The position of the centroid of the peak indicates the hydrodynamic size, which increases with concentration. Meanwhile, the width of the peak also increases, showing that monodispersity becomes less important with increasing concentration. Among the concentrations of 0.5, 0.75 and 1 wt.%, the 0.5 wt.% suspension has both the smallest hydrodynamic size of the NPs (less than 350 nm) and the best monodispersity. The 0.5 wt.% NPs suspension is thus selected for further optical characterizations in the following sections.

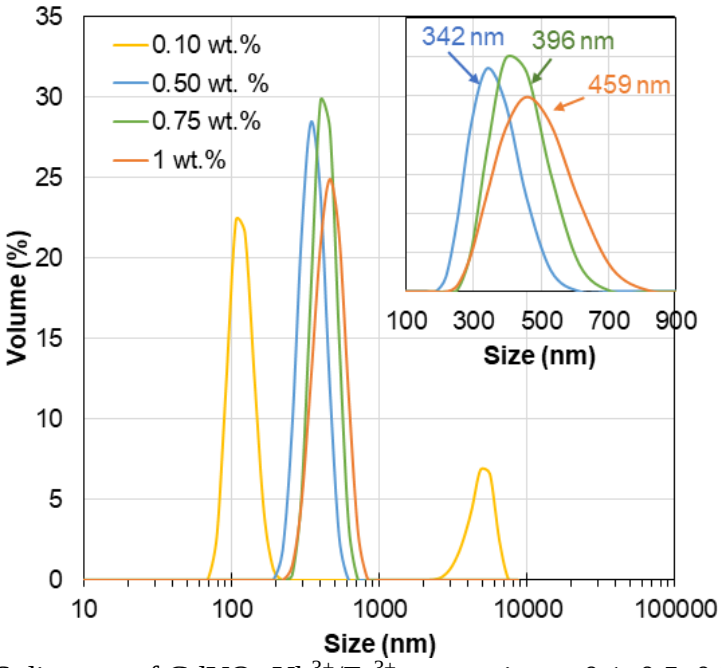

Figure 2.9: DLS diagram of $GdVO_4:Yb^{3+}/Er^{3+}$ suspension at 0.1, 0.5, 0.75 and 1 wt.%.

2) Rheological properties

The viscosity of the 0.5 wt.% and 1% suspensions is measured at different temperatures using pure Nycobase as a reference. Figures 2.10a and 2.10b show the measured viscosities of 0.5 and 1 wt.% and the reference pure Nycobase at 293 to 373 K, respectively. As pure Nycobase is a Newtonian fluid, its viscosity does not change with shear rate, which is thus presented by a line in Figure 2.10. When the shear rate is above 10 s^{-1}, the difference in viscosity between the 0.5 and 1.0 wt.% suspensions and pure Nycobase (< 2.97% and < 4.65%, respectively) can hardly be observed within the experimental uncertainty range (< 5%). This means that the dispersion of NP does not modify the viscosity of the base oil, thus the tribological behavior of the mechanical contact should be not affected due the presence of the NP. At low shear rate (< 10 s^{-1}), the fluid regime may not be stable, the measured viscosity is thus more inaccurate. Moreover, at 293K, under high shear rate (> 8000 s^{-1}), the viscosity decreases very slightly with increasing shear rate for suspensions, which can be explained by the heating effect induced by shear which decreases the viscosity.[1]

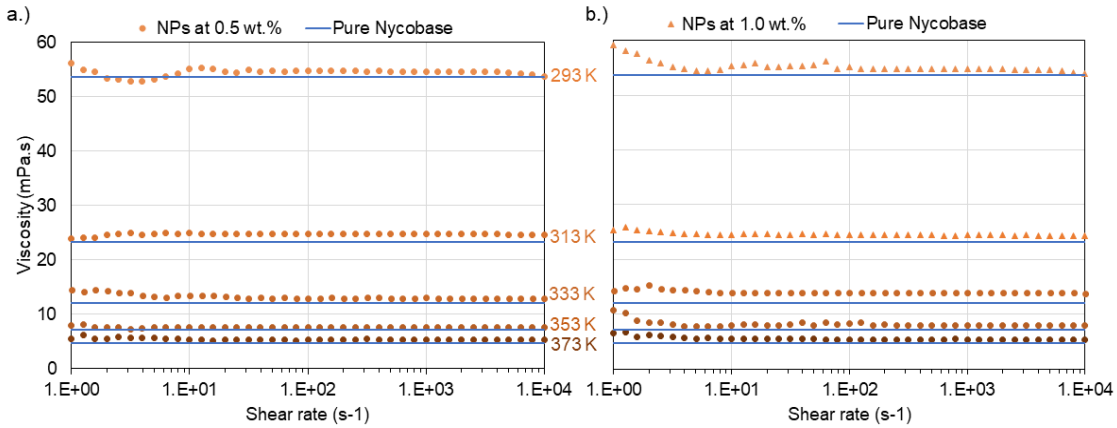

Figure 2.10: Viscosity of $GdVO_4:Yb^{3+}/Er^{3+}$ NPs suspension at 293 – 373 K under a shear rate of 1 - 10^4 s^{-1} for a) 0.5 wt.% NPs suspension (in dot) and pure Nycobase (in line); b) 1.0 wt.% NPs suspension (in triangle symbol) and pure Nycobase (in line).

3) Thermal conductivity

As shown in Table 2.1, pure Nycobase has a very low thermal conductivity, while dispersing the NPs at 0.5 wt.% do not change the thermal property of the fluid. Thus, heat dissipation can be neglected in the fluid matrix.

Table 2.1: Experimental thermal conductivity of the NPs suspension at room temperature (20°C).

Samples	Effusivity (Ws½/m²K)	k (W/mK)
Nycobase	489.2	0.16
0.5 wt.% NPs suspension	490.6	0.16

2.3.5 Dispersion of NPs in solid matrices

$GdVO_4$: Yb^{3+}/Er^{3+} NPs are also encapsulated in solid media to explore their potential application in optical thermometry for the local temperature measurement, such as measuring the local temperature of the near-surface layer of a solid in tribology. The solid matrices were chosen as hybrid glass and PDMS. The concentration of NPs in hybrid silica is limited to 5 wt.% through the sol-gel process, whereas PDMS can support NPs up to 50 wt.% or even higher.

1) Size of NPs aggregates

The aspects of the NPs/matrix mixtures at 5 wt.% are shown in Figure 2.11a for the hybrid silica glass and in Figure 2.11b for the PDMS, they became white with some transparency after the dispersion of the NPs.

The dispersion of NPs in the hybrid silica glass was observed by backscattering electronic microscopy. Figure 2.11c shows a cross-sectional view of a slice of hybrid glass into which 5 wt.% NPs were inserted by the sol-gel process, in which the white dots are the $GdVO_4$ NPs, approximately 1 µm in size (Figure 2.12). The dispersion of the $GdVO_4$ NPs can be considered homogeneous. Compared with dispersion in a fluid, the $GdVO_4$ NPs aggregated to a greater extent when dispersed in hybrid silica glass. However, unlike NPs in suspension, the solids are not limited to the interface thickness. The size of around 5 µm is satisfying for temperature measurements in tribological contact (less than 1 mm of diameter) by now, as the spatial resolution will be limited by the laser beam diameter (around 10 µm).

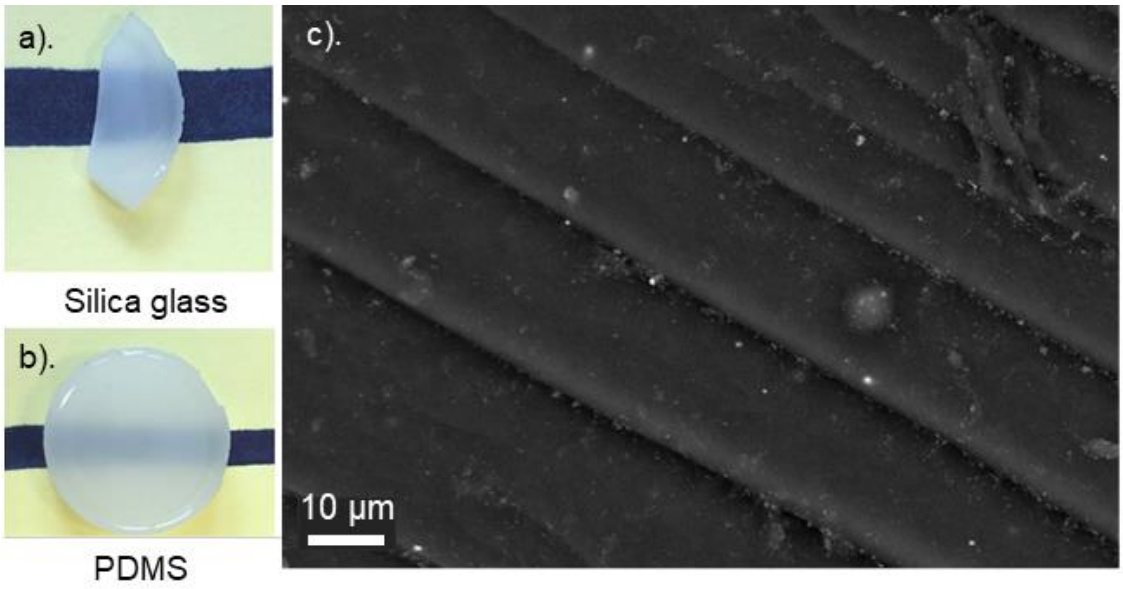

Figure 2.11: Photos of $GdVO_4$ NPs composites a.) with silica glass; b.) with PDMS; c.) Backscattered electron image of the metallized slice of the $GdVO_4$ NPs/silica glass composite.

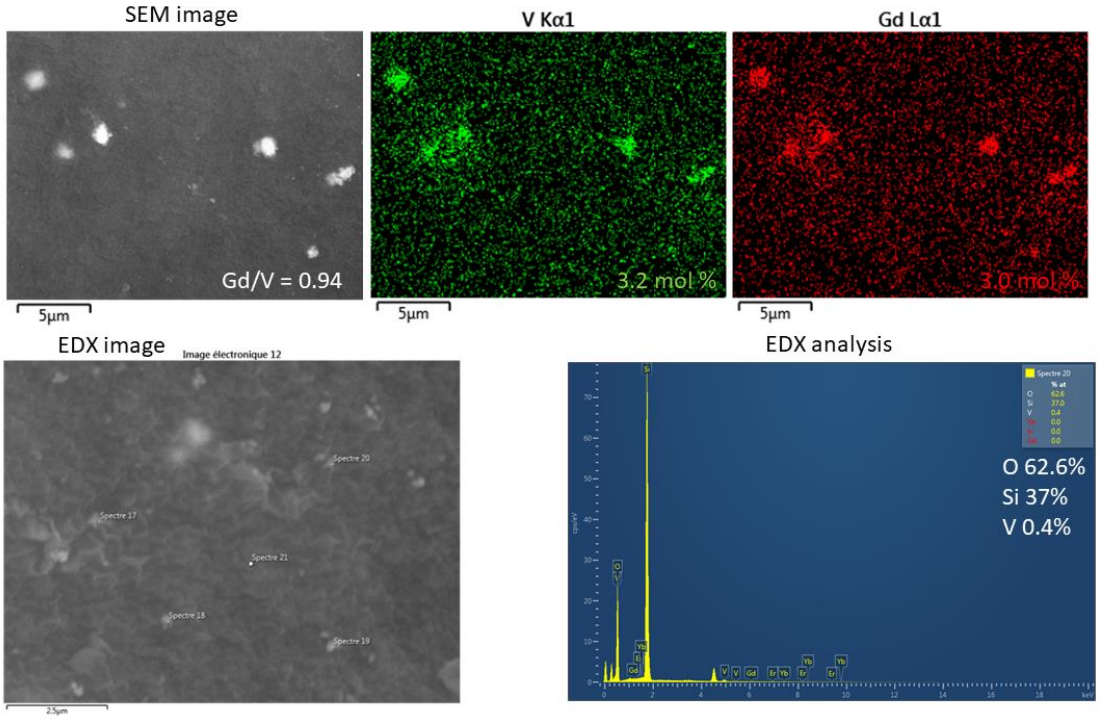

Figure 2.12: SEM image and EDX analysis of the metallized slice of the $GdVO_4$ NPs/silica glass composite, associated elemental mapping of vanadium and gadolinium.

2) Mechanical properties

Mechanical compressive tests were conducted on the High Pression Torsion test rig at LaMCoS. The analysis was carried out for pure silica glass monoliths, NPs dispersed silica glass monoliths, pure PDMS monoliths and film. Figure 2.13 shows the experimental curves for pure silica glass and PMDS film. The top of the blue line stands for the applied normal (Z axis of the experimental setup) force up to the programmed value (16.3 kN). The maximum applied force was determined by a prior mechanical test, which is the limited force just before the damage of silica glass sample. At the bottom of Figure 2.13, the orange line stands for displacement of the moving part of the experimental setup. It is measured with 3 displacement sensors along the Z axis (Figure 2.3).

Thus, the corresponding deformation (displacement divided by the initial height) of the samples under the effect of the applied force can be calculated. The deformation becomes greater with the increasing applied force, and the deformation of both samples is elastic for the given normal applied force. More data is completed in Table 2.2. Compared with silica glass, the PDMS monolith has a higher deformation level (64%), and even higher in the PDMS film (86%). The addition of NPs at 5 wt.% to the silica glass has no significant impact on the mechanical properties. Only the silica glass with NPs has been tested thus far. It is assumed that the mechanical properties of PDMS with NPs (up to 5 wt.%) are not affected by the additional nanoparticles.

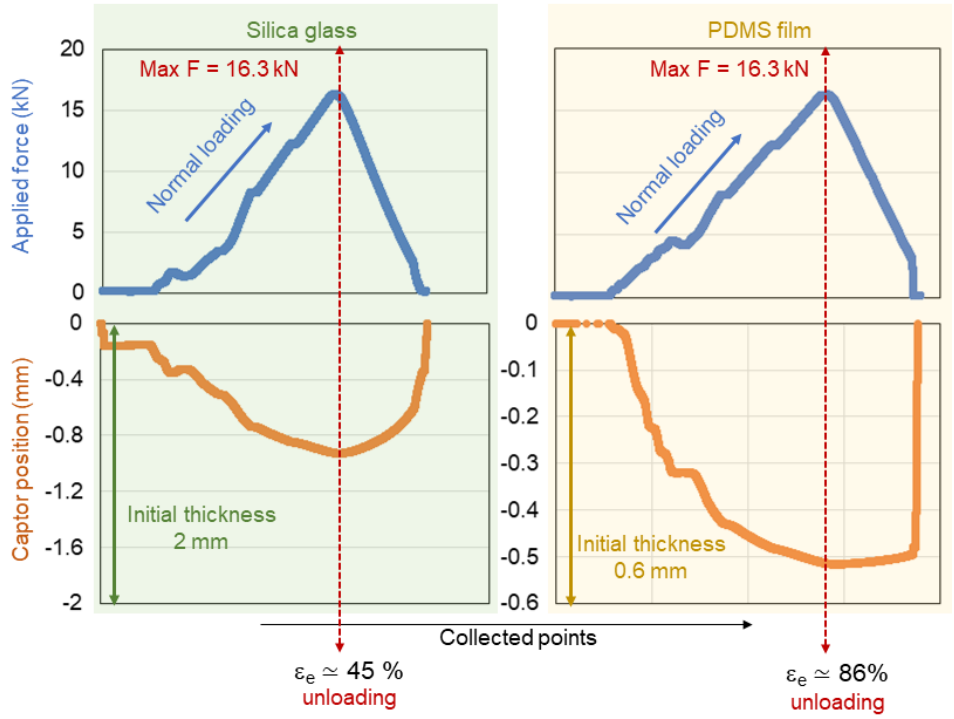

Figure 2.13: Applied normal force (in blue line) and sensor vertical displacement (in orange line) (deformation of solid matrices under the maximal applied axial load is indicated), a) hybrid silica glass and b) PDMS (ε_e stands for deformation level).

Table 2.2: Mechanical resistance of solids matrices at room temperature (20°C) under 16.3 kN applied force.

Samples	Diameter d (mm)	Thickness t (mm)	P Max (MPa)	Deformation (%)
Silica Glass monoliths	11.4	2.0	159.5	45.5(5)
Silica Glass (+ 5% wt. NPs) monoliths	11.3	2.0	162.5	46.5(5)
PDMS monoliths	25	2.5	33.1	64.4(3)
PDMS film	25	0.6	33.1	86.1(8)

3) Thermal conductivity

Like the fluid matrix, the solid matrices have a very low thermal conductivity (Table 2.3), so heat dissipation can also be neglected. Dispersion of NPs at 5 wt.% has no significant impact on the thermal conductivity of PDMS monoliths. The impact of NPs dispersion in silica glass is assumed to be negligible, as data from silica glass with 5 wt.% NPs was not taken into account due to the sample diameter being too small for the measurement.

Table 2.3: Experimental thermal conductivity of the solid matrices at room temperature (20°C).

Samples	**Effusivity** **($Ws^{1/2}/m^2K$)**	**k** **(W/mK)**
Silica glass	485.1	0.16
PDMS	601.6	0.24
5 wt.% NPs solid in PDMS	610.4	0.25

2.4 Lanthanide complexes (Ln = Y; Tb; Eu)

2.4.1 General of lanthanide β-diketonate complexes

1) β-diketones complexes

Through coordination chemistry synthesis, complexes can consist of lanthanide ions as the central metallic atom and surrounding organic ligands. Among the different families of lanthanide complexes, this section focuses on the β-diketone complex. The β-diketones consist of two carbonyl groups separated by a carbon atom (α-carbon).[36] In most of these ligands, the substituents on the α-carbon are hydrogen atoms. Multiple substitutions can be envisaged on carbons 1 and 5, by alkyl, alkyl-fluorinated, or aromatic or heteroaromatic groups. The simplest β-diketone is acetylacetone (acac), where the substituents on both carbonyl groups are methyl.[37] In this work, trifluoroacetylacetone (tfa) is employed as a ligand to obtain PL lanthanide complexes.

2) Synthesis of Ln^{3+} complex

The synthesis of Ln complex involves the coordination of central metal ions with one or more organic ligands. Various synthesis methods, such as sublimation,[38] ionization,[39] hydro or solvothermal,[40] can be employed. Crystallization is commonly used to purify coordination complexes. By forming single crystals, the purity of the Ln^{3+} complex is maximized, and a homogeneous structure is obtained. To favor the formation of singles crystals, the synthesis protocol must be carefully controlled, with conditions such as the temperature, humidity, concentration of precursor and cooling speed playing crucial roles.[41] Therefore, coordination of the Ln^{3+} complex in solution by the assembly of dissolved Ln^{3+} ions and deprotronated ligands minimizes solubility problems, which is thus preferable to form single crystals. In this work, the Ln^{3+} complex is synthesized in a basic alcoholic solution by dissolving the Ln^{3+} ions and deprotonated ligands. The process is followed by a slow crystallization step achieved through gradual cooling based.

Details of the synthesis of the Ln complex can be found in section 2.4.2.

3) Nuclearity of Ln complexes

The synthesis of lanthanide complex can involve partial hydrolysis of Ln^{3+} ions, with the use of organic ligands that favor metal aggregation over polycondensation, leading to the formation of discrete complexes rather than extended polymer networks. The choice of ligands plays a crucial role in modulating the structure and nuclearity of the complexes, which in turn influences their optical or magnetic properties. Furthermore, the nuclearity of the complexes can also be controlled by adjusting the pH of the solvent. Recent work has reported that the polynuclear Ln^{3+} complex is formed during the controlled hydrolysis of Ln^{3+} in a high pH solution, whereas the mononuclear Ln^{3+} complex is obtained in an acidic solution.[42] In this work, we use the same synthesis protocol, and focus on the influence of different ligands on the structure and nuclearity of Ln^{3+} complexes. The β-diketone ligands [acac], [tfa] and the ligand 1,10-phenanthroline [phen] will be studied in this section.

4) Photoluminescence of Ln^{3+} complexes

The objective is to explore the PL properties of the synthesized Ln^{3+} complexes, and their potential for development as pressure sensors in tribological measurements. Compared with inorganic compounds, Ln^{3+} complexes offer greater structural flexibility, allowing a wider range of structural variations under compression.[43] However, a major drawback of Ln^{3+} complexes is their high sensitivity to the surrounding environment, making the luminescent quenching occurs easily. Therefore, organic ligands must be able to enhance the intensity of PL emission from Ln^{3+} emitters in the complex. Typically, the organic ligands used in complexes are capable of absorbing UV light over a broad absorption band. Sensitization of Ln^{3+} by another means, namely a good light absorber, has been studied and is known as the '*Antenna effect'*.[44] In a Ln^{3+} complex, the antenna effect can be very effective due to the strong interaction between the ligand and the metal.[44–51] The S_1 singlet excited state of the ligand can be deactivated by the non-relaxation process (NR) or intersystem crossing (ISC) to the T_1 triplet, and then energy transfer (ET) continues from T_1 to the Ln^{3+} emissive level. The ligands [acac], [tfa] and [phen] will be studied as sensitizers of Ln^{3+} ions in a Ln^{3+} complex (Figure 1.13 see in Chapter 1, section 1.3.2). Based on previous work concerning the study of β-diketonate complexes,[41,52,53] Tb^{3+} and Eu^{3+} complexes were developed by varying the ligands in order to obtain PL complexes efficient for pressure sensing. As Tb^{3+} is a well-known sensitizer of Eu^{3+} due to the strong match of the energy level gap ($^5D_4 \rightarrow {}^7F_5 = {}^7F_1 \rightarrow {}^5D_1$),[54–61] the efficient Tb^{3+}-Eu^{3+} energy transfer process can thus be expected, which may lead to pressure sensitivity (see chapter 4). Furthermore, as the emission peaks of Tb^{3+} and Eu^{3+} are mostly distinct, it is possible to analyze their emissions separately. Dilution with optically neutral ions such as Y^{3+} can improve the intensity of the emission due to the protection of the emitter from concentration quenching,[62] the Y^{3+}-diluted complexes are also studied.

By varying the nature of the ligands, three types of Ln-complexes were synthesized and named [Ln_1], [Ln_2] and [Ln_9] because of their nuclearities.

Table 2.4: Ln complex synthesis.

Reagents	[Ln_1] [$Ln(acac)_3(phen)$]	[Ln_2] [$Ln_2(\mu\text{-OMe})(tfa)_4(phen)_2$]	[Ln_9] [$Ln_9(acac)_{16}(\mu_3\text{-OH})_8(\mu_4\text{-O})(\mu_4\text{-OH})$]
[phen]*	x	x	/
[acac]*	x	/	x
[tfa]*	/	x	/

*[phen] =1,10-phenanthroline; [acac] = acetylacetone; [tfa] = trifluoro acetylacetone

2.4.2 Materials and Methods

1) Materials

Commercial chemicals reagents and solvent were used without further purification. Lanthanide ions: YCl_3 hydrated (Alfa Aesar 99.9%), $TbCl_3$ hexahydrated (Thermo scientific 99.9%), $ErCl_3$ hydrated (Alfa Aesar 99.9%); Ligands: 1,10-phenanthroline (1,10-phenanthroline powder monohydrate, 99+%, Alfa Aesar), acetylacetone (2.4-pentanedion Reagent plus >99%, Sigma-Aldrich), trifluoro acetylacetone (1,1,1-Trifluoro-2,4-pentanedione, Sigma-Aldrich); Additives: triethylamine (Et_3N, > 99.5% Sigma); Solvent: MeOH (Methanol anhydrous, Sigma); EtOH (Ethanol anhydrous, Sigma).

2) Synthesis methods

The Ln^{3+}-complexes were prepared on the basis of literature synthesis.[41,53] By varying the nature of ligands, three types of Ln-complexes are synthesized. The alcoholic solution of Ln^{3+} was prepared by dissolving hydrated $LnCl_3$ in MeOH, various compositions of Ln^{3+} have been synthesized for further characterization. Ligand [phen] was then added to the MeOH solution. After the solid compounds had dissolved, ligand [acac] or [tfa] was added to the solution with mechanical stirring. The mixture was stirred for 30 minutes at room temperature, then Et_3N (15 vol.% of MeOH) was added. The solution was then stirred for a further 15 minutes and stored in the refrigerator at 3 - 5°C for subsequent crystallization. After 24 - 48 hours, the colorless crystals formed were separated from the solution and washed with a small amount of EtOH. More information is completed in Table 2.5.

Table 2.5: Concentrations (M) of the reagents for Ln complex synthesis.

Reagents	$[Ln_1]$ $[Ln(acac)_3(phen)]$	$[Ln_2]$ $[Ln_2(\mu\text{-OMe})(tfa)_4(phen)_2]$	$[Ln_9]$ $[Ln_9(acac)_{16}(\mu_3\text{-}OH)_8(\mu_4\text{-}O)(\mu_4\text{-}OH)]$
$LnCl_3$ (MeOH)	0.2 M (Eu; Tb; Y)	0.2 M (Eu; Tb)	
[phen]*	0.2	0.2	/
[acac]*	0.6	/	0.6
[tfa]*	/	0.6	/

*[phen] =1,10-phenanthroline; [acac] = acetylacetone; [tfa] = trifluoro acetylacetone

3) Characterizations methods

The powder X-ray diffraction diagram are performed by Bruker D8 Advance diffractometer, equipped with the Cu Kα radiation (λ = 1.54060 Å), under 45 kV and 30 mA at room temperature. The crystal structures are determined by single-crystal X-ray diffractometer. The single-crystal was selected and mounted on an XtaLAB Synergy, Dualflex,HyPix-Arc 100 diffractometer (Centre Diffractométrie Henri Longchambon, univ

Lyon1). Data collection was achieved at 100.0(3) K using Molybdenum X-ray radiation (λ = 0.71073 Å). Intensities were collected by means of the CrysalisPro software.[63] Reflection indexing, unit-cell parameters refinement, Lorentz-polarization correction, peak integration and background determination were carried out with the CrysalisPro software.

The crystal structure was solved by direct methods using the ShelXT[64] and refined using ShelXL.[65] Structure was refined using full-matrix least-squares on F^2 within the Olex2 suite.[66] All non-hydrogen atoms were refined with anisotropic displacement parameters unless specified otherwise. Disordered portions were modelled using refined partial occupancies. Geometric and vibrational restraints were applied where appropriate to ensure physically reasonable models. In the case of metallic position within the mononuclear complex [Ln_1], Tb^{3+} and Y^{3+} ions were fixed at the same crystallographic position and restraints on their position as well as their anisotropic displacement parameters were fixed. Their respective occupancies were refined fixing the sum equal to 1.

Scanning electron microscopy (SEM) images and elemental EDX spectra of the complex were captured by the Zeiss Merlin Compact operating at 20 kV. The homogeneity of the elemental composition was confirmed by EDX analysis.

The DLS and rheological measurements are the same as in section 2.3.2.

2.4.3 Structural characterizations of Ln^{3+} complex

1) Physical aspects

The crystal obtained after purification is a colorless solid. As shown in Figure 2.14, the crystals of [Ln_1] are transparent needle-like solids with a length of 4 – 6 mm, the crystals of [Ln_2] are a white powder and the crystals of [Ln_9] are transparent platelets solids with a size length about 5 mm.

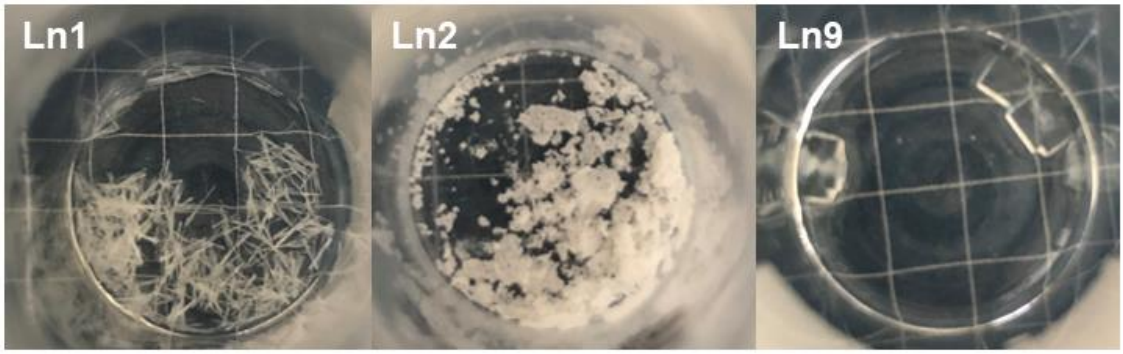

Figure 2.14: Photos of synthesized Ln^{3+} complexes.

2) Crystal structure determinations

- **Complex [Ln_1] [$Ln(acac)_3(phen)$]**

After soft grinding, the powder of [Ln_1] complexes was analyzed by X-ray diffraction. Figure 2.15a shows the X-ray powder diagram of the complex at different compositions. The structure is very similar to the reference (CCDC 1482080[67,68]): $C_{27}H_{29}N_2O_6Ln$ (Ln^{3+}= Tb^{3+}, Eu^{3+}), corresponding to one Ln^{3+}, three ligand [acac] and one ligand [phen] per molecule. The slight difference in the peak around 12° are not yet explained but numerous references relate

polymorphism cases in [phen] coordinated complex. For instance, $Tb(phen)_2(NO_3)_3$ is known to present two polymorphs, which differs just by the angle between the two phen groups.[69,70] The structural resolution of the $[Eu_{0.01}Tb_{0.20}Y_{0.79}(acac)_3(phen)]$ complex on a single crystal was carried out and confirms that it has the same structure as the monometallic Tb or Eu complexes.[63]

The $[Eu_{0.01}Tb_{0.20}Y_{0.79}(acac)_3(phen)]$ compound is a mononuclear complex in which the Ln^{3+} ion is coordinated by three deprotonated acac- ligands and one neutral phenanthroline. Its refined formula is therefore $[Ln(acac)_3(phen)]$ (Figure 2.15b). Metal position occupancy was refined to the following values: 85.5(8) % of Y^{3+} and 14.5(8) of Tb^{3+}. It was not possible to highlight the presence of Eu^{3+} as its proportion during synthesis was of the order of 1% (molar). However, its presence was confirmed by optical measurements. Data on the crystal lattice is given in Table 2.6. All C-O bond lengths in the complex are very close to each other, ranging from 1.26(1) Å to 1.271(9) Å (Table A1), confirming that the charge, once the ligand is deprotonated by the base, is delocalized throughout the β-diketone. All Tb/Y-O bond lengths, from 2.300(5) Å to 2.333(5) Å, and Tb/Y-N bong lengths, from 2.534(6) Å to 2.565(6) Å, agree with those already reported in the literature.[67,68] The Ln^{3+} ion is in a $\{O_6N_2\}$ environment that can be likened to a square antiprism (D_{4d}, Table A2). The shortest Tb/Y···Tb/Y distance is equal to 8.003 Å along the [011] direction within the unit-cell (Figure 2.15c).

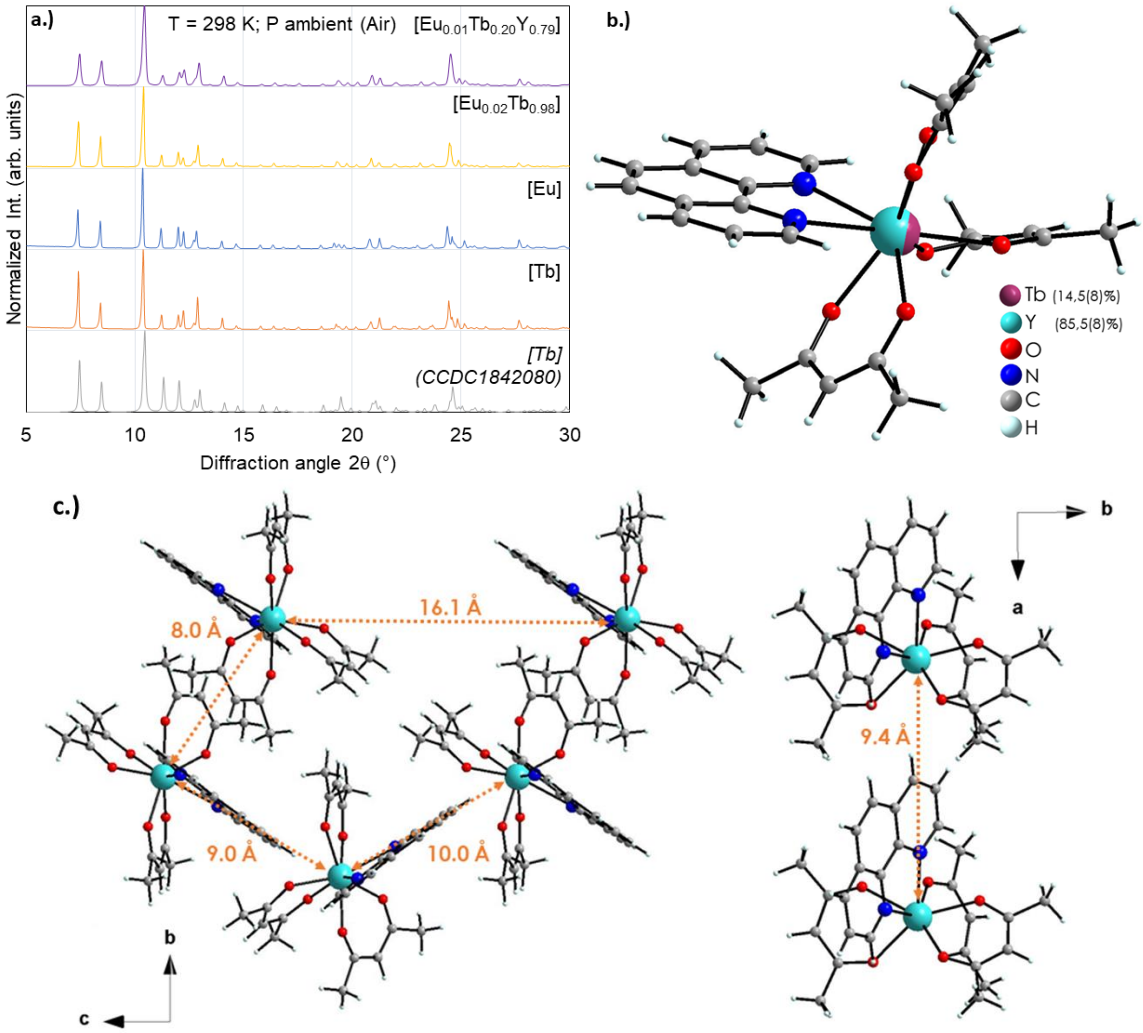

Figure 2.15: a.) X-Ray diffraction patterns of [Ln(acac)$_3$(phen)] with different compositions, the reference [Tb(acac)$_3$(phen)] (CCDC 1842080) from the work of Bukvetskii *et al*..[67] b.) Molecular structure of [Eu$_{0.01}$Tb$_{0.20}$Y$_{0.79}$(acac)$_3$(phen)]; c.) Distances between the Ln atoms.

- **Complex [Ln$_2$] [Ln$_2$(μ-OMe)$_2$(tfa)$_4$(phen)$_2$]**

The powder XRD diagrams as shown in Figure 2.16a are all similar in different compositions. The refinements of [Ln$_2$] crystal structure were carried out in case of Tb^{3+} based complex and lead to the following general formula: [Ln$_2$(μ-OMe)$_2$(tfa)$_4$(phen)$_2$]. Within this binuclear complex, each Ln^{3+} metal center is coordinated by two deprotonated trifluoro-acetylacetonate ligands and one neutral phenanthroline. Their coordination spheres are completed by two μ-OMe ligands forming a double bridge between the lanthanide ions (Figure 2.16b). Data on the crystal lattice is given in Table 2.6. The C-O bond lengths of trifluoro-acetylacetonate ligand in the complex [Ln$_2$] are comparable, ranging from 1.237(8) Å to 1.255(8) Å (Table A1a), but appear to be shorter than those in [Ln$_1$]. The difference in bond length between the C-O bonds in trifluoro-acetylacetonate and acetylacetonate can be attributed to a higher electronegativity of fluorine than that of hydrogen. The large positive

charge on the C atom in trifluoro-acetylacetonate leads to a strong C-O bond, so the bond length is shorter. On the contrary, the Ln-O bond and Ln-N bond lengths are close to those observed in [Ln_1]. In this binuclear complex, the intramolecular distance between the two combined Ln ions is 3.732 Å, and the shortest Ln-Ln intermolecular distance is equal to 9.294 Å and (Figure 2.16c).

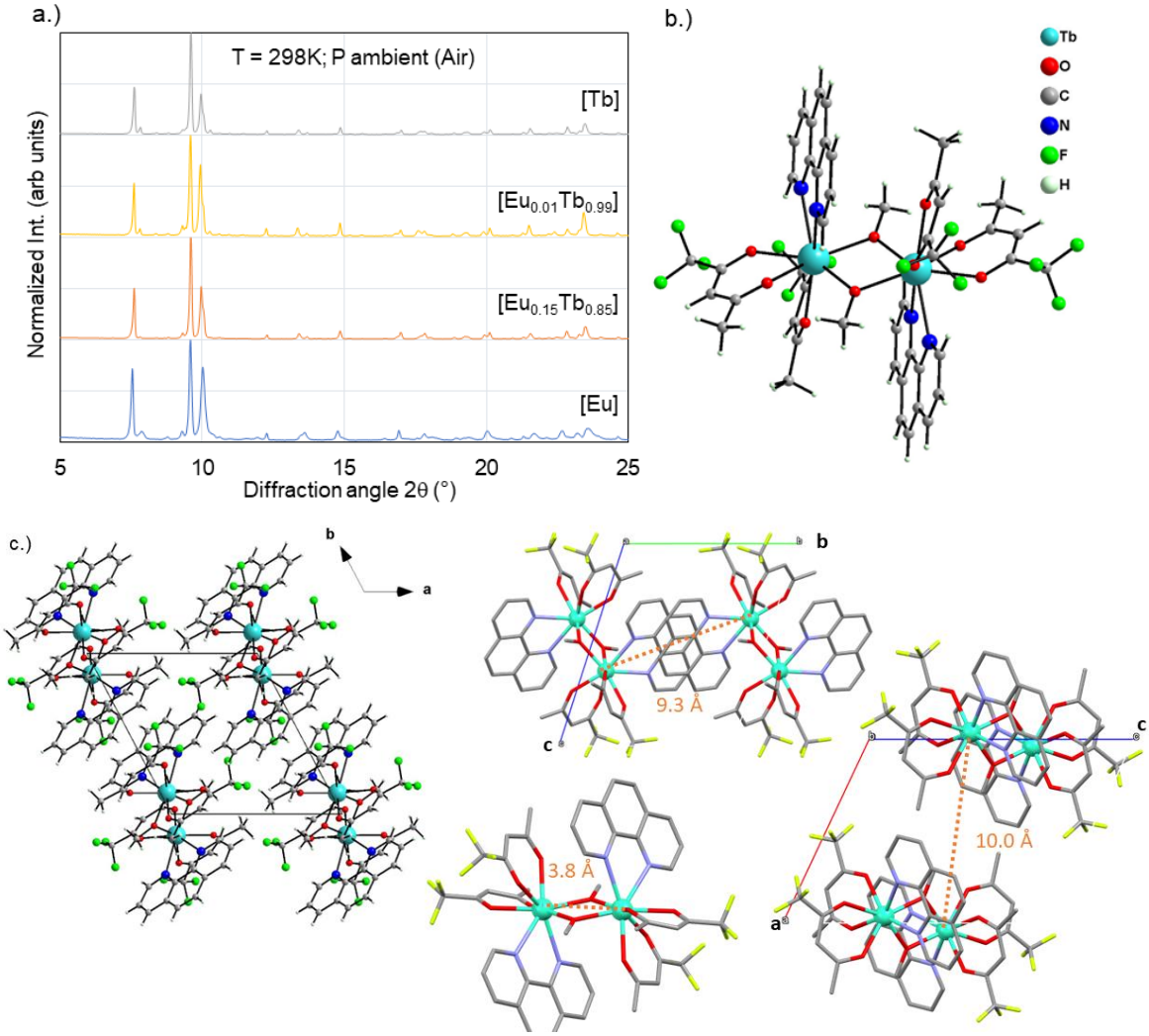

Figure 2.16: a) X-Ray diffraction patterns of [$Ln_2(\mu\text{-OMe})_2(tfa)_4(phen)_2$] with different compositions. b) Molecular structure of [$Tb_2(\mu\text{-OMe})_2(tfa)_4(phen)_2$]. c) Distances between the Ln atoms in the complex [$Tb_2(\mu\text{-OMe})_2(tfa)_4(phen)_2$].

- **Complex [Ln_9] [$Ln_9(acac)_{16}(\mu_3\text{-OH})_8(\mu_4\text{-O})(\mu_4\text{-OH})$]**

As shown in Figure 2.17a, the XRD powder diagrams of the [Ln_9] complex synthesized at different compositions are all similar to the reference[41] (reported structure: CCDC 711969 [$Eu_9(acac)_{16}(\mu_3\text{-OH})_8(\mu_4\text{-O})(\mu_4\text{-OH})$]. The reported crystal structure is presented in Figure 2.17b. There are two pentanuclear square pyramids of Ln atoms aligned face to face along the central axis. The base of the pyramid consists of four Ln atoms, shearing an apical metallic atom. The central Ln atom is connected to the others Ln atoms by eight μ_3-OH ligands, forming a near perfect square anti-prism local symmetry (Figure 2.17b). Crystal lattice data are given in Table 2.6. The C-O bond of the acetylacetonate ligand in the [Ln_9] complex

ranges from 1.24(3) Å to 1.36(2) Å (Table A1). Ln-O bond lengths ranged from 2.32 (1) Å to 2.638 Å, most of them are longer than those in the [Ln_1] complex. The shortest Ln-Ln intermolecular distance is 10.136 Å and the intramolecular distance is 3.783 Å (Figure 2.17c).

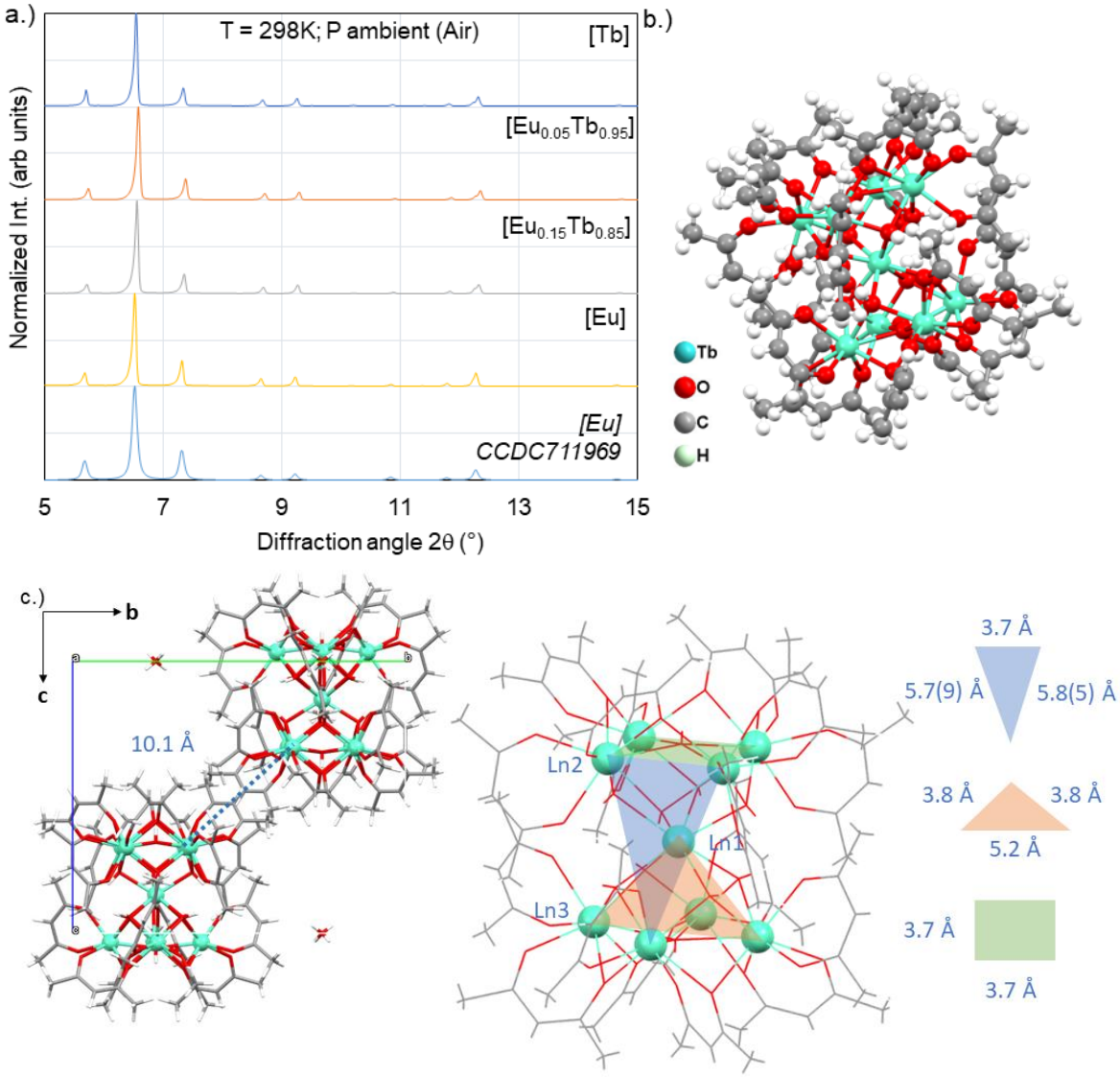

Figure 2.17: a) X-Ray diffraction patterns of [$Ln_9(acac)_{16}(\mu_3\text{-}OH)_8(\mu_4\text{-}O)(\mu_4\text{-}OH)$] with different compositions, reference [$Eu_9(acac)_{16}(\mu_3\text{-}OH)_8(\mu_4\text{-}O)(\mu_4\text{-}OH)$] (CCDC 711969). b) The reported molecular structure of [$Tb_9(acac)_{16}(\mu_3\text{-}OH)_8(\mu_4\text{-}O)(\mu_4\text{-}OH)$]. c) Distances between Ln atoms in the complex [$Tb_9(acac)_{16}(\mu_3\text{-}OH)_8(\mu_4\text{-}O)(\mu_4\text{-}OH)$]. (All the data come from the CCDC 711969, Petit *et al.* [41])

Table 2.6: Crystal data of refinements for Ln complexes

Sample	[Ln_1]	[Ln_2]	[Ln_9][41]
Refined formula	$C_{27}H_{29}N_2O_6Ln$	$C_{46}H_{38}F_{12}N_4O_{10}Ln_2$	$C_{80}H_{123}O_{43}Ln_9$
Molecular weight (g.mol^{-1})	576.6 ($Tb_{0.145(8)}Y_{0.855(8)}$)	1352.7 (Tb_2)	3203.2 (Tb_9)
Crystal system	monoclinic	triclinic	tetragonal
Space group	$P2_1/n$	$P\bar{1}$	P4/n
Unit-cell parameters	a = 9.4135(3) Å b = 20.7817(6) Å c = 14.4473(4) Å β = 98.247(3)° V = 2797.1(1) Å^3	a = 10.733(5) Å b = 10.862(5) Å c = 12.993(5) Å α = 97.702(5)° β = 109.622(5)° λ= 112.978(5)° V = 1250.7(1) Å^3	a = 19.1714(7) Å c = 15.5661(6) Å V = 5721.2(4) Å^3
Z*	4	2	2
T (K)	100.0(3)	293	290
μ (mm^{-1})*	2.190	2.908	5.617
Density	1.369	1.796	1.879
Crystal size (mm^3)	0.07×0.10×0.59	0.14×0.27×0.35	0.02×0.09×0.10
Crystal colour	colorless	colorless	colorless
Crystal shape	block	plate	plate
No. reflections used	50 454	4817	3372
No. refined parameters	3 280	3 340	300
R / R_w (I / σ(I) > 2)*	0.0756 / 0.0924	0.0429 / 0.0612	0.0444 / 0.0998
S*	1.395	1.066	/
$\Delta\rho_{max}$ / $\Delta\rho_{min}$ (e$^-$.Å^{-3})*	+1.52 / -1.57	+1.69 / -0.63	+1.48 / -1.16

Absorption correction	multi-scan	analytical	multi-scan

*The definitions of the parameters can be found in Table A3.

The above results show that the structures of [Ln_1], [Ln_2] and [Ln_9] are not affected by the Eu/Tb/Y ratio. However, the different ligands have an impact on the nuclearity of the Ln complex. By adding bulky ligands such as [phen], the formation of the complex with a small nuclearity is favoured. The structure of [Ln_2] [$Ln_2(\mu\text{-OMe})_2(tfa)_4(phen)_2$] has not been found in the reports published by now, furthers studies on the impact of the ligand [tfa] on the nuclearity and structure of the Ln complex should be considered. We noted that during the synthesis, the ligand/Ln^{3+} ratio has not been modified in this work, the influence of the ligand/Ln^{3+} ratio on the structure should also be studied in the future.

3) Dispersion of Ln in the crystal

To determine the distribution of Ln in various complexes, the complexes [Ln_1], [Ln_2] and [Ln_9] at the composition [$Eu_{0.15}Tb_{0.85}$] are analyzed by EDX. As shown in Figure 2.18, respectively, the dispersion of Ln in the complex [Ln_1], [Ln_2] and [Ln_9] complex at [$Eu_{0.15}Tb_{0.85}$] is homogeneous in the point-by-point analysis. Compared with the theoretical value of the Eu/Tb ratio at 0.17, the measured Eu/Tb ratio of the [Ln_1], [Ln_2] and [Ln_9] complexes are 0.13, 0.20 and 0.20, respectively (Figure 2.18). The measurements are considered accurate because the Eu concentration is too low compared to other elements in the molecule.

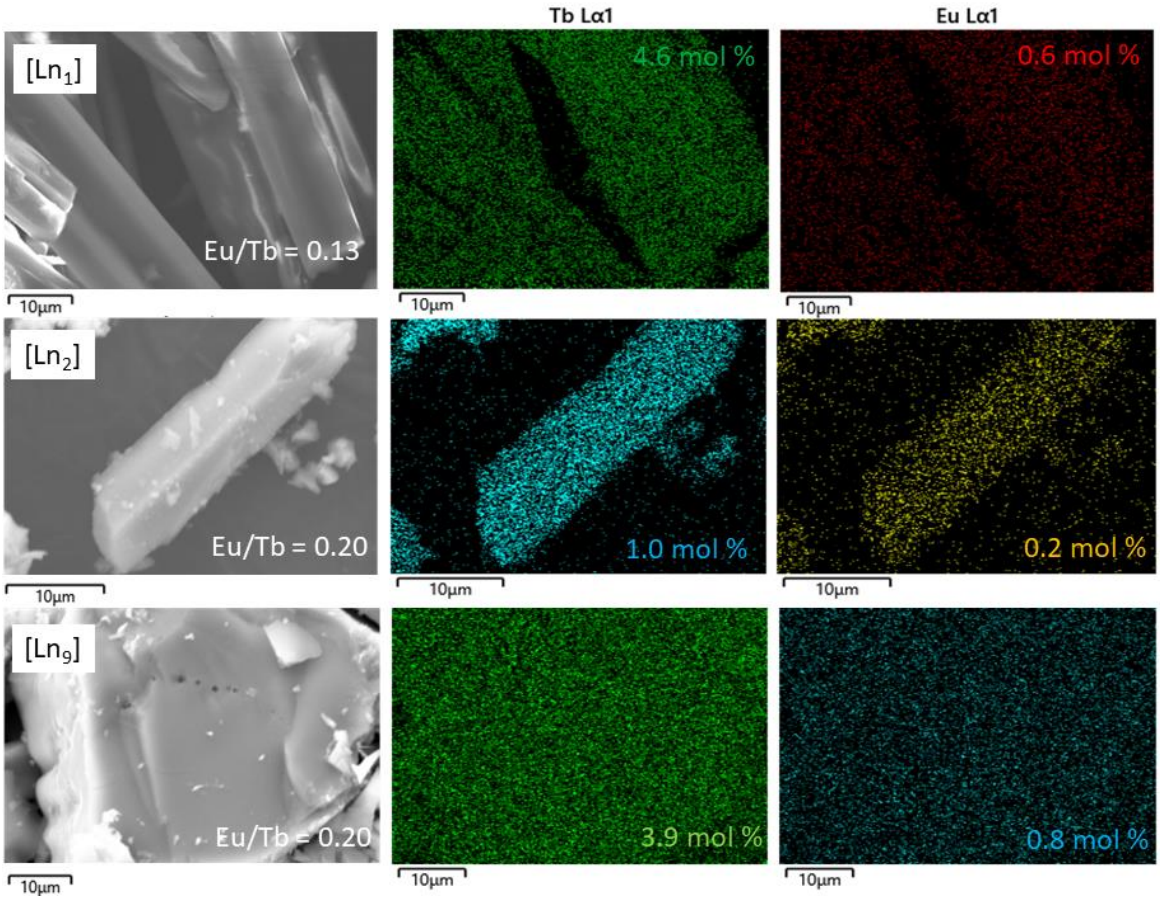

Figure 2.18: EDX analysis of complexes [Ln_1], [Ln_2] and [Ln_9] with composition [$Eu_{0.15}Tb_{0.85}$]: SEM image, associated elemental mapping of terbium and europium.

In the case of the yttrium-containing [Ln_1] complex, EDX analysis was carried out for the complex with the composition [$Eu_{0.01}Tb_{0.20}Y_{0.79}$]. Figure 2.19 shows that the dispersion of the elements yttrium and terbium is homogenous; europium is not detectable at low concentrations. The global ratio of Tb/Y is 0.30, whereas the theoretical value is 0.25. The difference may be due to the Yttrium is highly hydroscopic, which can affect the accuracy of the EDX measurement.

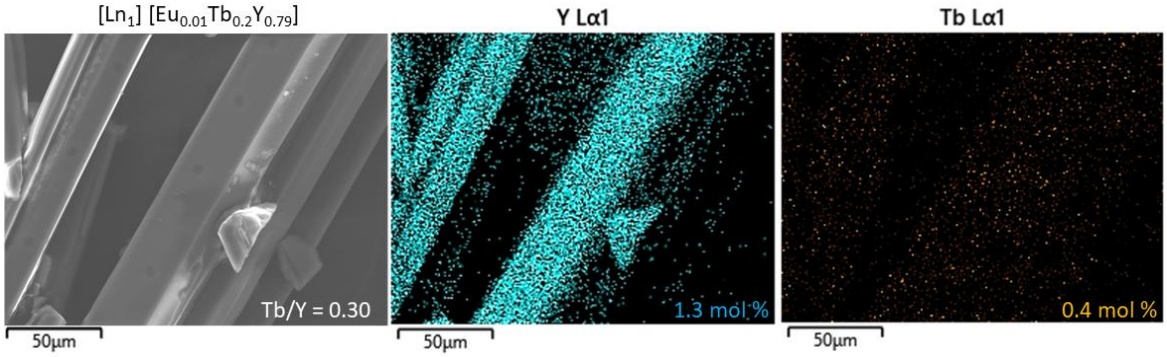

Figure 2.19: EDX analysis of the [Ln_1] [$Eu_{0.01}Tb_{0.2}Y_{0.79}$] complex: SEM image, associated elemental mapping of Yttrium and Terbium.

Regarding the photoluminescent properties of the Ln^{3+} complex, varying the nuclearity may provide substantial interests in the modulation of Ln^{3+}-Ln^{3+} energy transfer by varying the Ln^{3+}-Ln^{3+} distance. The presence of organic ligands (phen, acac and tfa) should optimize the emission of the complex through the antenna effect,[46,57,67,71–78] while the interionic distance between Ln^{3+}-Ln^{3+} is less than 10 Å (Table A1d). Therefore, efficient absorption by the ligand to excite the Ln^{3+} emitter should be observed, and energy transfer between Tb^{3+}-Eu^{3+} should be allowed in the system.[54–61] In chapter 4, the photoluminescent properties of the Ln complexes, [Ln_1], [Ln_2] and [Ln_9] will be discussed, particularly with respect to their pressure-dependent photoluminescence.

2.4.4 Suspension of [Ln_1] [$Eu_{0.01}Tb_{0.20}Y_{0.79}$] complex

The synthesized crystals of the [Ln_1] complex at [$Eu_{0.01}Tb_{0.20}Y_{0.79}$] are softly grinded for 5 mins into a fine powder, then dispersed in the lubricant (Nycobase 5750) at 0.1, 0.5 and 1.0 wt.% for further analysis. The suspensions are stirring with a bar magnet for 30 minutes to obtain a homogenous dispersion.

1) Hydrodynamic size of Ln complex crystals

As before, the hydrodynamic size of the crystals in the suspension was measured by DLS. As shown in Figure 2.20, the measured hydrodynamic size of the crystals in the suspension is less than 1 µm, the crystals in the 0.1 and 0.5 wt.% suspensions are monodispersed. The size of crystals in the 1.0 wt.% suspension falls into two populations, most around 80 nm and others are at 615 nm. As the maximum hydrodynamic sizes (615 nm) of the crystals are acceptable for tribology measurements in fluid lubricant at 1.0 wt.%, this concentration was selected to optimize the quality of the spectral emission in further characterizations.

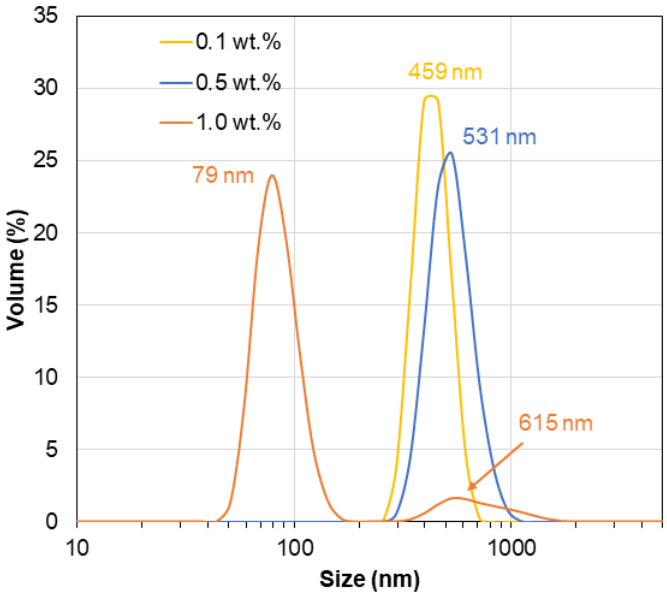

Figure 2.20: DLS diagram of the [Ln_1] [$Eu_{0.01}Tb_{0.20}Y_{0.79}$] crystals suspension at 0.1, 0.5 and 1 wt.%.

2) Rheological properties

The viscosity of the colloidal suspension of crystals at 1.0 wt.% was analyzed by rheometer with PP40 (gap at 0.2 mm), at different temperatures (293—353K, ± 0.03K) and imposing a shear rate (range between 1 to 10^4 s^{-1}). Pure Nycobase fluid is measured as a reference at the same time, as shown in Figure 2.21 in the blue line. Up to 353K, the viscosity of the 1.0 wt.% crystals suspension is identical to the viscosity of pure Nycobase, even at high shear rate (10^4 s^{-1}). As previously mentioned in the $GdVO_4$ NPs suspension, shear-induced heating has been observed at 293 K under high shear rate (> 2000 s^{-1}), resulting in a decrease in fluid viscosity.[1] Note that the difference between the viscosity of pure Nycobase reported here in Figure 2.21 and the one reported in Figure 2.10. Two different batches of the commercial product were used. Dispersion of the crystals of the $[Eu_{0.01}Tb_{0.2}Y_{0.79}]$ complex at 1.0 wt.% has no significant impact on the rheological properties of the lubricant. Optical characterizations of the complexes and the crystals suspension will be presented in the following section.

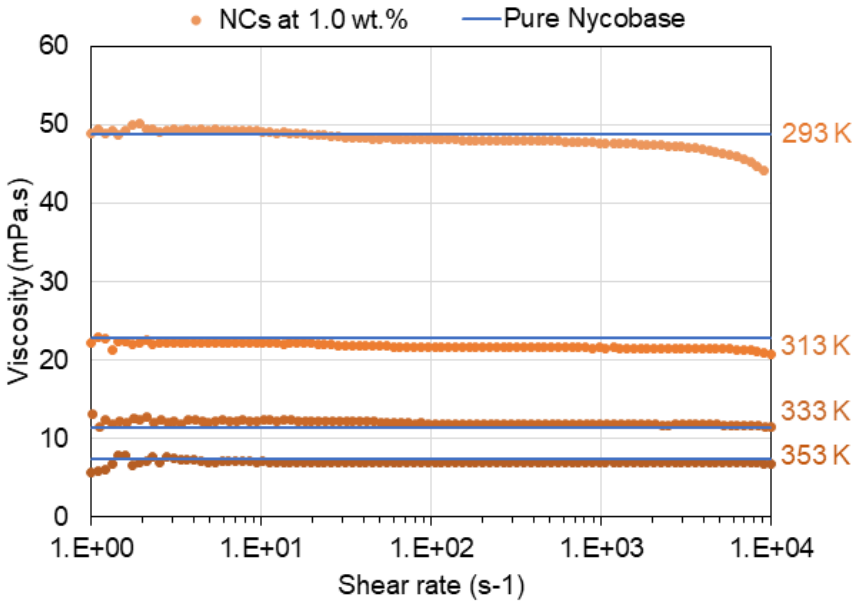

Figure 2.21: Viscosity of 1.0 wt.% $[Eu_{0.01}Tb_{0.2}Y_{0.79}]$ complex crystals suspension at 293 – 353 K under a shear rate of 1 - 10^4 s^{-1} for crystals suspension (in triangle symbol) and pure Nycobase (in line).

2.4.5 Outlook: incorporation of Ln complex in solid

The incorporation of the Ln^{3+} complex in a solid matrix, hybrid silica glass or PDMS will be the next step of this work. However, the dissolution of Ln^{3+} complex in alcoholic solvent is the main obstacle to the dispersion of the crystals of Ln complex into silica glass. The stability of the crystals of Ln^{3+} complex into PDMS matrix is higher, the crystals/PDMS mixture will be further characterized.

2.5 Conclusion

This chapter has provided the structural characterizations of PL sensors and the mechanical analysis of PL sensors dispersed in matrices. Structural and mechanical characterizations of $GdVO_4$ NPs and NPs dispersed into matrices show the possibility of developing $GdVO_4$ NPs as PL nanosensor for further tribological measurements. The synthesized $GdVO_4$ NPs are well crystallized in small size < 50 nm. However, the hydrodynamic size of the NPs dispersed in suspension is slightly larger than expected, further surface functionalization can be studied to reduce the dispersed size. Moreover, to optimize the crystallization of the NPs for the increase in photoluminescent emission intensity, higher temperature is required for the annealing of the NPs. Considering the condition of maintaining the small size of the NPs after annealing at high temperature, further optimizations of the synthesis can be explored, such as the solvothermal methods.[35]

Dispersion of the NPs is homogeneous with good monodispersity in the fluid lubricant, as well as in the solid matrix. Moreover, it should be highlighted that dispersing the NPs at low concentration in the fluid (0.5 wt.%) or in the solid matrices (5 wt.%) did not change the physical and mechanical properties of the material. This result is crucial for further investigation of the optical properties of $GdVO_4$ NPs. In chapter 3, photoluminescent properties of $GdVO_4$: Yb^{3+}/Er^{3+} will be presented, including their thermometry in different media. The applicability of $GdVO_4$: Yb^{3+}/Er^{3+} NPs as a thermometer will be discussed, considering the effect of laser, NPs concentrations and pressure.

Ln^{3+} complexes of different nuclearities are later studied. Following the same synthesis, by varying the ligands, [Ln_1], [Ln_2] and [Ln_9] complexes are obtained with high purity and homogeneity. The Ln^{3+}-Ln^{3+} distance ranges from 3 Å to 8 Å depending on the different nuclearities. This Ln^{3+}-Ln^{3+} distance can be very interesting for the energy transfer of Tb^{3+} to Eu^{3+} in PL studies. Following the Förster Resonance Energy Transfer (FRET) theory, the ET rate is strongly dependent on the Ln^{3+}-Ln^{3+} distance. By designing a system involving Tb^{3+} to Eu^{3+} with ET rates sensitive to structural contraction induced by pressure, it would be possible to create a pressure sensing system based on the relative emission intensity. The presence of organic ligands creates the '*Antenna effect'*, resulting in enhanced emission intensity of Ln^{3+} ions within the complex. This phenomenon contributes to the study of the photoluminescent properties of Ln^{3+} complexes. In addition, the dispersion of Ln complexes in a fluid lubricant is analyzed, demonstrating satisfactory hydrodynamic sizes of complex crystals and favorable rheological properties of suspensions. These findings provide a solid basis for further exploration of the photoluminescent properties of Ln^{3+} complexes (chapter 4).

References

(1) Albahrani, S. M. B.; Seoudi, T.; Philippon, D.; Lafarge, L.; Reiss, P.; Hajjaji, H.; Guillot, G.; Querry, M.; Bluet, J. M.; Vergne, P. Quantum Dots to Probe Temperature and Pressure in Highly Confined Liquids. *RSC Adv.* **2018**, *8* (41), 22897–22908. https://doi.org/10.1039/C8RA03652G.

(2) Seoudi, T.; Philippon, D.; Fillot, N.; Lafarge, L.; Devaux, N.; Mondelin, A.; Vergne, P. CdSe-Based Quantum Dots as In Situ Pressure and Temperature Non-Intrusive Sensors in Elastohydrodynamic Contacts. *Tribol. Lett.* **2020**, *68* (3). https://doi.org/10.1007/s11249-020-01312-x.

(3) Seoudi, T. Non-Intrusive CdSe-Based Quantum Dots for Sensing Pressure and Temperature in Lubricated Contacts, Thesis in Université Claude Bernard Lyon 1, 2020.

(4) Mohamed Baqer Albahrani Sayed. Photoluminescent CdSe/CdS/ZnS Quantum Dots for Temperature and Pressure Sensing in Elastohydrodynamic Contacts, Thesis in Université Claude Bernard Lyon 1, 2017.

(5) Bair, S. S.; Andersson, O.; Qureshi, F. S.; Schirru, M. M. New EHL Modeling Data for the Reference Liquids Squalane and Squalane Plus Polyisoprene. *Tribol. Trans.* **2018**, *61* (2), 247–255. https://doi.org/10.1080/10402004.2017.1310339.

(6) Porras-Vazquez, A. A Molecular Approach to the Ultimate Friction Response of Confined Fluids, Thesis in INSA Lyon, 2019.

(7) Sanchez, C.; Lebeau, B.; Chaput, F.; Boilot, J. P. Optical Properties of Functional Hybrid Organic-Inorganic Nanocomposites. *Adv. Mater.* **2003**, *15* (23), 1969–1994. https://doi.org/10.1002/adma.200300389.

(8) Chateau, D.; Chaput, F.; Lopes, C.; Lindgren, M.; Brännlund, C.; Öhgren, J.; Djourelov, N.; Nedelec, P.; Desroches, C.; Eliasson, B.; Kindahl, T.; Lerouge, F.; Andraud, C.; Parola, S. Silica Hybrid Sol-Gel Materials with Unusually High Concentration of Ptorganic Molecular Guests: Studies of Luminescence and Nonlinear Absorption of Light. *ACS Appl. Mater. Interfaces* **2012**, *4* (5), 2369–2377. https://doi.org/10.1021/am2015537.

(9) Barthel, E. Adhesive Elastic Contacts – JKR and More. *J. Phys. D. Appl. Phys.* **2008**.

(10) Johnston, I. D.; McCluskey, D. K.; Tan, C. K. L.; Tracey, M. C. Mechanical Characterization of Bulk Sylgard 184 for Microfluidics and Microengineering. *J. Micromechanics Microengineering* **2014**, *24* (3). https://doi.org/10.1088/0960-1317/24/3/035017.

(11) Savchuk, O. A.; Carvajal, J. J.; Cascales, C.; Massons, J.; Aguiló, M.; Díaz, F. Thermochromic Upconversion Nanoparticles for Visual Temperature Sensors with High Thermal, Spatial and Temporal Resolution. *J. Mater. Chem. C* **2016**, *4* (27), 6602–6613. https://doi.org/10.1039/c6tc01841f.

(12) Bhiri, N. M.; Dammak, M.; Aguiló, M.; Díaz, F.; Carvajal, J. J.; Pujol, M. C. Stokes and Anti-Stokes Operating Conditions Dependent Luminescence Thermometric Performance of Er3+-Doped and Er3+, Yb3+ Co-Doped GdVO4 Microparticles in the Non-Saturation Regime. *J. Alloys Compd.* **2020**, *814*, 152197. https://doi.org/10.1016/j.jallcom.2019.152197.

(13) Dwivedi, A.; Kumar, D.; Rai, S. B.; Rai, A. K. Effect of Host on the Radiative (Upconversion Emission) as Well as Non-Radiative Relaxation (Laser Induced Optical Heating) in Tm3+/Yb3+ Co-Doped Phosphors. *J. Lumin.* **2020**, *226* (June), 117421. https://doi.org/10.1016/j.jlumin.2020.117421.

(14) Marqueño, T.; Errandonea, D.; Pellicer-Porres, J.; Martinez-Garcia, D.; Santamaria-Pérez, D.; Muñoz, A.; Rodríguez-Hernández, P.; Mujica, A.; Radescu, S.; Achary, S. N.; Popescu, C.; Bettinelli, M. High-Pressure Polymorphs of Gadolinium Orthovanadate: X-Ray Diffraction, Raman Spectroscopy, and Ab Initio Calculations. *Phys. Rev. B* **2019**, *100* (064106).

(15) Huignard, A.; Gacoin, T.; Boilot, J.-P. Synthesis and Luminescence Properties of Colloidal YVO 4: Eu Phosphors. *Chem. Mater.* **2000**, *12*, 1090–1094. https://doi.org/10.1016/j.jallcom.2011.07.079.

(16) Huignard, A.; Buissette, V.; Laurent, G.; Gacoin, T.; Boilot, J. P. Synthesis and Characterizations of YVO4: Eu Colloids. *Chem. Mater.* **2002**, *14* (5), 2264–2269. https://doi.org/10.1021/cm011263a.

(17) Erdei, S. Preparation of YVO4 Powder from the Y2O3 + V2O5 + H2O System by a Hydrolysed Colloid Reaction (HCR) Technique. *J. Mater. Sci.* **1995**, *30* (19), 4950–4959.

https://doi.org/10.1007/BF01154509.

(18) CHANG, C.; MAO, D. Thermal Dehydration Kinetics of a Rare Earth Hydroxide, Gd (OH) 3. *Int. J. Chem. Kinet.* **2007**, *39* (2), 75–81.

(19) Gavrilović, T. V.; Jovanović, D. J.; Smits, K.; Dramićanin, M. D. Multicolor Upconversion Luminescence of GdVO4:Ln3+/Yb3+ (Ln3+ = Ho3+, Er3+, Tm3+, Ho3+/Er3+/Tm3+) Nanorods. *Dye. Pigment.* **2016**, *126*, 1–7. https://doi.org/10.1016/j.dyepig.2015.11.005.

(20) Paz-Buclatin, F.; Rivera-López, F.; González, O.; Martín, I. R.; Martin, L. L.; Jovanović, D. J. GdVO4:Er3+/Yb3+ Nanocrystalline Powder as Fluorescence Temperature Sensor. Application to Monitor the Temperature of an Electrical Component. *Sensors Actuators, A Phys.* **2019**, *299*. https://doi.org/10.1016/j.sna.2019.111628.

(21) Buissette, V.; Huignard, A.; Gacoin, T.; Boilot, J. P.; Aschehoug, P.; Viana, B. Luminescence Properties of YVO4:Ln (Ln = Nd, Yb, and Yb-Er) Nanoparticles. *Surf. Sci.* **2003**, *532–535*, 444–449. https://doi.org/10.1016/S0039-6028(03)00203-6.

(22) Childs, P. R. N.; Greenwood, J. R.; Long, C. A. Review of Temperature Measurement. *Rev. Sci. Instrum.* **2000**, *71* (8), 2959–2978. https://doi.org/10.1063/1.1305516.

(23) Quintanilla, M.; Henriksen-Lacey, M.; Renero-Lecuna, C.; Liz-Marzán, L. M. Challenges for Optical Nanothermometry in Biological Environments. *Chem. Soc. Rev.* **2022**, *51* (11), 4223–4242. https://doi.org/10.1039/d2cs00069e.

(24) Descartes, S.; Desrayaud, C.; Rauch, E. F. Inhomogeneous Microstructural Evolution of Pure Iron during High-Pressure Torsion. *Mater. Sci. Eng. A* **2011**, *528* (10–11), 3666–3675. https://doi.org/10.1016/j.msea.2011.01.029.

(25) Michael Shockley, J.; Desrayaud, C.; Chromik, R. R.; Descartes, S. Significance of Al2O3 Particle Morphology in the Microstructure Evolution of Cold-Sprayed Al-Al2O3 during Unconstrained High-Pressure Torsion. *Mater. Sci. Eng. A* **2017**, *684* (December 2016), 510–516. https://doi.org/10.1016/j.msea.2016.12.078.

(26) Zhang, Y.; Sao-Joao, S.; Descartes, S.; Kermouche, G.; Montheillet, F.; Desrayaud, C. Microstructural Evolution and Mechanical Properties of Ultrafine-Grained Pure α-Iron and Fe-0.02%C Steel Processed by High-Pressure Torsion: Influence of Second-Phase Particles. *Mater. Sci. Eng. A* **2020**, *795* (May), 139915. https://doi.org/10.1016/j.msea.2020.139915.

(27) SCHÖFFEL, M. Multifunctional Rare Earth Vanadate Nanoparticles : Luminescent Labels , Oxidant Sensors and Magnetic Resonance Imaging Contrast Agents To Cite This Version : Multifunctional Rare Earth Vanadate Nanoparticles : Luminescent Labels , Oxidant Sensors and Mag, 2012.

(28) BROCH, E. Crystal Structure of Yttrium Vanadate [In German]. *Zeitschrift für Phys. Chemie* **1933**, *20* (1), 345–350.

(29) Graulis, S.; Chateigner, D.; Downs, R. T.; Yokochi, A. F. T.; Quirós, M.; Lutterotti, L.; Manakova, E.; Butkus, J.; Moeck, P.; Le Bail, A. Crystallography Open Database - An Open-Access Collection of Crystal Structures. *J. Appl. Crystallogr.* **2009**, *42* (4), 726–729. https://doi.org/10.1107/S0021889809016690.

(30) Perrella, R. V.; De Sousa Filho, P. C. High-Sensitivity Dual UV/NIR-Excited Luminescence Thermometry by Rare Earth Vanadate Nanoparticles. *Dalt. Trans.* **2020**, *49* (3), 911–922. https://doi.org/10.1039/c9dt04308j.

(31) Yang, L.; Peng, S.; Zhao, M.; Yu, L. New Synthetic Strategies for Luminescent YVO 4 :Ln 3+ (Ln = Pr, Sm, Eu, Tb, Dy, Ho, Er) with Mesoporous Cell-like Nanostructure . *Opt. Mater. Express* **2018**, *8* (12), 3805. https://doi.org/10.1364/ome.8.003805.

(32) Zhou, Y.; Ledoux, G.; Philippon, D.; Descartes, S.; Martini, M.; He, S.; Desroches, C.; Fournier, D.; Journet, C.; Bois, L. Laser-Induced Heating in GdVO 4 : Yb 3 + / Er 3 + Nanocrystals for Thermometry. *ACS Appl. Nano Mater.* **2022**, *5*, 16388–16401. https://doi.org/10.1021/acsanm.2c03466.

(33) Alkahtani, M.; Alfahd, A.; Alsofyani, N.; Almuqhim, A. A.; Qassem, H.; Alshehri, A. A.; Almughem, F. A.; Hemmer, P. Photostable and Small Yvo4:Yb,Er Upconversion Nanoparticles in Water.

Nanomaterials **2021**, *11* (6). https://doi.org/10.3390/nano11061535.

(34) Liu, L.; Yue, S.; Zhang, Y.; Qin, R.; Liu, L.; Zhang, D.; Sun, R.; Chen, L. One-Pot Reverse Microemulsion Synthesis of Core-Shell Structured YVO4:Eu3+@SiO2 Nanocomposites. *Opt. Mater. (Amst).* **2015**, *39* (3), 207–210. https://doi.org/10.1016/j.optmat.2014.11.027.

(35) Mialon, G.; Gohin, M.; Gacoin, T.; Boilot, J. P. High Temperature Strategy for Oxide Nanoparticle Synthesis. *ACS Nano* **2008**, *2* (12), 2505–2512. https://doi.org/10.1021/nn8005784.

(36) Aromí, G.; Gamez, P.; Reedijk, J. Poly Beta-Diketones: Prime Ligands to Generate Supramolecular Metalloclusters. *Coord. Chem. Rev.* **2008**, *252* (8–9), 964–989. https://doi.org/10.1016/j.ccr.2007.07.008.

(37) Volpe, M.; Bombieri, G.; Clemente, D. A.; Foresti, E.; Grillone, M. D. Synthesis and Physico-Chemical Characterization of a New Series of Hydroxide Ion Acetylacetonate Lanthanide(III) - Ditungsten Decacarbonyl Hydride Complexes. *J. Alloys Compd.* **2004**, *374* (1–2), 382–386. https://doi.org/10.1016/j.jallcom.2003.11.153.

(38) Zhou, S. L.; Wang, S. W.; Yang, G. S.; Liu, X. Y.; Sheng, E. H.; Zhang, K. H.; Cheng, L.; Huang, Z. X. Synthesis, Structure, and Catalytic Activity of Tetracoordinate Lanthanide Amides [(Me3Si)2N]3Ln(μ-Cl)Li(THF)3 (Ln = Nd, Sm, Eu). *Polyhedron* **2003**, *22* (7), 1019–1024. https://doi.org/10.1016/S0277-5387(03)00042-1.

(39) Holzer, C.; Wernbacher, A. M.; Senekowitsch, J. M.; Gatterer, K.; Kelterer, A. M. A Theoretical Study on Trivalent Europium: From the Free Ion to the Water Complex. *J. Phys. Chem. A* **2014**, *118* (49), 11499–11511. https://doi.org/10.1021/jp509253e.

(40) Marques, L. F.; Correa, C. C.; Garcia, H. C.; Martins Francisco, T.; Ribeiro, S. J. L.; Dutra, J. D. L.; Freire, R. O.; Machado, F. C. Theoretical and Experimental Spectroscopic Studies of the First Highly Luminescent Binuclear Hydrocinnamate of Eu(III), Tb(III) and Gd(III) with Bidentate 2,2'-Bipyridine Ligand. *J. Lumin.* **2014**, *148*, 307–316. https://doi.org/10.1016/j.jlumin.2013.12.021.

(41) Petit, S.; Baril-Robert, F.; Pilet, G.; Reber, C.; Luneau, D. Luminescence Spectroscopy of Europium(III) and Terbium(III) Penta-, Octa- and Nonanuclear Clusters with β-Diketonate Ligands. *J. Chem. Soc. Dalt. Trans.* **2009**, No. 34, 6809–6815. https://doi.org/10.1039/b822883c.

(42) Wang, R.; Liu, H.; Carducci, M. D.; Jin, T.; Zheng, C.; Zheng, Z. Lanthanide Coordination with α-Amino Acids under near Physiological PH Conditions: Polymetallic Complexes Containing the Cubane-like [Ln4(M3-OH)4]8+ Cluster Core. *Inorg. Chem.* **2001**, *40* (12), 2743–2750. https://doi.org/10.1021/ic001469y.

(43) Kato, M.; Ishii, K. *Soft Crystals*; 2023. https://doi.org/10.1007/978-981-99-0260-6.

(44) De Andrade, A. V. M.; Longo, R. L.; Simas, A. M.; De Sá, G. F. Theoretical Model for the Prediction of Electronic Spectra of Lanthanide Complexes. *J. Chem. Soc. - Faraday Trans.* **1996**, *92* (11), 1835–1839. https://doi.org/10.1039/FT9969201835.

(45) Kleinerman, M. Energy Migration in Lanthanide Chelates. *J. Chem. Phys.* **1969**, *51* (6), 2370–2381. https://doi.org/10.1063/1.1672355.

(46) Zahariev, T.; Shandurkov, D.; Gutzov, S.; Trendafilova, N.; Enseling, D.; Jüstel, T.; Georgieva, I. Phenanthroline Chromophore as Efficient Antenna for Tb 3 + Green Luminescence : A Theoretical Study. *Dye. Pigment.* **2021**, *185* (PA), 108890. https://doi.org/10.1016/j.dyepig.2020.108890.

(47) Bünzli, J. C. G.; Piguet, C. Taking Advantage of Luminescent Lanthanide Ions. *Chem. Soc. Rev.* **2005**, *34* (12), 1048–1077. https://doi.org/10.1039/b406082m.

(48) Kitagawa, Y.; Ferreira Da Rosa, P. P.; Hasegawa, Y. Charge-Transfer Excited States of π- And 4f-Orbitals for Development of Luminescent Eu(Iii) Complexes. *Dalt. Trans.* **2021**, *50* (42), 14978–14984. https://doi.org/10.1039/d1dt03019a.

(49) Kitagawa, Y.; Kumagai, M.; Nakanishi, T.; Fushimi, K.; Hasegawa, Y. The Role of π-f Orbital Interactions in Eu(III) Complexes for an Effective Molecular Luminescent Thermometer. *Inorg. Chem.* **2020**, *59* (9), 5865–5871. https://doi.org/10.1021/acs.inorgchem.9b03492.

(50) Yamamoto, M.; Kitagawa, Y.; Nakanishi, T.; Fushimi, K.; Hasegawa, Y. Ligand-Assisted Back Energy Transfer in Luminescent TbIII Complexes for Thermosensing Properties. *Chem. - A Eur. J.* **2018**, *24* (67),

17719–17726. https://doi.org/10.1002/chem.201804392.

(51) Maouche, R.; Belaid, S.; Benmerad, B.; Bouacida, S.; Freslon, S.; Daiguebonne, C.; Suffren, Y.; Calvez, G.; Bernot, K.; Roiland, C.; Le Pollès, L.; Guillou, O. Luminescence Properties of Lanthanide Complexes-Based Molecular Alloys. *Inorganica Chim. Acta* **2020**, *501* (October 2019), 119309. https://doi.org/10.1016/j.ica.2019.119309.

(52) Knighton, R. C.; Soro, L. K.; Lecointre, A.; Pilet, G.; Fateeva, A.; Pontille, L.; Francés-Soriano, L.; Hildebrandt, N.; Charbonnière, L. J. Upconversion in Molecular Hetero-Nonanuclear Lanthanide Complexes in Solution. *Chem. Commun.* **2021**, *57* (1), 53–56. https://doi.org/10.1039/d0cc07337g.

(53) Baril-Robert, F.; Petit, S.; Pilet, G.; Chastanet, G.; Reber, C.; Luneau, D. Site-Selective Lanthanide Doping in a Nonanuclear Yttrium(III) Cluster Revealed by Crystal Structures and Luminescence Spectra. *Inorg. Chem.* **2010**, *49* (23), 10970–10976. https://doi.org/10.1021/ic1011082.

(54) Edgar, A. *Luminescent Materials*; 2007. https://doi.org/10.1007/978-0-387-29185-7_40.

(55) Carneiro Neto, A. N.; Moura, R. T.; Shyichuk, A.; Paterlini, V.; Piccinelli, F.; Bettinelli, M.; Malta, O. L. Theoretical and Experimental Investigation of the Tb3+ → Eu3+ Energy Transfer Mechanisms in Cubic A3Tb0.90Eu0.10(PO4)3 (A = Sr, Ba) Materials. *J. Phys. Chem. C* **2020**, *124* (18), 10105–10116. https://doi.org/10.1021/acs.jpcc.0c00759.

(56) Baur, F.; Glocker, F.; Jüstel, T. Photoluminescence and Energy Transfer Rates and Efficiencies in Eu3+ Activated Tb2Mo3O12. *J. Mater. Chem. C* **2015**, *3* (9), 2054–2064. https://doi.org/10.1039/c4tc02588a.

(57) Lin, L.; Li, Z.; Wang, Z.; Feng, Z.; Huang, F.; Dai, Q.; Zheng, Z. Hypersensitive and Color-Tunable Temperature Sensing Properties of (Eu,Tb)(AcAc)3phen via Phonon-Assisted Energy Transfer. *Opt. Mater. (Amst).* **2020**, *110* (August), 110532. https://doi.org/10.1016/j.optmat.2020.110532.

(58) Carneiro Neto, A. N.; Mamontova, E.; Botas, A. M. P.; Brites, C. D. S.; Ferreira, R. A. S.; Rouquette, J.; Guari, Y.; Larionova, J.; Long, J.; Carlos, L. D. Rationalizing the Thermal Response of Dual-Center Molecular Thermometers: The Example of an Eu/Tb Coordination Complex. *Adv. Opt. Mater.* **2022**, *10* (5), 1–12. https://doi.org/10.1002/adom.202101870.

(59) Hasegawa, Y.; Kitagawa, Y. Thermo-Sensitive Luminescence of Lanthanide Complexes, Clusters, Coordination Polymers and Metal–Organic Frameworks with Organic Photosensitizers. *J. Mater. Chem. C* **2019**, *7*, 7494–7511. https://doi.org/10.1039/c9tc00607a.

(60) Gontcharenko, V. E.; Kiskin, M. A.; Dolzhenko, V. D.; Korshunov, V. M.; Taydakov, I. V; Belousov, Y. A. Mono- and Mixed Metal Complexes of Eu3+, Gd3+, and Tb3+ with a Diketone, Bearing Pyrazole Moiety and CHF2-Group: Structure, Color Tuning, and Kinetics of Energy Transfer between Lanthanide Ions. *Molecules* **2021**, *26* (2655), 1–15.

(61) Blais, C.; Daiguebonne, C.; Suffren, Y.; Bernot, K.; Calvez, G.; Le Pollès, L.; Roiland, C.; Freslon, S.; Guillou, O. Investigation of Intermetallic Energy Transfers in Lanthanide Coordination Polymers Molecular Alloys: Case Study of Trimesate-Based Compounds. *Inorg. Chem.* **2022**, *61* (30), 11897–11915. https://doi.org/10.1021/acs.inorgchem.2c01650.

(62) Dudar, S. S.; Sveshnikova, E. B.; Shablya, A. V; Ermolaev, V. L. Nonradiative Energy Transfer as a Method for Investigation of Self-Assembling Nanostructures of Lanthanide Complexes in Solutions. *High energy Chem.* **2007**, *41* (3), 189–197. https://doi.org/10.1134/S0018143907030034.

(63) Rigaku Oxford Diffraction. AutoChem 4.0 Software System in Conjunction with Olex2 1.3. *Rigaku Corporation, Wroclaw, Poland*. 2022.

(64) Sheldrick, G. M. SHELXT - Integrated Space-Group and Crystal-Structure Determination. *Acta Crystallogr. Sect. A Found. Crystallogr.* **2015**, *71* (1), 3–8. https://doi.org/10.1107/S2053273314026370.

(65) Sheldrick, G. M. Crystal Structure Refinement with SHELXL. *Acta Crystallogr. Sect. C Struct. Chem.* **2015**, *71* (Md), 3–8. https://doi.org/10.1107/S2053229614024218.

(66) Dolomanov, O. V.; Bourhis, L. J.; Gildea, R. J.; Howard, J. A. K.; Puschmann, H. OLEX2: A Complete Structure Solution, Refinement and Analysis Program. *J. Appl. Crystallogr.* **2009**, *42* (2), 339–341. https://doi.org/10.1107/S0021889808042726.

(67) Bukvetskii, B. V.; Mirochnik, A. G.; Shishov, A. S. Triboluminescence and Crystal Structure of

Centrosymmetric Complex Tb(AcAc)3Phen. *J. Lumin.* **2018**, *195* (October 2017), 44–48. https://doi.org/10.1016/j.jlumin.2017.10.074.

(68) Watson, W. H.; Williams, R. J.; Stemple, N. R. The Crystal Structure of Tris(Acetylacetonato)(1,10-Phenanthroline) Europium(III). *J. Inorg. Nucl. Chem.* **1972**, *34* (2), 501–508. https://doi.org/10.1016/0022-1902(72)80428-7.

(69) Ogata, S.; Ishii, A.; Lu, C. L.; Kondo, T.; Yajima, N.; Hasegawa, M. Polymorphism-Based Luminescence of Lanthanide Complexes with a Deuterated 1,10-Phenantholine. *J. Photochem. Photobiol. A Chem.* **2017**, *334*, 55–60. https://doi.org/10.1016/j.jphotochem.2016.10.031.

(70) Werner, F.; Tada, K.; Ishii, A.; Hasegawa, M. The Key Role of Accurate Lattice Parameters in Revealing Subtle Structural Differences — a Case Study in the System [Ln (Phen / Phen-d 8) 2 (NO 3) 3] †. *CrystEngComm* **2009**, *2* (3), 1197–1200. https://doi.org/10.1039/b904694c.

(71) Alexander, O. T.; Kroon, R. E.; Brink, A.; Visser, H. G. Symmetry Correlations between Crystallographic and Photoluminescence Study of Ternary β-Diketone Europium(III) Based Complexes Using 1,10-Phenanthroline as the Ancillary Ligand. *Dalt. Trans.* **2019**, 16074–16082. https://doi.org/10.1039/c9dt02580d.

(72) Nehra, K.; Dalal, A.; Hooda, A.; Singh, S.; Singh, D.; Kumar, S.; Singh, R.; Kumar, R.; Kumar, P. Red Luminous Eu (III) Complexes : Preparation , Spectral , Optical and Theoretical Evaluation. *Inorganica Chim. Acta* **2022**, *539* (January), 121007. https://doi.org/10.1016/j.ica.2022.121007.

(73) Yu, Z.; Shen, L.; Li, D.; Yue, E.; Pun, B.; Zhao, X.; Lin, H. Fluctuation of Photon-Releasing with Ligand Coordination in Polyacrylonitrile-Based Electrospun Nanofibers. *Sci. Rep.* **2020**, *10* (926), 1–13. https://doi.org/10.1038/s41598-020-57641-3.

(74) Ilmi, R.; Kansız, S.; Dege, N.; Khan, M. S. Synthesis , Structure , Hirshfeld Surface Analysis and Photophysical Studies of Red Emitting Europium Acetylacetonate Complex Incorporating a Phenanthroline Derivative. *J. Photochem. Photobiol. A Chem.* **2019**, *377* (April), 268–281. https://doi.org/10.1016/j.jphotochem.2019.03.036.

(75) Maouche, R.; Belaid, S.; Benmerad, B.; Daiguebonne, C.; Su, Y.; Bernot, K.; Guillou, O. Highly Luminescent Europium-Based Heteroleptic Coordination Polymers with Phenantroline and Glutarate Ligands. *Inorg. Chem.* **2021**, *60*, 3707–3718. https://doi.org/10.1021/acs.inorgchem.0c03417.

(76) Shurygin, A. V; Vovna, V. I.; Korochentsev, V. V; Mirochnik, A. G.; Kalinovskaya, I. V; Sergienko, V. I. Electronic Structure and Optical Properties of Ln (III) Nitrate Adducts with 1 , 10-Phenanthroline. *Spectrochim. Acta Part A Mol. Biomol. Spectrosc.* **2019**, *213* (3), 176–183. https://doi.org/10.1016/j.saa.2019.01.033.

(77) Mirochnik, A. G.; Bukvetskii, B. V; Zhikhareva, P. A.; Karasev, V. E. Crystal Structure and Luminescence of the [Eu (Phen) 2 (NO 3) 3] Complex . The Role of the Ion-Coactivator. *Russ. J. Coord. Chem.* **2001**, *27* (6), 475–480.

(78) Zahariev, T.; Trendafilova, N.; Georgieva, I. Spectroscopic and Photophysical Properties of [Eu (Phen) 2] X 3 3) Complexes , Incorporated into SiO 2 -Based Matrices : Theoretical Study. *Mater. Today Proc.* **2022**, *61*, 1292–1299. https://doi.org/10.1016/j.matpr.2022.05.054.

Chapter 3:

Photoluminescent Lanthanide inorganic nanoparticles as temperature sensor

The work presented in this chapter has been published in the following papers:

A. Zhou, Y.; Ledoux, G.; Bois, L.; Descartes, S.; Bouscharain, N.; Chassagneux, F.; Martini, M.; Midiladji Bakary, Y.; Journet, C.; Philippon, D. Er3+ Doped Nanoparticles as Upconversion Thermometer Probe in Confined Fluids. *Phys. Chem. Chem. Phys.* **2023**. https://doi.org/10.1039/D3CP02218H.

B. Zhou, Y.; Ledoux, G.; Philippon, D.; Descartes, S.; Martini, M.; He, S.; Desroches, C.; Fournier, D.; Journet, C.; Bois, L. Laser-Induced Heating in GdVO 4 : Yb 3 + / Er 3 + Nanocrystals for Thermometry. *ACS Appl. Nano Mater.* **2022**, *5*, 16388–16401. https://doi.org/10.1021/acsanm.2c03466.

3 Photoluminescent Lanthanide inorganic nanoparticles as temperature sensor

3.1 Introduction

The luminescent intensity ratio (LIR) is well known as a self-referencing measurement method. Er^{3+} has thermally coupled energy levels ($^2H_{11/2}$ and $^4S_{3/2}$) that are suitable for temperature *measurement in* the 293-473 K range, with high sensitivity. The relatively small gap between the energy levels (around 600-800 cm^{-1}) allows excited electrons to be thermally promoted to the higher level. The proportion of thermally promoted electrons follows the Boltzmann distribution, making it possible to calibrate the temperature by measuring the ratio of the emission intensity of its two thermally coupled energy levels.

The structural analysis of $GdVO_4$: Yb^{3+}/Er^{3+} nanoparticles (NPs) in the previous chapter shows the preliminary conditions to apply the $GdVO_4$: Yb^{3+}/Er^{3+} NPs as a thermo-sensor in tribological measurements. When the NPs are dispersed in the matrix, the dispersion is homogeneous and monodispersed. The dispersed sizes are suitable for tribological measurement with appropriate spatial resolutions. Furthermore, the original rheological properties of the fluid are not affected by the dispersed NPs at the concentration studied. The above results confirm that $GdVO_4$: Yb^{3+}/Er^{3+} NPs could be a satisfactory thermo-sensor.

This chapter first addresses the photoluminescent properties of $GdVO_4$: Yb^{3+}/Er^{3+} NPs, in powder form. Under excitation via the upconversion (UC) process, spatial resolution and measurement accuracy are optimized, because NIR light provides more penetration than visible light, and the matrices can emit light under visible light excitation. However, the laser-induced heating effect is well known in the UC process with continuous-wave NIR laser. We therefore focus on the adverse thermal effects of lasers on Er^{3+} ratiometric thermometry at down and upconversion luminescence, under visible and NIR excitation, respectively. The laser heating phenomenon in UC doped Er^{3+} nanoparticles is first analyzed at different temperatures and then calibrated as a function of the laser power density. We propose a method to calculate the temperature difference induced by the thermal effect of the laser, which can be used to compensate the difference caused by laser heating using UC Er^{3+} doped NPs.

Secondly, the applicability of the UC thermometer, Er^{3+} doped NPs are studied in different matrices. We focus on the effects of laser heating on UCNPs dispersed in a medium, fluid or solid, to evaluate how heat dissipation influences temperature calibration measurements. The thermal effect of laser on $GdVO_4$: Yb^{3+}/Er^{3+} NPs powder was studied with 488 nm and 970 nm excitation at different laser intensities and temperatures up to 300°C. $GdVO_4$: Yb^{3+}/Er^{3+} NPs are also dispersed in fluid and solid media at two NP concentrations. The experiments are performed in the non-saturation regime of the NIR laser in order to maintain the 2-photon ETU condition.

Last, thermometry of the NPs suspension is performed under high pressure (up to 1 GPa). Very high pressure (up to 25 GPa) can cause variations in Er^{3+}- doped materials due to structural change such as shortening of interionic distances, shifting energy levels. $GdVO_4$ is

known to exhibit a phase transition from a zircon-like to a scheelite-like structure at 6.8 GPa, this nanosensor should be used exclusively in a pressure range below 6 GPa.[1] Up to 6 GPa, the pressure sensitivity of some fluorides doped with Er^{3+} has been reported: variations in lifetime, emission intensity and peak centroid. Nonetheless, pressure sensitivity up to 1 GPa has not yet been reported by Ln-doped nanoparticles. The photoluminescent thermometry of the dispersed $GdVO_4$: Yb^{3+}/Er^{3+} nano-sensor is characterized up to 423K. The effect of pressure on the dispersed suspension of the $GdVO_4$: Yb^{3+}/Er^{3+} nano-sensor is studied in a diamond anvil cell (DAC) at pressures up to 1 GPa and at different temperatures.

3.2 Technologies and methods

3.2.1 Photoluminescent characterizations

For the optical characterizations, the absorption spectrum of the NPs powder was acquired by LAMBDA 365 UV/Vis (Perkin Elmer) Spectrophotometer from 350 to 1100 nm, in an integrating sphere. The emission spectra were obtained by a modular spectrofluorometer, upon excitation of a continuous-wave NIR laser (970 nm, MDL-2W) focused on the sample to a spot size of 4 mm^2. The spectrometer is equipped with a detector (CCD, Short Focal Length Triple Grating Imaging Spectrographs, TRIAX 320 HORIBA) and an optical fiber. At ambient pressure, the NPs powder was deposed on a silicon slice for better thermal transfer, the fluid (Nycobase 5750) was poured into a sapphire bowl closed with a glass lid for the emission acquisition. Data were collected after 10 s of temperature and laser stabilization, from 293 to 573 K (each 5 K) for the powder and from 298 to 423 K (each 5 K) for the fluid. The temperature was controlled by a thermo-cell (LINKAM Optical DSC600 cell). The experimental set-up is shown in Scheme 3.1.

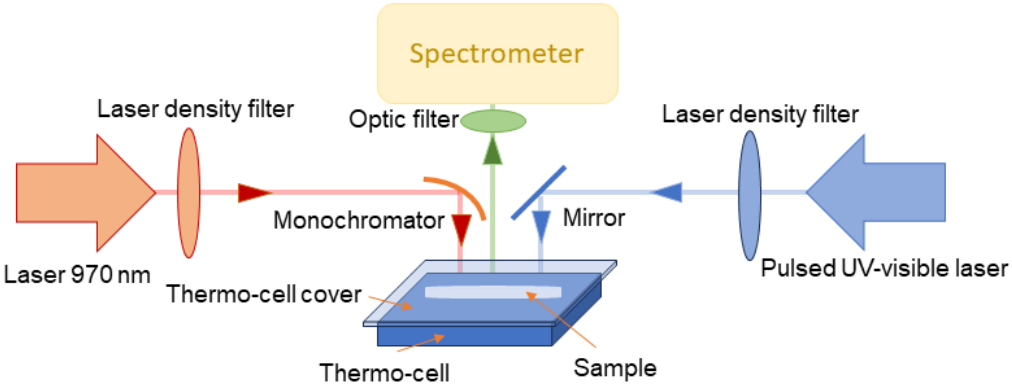

Scheme 3.1: Experimental set-up for photoluminescent temperature calibration (Pulsed UV-visible laser at 488 nm in this part).

3.2.2 High-pressure measurements

Temperature calibrations under pressure were carried out using a high-pressure diamond anvil cell (DAC), as shown in Figure 3.1, with a working hydrostatic pressure range up to 1.3

GPa in Nycobase. According to the method described in a previous work,[2] the DAC (MDAC type BHP for Biology 100° symmetrical aperture, Betsa) consists of a 1.4 mm culet diamond anvil and a 0.4 mm thick diamond window, with a nickel gasket between them. The nickel gasket thickness was about 0.2 mm and comprises a hole of 0.5 mm in diameter. The pressure inside the DAC was increased and maintained in the cell by inflating an internal membrane with helium. A heating ring (External Heating System, Betsa) was placed around the DAC for temperature regulation. A thermocouple inserted next to the metal seal in the DAC was used to measure the temperature of the sample with a precision of ± 1 K.

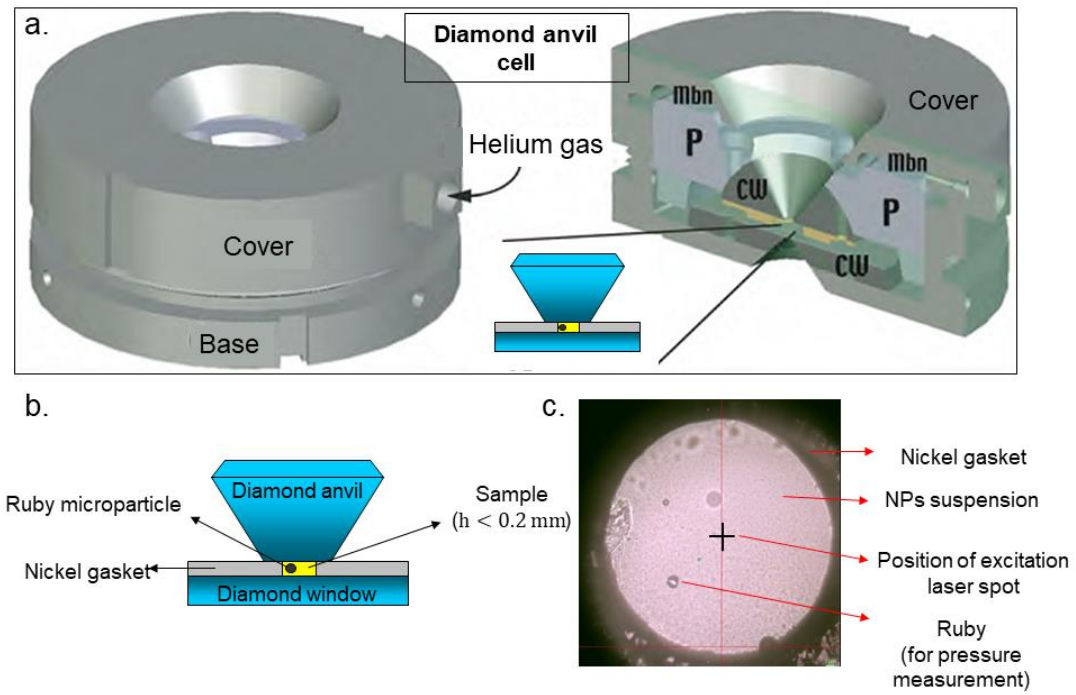

Figure 3.1: a) Full and cross-section view of the DAC. b) Scheme of the DAC. c) Optical image of the sample during the under-pressure experiment.

During the experiments, a small amount of suspended sample (< 1µL) was introduced into the hole in the seal. The hydrostatic pressure inside the DAC was determined by introducing ruby microparticles (> 3µm) as a pressure sensor for calibration using their photoluminescent wavelength shift of the R1 line. These ruby microparticles were excited by a continuous 460 nm laser (Scheme 3.2). The wavelength position of the emission spectrum was referenced with an Argon lamp (Avalight-CAL-Mini,) with the peak at 696.54 nm. The calibration of the hydrostatic pressure was based on previous literature.[3,4] Based on previous work,[2] the pressure uncertainty can be considered to be of the order of 30-50 MPa.

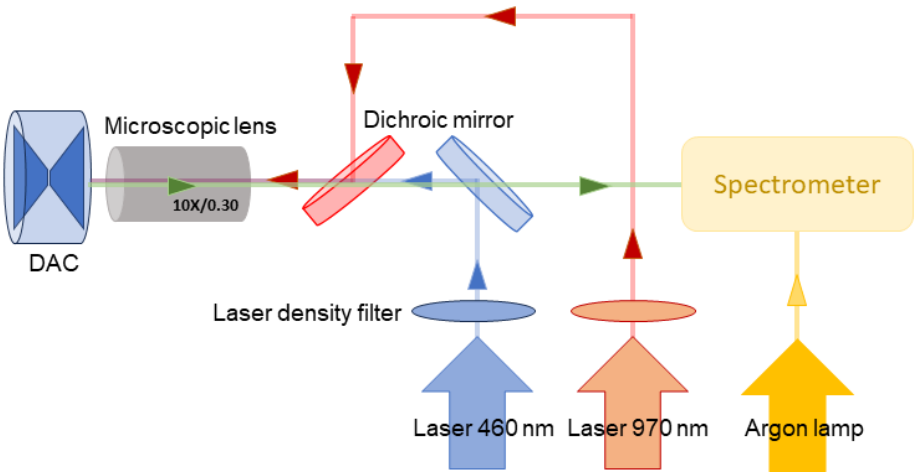

Scheme 3.2: Experimental set-up of DAC-coupled to the spectrometer

3.2.3 Data processing

The thermometry of Er^{3+} doped materials has been analyzed by LIR theory. The population ratio on two thermally coupled energy levels (N_{L2} and N_{L1}) varies with temperature according to Equation 3.1. As the population of the energy level (N) is directly proportional to the emitted intensities (I), the LIR also follows the Boltzmann distribution.

$$LIR = \frac{N_{L2}}{NL_1} = \frac{I_{L2}}{I_{L1}} = \frac{g_2\sigma_2\omega_2}{g_1\sigma_1\omega_1} exp(-\frac{(E_2 - E_1)}{k_B T}) = B\, exp(-\frac{\Delta E}{k_B T})$$

Equation 3. 1

In the Boltzmann Equation 3.1, N_i denotes the population of excited ions, and I_i is the emitted intensity for a given level *i*. The pre-exponential constant B includes the g_i , σ_i , ω_i, which are the degeneracy, the emission cross section, and the angular frequency of transitions for a given level *i*, respectively. ΔE is the energy gap between the two thermally coupled energy levels, k is the Boltzmann constant, and T is the absolute temperature.[5] ΔE can be determined by the calibration curve of Ln(LIR) versus 1/T. Compared to the theoretical value, this experimental value can be used to check the accuracy of the temperature value.

The emission band areas of the peaks were integrated by using Simpson ‘s rule to calculate the average of the total emitted intensities for each transition.[6] The Er^{3+} emission spectra was collected and then analyzed by MATLAB software. The integrated area ranges were 540 - 567 nm (L_1: $^4S_{3/2}$ to $^4I_{15/2}$) and 512 - 540 nm (L_2: $^2H_{11/2}$ to $^4I_{15/2}$) as Figure 3.2 shows.

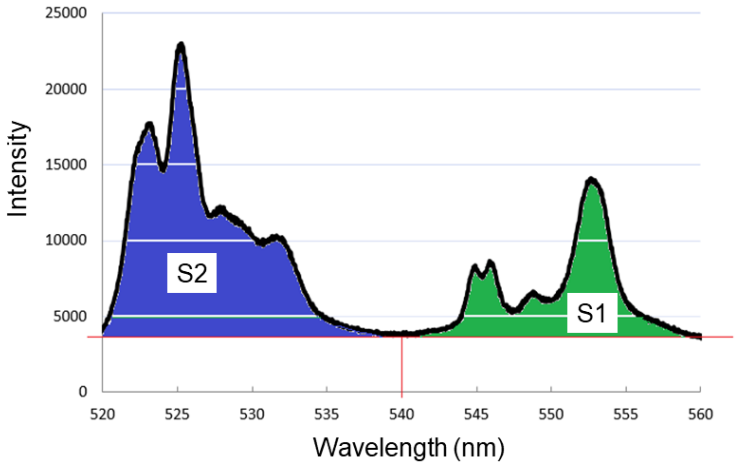

Figure 3.2: Peak surface integration: S2 (blue: 520 to 540 nm), S1(green: 540 to 560 nm).

The LIRs of the Er^{3+} peaks (L_1 and L_2) were processed with Excel software for plotting and data analysis. The intrinsic experimental uncertainty on the emission intensity (δI/I) is detector dependent and is mainly determined by the value of the signal-to-noise ratio (SNR). The SNR of the CCD detector used in our measurement is stated by the manufacturer as 0.05% at best. However, the detector operates with more uncertainty and, therefore, the δI/I values are always higher than the indicated intrinsic SNR. The SNR is estimated experimentally for each spectrum by dividing the baseline spectral fluctuation by the peak intensity (N_{L2} and N_{L1}). The experimental uncertainty is then determined by Equation 3.2.

$$\frac{\delta(LIR)}{LIR} = \sqrt{(\frac{\delta I_1}{I_1})^2 + (\frac{\delta I_2}{I_2})^2}$$

Equation 3. 2

In addition, the relative thermal sensitivity S_R, defined by Equation 3.3, is also an important indicator of the measurement reliability.[7]

$$S_R = \frac{1}{LIR} \times \frac{d(LIR)}{dT} = \frac{\Delta E}{k_B T^2}$$

Equation 3. 3

3.3 $GdVO_4$: Er^{3+}/Yb^{3+} nanoparticles powder as a thermometric sensor

3.3.1 Thermometry based on the Boltzmann distribution

1) Photoluminescent properties

In Figure 3.3a, the blue line shows the absorption spectrum of $GdVO_4$: Yb^{3+}/Er^{3+} NPs in the wavelength range of 350–1100 nm. $GdVO_4$: Yb^{3+}/Er^{3+} NPs absorb NIR light (985 nm) and some visible light. The green lines represent the emission spectra of $GdVO_4$: Yb^{3+}/Er^{3+} (solid line: under a 970 nm laser at 2.5 W/cm², dashed line: under a 488 nm laser at 50 mW/cm²). Both spectra show strong bands in the green region, and some weak bands in the red emission

region.[8–10] Comparing these emission spectra, the main Er^{3+} transitions appear under both excitations (970 nm or 488 nm): 525, 555 and 665 nm corresponding to $^2H_{11/2}$, $^4S_{3/2}$ and $^4F_{9/2}$ to the ground state respectively. The additional Er^{3+} transition ($^2H_{9/2} \rightarrow {}^4I_{13/2}$, emission at 535 - 570 nm, Figure 1.15) has been observed under continuous-wave laser excitation intensities above 10 W/cm² in recent works.[11–13] This emission peak can lead to temperature calibration errors as it overlaps with the green luminescence used for thermometry ($^4S_{3/2} \rightarrow {}^4I_{15/2}$). Therefore, it has been carefully checked and it has not been observed in our work.

As shown in Figure 3.3b, these two excitation mechanisms are different. Under the excitation by a 488 nm laser, Er^{3+} electrons are promoted to the $^4F_{7/2}$ state, and then decay into the emitting states by non-radiative relaxation, called down-shifting (DS). Conversely, by exciting at 970 nm, Er^{3+} can be excited by two-sequentially absorbed photons (Ground-state absorption (GSA) and excited-state absorption (ESA), respectively shown in the black arrow)[14] to the $^4F_{7/2}$ excited state and generates the same emissions,[15–18] this process was afterward confirmed in our experiments. However, since the absorption effective cross section of Yb^{3+} in the NIR region ($^2F_{7/2}$ to $^2F_{5/2}$) is much larger than that of Er^{3+} ($^2I_{15/2}$ to $^4I_{11/2}$), the energy transfer between Yb^{3+} and Er^{3+} (the ETU process) will be the most important process.[19] It can also be noted that the existence of other cross-relaxations and of some back energy transfer (BET) from erbium to ytterbium (Figure 3.3b).[17,20–22] In both excitation processes, the non-radiative relaxations are larger in the UC process than in the DS process, *i.e.* the quantum yield is lower.

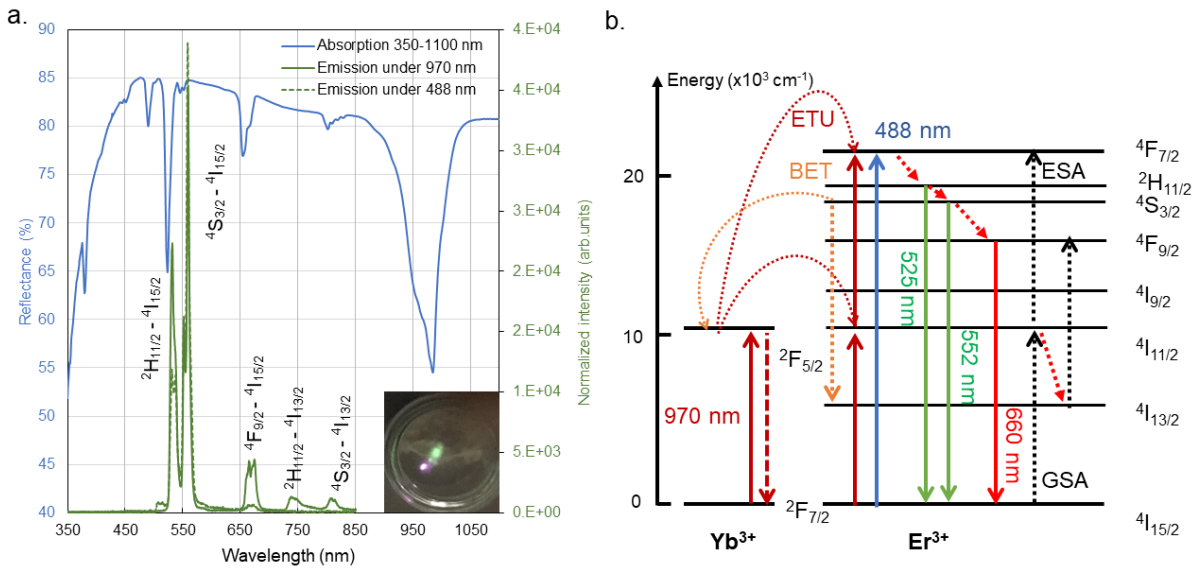

Figure 3.3: a) Absorption & emission spectra of the $GdVO_4:Yb^{3+}/Er^{3+}$ powder sample. Inset: Photograph of the $GdVO_4:Yb^{3+}/Er^{3+}$ powder sample with a 980 nm handheld laser pen. b) The UC process between Er^{3+} & Yb^{3+} under NIR excitation and the DS process under direct excitation at 488 nm.

1) Luminescent-intensity-ratio based thermometry

The temperature was calibrated up to 573 K with the NPs powder under NIR laser at 2.5 W/cm². As shown in Figure 3.4a, the population of the $^2H_{11/2}$ state increases while the $^4S_{3/2}$ state decreases with increasing temperature according to the Boltzmann distribution,[10,23] the intensity of the peak centered at 530 nm increases while the peak centered at 550 nm decreases with temperature. The ratiometric thermometry following the Boltzmann distribution was proven by the temperature calibration, the LIR values varying with temperature (Figure 3.4b). According to the Boltzmann equation (Equation 3.1), Ln (LIR) is linearly proportional to 1/T up to 573 K, and more importantly, this variation is reversible. The slopes calculated by the fitted trendline of the calibration curves are used to estimate the energy gap (ΔE) in Equation 3.1, as shown in Table 3.1.

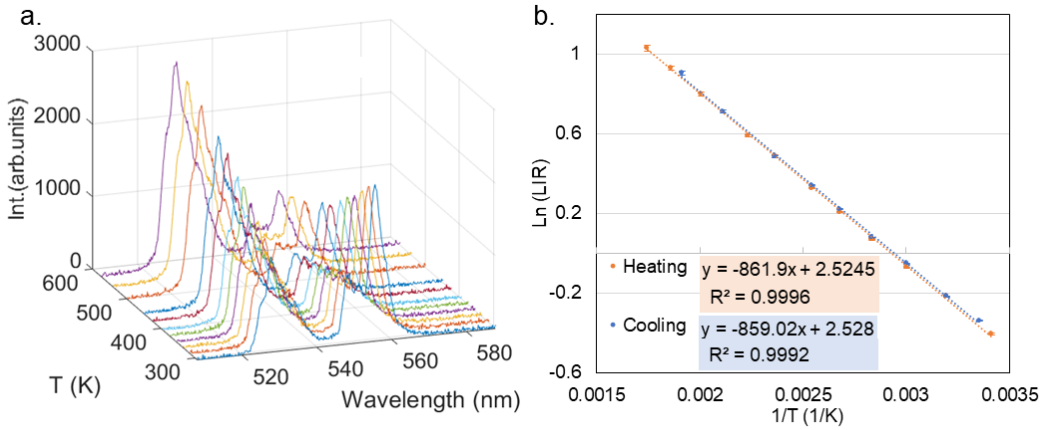

Figure 3.4: $GdVO_4:Yb^{3+}/Er^{3+}$ powder upon NIR laser at 2.5 W/cm²: a) Emission spectra at 293 – 573 K. b) Temperature calibration curve and fitted trendline equations, error bars determined by uncertainty (Equation 3.2).

2) Impact of excitation source in thermometry

Assuming that laser-induced heating can impact the temperature measurement, the influence of excitation source on the thermometry has been studied. In this section, the excitations via UC and DS process are used, various laser intensities are also studied. When excited by an unfocused 488 nm laser, two laser power densities are used: approximately at 50 mW/cm² as the maximum density and at 5 mW/cm² as the reduced density. For excitation by a 970 nm laser, eight different laser power densities are applied, ranging from 0.3 W/cm² to 15.8 W/cm². Under NIR excitation, the luminescent signals at 0.3 W/cm² are too weak to be analyzed, so the temperature calibration was started at 1.3 W/cm². Under these conditions, we avoid saturation of the intermediate upconversion levels, and the thermometry will only work in a unsaturated excitation regime.[24]

Figure 3.5 shows the emission spectra at 20°C via DS (Figure 3.5a) and UC (Figure 3.5b). The emission intensity increases with the laser power density, which is related to the increase in the electron population in the excited state of Er^{3+}. There is no emergence of a new peak at high laser power density; in particular, the $^2H_{9/2} \rightarrow {}^4I_{13/2}$ intruding emission from Er^{3+} was absent in the studied laser power density range. This phenomenon was considered as an

important interference for the calculation of LIR.[12,13,25] In addition, it should be noted that the resolution is different between the two excitation conditions due to the different detector configuration, and the different range of laser intensities.

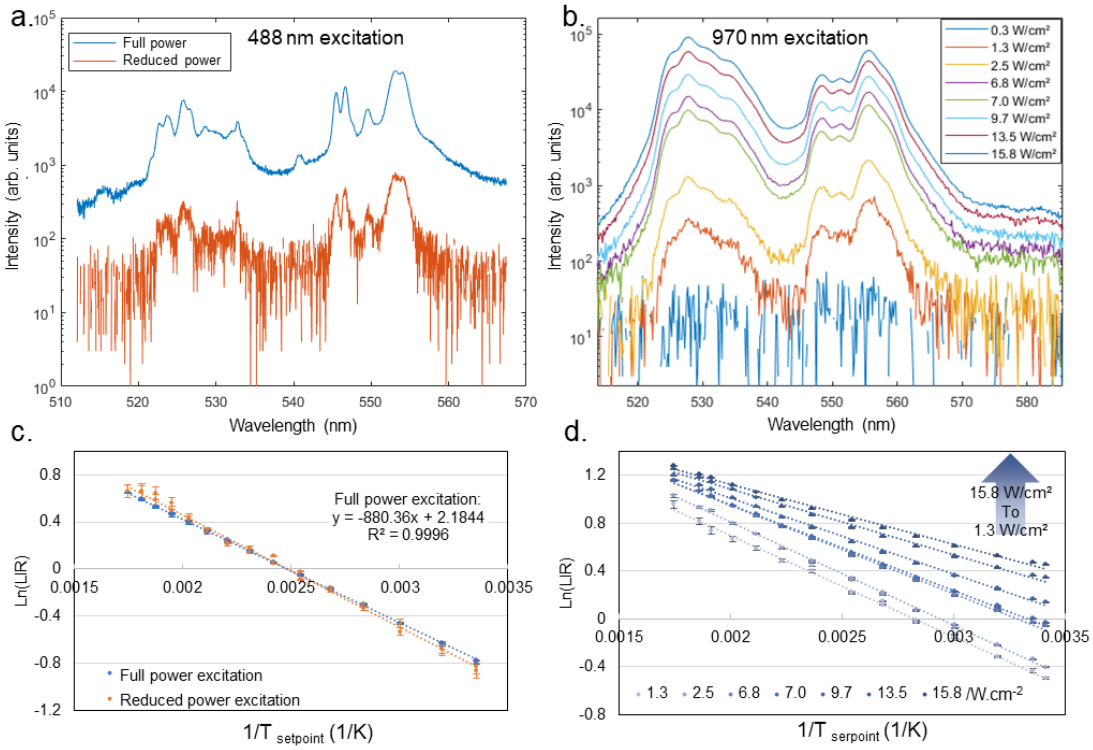

Figure 3.5: a) Emission spectra of the $GdVO_4$: Yb^{3+}/Er^{3+} powder sample under excitation at 488 nm at full laser power density and at reduced laser power density. b) Emission spectra of the $GdVO_4$: Yb^{3+}/Er^{3+} powder sample under excitation at 970 nm at 8 different laser intensities (0.3–15.8 W/cm²). c) Temperature calibration under excitation at 488 nm at two laser intensities. d) Temperature calibration under excitation at 970 nm at different laser intensities.

In Figures 3.5c and 3.5d, Ln(LIR) is plotted as a function of the setpoint temperature (named $T_{setpoint}$), each calibration curve is linear and reversible in the temperature range studied (20 – 300°C). It is observed that the calibration curves overlap in the DS system (Figure 3.5c), while the intrinsic uncertainty of the curve at reduced laser intensity was relatively large. It's important to note that the reliability of the temperature calibration may depend on the uncertainty, calibration at full laser power excitation should be more reliable. On the other hand, the temperature calibration curves for the UC process change with laser intensity, and the uncertainty decreases when laser intensity increases. (Figure 3.5d).

The laser power density influences the ratiometric thermometry in the UC system but not in the DS system. The slope of the calibration curves can be used to calculate the inferred energy difference (ΔE_{LIR}) using the Boltzmann equation (Equation 3.1), and the ΔE_{LIR} is considered as an indicator of the reliability of the temperature measurement.[7] If no laser effect occurs, the value of ΔE should remain constant. In Table 3.1, the ΔE_{LIR} calculated by the

slope of temperature calibration curves via DS excitation indeed remains constant when the laser power density changes, whereas the ΔE_{LIR} of the UC system decreases as the laser power density increases. The ΔE_{LIR} values and the pre-exponential constant B were plotted as a function of the laser intensity in Figure 3.6a. Since laser power density does not influence either the ratiometric thermometry or the pre-exponential constant, for further comparison, the ΔE_{LIR} and B, calculated by DS at 50 mW/cm², were set to 0 W/cm² (Figure 3.6a). Note that the ΔE_{LIR} for low NIR laser intensities is similar to the ΔE_{LIR} of the DS system. For high NIR laser intensities, it decreases when the laser power density increases. The B value decreases as the laser density increases and it is explained by the fact that non-radiative process increases.[14] The relative sensitivities were calculated by using Equation 3.3, and it decreases with increasing laser intensity (Figure 3.6b). It is assumed that this decrease is actually caused by an increase in temperature.[19]

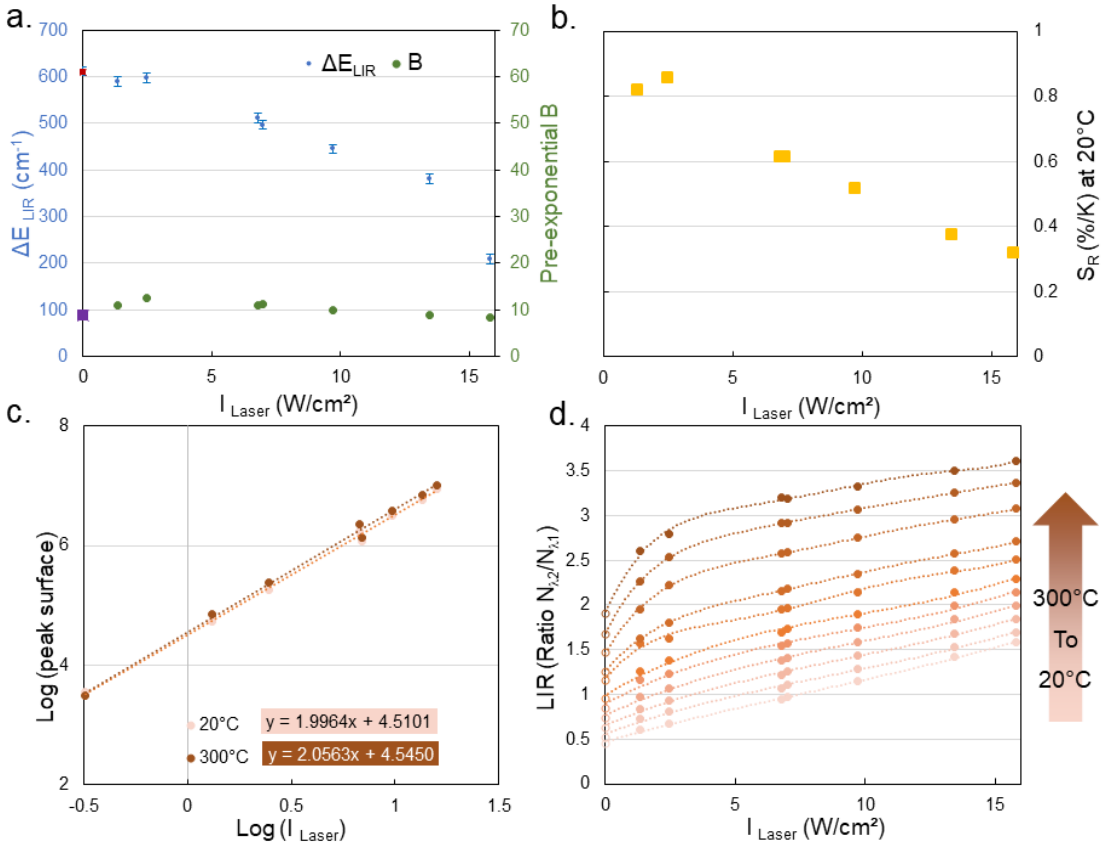

Figure 3.6: a) Energy gap ΔE_{LIR} (blue marks) and pre-exponential constant B (green marks) calculated from the calibration curves for each laser power density (DS series in square marks (red and purple, respectively) at 0 W/cm² for comparison). b) Relative sensitivity S_R at 20°C (setpoint temperature) for each laser intensity. c) Relationship between the sum of $\lambda_1+\lambda_2$ surface peaks and the laser intensity at 20°C and 300°C. d) LIR at different laser intensities from 20°C to 300 °C under NIR laser, in comparison with the DS process (50 mW/cm² of 488 nm laser excitation) shown by the hollow dots.

Table 3.1. Calculated energy gaps ΔE_{LIR} from calibration curve

Excitation[§]	**488 nm**		**970 nm**												
I_{Laser} (W/cm²)	50.10^{-3}	5.10^{-3}	1.3	2.5	6.8	7.0	9.7	13.5	15.8	9.7	13.5	15.8	9.7	13.5	15.8
Media	Powder									0.5 wt.% in suspension			5 wt.% in glass		
Slope[¤]	-880	-955	-848	-859	-737	-715	-641	-549	-301	-894	-924	-890	-771	-767	-789
B	9	11	11	12	11	11	10	9	8	11	12	11	7	7	8
ΔE_{LIR} (cm^{-1})	612	663	589	597	512	497	445	382	209	622	642	618	536	533	548
Uncertainty (%)	2.7	16.1	6.1	1.9	0.5	0.4	0.3	0.3	0.3	30.3	20.0	19.2	35.4	14.8	10.4

[§]Excitation under 488 nm pulsed laser, or under 970 nm continuous laser.

[¤]Slopes of the calibration curves, ΔE (energy gap determined by linear regression in Figures 3.3c, 3.3d, 3.7a and 3.7b) and B (pre-exponential constant calculated by the curves) for each temperature calibration curve (Equation 3.1).

3) Laser-induced heating in UC process

In two photons systems, the excited population increases quadratically with the laser power density. The sum of peak surface S1 (peak N1: 540 to 560 nm) and S2 (peak N2: 520 to 540 nm) is integrated (Figure 3.2) and plotted as a function of the laser intensity (Figure 3.6c). The slopes are around 2 at extreme temperatures (20°C and 300°C). Such behavior is a crucial indication that the excitation system is always a 2-photons system in the studied temperature range. Since the doped concentration of Er^{3+} is relatively low (2 mol%), the ETU process from Yb^{3+} to Er^{3+} should be the most important mechanism under our conditions. Furthermore, no new transition has been observed in the emission spectra and the calibration curve is always linear up to the maximum laser power density studied, the non-saturation regime of the excitation was also verified. Thus, the LIR value can only be affected by the temperature variation.

The chart of LIR versus laser intensity at different temperatures (Figure 3.6d), shows that the LIR values change not only with the temperature but also with the laser intensity. The series of total laser power density per DS excitation are represented by the hollow markers at 0 W/cm² in the chart. The laser intensity does not change the temperature calibration in DS system (Figure 3.5c), *i.e.*, in the case of temperature calibration at 488 nm, regardless of the laser power density, the equation of the curve corresponds to the Boltzmann distribution (Equation 3.1). On the other hand, the LIR value under UC excitation increases with the laser intensity for a given temperature. As the LIR value is directly proportional to the temperature, it can be assumed that the temperature increases with the laser intensity; the NIR laser heats the sample during the temperature calibration measurements. It should be also noted that the induced heating phenomena highly depends on the sensitizer content used.[17,26–28]

3.3.2 Self-calibration/correction of laser heating by thermometry

As shown previously in Figure 3.5c, the laser heating is negligible in the DS system, the temperature calibration under 488 nm laser at 50 mW/cm² can therefore be considered as a correct distribution corresponding to Boltzmann's law (Equation 3.1). Therefore Equation 3.1 can be linearized under the form of Equation 3.4 using the logarithm function. Thus, the constants of Equation 3.4 are determined using a linear regression on the curve (Figure 3.5c), and this equation is used in the following as a reference.

$$Ln(LIR) = 2.1844 + \frac{(-880.36)}{T_{LIR}}$$

Equation 3. 4

Equation 3.4 is then used to estimate the temperature of the sample measured by LIR values (named T_{LIR}) for various laser intensities and temperature setpoints for UC system. Considering that only laser heating occurs in the previous experiments, it is therefore possible to calculate the temperature change due to the contribution of the laser heating (named δT) and set by the temperature controller as follows:

$$\delta T = T_{LIR} - T_{setpoint}$$

Equation 3. 5

These values were, as expected, positive because the measured temperatures (T_{LIR}) were higher than the setpoint temperatures ($T_{setpoint}$) during the calibration. δT is plotted as a function of $T_{setpoint}$ for different laser intensities (I_{laser}) in Figure 3.7a for all LIR data collected during the temperature calibration under NIR excitation. It varies with I_{laser} and $T_{setpoint}$. $T_{setpoint}$ interferes slightly with δT and this influence becomes more important as $T_{setpoint}$ increases. The low laser intensity series (1.3 W/cm² with hollow points) shows more fluctuations than the others because of its relatively important uncertainty, so they were not taken in calculation of laser heating correction. The curves of δT versus I_{laser} for each $T_{setpoint}$ (20 - 300°C) are plotted in Figure 3.7b. It can be observed that δT is linearly proportional to I_{laser} when $T_{setpoint}$ is below 150°C. For a $T_{setpoint}$ above 150°C, linearity is only respected when the laser intensity is higher than 5 W/cm². All slopes of curves are almost equal, however the intercepts increase with $T_{setpoint}$.

Assuming that the δT is totally caused by laser-induced heating, the relation between δT and $T_{setpoint}$ is consistent with the literature:[29] the thermal effect of laser becomes more important with increasing temperature, which has been explained by the fact that the relaxation rate of the multiphonon increases with temperature, and thus the thermal effect of the laser becomes more important at high temperature. Furthermore, the linearity of δT as a function of I_{laser} is also consistent with Sun's *et al.* results which show linearity between the laser induced heating and the laser power density used at room temperature.[17] The direct proportion between the δT and the $I_{laser\ heating}$ respects the fact that in the non-linear optics, the laser-induced heat increases as the laser intensity increases.

The above information shows that the laser-induced heating temperature is affected by the laser intensity. In order to correct the laser-induced heating temperature in thermometric calibration, all the data collected from 20°C to 300°C for the laser intensity of 2.5-15.8 W/cm^2

were fitted by a polynomial regression model with multiple predictors (here I_{laser} and T_{LIR}) and cross terms (here $I_{laser}.T_{LIR}$) according to the following equation:

$$T_{corrected} = C1 + C2 * I_{laser} + C3 * T_{LIR} + C4 * I_{laser}^2 + C5 * T_{LIR}^2 + C6 * I_{laser} * T_{LIR}$$

Equation 3. 6

where $T_{corrected}$ is the corrected temperature at a given laser intensity and for a given measured temperature (T_{LIR} from LIR Equation 3.4). $T_{corrected}$ were plotted according to the Equation 3.6 (with constant values (C1-C5) gathered in Table 3.2) in Figure 3.7c. Figure 3.7c shows that the corrected temperatures values (line) are in good agreement with the setpoint temperature (symbols), with less than 5% of error. This observation confirms that the proposed model is well adapted for the correction of the laser heating temperature. This result is corroborated by Figure 3.7d where $T_{corrected}$ is drawn as a function of $T_{setpoint}$ and where all the data collapses on the line. It's important to note that this calibration equation (Equation 3.6) could be applied for any correction of laser-induced heating, but the constant values could vary slightly depending on the experimental conditions, such as the optical performance of the thermo-sensor or the dispersed media, which will be further discussed in section 3.4.1.

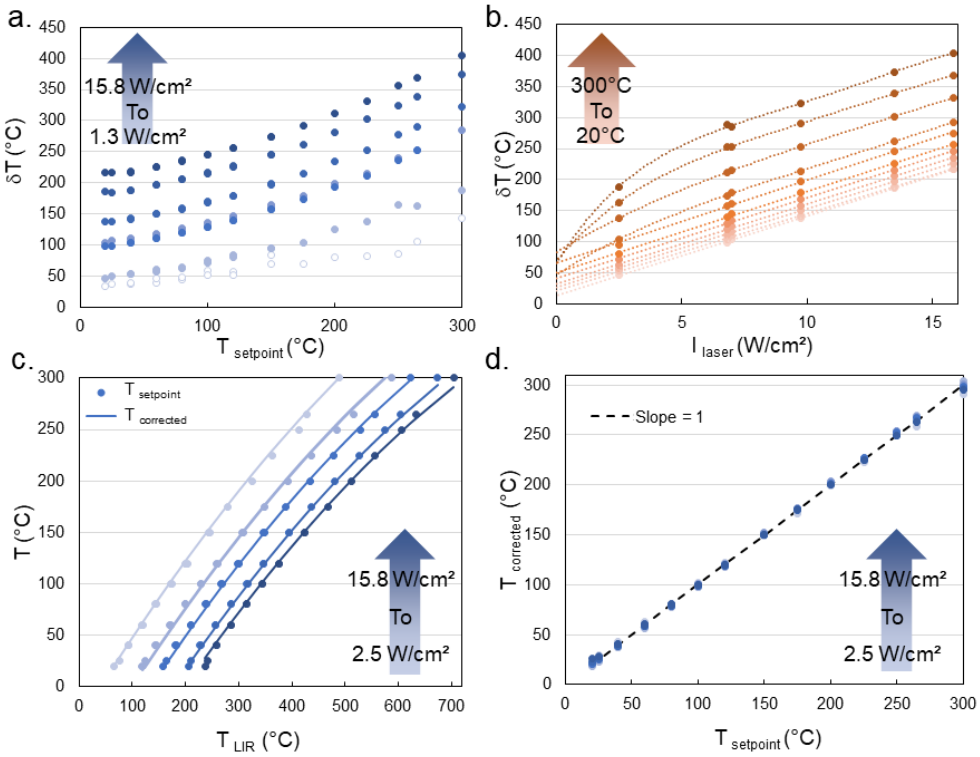

Figure 3.7: a) Estimated temperature induced by laser heating at different laser intensities (1.3 – 15.8 W/cm²) for regulated temperature from 20°C to 300 °C. b) Effect of temperature on the estimated temperature of laser heating at different laser intensities. c) Corrected temperature ($T_{corrected}$) (line) at different estimated temperature (T_{LIR}) compared with setpoint temperature (point). d) Application of correction module for laser heating temperature.

Table 3.2: Constant value in equation of laser-induced heating correction

$T_{corrected} = C1 + C2 * I_{laser} + C3 * T_{LIR} + C4 * I_{laser}^2 + C5 * T_{LIR}^2 + C6 * I_{laser} * T_{LIR}$						
	C1	C2	C3	C4	C5	C6
Free powder	-2.8348	-11.0246	0.7946	0.0572	-0.0003	0.0047
50 wt.% in PDMS	10.5742	-12.8556	0.7364	0.2888	0.0002	-0.0251

Previous observations show a great interest in the thermometry application of $GdVO_4$: Yb^{3+}/Er^{3+} nanoparticles. The calibration of the laser heating becomes possible to correct the laser-induced error, and then to precisely calibrate the $GdVO_4$: Yb^{3+}/Er^{3+} nanoprobes in thermometry measurements. Knowing that the laser-induced thermal effect occurs, and this effect rises with environmental temperature, the correction of the laser heating is necessary for upconversion probes to avoid any error in the temperature measurement. In addition, this laser-induced heating temperature calibration method could also be used for some applications, where upconversion NPs can be both the heater and the temperature sensor. Attention should be paid to the structural change of the material caused by high laser-induced heating temperature, it could reach 700°C upon laser intensity of 15.8 W/cm² and at environmental temperature of 300°C. The $GdVO_4$ nanoparticles have been observed by Gavrilović *et al.*[30] that after calcination of 2 h at 800°C, their size has slightly increased, and their crystal phase has not changed. Therefore, we do not expect for any structural transformation of the nanoparticle under short time excitation by NIR laser. However, this temperature could cause irreversible structural change in other nanoparticles.

We conclude that in the application of $GdVO_4$: Yb^{3+}/Er^{3+} NPs as UC thermometer, laser-induced heating could be avoided by using low laser intensity. Furthermore, the laser-induced heating effect has not been observed under visible light excitation. However, for applications as temperature sensors, NPs must be included at a given concentration in a given medium. Using visible light can cause matrix emission, which affects the accuracy of photoluminescent sensing by NPs. To reduce matrix emission and optimize spatial resolution, NIR laser excitation is chosen.

3.4 Applicability in various medium

3.4.1 Laser heating in dispersed medium

Laser-induced heating can be affected by environmental conditions, such as, among others, the chemical or physical impact of the medium, the concentration of the nanoprobes, the optical compatibility of the medium. These effects can be critical to obtain correct temperature measurement results.[31] In the following, in order to determine the impact of environmental factors on temperature calibration (including laser-induced heating), the $GdVO_4$: Yb^{3+}/Er^{3+} nanoprobes were dispersed in three different media, one liquid and two solids, at different concentrations. The dispersed media are optically transparent, showing negligible absorption of NIR light compared to the NPs powder (Figure 3.8, the oil stands for the lubricant Nycobase 5750). Therefore, the NIR laser heating on the pure media is not

considered in this study. The mixtures were excited by a NIR laser at different intensities for temperature calibration.

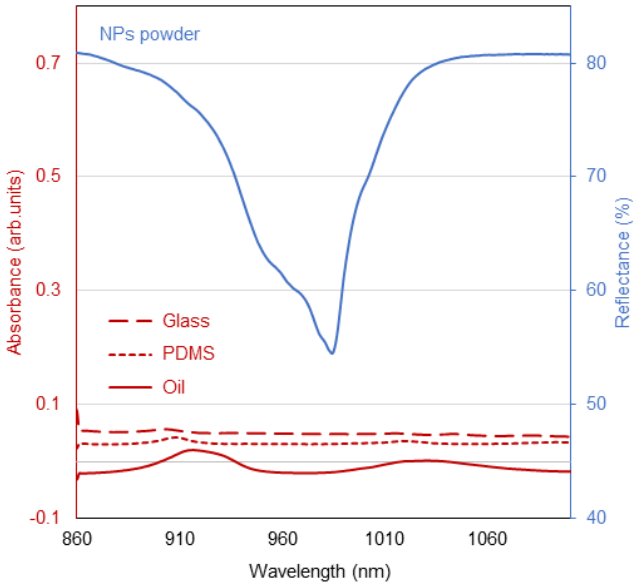

Figure 3.8: Absorbance spectra for the pure matrix (oil (Nycobase 5750), glass, PDMS) and reflectance spectra for the NPs powder in the range of NIR light.

1) Dispersion in a fluid medium at low concentration.

A low concentration suspension in oil at 0.5 wt.% of NPs was prepared. The emission intensity is low due to the low concentration of the luminescent probe in the suspension (Figure 3.9a), so the experimental uncertainty is quite large despite the relatively high laser power density used. As with the NPs powder, the emission intensity increases as the laser intensity increases, and the uncertainty becomes lower with higher laser intensity. However, the temperature calibrations curves (Figure 3.10a) from 25°C to 150°C, are all superimposed at various laser intensity (9.7 to 15.8 W/cm²). The integrated peak surface of S1 and S2 is plotted as a function of laser intensity for the NPs suspension (Figure 3.9b). A linear relationship with a slope of the curve close to 2 was observed, which is very similar to the case of free NPs powder (Figure 3.6c) which means that the excitation process is a UC involving two-photons absorption. The LIR values only change with temperature but not with laser intensity (Figure 3.9c), and the calculated energy gaps (ΔE_{LIR}) are similar at different laser intensities (Table 3.1). Laser-induced heating is not observed in the 0.5 wt.% suspension of NPs in oil.

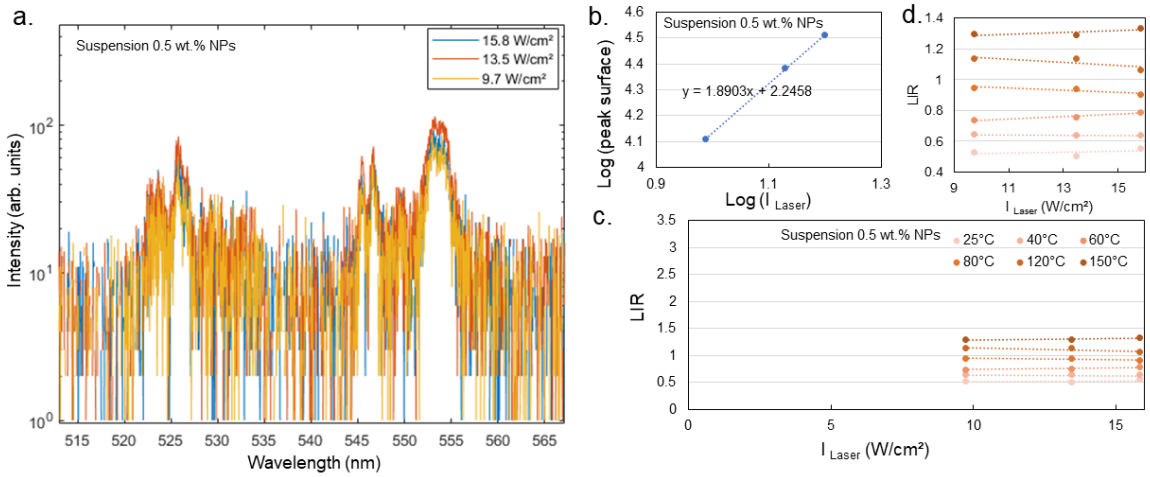

Figure 3.9: Suspension at 0.5 wt.% NPs in oil: a) Emission spectra at different laser intensities. b) Relationship between the average of the sum of the N1+N2 surface peaks and the laser intensity at studied temperature (25°C to 150°C). c) Graph of LIR at different laser intensities at different setup temperatures (25°C to 150 °C) and d) the zoomed in graph of LIR.

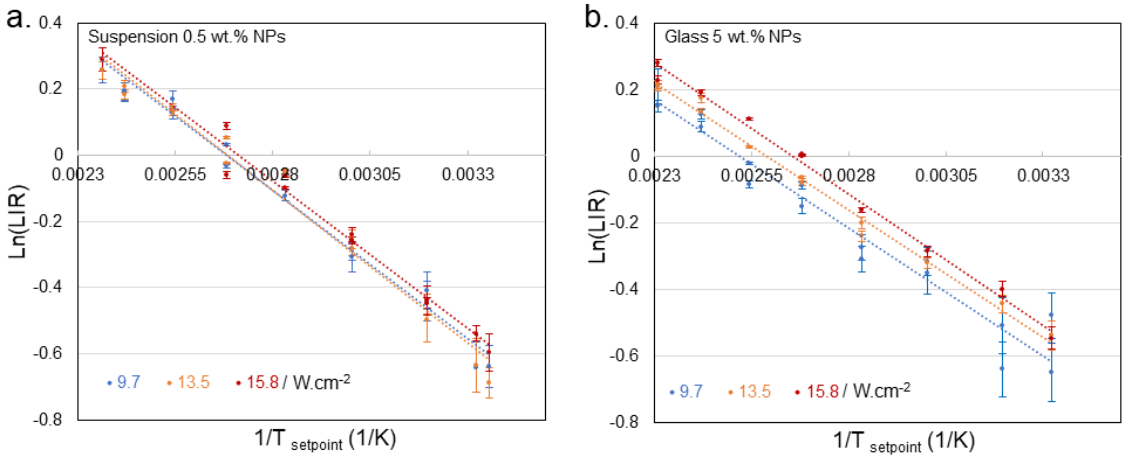

Figure 3.10: a) Temperature calibration of the suspension at 0.5 wt.% NPs. b) Temperature calibration of the glass at 5 wt.% NPs.

2) Dispersion in a solid medium at low concentration.

Considering the dispersion capacity of NPs in the hybrid glass and PDMS, we used 5 wt. % of NPs to increase the emission intensity. The luminescence spectra of NPs dispersed in the hybrid glass are shown in Figure 3.11a. The emission spectra are noisy, and the experimental uncertainty is relatively high. In the temperature range from 25°C to 160°C, the temperature calibration curves do not change, and the slope remains constant as the laser intensity varies (Figure 3.10b & Table 3.1). Excitation is always a UC process with two-photons absorption for all temperatures and laser intensities (Figure 3.11b), and the LIR is held constant at constant temperature (Figure 3.11c). A simple comparison with 5 wt.% NPs in PDMS is performed for two laser intensities (6.8 and 15.8 W/cm²) at 25°C. The LIR value does not change with the laser intensity. The previous results are confirmed by the calculated ΔE_{LIR} values (Table 3.1) for the 5 wt.% NPs in the hybrid glass: ΔE remains constant as the laser intensity changes. Compared to other calibrations without laser heating effect, like the

calibration of 0.5 wt.% NPs suspension in oil and that of NPs powder under low laser intensity (≥ 2.5 W/ cm²), the calibration of 5 wt. % NPs in solid shows a lower ΔE value. We assume that this difference is caused by the slight laser-induced heating in the solid. However, this heating did not change under different laser intensities up to 15.8 W/cm². We can conclude that the calibration curves were not interfered by the excitation laser intensity in the 5 wt.% NPs hybrid glass or PDMS in the temperature range [25°C – 160°C] and laser intensity range [9.7 – 15.8 W/cm²].

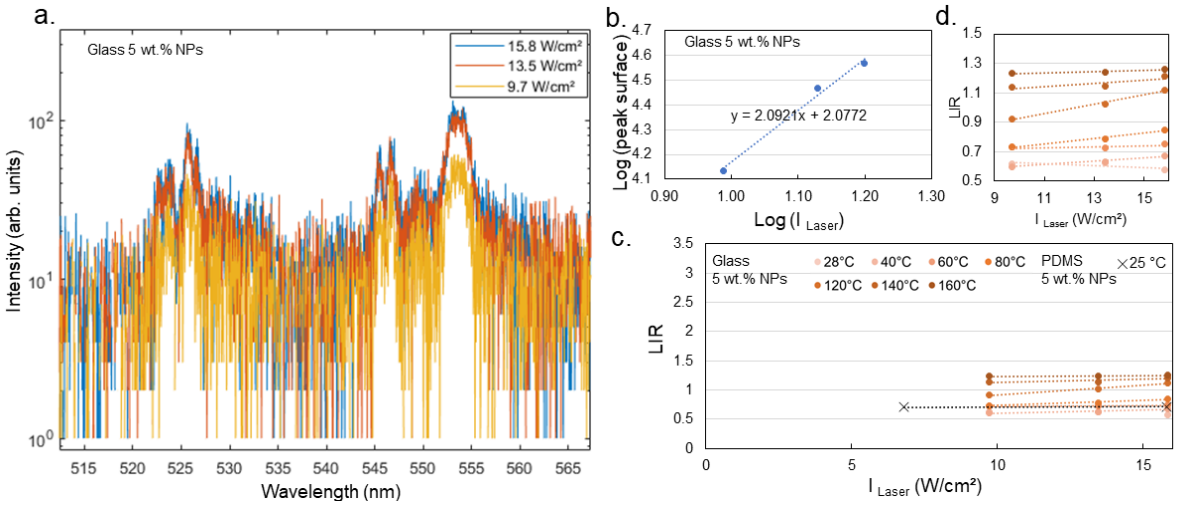

Figure 3.11: Glass at 5 wt.% NPs: a) Emission spectra at different laser intensities. b) Relationship between the average of the sum of the N1+N2 surface peaks and the laser intensity at studied temperature (25°C to 160°C). c) Graph of LIR at different laser intensities at different setup temperatures (25°C to 160 °C) and d) the zoomed in graph of LIR.

3) Dispersion in a medium at high concentration.

In the previous section, it was observed that for a low concentration dispersion of NPs in a medium, solid or fluid, the influence of the excitation laser intensity can be neglected. However, a decreasing concentration of NPs degrades the signal-to-noise ratio of the emission spectrum, then the experimental accuracy. For our further study on temperature measurement under tribological conditions, we need to increase the probe concentration to optimize accuracy of measurement without being perturbed by laser-induced heating problems. However, we noted that the dispersion of NPs at high concentrations in fl uid lubricants has an impact on the rheological properties of the fluid. Thus, a high concentration of NPs may be advantageous for enhancing the accuracy of measurements in solid matrices. In this study, we examined the effect of NPs concentrations on the laser-induced heating phenomenon in solid media. Specifically, we investigated the maximum dispersion concentration of NPs in both solid and fluid matrices for comparative analysis. The dispersion capacity of $GdVO_4$: Yb^{3+}/Er^{3+} NPs in a sol-gel hybrid glass is not high. Thus, only the PDMS matrix is considered in the following.

Using the same dispersion method, 50 wt.% of $GdVO_4$: Yb^{3+}/Er^{3+} NPs were dispersed in oil and PDMS. When the concentration of NPs is extremely high, the oil suspension and the solid completely lose their transparency. The emission intensity gets higher when the NPs

concentration is higher. The high concentrated materials can be excited under low laser power density (1.3 W/cm²) (Figures 3.12a and 3.13a). However, Figures 3.12b and 3.13c show that the LIR changes not only with temperature but also with laser intensity, for 50 wt.% in the suspension and in the PDMS respectively, which was observed in a contrasting manner in Figures 3.9c and 3.11c.

The temperature calibration curves are plotted in Figure 3.12c for the NPs suspension, for the 50 wt.% NPs in oil at 2.5 W/cm² and for the 0.5 wt.% at 15.8 W/cm². The slope of those two curves is close to each other as well as the calculated ΔE_{LIR}. This observation shows that in the suspension at high concentration of NPs, the laser heating could be overcome under low laser intensity same performance as powder. In Figure 3.13b, the temperature calibration curves for 50 wt.% of NPs in PDMS at different laser intensities are plotted. The laser heating occurs after 2.5 W/cm², the calculated ΔE_{LIR} decreases with the laser intensity. As expected, the materials at high NPs concentration react like NPs powder with respect to the laser heating phenomenon.

As performed for free powder NPs, the Equation 3.5 was applied to correct the laser-induced heating temperature (constant values see Table 3.2) on 50 wt.% NPs in PDMS (Figure 3.13d). Compared to the regression model fitted for free powder of NPs, their coefficients of I_{laser} (C2), as well as T_{LIR} (C3) are nearly the same.

It's important to note that some samples containing a high concentration of NPs were destroyed by laser-induced overheating after the experiments. We observed significant darkening on the surface of high concentrated PDMS after high laser density excitation. When the laser intensity and temperature are high during calibration, the ambient temperature can easily reach the flash point or melting point of the materials. However, without laser heating calibration, it is difficult to estimate the $T_{laser\ heating}$ on a given I_{laser}. To avoid any unexpectable sample damage, it is necessary to verify the laser heating phenomenon before any experiment using UC nanoparticles as a sensor.

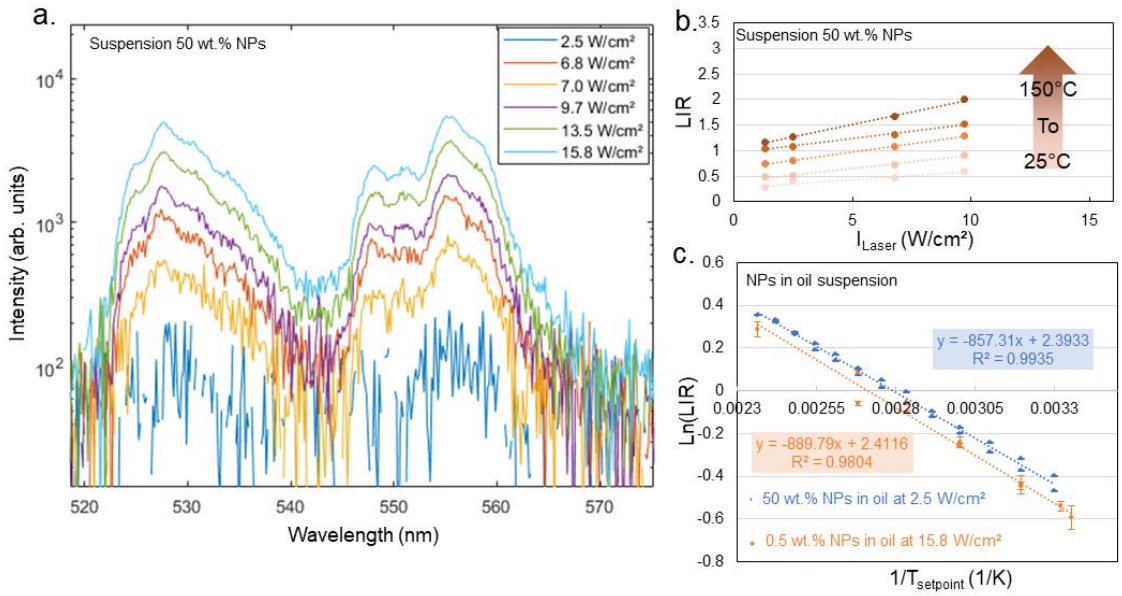

Figure 3.12: Suspension at 50 wt.% NPs in oil: a) Emission spectra at different laser intensities. b) LIR at different laser intensities at different setup temperature (25°C to 150 °C).

c) Calibration of the temperature of the suspension to 50 wt.% NPs (blue) at 2.5 W/cm² and at 0.5 wt. % NPs (yellow) at 15.8 W/cm².

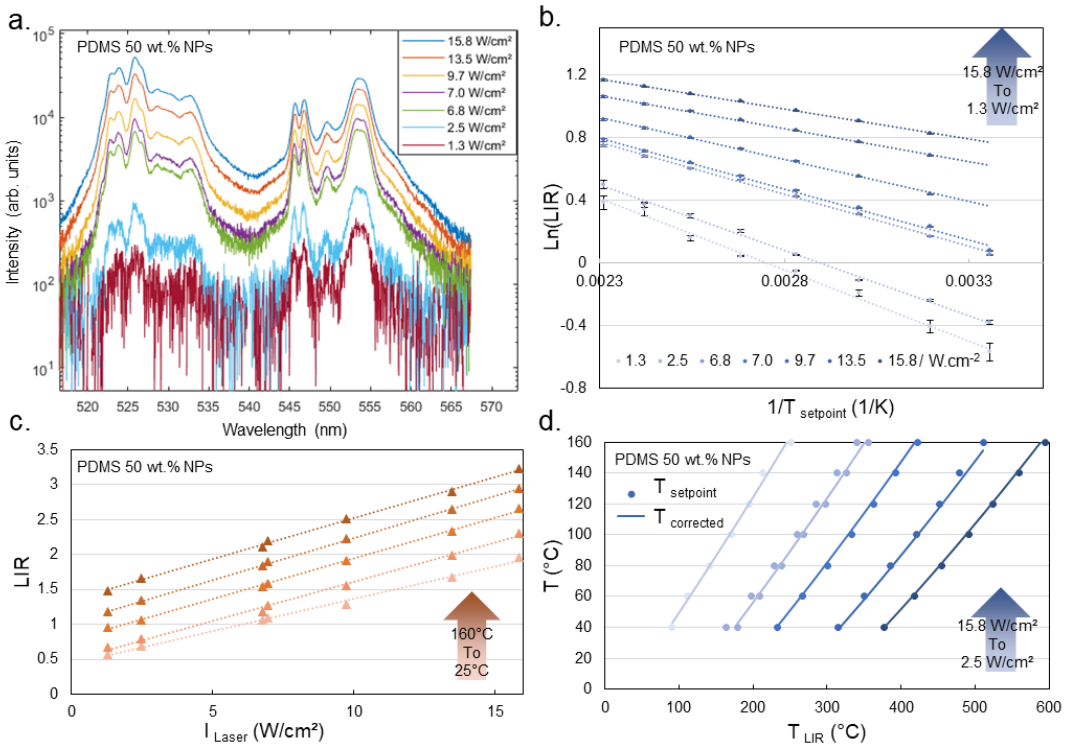

Figure 3.13: PDMS at 50 wt.% NPs: a) Emission spectra at different laser intensities. b) Temperature calibration under excitation at 970 nm at different laser intensities. c) LIR at different laser intensities at different setup temperature (25°C to 160 °C). (d) Application of correction module for laser heating temperature.

We can conclude that the concentration of $GdVO_4$: Yb^{3+}/Er^{3+} NPs dispersion in the medium has an impact on the laser heating phenomenon. The concentration of the NPs is a critical parameter that decides whether laser heating occurs or not in the studied medium. In our work, laser heating occurs when the NPs concentration is very high (50 wt.%) but not when the concentration is low (0.5 wt.% in a fluid suspension and 5 wt.% in a hybrid glass or PDMS). The laser-induced heating causes significant temperature calibration error and can even destroy the material. Therefore, when $GdVO_4$: Yb^{3+}/Er^{3+} NPs are used in a medium as thermometric nanoprobes, the phenomenon of laser-induced heating deserves to be studied beforehand. Since laser heating can occur in all UC systems, experiments with UC nanoprobes should pay attention to laser heating. In summary, by using the $GdVO_4$: Yb^{3+}/Er^{3+} NPs as UC nano sensor on temperature measurement, low concentration of NPs in medium or low laser intensity should be used to avoid the error caused by laser-induced heating. To optimize the UC emission, the high concentration of NPs dispersion could be applied only with a laser-induced heating correction. Moreover, we noted that in dynamic contact for tribological applications, temperature measurement by $GdVO_4$: Yb^{3+}/Er^{3+} NPs should not significantly be influenced by NIR-laser-induced heating. Heat dissipation becomes even more important in dynamic fluid environments. Importantly, since $GdVO_4$: Yb^{3+}/Er^{3+} NPs are

exposed to a fixed laser, the duration of irradiation is too brief to cause significant heating of the NPs in flowing lubricants.

3.4.2 Thermometry under varying pressure (NPs suspension)

For further application in tribology, the temperature measurement must be valid under specific conditions, such as high pressure and high shear rates (up to $10^6\ s^{-1}$). Pressure is one of the key parameters that vary in tribological contact. In this section, we studied the effect of a hydrostatic pressure up to 1 GPa (even if in mechanical contact higher pressure might be reached) on the LIR thermometry of Er^{3+}doped nanoparticles. As the nano-sensor will be used in a specific medium for further tribological measurements, the $GdVO_4:Yb^{3+}/Er^{3+}$ upconversion nano-sensor was dispersed in a lubricant. According to previous studies on the laser heating effect, the 0.5 wt.% NPs suspension in Nycobase is selected for the pressure-coupling thermometry studies. The photoluminescent thermometry of the NPs suspension was studied under pressure (up to 1.1 GPa) in a DAC at every 20 K from 293 K to 353 K, under a 13.5 W/cm² NIR laser as in the previous experiments. Here the experiments were limited to 1.1 GPa because above this pressure, the pressure might be no more hydrostatic.[32]

1) Impact of hydrostatic pressure on LIR

To study the effect of pressure on the LIR of NPs, two sets of data were collected in the DAC under isothermal conditions. The first group, called $P_{constant}$, is a repeated measurement at the same temperature and pressure (the lowest pressure for the corresponding temperature). The second group, called $P_{varying}$ is a sequence of measurements at a given temperature for a variable pressure. The emission spectra are presented in Figure 3.14a at varying temperature and constant pressure (P = 0.6 GPa), showing that increasing temperature increases the emission intensity of peak λ_2 and decreases that of the peak λ_1. Conversely, Figure 3.14b shows the negligible change in emission intensity under varying pressure at constant temperature. Therefore, at a hydrostatic pressure 0.6 GPa, the LIR always varies with temperature, whereas at constant temperature, the LIR shows no sensitivity to pressure.

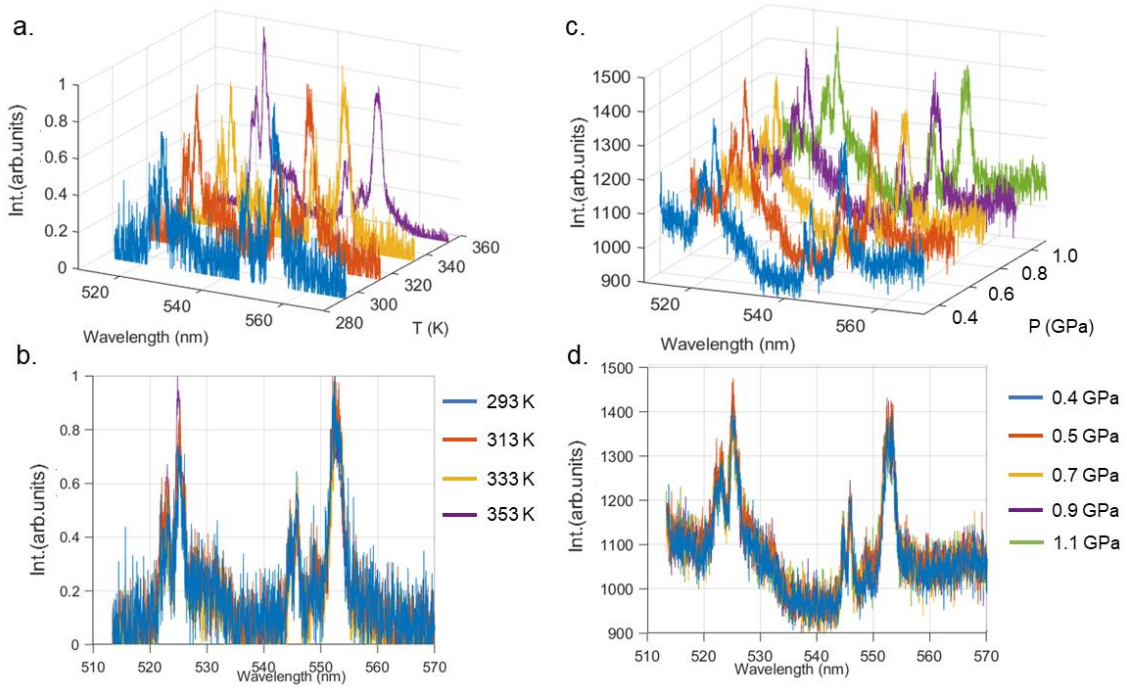

Figure 3.14: $GdVO_4$:Yb^{3+}/Er^{3+} suspended at 0.5 wt.% in DAC upon NIR laser at 13.5 W/cm²: a) and b) Emission spectra at 293 – 353 K under 0.6 GPa; c) and d) Emission spectra at 313 K under 0.4 – 1.1 GPa.

1) Impact of hydrostatic pressure on peak shifting

The photoluminescent peak shift is always considered as a pressure-sensitive parameter. Thus, the peak position (originally at 553 nm) has been verified under varying pressure at different temperatures. As shown in Figure 3.15, at 333K, the corrected peak position shifts slightly to higher wavelength, with 0.2 nm/GPa. This result agrees with the value reported in the study of $NaBiF_4$: Yb^{3+}/Er^{3+} nanoparticles by Antoniak *et al.*,[33] who found that the emission peak of the $^4S_{3/2} \rightarrow {}^4I_{15/2}$ transition shifts 0.17 nm/ GPa up to 14 GPa. Besides the series at 333 K, the peak positions at other temperatures studied show an undetectable shift up to 1 GPa. In the data processing, the LIR calculations are based on the integrated surface of the emission peak, so the shift of the Er^{3+} peak (< 0.2 nm/GPa) of the $^4S_{3/2} \rightarrow {}^4I_{15/2}$ transition is not significant for the LIR calculation, as well as the other thermo-coupled peak (centered at 530 nm). Therefore, the shift in the Er^{3+} peak emission is not considered in the LIR-based thermometry.

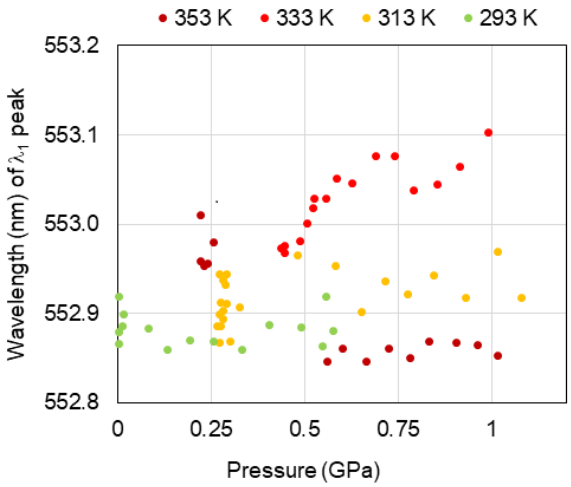

Figure 3.15: $GdVO_4:Yb^{3+}/Er^{3+}$ suspended at 0.5 wt.% in DAC upon NIR laser at 13.5 W/cm², corrected position of Er^{3+} emission peak (transition $^4S_{3/2} \rightarrow {}^4I_{15/2}$) under pressure at different temperatures.

2) T-P coupling thermometry

According to the previous results, the LIR is sensitive to temperature but not pressure. Therefore, temperature calibrations under varying pressure can be valid as under ambient pressure. As shown in Figure 3.16a, the Ln(LIR) under $P_{constant}$ is plotted by a hollow point for each temperature, and the Ln(LIR) under $P_{varying}$ is plotted by a solid symbol for each temperature as well. The LIR value under $P_{constant}$ and $P_{varying}$ do not change with increasing pressure but only with temperature. An analysis of variance is conducted to conclude the influence of pressure on the LIR variation. In Table 3.3, the variance (VAR) at $P_{constant}$ (here the residual variance) and that at $P_{varying}$ (here the explained variance) are calculated for each temperature. The uncertainties calculated by SNR of emission spectra are listed. The VAR($P_{varying}$) is always lower than the VAR($P_{constant}$). This means that the distribution of the LIR value is less dispersed when the pressure varies than when the pressure is constant. This means that the pressure has no effect on the LIR variation. To confirm this result, the ratio VAR($P_{varying}$)/VAR($P_{constant}$) was calculated and found to be less than 1. This result shows that the slight change in the LIR value under isothermal conditions cannot be explained by the variation in pressure. Then, the LIR value is independent of pressure (up to 1.1 GPa) in the temperature range studied.

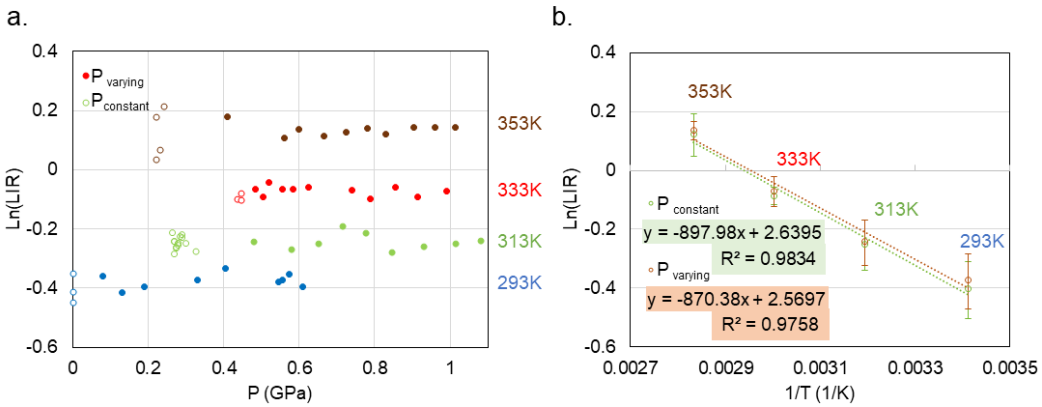

Figure 3.16: $GdVO_4:Yb^{3+}/Er^{3+}$ suspended at 0.5 wt.% upon NIR laser at 13.5 W/cm²: a) Distribution of Ln(LIR) values at four temperature (293 to 353 K) under constant pressure (hollow point) and pressure varying up to 1.1 GPa (solid point). b) Temperature calibration curve and the fitted trendline equations under constant pressure (green) and pressure varying (brown), error bars determined by the standard deviation of overall data**.**

Therefore, the thermometric validity of NPs suspended under pressure was investigated by averaging Ln(LIR) under $P_{constant}$ as well as $P_{varying}$ for each temperature. As shown in Figure 3.16b, the temperature calibration curve under $P_{constant}$ and $P_{varying}$ are both linear as a function of 1/T and overlap with each other. The $\Delta E_{estimated}$ by their slopes are therefore very close, 624 and 605 cm^{-1} respectively (Table 3.4). This observation confirmed that the LIR of suspended NPs $GdVO_4:Yb^{3+}/Er^{3+}$ is independent from pressure (up to 1GPa), and therefore the NPs are able to measure temperature by their emission without any effect caused by pressure variation.

Table 3.3: The average of LIR and variance of LIR for each temperature in DAC.

	P Constant			**P Varying**			
T (K)	P (GPa)	SNR(%)	VAR	P max (GPa)	SNR(%)	VAR	**VAR ratio***
293	0.01	6.47	2.54E-03	0.61	6.48	6.30E-04	**0.25**
313	0.29	6.55	5.27E-04	1.08	5.97	5.00E-04	**0.95**
333	0.45	2.74	2.92E-04	0.99	4.22	2.81E-04	**0.96**
353	0.23	8.28	7.49E-03	1.02	3.47	4.06E-04	**0.05**

*VAR ratio: the ratio of VAR $P_{Varying}$/ VAR $P_{Constant}$

Table 3.4: The estimated energy gap (ΔE) and the uncertainty of temperature calibration curves.

	Y offset	**B**	**Slope**	**$\Delta E_{estimated}$**	**δLIR/LIR (average)**
NPs suspension ($P_{Constant}$)	2.6395	14	-897.98	624	14.18%
NPs suspension ($P_{Varying}$)	2.5697	13	-870.38	605	12.84%

To summarize, if we compare the temperature calibration curve at the same laser pumping power (13.5 W/cm²) of the 0.5 wt.% NPs suspension in our previous results (Table 3.1: $\Delta E_{estimated}$ = 642), the $\Delta E_{estimated}$ obtained by the slope of the calibration curve could be considered as the same, which confirms the reliability of these NPs $GdVO_4$: Yb^{3+}/Er^{3+} for temperature measurement under a pressure up to 1 GPa. The uncertainty of the measurement depends on the intensity of the emission, the quantity of NPs in the suspension being much less important than in the powder, the uncertainty has become important in the suspension. It is important to note that the configuration of the optical experiments is different between the temperature calibration under pressure in the DAC and at atmospheric pressure with a thermal controller, which may imply differences in the illuminations and therefore uncertainty in the emission intensity, and consequently in the LIR value. This may be the reason for a slight shift in the constant B in the Boltzmann equation. However, once the ΔE is consistent with the previous result, the $GdVO_4$: Yb^{3+}/Er^{3+} NPs can be validated as thermometric and pressure independent probe.

3.5 Conclusion and perspectives

This chapter presented the photoluminescent properties of $GdVO_4$: Yb^{3+}/Er^{3+} NPs. The NPs provide accurate and reversible thermometry from 293 to 673 K under excitation by visible blue light and NIR light. Under NIR laser excitation via the upconversion process, a heating effect was observed from the laser during the emission of $GdVO_4$: Yb^{3+}/Er^{3+} nanoparticles powder. This effect became more significant with increasing laser intensity and temperature. The photoluminescence properties of $GdVO_4$: Yb^{3+}/Er^{3+} nanoparticles in a dispersed medium are also studied, their thermometry was still valid. The laser heating effect is typically considered negligible at low concentrations, such as 0.5 wt.% and 5 wt.%. However, it becomes significant at high concentrations (50 wt.%).

To optimize the accuracy of temperature measurement, the $GdVO_4$: Yb^{3+}/Er^{3+} nanoparticles are excited by a high NIR laser intensity with the proposed laser-induced heating temperature correction. With a given laser intensity, the correction can be achieved for NPs in powder form and for NPs dispersed at high concentration in a solid. The above results show that laser-induced heating has a crucial impact on the accuracy of temperature measurement using the UC nano sensor. However, the use of $GdVO_4$: Yb^{3+}/Er^{3+} nanoparticles as temperature sensors will provide a reliable measurement method as the laser-induced heating can be corrected.

In order to apply NPs in frictional contact for temperature sensing, temperature calibration was performed under hydrostatic pressure (up to 1.1 GPa) in a DAC. The suspension of NPs in Nycobase was selected. The result confirmed the independence of the LIR from pressure, and the calibration curve under variable pressure is superimposed on that under constant pressure. Therefore, the incorporation of these $GdVO_4$: Yb^{3+}/Er^{3+} nanosensors into the lubricant leads to the formation of a suspension that allows temperature measurement by the LIR method without being disturbed by the influence of pressure.

The next step is to verify the stability of $GdVO_4$: Yb^{3+}/Er^{3+} NPs as upconversion thermometer under shearing. The shearing-temperature coupling temperature calibration of $GdVO_4$: Yb^{3+}/Er^{3+} NPs in a confined fluid under a high shear rate (10^4 s^{-1}) is now being prepared. Then, the $GdVO_4$: Yb^{3+}/Er^{3+} NPs will be applied in an *in situ* tribological contact for temperature sensing. The NPs will be inserted into fluid lubricants and solid matrices for friction tests.

References

(1) Marqueño, T.; Errandonea, D.; Pellicer-Porres, J.; Martinez-Garcia, D.; Santamaria-Pérez, D.; Muñoz, A.; Rodríguez-Hernández, P.; Mujica, A.; Radescu, S.; Achary, S. N.; Popescu, C.; Bettinelli, M. High-Pressure Polymorphs of Gadolinium Orthovanadate: X-Ray Diffraction, Raman Spectroscopy, and Ab Initio Calculations. *Phys. Rev. B* **2019**, *100* (064106).

(2) Seoudi, T.; Philippon, D.; Fillot, N.; Lafarge, L.; Devaux, N.; Mondelin, A.; Vergne, P. CdSe-Based Quantum Dots as In Situ Pressure and Temperature Non-Intrusive Sensors in Elastohydrodynamic Contacts. *Tribol. Lett.* **2020**, *68* (3). https://doi.org/10.1007/s11249-020-01312-x.

(3) Grasset, O. Calibration of the R Ruby Fluorescence Lines in the Pressure Range [0-1 GPa] and the Temperature Range [250-300 K]. *High Press. Res.* **2001**, *21* (3–4), 139–157. https://doi.org/10.1080/08957950108201020.

(4) Mao, H. K.; Xu, J.; Bell, P. M. Calibration of the Ruby Pressure Gauge to 800 Kbar under Quasi-Hydrostatic Conditions. *J. Geophys. Res.* **1986**, *91* (B5), 4673. https://doi.org/10.1029/jb091ib05p04673.

(5) Wade, S. A.; Collins, S. F.; Baxter, G. W. Fluorescence Intensity Ratio Technique for Optical Fiber Point Temperature Sensing. *J. Appl. Phys.* **2003**, *94* (8), 4743–4756. https://doi.org/10.1063/1.1606526.

(6) Rakov, N.; Maciel, G. S.; Xiao, M. Upconversion Fluorescence and Its Thermometric Sensitivity of Er3+:Yb3+ Co-Doped SrF2 Powders Prepared by Combustion Synthesis. *Electron. Mater. Lett.* **2014**, *10* (5), 985–989. https://doi.org/10.1007/s13391-014-4030-9.

(7) Li, L.; Qin, F.; Zhou, Y.; Zheng, Y.; Zhao, H.; Zhang, Z. Approximate Energy Gaps, Dissimilar Relative Thermal Sensitivities. *Sensors Actuators, B Chem.* **2018**, *269*, 203–209. https://doi.org/10.1016/j.snb.2018.04.158.

(8) Perrella, R. V.; De Sousa Filho, P. C. High-Sensitivity Dual UV/NIR-Excited Luminescence Thermometry by Rare Earth Vanadate Nanoparticles. *Dalt. Trans.* **2020**, *49* (3), 911–922. https://doi.org/10.1039/c9dt04308j.

(9) Savchuk, O. A.; Carvajal, J. J.; Massons, J.; Cascales, C.; Aguiló, M.; Díaz, F. Novel Low-Cost, Compact and Fast Signal Processing Sensor for Ratiometric Luminescent Nanothermometry. *Sensors Actuators, A Phys.* **2016**, *250*, 87–95. https://doi.org/10.1016/j.sna.2016.08.031.

(10) Sedlmeier, A.; Achatz, D. E.; Fischer, L. H.; Gorris, H. H.; Wolfbeis, O. S. Photon Upconverting Nanoparticles for Luminescent Sensing of Temperature. *Nanoscale* **2012**, *4* (22), 7090–7096. https://doi.org/10.1039/c2nr32314a.

(11) Quintanilla, M.; Henriksen-Lacey, M.; Renero-Lecuna, C.; Liz-Marzán, L. M. Challenges for Optical Nanothermometry in Biological Environments. *Chem. Soc. Rev.* **2022**, *51* (11), 4223–4242. https://doi.org/10.1039/d2cs00069e.

(12) Xia, X.; Volpi, A.; Roh, J. Y. D.; De Siena, M. C.; Gamelin, D. R.; Hehlen, M. P.; Pauzauskie, P. J. The Impact of 2H9/2 → 4I13/2 Emission from Er3+ Ions on Ratiometric Optical Temperature Sensing with Yb3+/Er3+ Co-Doped Upconversion Materials. *J. Lumin.* **2021**, *236* (December 2020), 118006. https://doi.org/10.1016/j.jlumin.2021.118006.

(13) Martins, J. C.; Bastos, A. R. N.; Ferreira, R. A. S.; Wang, X.; Chen, G.; Carlos, L. D. Primary Luminescent Nanothermometers for Temperature Measurements Reliability Assessment. *Adv. Photonics Res.* **2021**, *2* (5), 2000169. https://doi.org/10.1002/adpr.202000169.

(14) Bhiri, N. M.; Dammak, M.; Aguiló, M.; Díaz, F.; Carvajal, J. J.; Pujol, M. C. Stokes and Anti-Stokes Operating Conditions Dependent Luminescence Thermometric Performance of Er3+-Doped and Er3+, Yb3+ Co-Doped GdVO4 Microparticles in the Non-Saturation Regime. *J. Alloys Compd.* **2020**, *814*. https://doi.org/10.1016/j.jallcom.2019.152197.

(15) Wujczyk, M.; Watras, A.; Szyszka, K.; Wiglusz, R. J. Influence of Vanadium Concentration on Up-Conversion Luminescence in Er3+–Yb3+ and Tm3+–Yb3+ Ions Pair Co-Doped YVxP1−xO4 Solid State Solution. *J. Alloys Compd.* **2021**, *884*, 161022. https://doi.org/10.1016/j.jallcom.2021.161022.

(16) Buissette, V.; Huignard, A.; Gacoin, T.; Boilot, J. P.; Aschehoug, P.; Viana, B. Luminescence Properties of YVO4:Ln (Ln = Nd, Yb, and Yb-Er) Nanoparticles. *Surf. Sci.* **2003**, *532–535*, 444–449.

https://doi.org/10.1016/S0039-6028(03)00203-6.

(17) Sun, J.; Zhang, Z.; Suo, H.; Chen, Y.; Xiang, J.; Guo, C. Temperature Self-Monitoring Photothermal Nano-Particles of Er3+/Yb3+ Co-Doped Zircon-Tetragonal BiVO4. *Ceram. Int.* **2021**, *47* (1), 409–415. https://doi.org/10.1016/j.ceramint.2020.08.147.

(18) Cho, Y.; Song, S. W.; Lim, S. Y.; Kim, J. H.; Park, C. R.; Kim, H. M. Spectral Evidence for Multi-Pathway Contribution to the Upconversion Pathway in NaYF4:Yb3+,Er3+ Phosphors. *Phys. Chem. Chem. Phys.* **2017**, *19* (10), 7326–7332. https://doi.org/10.1039/c7cp00048k.

(19) Paz-Buclatin, F.; Rivera-López, F.; González, O.; Martín, I. R.; Martin, L. L.; Jovanović, D. J. GdVO4:Er3+/Yb3+ Nanocrystalline Powder as Fluorescence Temperature Sensor. Application to Monitor the Temperature of an Electrical Component. *Sensors Actuators, A Phys.* **2019**, *299*. https://doi.org/10.1016/j.sna.2019.111628.

(20) Liu, J.; Deng, H.; Huang, Z.; Zhang, Y.; Chen, D.; Shao, Y. Phonon-Assisted Energy Back Transfer-Induced Multicolor Upconversion Emission of Gd2O3:Yb3+/Er3+ Nanoparticles under near-Infrared Excitation. *Phys. Chem. Chem. Phys.* **2015**, *17* (23), 15412–15418. https://doi.org/10.1039/c5cp01632k.

(21) Li, T.; Guo, C.; Li, L. Up-Conversion Luminescence of Er^3+-Yb^3+ Co-Doped CaIn_2O_4. *Opt. Express* **2013**, *21* (15), 18281. https://doi.org/10.1364/oe.21.018281.

(22) Oh, J. H.; Moon, B. K.; Choi, B. C.; Jeong, J. H.; Choi, H.; Kim, J. H. Reinterpretation of the Red Emission Pathway in β-NaYF4:Yb3+, Er3+. *Ceram. Int.* **2017**, *43* (2), 2517–2522. https://doi.org/10.1016/j.ceramint.2016.11.053.

(23) Jaque, D.; Vetrone, F. Luminescence Nanothermometry. *Nanoscale* **2012**, *4* (15), 4301–4326. https://doi.org/10.1039/c2nr30764b.

(24) Marciniak, L.; Waszniewska, K.; Bednarkiewicz, A.; Hreniak, D.; Strek, W. Sensitivity of a Nanocrystalline Luminescent Thermometer in High and Low Excitation Density Regimes. *J. Phys. Chem. C* **2016**, *120* (16), 8877–8882. https://doi.org/10.1021/acs.jpcc.6b01636.

(25) Rühl, P.; Wang, D.; Garwe, F.; Müller, R.; Haase, M.; Krämer, K. W.; Paa, W.; Heintzmann, R.; Heinemann, S. H.; Stafast, H. Notes on Thermometric Artefacts by Er3+ Luminescence Band Interference. *J. Lumin.* **2021**, *232* (December 2020), 18–21. https://doi.org/10.1016/j.jlumin.2020.117860.

(26) Tikhomirov, V. K.; Driesen, K.; Rodriguez, V. D.; Gredin, P.; Mortier, M. Optical Nanoheater Based on the Yb3+-Er3+ Co- Doped Nanoparticles V.K. *Opt. Express* **2009**, *17* (14), 11794–11798.

(27) Suo, H.; Zhao, X.; Zhang, Z.; Guo, C. Ultra-Sensitive Optical Nano-Thermometer LaPO4: Yb3+/Nd3+ Based on Thermo-Enhanced NIR-to-NIR Emissions. *Chem. Eng. J.* **2020**, *389* (February), 124506. https://doi.org/10.1016/j.cej.2020.124506.

(28) Xu, S.; Xiang, S.; Zhang, Y.; Zhang, J.; Li, X.; Sun, J.; Cheng, L.; Chen, B. 808 Nm Laser Induced Photothermal Effect on Sm3+/Nd3+ Doped NaY(WO4)2 Microstructures. *Sensors Actuators, B Chem.* **2017**, *240*, 386–391. https://doi.org/10.1016/j.snb.2016.08.176.

(29) Riseberg, L. A.; Moos, H. W. Multiphonon Orbit-Lattice Relaxation of Excited States of Rare-Earth Ions in Crystals. *Phys. Rev.* **1968**, *174* (2), 429–438. https://doi.org/10.1103/PhysRev.174.429.

(30) Gavrilović, T. V.; Jovanović, D. J.; Lojpur, V.; Dramićanin, M. D. Multifunctional Eu3+- and Er3+/Yb3+-Doped GdVO4 Nanoparticles Synthesized by Reverse Micelle Method. *Sci. Rep.* **2014**, *4*, 1–9. https://doi.org/10.1038/srep04209.

(31) Bednarkiewicz, A.; Marciniak, L.; Carlos, L. D.; Jaque, D. Standardizing Luminescence Nanothermometry for Biomedical Applications. *Nanoscale* **2020**, *12* (27), 14405–14421. https://doi.org/10.1039/d0nr03568h.

(32) Klotz, S.; Chervin, J. C.; Munsch, P.; Le Marchand, G. Hydrostatic Limits of 11 Pressure Transmitting Media. *J. Phys. D. Appl. Phys.* **2009**, *42* (7). https://doi.org/10.1088/0022-3727/42/7/075413.

(33) Antoniak, M. A.; Zelewski, S. J.; Oliva, R.; Żak, A.; Kudrawiec, R.; Nyk, M. Combined Temperature and Pressure Sensing Using Luminescent NaBiF4:Yb,Er Nanoparticles. *ACS Appl. Nano Mater.* **2020**, *3* (5), 4209–4217. https://doi.org/10.1021/acsanm.0c00403.

Chapter 4:

Photoluminescent Lanthanide complex as pressure sensor

4 Photoluminescent Lanthanide complex as pressure sensor

4.1 Introduction

In recent decades, photoluminescent pressure sensors have received increasing attention in applications of basic science technology and engineering,[1–13] such as biology,[14] tribology, [15,16] and optics.[17]Among the numerous families of PL sensors, rare-earth based compounds are among the most interesting to develop. Compared with other PL sensors, lanthanide-based sensors are more reliable due to their long emission lifetime, sharp emission peak, low toxicity, and high functionalizability. The photoluminescent pressure sensitivity is often characterized by the shift in wavelength of the emission peak. When there are two or more species in a system, the relationship between them, such as energy transfer (ET), can be influenced by their distance from each other. Consequently, changes in pressure-induced structural contraction can be indirectly monitored by observing the relative emission of these species.

This chapter focuses on the photoluminescent pressure sensitivity of Ln complexes specifically within the pressure range below 1 GPa. Compared to the pure inorganic host, the coordination complex provides greater structural flexibility under pressure, resulting in greater sensitivity. Three Ln complexes will be presented, with different nuclearities ([Ln_1], [Ln_2] and [Ln_9]). The pressure sensitivity based on the shift of the emission peak of the Eu^{3+} complex will first be discussed.

Later, a novel method to measure pressure will be proposed, by adding a Tb^{3+} emitting sensitizer to the system, using the luminescent-intensity-ratio (LIR) of Tb/Eu to monitor the variation in pressure. Pressure sensitivity based on LIR is impacted by the variation in Tb-Eu energy transfer and therefore by the change in their distance from each other. Consequently, the impact of the structure, nuclearity and Ln-Ln distance of the complex on their pressure sensitivity will be discussed. Among all the complexes, the [Ln_1] mononuclear complex was characterized by lifetime measurements to determine the impact of Eu/Tb compositions on the efficiency of Tb-Eu ET. The O_2-quenching phenomenon has also been analyzed. Then, the [Ln_1] complex [$Eu_{0.01}Tb_{0.20}Y_{0.79}$] was further characterized by its applicability as a pressure sensor in tribological tests. The impact of temperature and shear rate on the LIR value will be shown.

4.2 Technologies and methods

4.2.1 Photoluminescent characterizations

The photoluminescent properties were analyzed by a modular spectrofluorometer, equipped with a pulsed multi-wavelength laser (EKSPLA NT230, 50 Hz). The laser spot was non-focused to protect the sample from being destroyed under high-power light. The emission spectra were obtained by a CCD detector (Newton^{EM} EMCCD Camera, Andor), and the excitation spectra and the lifetime measurements were performed by a PM detector (Photo-

multiplicator, Short Focal Length Triple Grating Imaging Spectrographs, TRIAX 320 HORIBA). The temperature variation was controlled by a thermo-cell (Optical DSC600 cell, LINKAM), supported by liquid nitrogen flux for low temperature (< 293 K). Data were collected after 10 s of temperature stabilization.

4.2.2 Emission spectra under pressure

Pressure calibration experiments (≤1 GPa) were performed in a high-pressure DAC: MDAC type BHP for Biology 100° symmetrical aperture, Betsa). The DAC was coupled with a focused continued laser (405 nm) with a micron-scale rounded spot. The laser power was measured in front of the diamond window, at around 0.5 mW. The emission signals were collected and analyzed using a CCD detector (U1000 Horiba Jobin-Yvon Spectrometer) as shown by the experimental set up in Figure 4.1. The mini crystals were dispersed in a solvent (Nycobase 5750 or Squalane) as a hydrostatic pressure medium. Based on the previous work at LaMCoS,[15] the DAC was equipped with a culet diamond anvil (1.4 mm), a thick diamond window (0.4 mm), and a nickel gasket between them. This elastic gasket allows buffering of the applied pressure and has a thickness of about 0.2 mm and is drilled with a 0.5 mm diameter hole in the middle. An internal membrane inflated by N_2 gas covers and closes the DAC to apply pressure. The temperature was regulated by a heating ring (External Heating System, Betsa) around the DAC, the inserted thermocouple was placed next to the metal gasket in the DAC, which allows measurement of the sample temperature with a precision of ±1 K. A small volume of suspended sample (< 1 µL) was introduced into the gasket hole during measurement, and several ruby microparticles (> 3 µm) were introduced with as a tool for internal pressure calibration. Data were collected after 20 min to ensure stabilization of pressure and temperature. Based on literature,[1,18] upon 405 nm excitation, the commercial ruby microparticles are used as a reliable pressure sensor by their photoluminescent wavelength shift R_1 (around 694.3 nm at ambient pressure). The spectral wavelength was corrected by a Neon lamp (ORIEL 6032, Oriel Corp.) with a peak at 703.24 nm. More details of DAC set up can be found in Chapter 3, section 3.2.2.

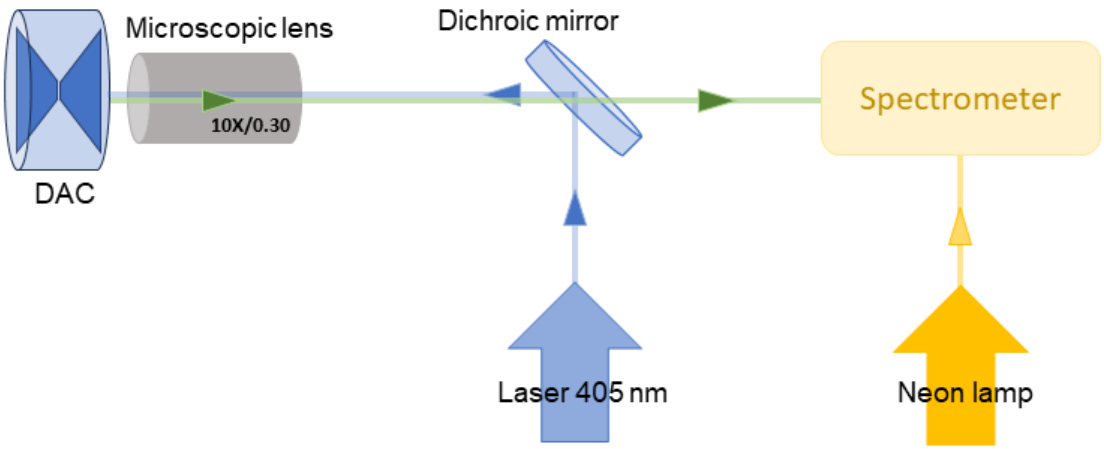

Figure 4.1: Schematic description of pressure coupling spectrometer.

4.2.3 Emission spectra under shearing

Photoluminescent spectra under shearing are acquired by a CCD detector (U1000 Horiba Jobin-Yvon Spectrometer), coupling with a rheometer (Physica MCR301, Anton Paar) with a parallel-plate geometry (PP40). The parameters are the same as the description in Chapter 2, section 2.3.2. Based on the previous work at LaMCoS,[19] the suspension sample was deposited on the glass plate, the volume of sample is 300 µL for every measurement. The emission signals are collected by an objective at r = (2/3)R (R = 20 mm) as shown in Figure 4.2. This distance has been chosen because in the case of the parallel-plate geometry, the shear rate is not constant along the radius. Actually, the shear rate and shear stress are increasing with the radius. The mean value of shear stress, calculated by integrating the value all other the surface, is approximately the local value calculated at (2/3)R. This is the main reason why the measurements were done at (2/3)R.

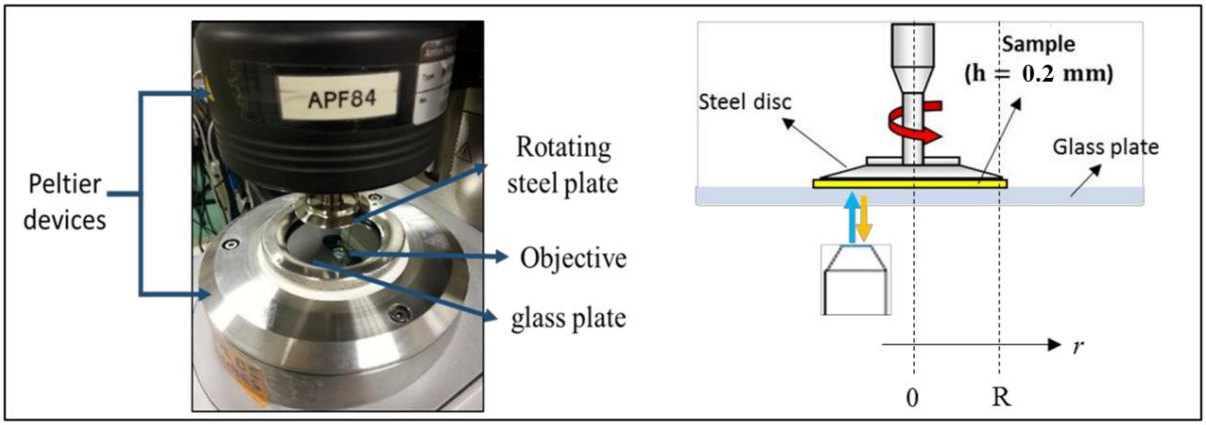

Figure 4.2: Rheometer coupling spectrometer set up. (Figure from ref.[19], thesis of T. Seoudi in 2020)

4.2.4 LIR calculations

The LIR of the emission of Tb^{3+} and Eu^{3+} were estimated by the integrated areas of the spectral band to include the overall emitted intensities for each sublevel's transition,[20] calculated in the Simpson's rule MATLAB program. The integrated area ranges were 520–560 nm (Tb^{3+} emission) and 595–635 nm (Eu^{3+} emission).

4.3 Peak-shift based manometry: $[Eu_9(acac)_{16}(\mu_3\text{-}OH)_8(\mu_4\text{-}O)(\mu_4\text{-}OH)]$

Due to the offset in energy levels induced by structural contraction and distortion, the emission peak shift is one of the most classic variables in pressure sensing. In this section, the pressure-dependent peak shift of the nonanuclear Europium complex will be studied.

4.3.1 Structural transition under pressure

As shown in Figure 4.3, the crystal structure of $[Ln_9]$ [Eu], three asymmetric sites of Eu^{3+} are observed: the four Eu ions consisting of the square base of the upper pyramid are named

as Eu2, and the four Eu atoms on the bottom pyramid are Eu3; the central atom connecting the two pyramids is named as Eu1.

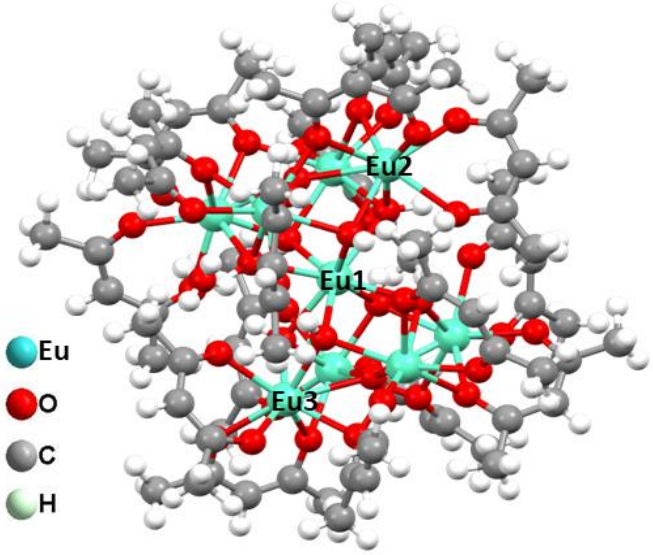

Figure 4.3: Structure of the [Ln_9] complex [$Eu_9(acac)_{16}(\mu_3\text{-}OH)_8(\mu_4\text{-}O)(\mu_4\text{-}OH)$].

At 298K, the [Ln_9] [Eu] exhibits visible red light under laser excitation at 405 nm. Electrons excited by the laser at 405 nm move to the excited state $^5L_6$ of Eu^{3+}, while the ligand [acac] can also be excited by the laser and then transfer energy to the $^5D_1$ level (Scheme 4.1). Emissions from the $^5D_0$ levels to the $^7F_1$, $^7F_2$ and $^7F_3$ levels are shown in Figure 4.4a. The most intense peak corresponding to the $^5D_0 \rightarrow {}^7F_2$ transition is located between 615 to 635 nm, splitting into four small peaks, and three of which form the multiplet peak centered at 620 nm (Figure 4.4a). In the tetragonal structure, the transition $^5D_0 \rightarrow {}^7F_2$ splits into four sublevels.[21] The transition $^5D_0 \rightarrow {}^7F_2$ is considered to be hypersensitive to the Eu^{3+} environment,[21–24] the corresponding peak centered at 620 nm in the complex [$Eu_9(acac)_{16}(\mu_3\text{-}OH)_8(\mu_4\text{-}O)(\mu_4\text{-}OH)$] is considered as a possible variable.

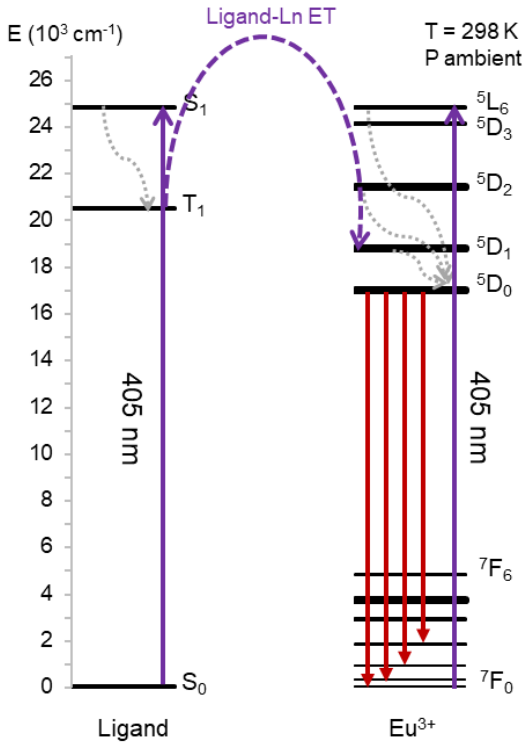

Scheme 4.1: Proposed excitation pathways under 405 nm laser excitation $[Eu_9(acac)_{16}(\mu_3\text{-}OH)_8(\mu_4\text{-}O)(\mu_4\text{-}OH)]$ complex. (ET: energy transfer; grey dotted arrows stand for nonradiative relaxations; red arrows stand for emissions).

The $[Ln_9]$ complex was introduced into the DAC for the compression test and the crystals were surrounded in Squalane for hydrostatic pressure. At 293 K, the $^5D_0 \rightarrow {}^7F_2$ peak remains stable below 550 MPa. At 550 MPa, the $^5D_0 \rightarrow {}^7F_2$ peak starts to deform, with two new peaks centered at 612 nm and 623 nm appearing, illustrated as peaks A and B, respectively by the blue arrows in Figure 4.4b. The appearance of peaks A and B under compression of the $[Ln_9]$ complex is permanent, and they persist after decompression. This deformation of the peak shape can be ascribed to the structural distortion of the $[Ln_9]$ complex under compression. The variation in the crystal lattice under the effect of the increase in hydrostatic pressure leads to a change in the structural symmetry of Eu^{3+}, resulting in a shift in the energy level. The $^5D_0 \rightarrow {}^7F_2$ peak shift of Eu^{3+} under varying pressure bellow 0.7 GPa at 293 K has been reported in cubic structural of CaF_2.[25] Furthermore, as the deformation of the original $^5D_0 \rightarrow {}^7F_2$ peak is an addition of new peaks A and B, we assume that the symmetric environment is changed only for part of Eu^{3+}. The intensity of peaks A and B increases rapidly with increasing pressure after their appearance, and then remains unchanged afterwards. Consequently, peak B is hidden when the intensity is weak, at 550 MPa, whereas the appearance of peak A is significant.

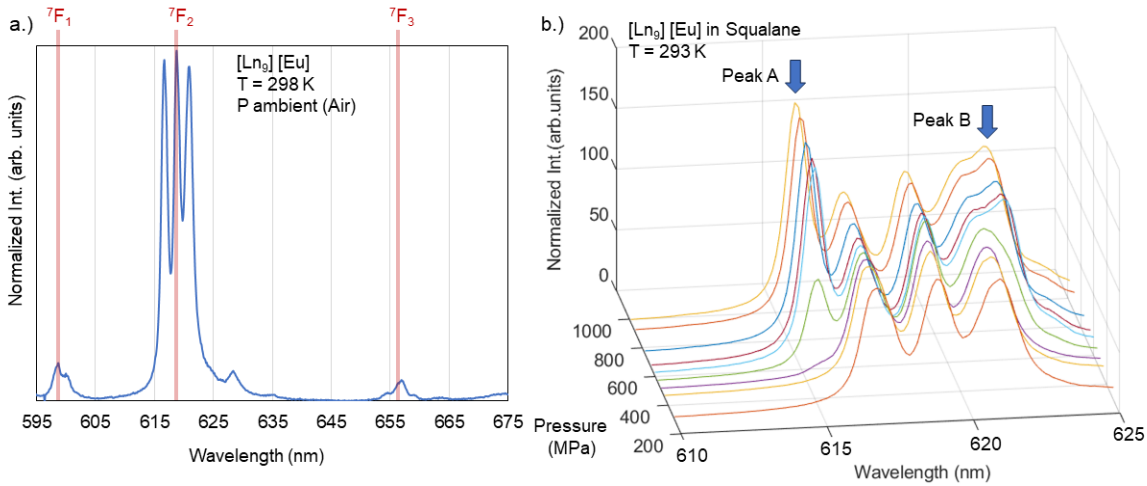

Figure 4.4: Emission spectra of $[Eu_9(acac)_{16}(\mu_3\text{-}OH)_8(\mu_4\text{-}O)(\mu_4\text{-}OH)]$ a) under ambient pressure and b) under varying hydrostatic pressure in Squalane (Emission intensity is normalized by the most intense peak, peak positions are not corrected by the intensity reference).

To check that this transition does not depend on the fluid used, another hydrophilic solvent, Nycobase 5750 is used. As shown in Figure 4.5, the appearance of peak A and peak B (too weak to be seen) is observed at the same pressure, 550 MPa.

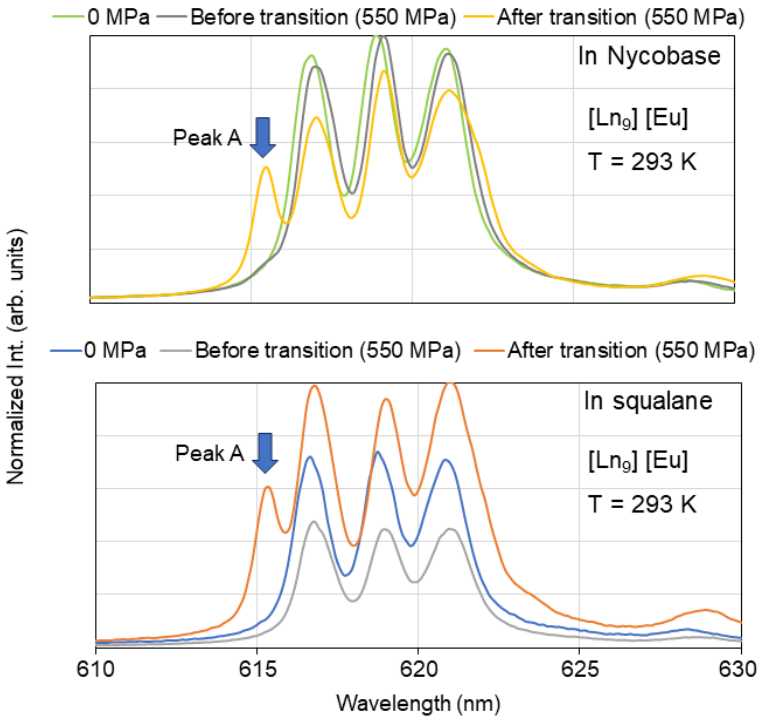

Figure 4.5: Zoomed emission spectra of $[Eu_9(acac)_{16}(\mu_3\text{-}OH)_8(\mu_4\text{-}O)(\mu_4\text{-}OH)]$ at 550 MPa in Nycobase (on top) and in Squalane (on the bottom) (Emission intensity is normalized by the most intense peak, peak positions are not corrected by the intensity reference).

4.3.2 Peak shift under pressure

The wavelength of the Eu^{3+} emission peak A from the $^5D_0 \rightarrow {}^7F_2$ transition is corrected by a neon lamp, and then plotted as a function of hydrostatic pressure in Nycobase and in Squalane, respectively, as shown in Figure 4.6. During the first cycle of pressure loading, peak A appears at 550 MPa, and remains and shifts to the right of the spectrum. The pressure-induced peak shift is highly reversible in both solvents at 293 K.

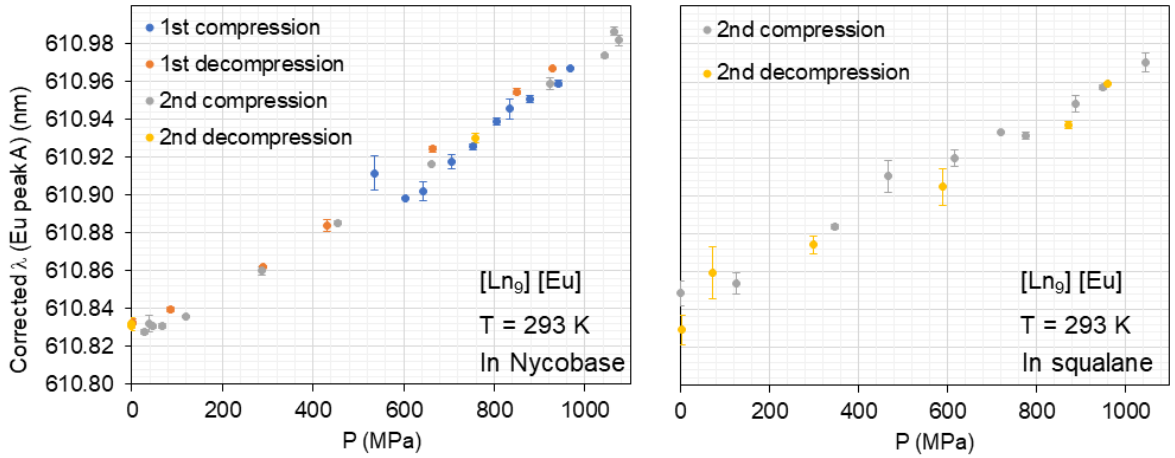

Figure 4.6: Corrected position of the Eu^{3+} peak A of $[Eu_9(acac)_{16}(\mu_3\text{-}OH)_8(\mu_4\text{-}O)(\mu_4\text{-}OH)]$ in Nycobase and in Squalane as a function of pressure.

The pressure calibration curves of the 2nd compression are shown in Figure 4.7 for Nycobase and Squalane. Peak positions vary linearly in direct proportion to pressure, with greater sensitivity to pressure for Nycobase (0.1488 nm/GPa) than for Squalane (0.1184 nm/GPa). Such results are correlated with previous reports on the red shift under pressure of Y_2O_3: Eu^{3+}.[22,26] The explanation of such behavior may be related to shielding effects of 4f electrons by outer electrons of Eu^{3+}. The generally forbidden transition 4f-4f of Eu^{3+} is allowed for the non-centrosymmetric structure due to the interaction of Eu^{3+} with odd parity crystal field. Consequently, the 4f-4f transition is highly sensitive to changes in the crystal field. Pressure-induced structural variation in the crystal lattice leads to shifts in energy levels, thus changes in emission properties as the shift of the emission peak.[26,27]

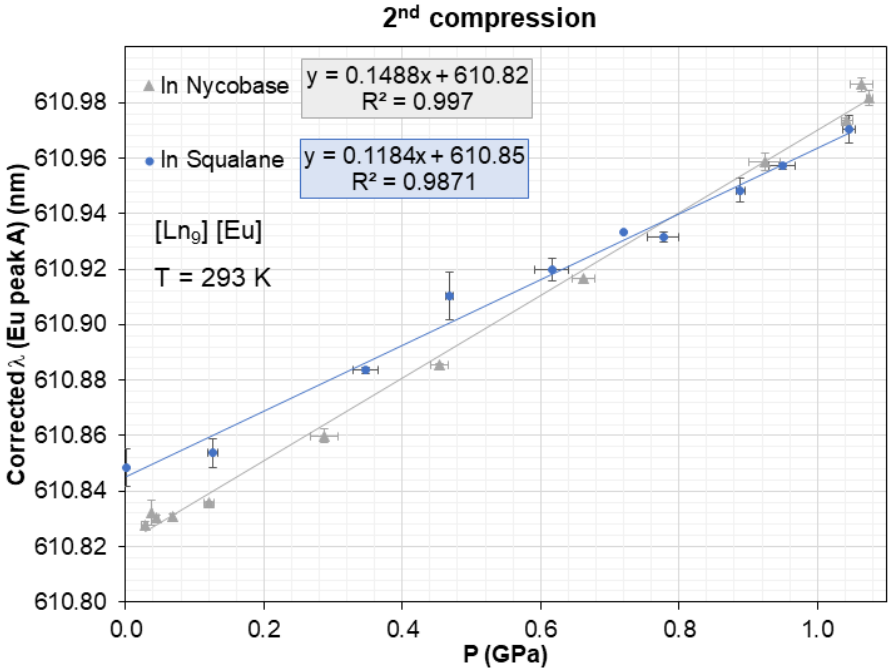

Figure 4.7: Pressure calibration curves based on the position of the Eu^{3+} peak A of $[Eu_9(acac)_{16}(\mu_3\text{-}OH)_8(\mu_4\text{-}O)(\mu_4\text{-}OH)]$ in Nycobase and in Squalane, the trendline are estimated by Excel.

The pressure sensibility of $[Eu_9(acac)_{16}(\mu_3\text{-}OH)_8(\mu_4\text{-}O)(\mu_4\text{-}OH)]$ based on the peak-shift has been studied for the $^5D_0 \rightarrow {}^7F_2$ transition. During the first cycle of pressure loading, a deformation of the peak centered at 620 nm has been observed at 550 MPa, and this variation is not reversible. The new peak centered at 610 nm shows a shift as a function of pressure. The sensibility is slightly greater for Nycobase than for Squalane. However, in low-range pressure measurements (up to 1 GPa), the sensibility should be enhanced. Moreover, by using the peak shift as a variable in the *in situ* pressure sensing, the peak shift must be corrected by a reference (see in the previous work in pressure sensing by CdSe-based QDs[15]). More importantly, this pressure sensitive peak shows up only after compression but not in the original structure, which means that this material is not applicable to pressure sensing.

4.4 Tb^{3+}-Eu^{3+} energy transfer in β-diketonate complexes

Knowing that the interionic distance strongly impacts the efficiency of Ln-Ln energy transfer (ET), pressure-induced structural contraction can be monitored by variation in emission properties. Tb^{3+} is a well-known sensitizer of Eu^{3+} due to the strong match of the energy level gap ($^5D_4 \rightarrow {}^7F_5 = {}^7F_1 \rightarrow {}^5D_1$).[28–35] Furthermore, as the emission peaks of Tb^{3+} and Eu^{3+} are mostly distinct, it is possible to analyze their emissions separately. ET between Tb^{3+}-Eu^{3+} has been reported in $[Ln_9]$ complex in previous studies.[36] This section focuses on the Tb^{3+}-Eu^{3+} ET process in Ln complexes. The impact of structures will be discussed in the

different complexes [Ln_1], [Ln_2] and [Ln_9]. As the nuclearity of the complexes is different, Tb^{3+} and Eu^{3+} ET can occur between molecules or within a single molecule.

4.4.1 Tb^{3+}-Eu^{3+} ET mechanism

The pathways of Tb^{3+}-Eu^{3+} ET are first analyzed by photoluminescent characterizations. As a simple example, the [Ln_1] complexes [Eu] and [Tb] are studied, which will be simplified as [Eu] and [Tb] in the following.

1) Spectral overlap and Tb^{3+}-Eu^{3+} ET

The emission spectra of the complex [Eu] and [Tb] under 365 nm excitation are shown in Figure 4.8a, the emissions of Eu^{3+} from $^5D_0$ are at 574 nm (to $^7F_0$), 580–590 nm (to $^7F_1$), 600–625 nm (to $^7F_2$), and 695–705 nm (to $^7F_4$). The emissions of Tb^{3+} from $^5D_4$ are at 480–510 nm (to $^7F_6$), 535–560 nm (to $^7F_5$), 575–600 nm (to $^7F_4$), 610–630 nm (to $^7F_3$), and 635–660 nm (to $^7F_2$), respectively. The main intense peak of Eu^{3+} (612 nm) is partially superimposed with one emission peak of Tb^{3+} (615 nm). In Figure 4.8b, the emission spectrum of Tb^{3+} is superimposed on the excitation spectrum of Eu^{3+} in its pure complex. The excitation spectrum of Eu^{3+} shows its main absorption: centered at 410 nm ($^7F_2$ to $^5D_3$), 465 nm ($^7F_0$ to $^5D_2$), 485 nm ($^7F_2$ to $^5D_2$), 525 nm ($^7F_0$ to $^5D_1$), 535 nm ($^7F_1$ to $^5D_1$), 580 nm ($^7F_0$ to $^5D_0$), and 590 nm ($^7F_1$ to $^5D_0$).

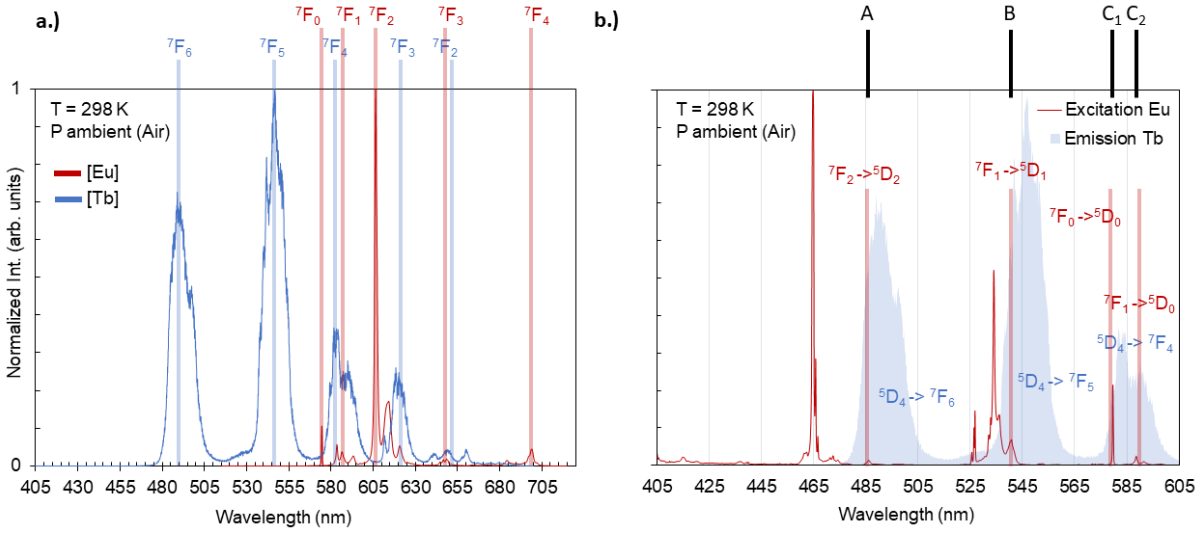

Figure 4.8: a) Emission spectra of [$Eu(acac)_3(phen)$] in red and [$Tb(acac)_3(phen)$] in blue, with the main energy transitions ($^5D_0$ (Eu^{3+}) and from $^5D_4$ (Tb^{3+}) written in red and in blue, respectively). b) Overlay of the Tb^{3+} emission spectrum (blue) with Eu^{3+} excitation spectrum of the emission at 612 nm, for $^5D_0 \rightarrow {}^7F_2$ transition (red line) in their pure complex, the assignment of the corresponding transitions of Eu^{3+} (in red) and Tb^{3+} (in blue), and the overlap noted as transitions A, B, C_1 and C_2.

In the emission spectrum of Tb^{3+}, four main overlaps are observed. According to the theory of Förster and Dexter,[37,38] these transitions centered at 486 nm, 540 nm, and 585 nm could be considered as the main pathways for Tb^{3+}-Eu^{3+} ETs at room temperature: $^5D_4 \rightarrow {}^7F_6$

= $^7F_2 \rightarrow {}^5D_2$, $^5D_4 \rightarrow {}^7F_5 = {}^7F_1 \rightarrow {}^5D_1$, and $^5D_4 \rightarrow {}^7F_4 = {}^7F_0$ (or $^7F_1$) $\rightarrow {}^5D_0$, respectively. These possible energy transfer pathways are denoted for simplicity as ET A, B, C_1, and C_2 in the proposed ET mechanism (Scheme 4.2).

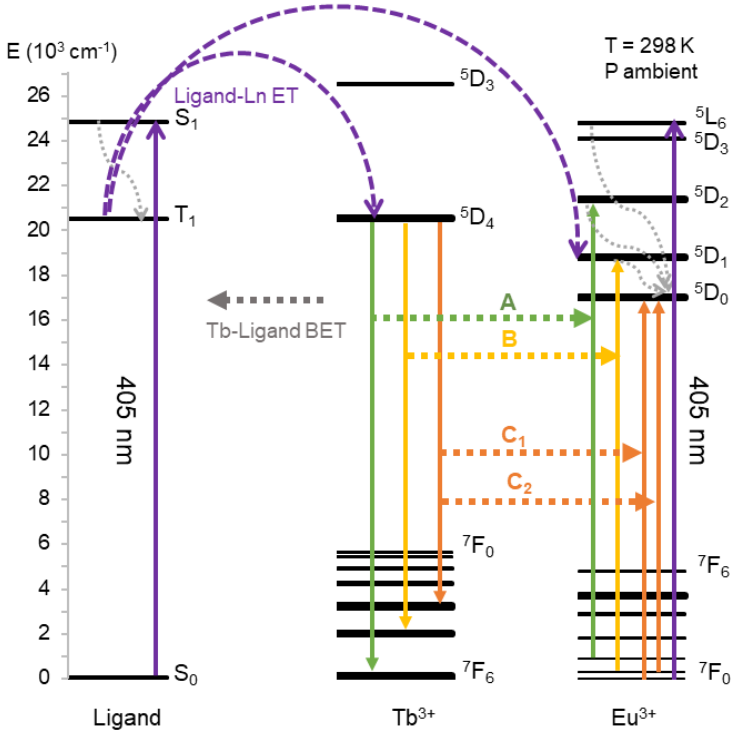

Scheme 4.2: Proposed energy transfer pathways under 405 nm laser excitation in the Ln complex (Ln = Tb, Eu). (ET: energy transfer; BET: Back energy transfer; grey dotted arrows stand for nonradiative relaxations).

2) Temperature impact on Tb^{3+}-Eu^{3+} ET: Excitation spectra

The proposed mechanism of Tb^{3+}-Eu^{3+} ET should be confirmed by the excitation spectra of the Ln complexes. The excitation spectra of Eu^{3+} and Tb^{3+} are then analyzed at room (293 K) and at low (93 K) temperature in the complex at different Ln^{3+} concentrations to analyze the impact of temperature on the Tb^{3+}-Eu^{3+} ET. As Eu^{3+} electrons can be de-excited at low temperature from $^7F_2$ or $^7F_1$ to $^7F_0$, the A or even B and C_2, ET becomes impossible.

At room temperature, the [Eu] and [Tb] complexes absorb energy from the organic ligand, as shown by a broad excitation band (405–420 nm)[39,40] at the top of Figure 4.9a & 4.9b, respectively. In the [Eu] complex, upon irradiation at 405 nm, electrons can be excited to the $^5L_6$ level, but there are no excited levels at this position for the [Tb] complex (Scheme 4.2). Thus, after excitation at 405 nm, Eu^{3+} can be excited by the organic ligand to the $^5D_1$ level[41–45] or irradiation to level $^5L_6$, whereas Tb^{3+} can be excited only by the energy transferred from the organic ligand (Scheme 4.2).[46]

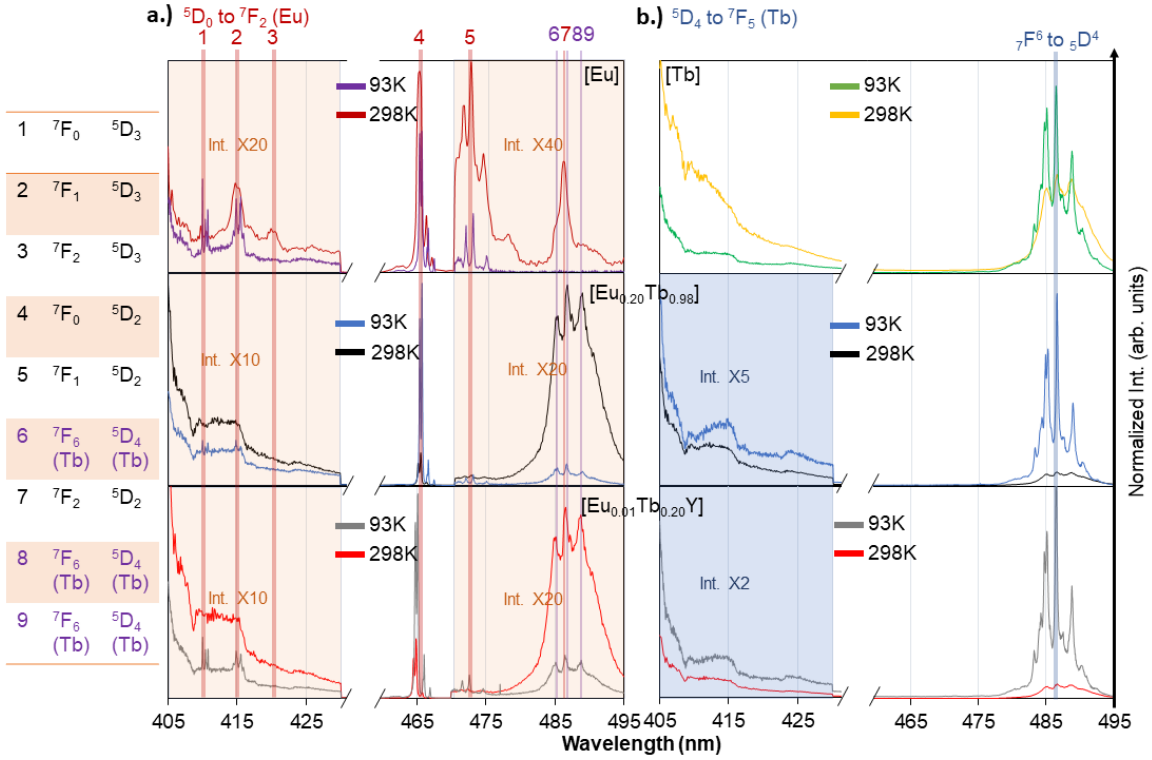

Figure 4.9: Excitation spectra of a) Eu^{3+} (emission 612 nm for the transition $^5D_0$ to $^7F_2$) and b) Tb^{3+} (emission 550 nm for the transition $^5D_4$ to $^7F_5$) in their pure complexes, and in $[Eu_{0.02}Tb_{0.98}(acac)_3(phen)]$ and $[Eu_{0.01}Tb_{0.2}Y_{0.79}(acac)_3(phen)]$ at 298 K and 93 K; The peak distributions of Eu^{3+} are presented in the table inserted. (The 'Int. X N' stands for Normalized intensity times, N)

By mixing Tb^{3+} and Eu^{3+} in the $[Ln_1]$ complex, the ET process can be visualized in the excitation spectra. Two compositions $[Eu_{0.02}Tb_{0.98}]$ and $[Eu_{0.01}Tb_{0.2}Y_{0.79}]$ of $[Ln_1]$ complexes are selected. The excitation spectra of the complexes $[Eu_{0.02}Tb_{0.98}]$ and $[Eu_{0.01}Tb_{0.2}Y_{0.79}]$ are shown in the middle and bottom of Figure 4.9, respectively. Here, compared to the [Eu] complex, the presence of Tb^{3+} adds an intense absorption peak centered at 485 nm, corresponding to the transition of Tb^{3+} from $^7F_6$ to $^5D_4$. However, the presence of Eu^{3+} does not have a significant impact on the Tb^{3+} excitation spectra, meaning that the BET of Eu^{3+} to Tb^{3+} is negligible in this current complex.

The impact of temperature can be observed in the overall excitation spectra of the [Eu] complex: the excitation intensity decreases considerably at 93 K compared to room temperature, whereas the excitation pathways from level $^7F_2$ disappear (peaks 3 and 7) as expected. The same peaks also disappear in the $[Eu_{0.02}Tb_{0.98}]$ and $[Eu_{0.01}Tb_{0.2}Y_{0.79}]$ complexes. The absorption of the organic ligand toward Tb^{3+} decreases at 93 K (Figure 4.9b, top). The effects of temperature on the Tb-Eu ET can also be observed in the $[Eu_{0.02}Tb_{0.98}]$ and $[Eu_{0.01}Tb_{0.2}Y_{0.79}]$ complexes. The Tb^{3+}absorption (peaks 6, 8 and 9, in the violet line) decreases significantly in the Eu^{3+} excitation spectra at low temperature due to the reduction in ET from Tb^{3+} (Figure 4.9a, middle and bottom). Furthermore, an increase in the overall excitation intensity of Tb^{3+}, and more significant at 486 nm (Figure 4.9b) allows us to confirm this deduction (Figure 4.9b, middle and bottom). Here, upon excitation at 405 nm, the cross-

relaxation of Tb^{3+} is not considered, because the highest energy level reached by Tb^{3+} through the ET ligand will be the $^5D_4$ level. However, cross-relaxation of Eu^{3+} should be observed when the Eu concentration is high.[28] However, these processes will not be problematic for our future experiments given the low concentration of Eu in the complex.

4.4.2 Structural impacts on ET

Possible pathways of Tb^{3+}-Eu^{3+} ET were determined by the above photoluminescent characterizations of the [Ln_1] complex. According to FRET theory, the distance dependence of the ET rate is given by R^6.[47] For Ln^{3+}-Ln^{3+} ET to occur, it is necessary for two Ln^{3+} ions to be in close proximity to each other, reaching a critical distance known as R_0. This critical distance is defined as the point at which the probability of ET and spontaneous deactivation of the ion donor starts to equalize. The R_0 is generally 10 Å in a dipole-dipole (Ln^{3+}-Ln^{3+}) FRET system. Consequently, the interionic distance is crucial for Tb^{3+} -Eu^{3+} ET to occur in the Ln complex. In this section, structural impacts will be discussed with the [Ln_1], [Ln_2] and [Ln_9] complexes.

Under 405 nm excitation, the emission spectra of the [Ln_1], [Ln_2] and [Ln_9] complexes of composition [$Eu_{0.15}Tb_{0.85}$] are shown in Figure 4.10. [The peak attributed to the Tb^{3+} $^5D_4 \rightarrow {}^7F_5$ transition, at 535–560 nm is visible in the spectra of [Ln_1] and [Ln_9], whereas this peak is too weak to be detected in the [Ln_2] complex. The Eu^{3+} peak from the transition at 610–630 nm ($^5D_0 \rightarrow {}^7F_2$) is intense in all complexes, but the peak shape is different due to the different Eu^{3+} symmetry sites in the complex.[21] We noted that the emission intensity of [Ln_9] is smaller than that of [Ln_2] and [Ln_1]. The *antenna effect* is strongly dependent on the type of ligand, which is assumed to be the reason for the difference in emission intensity of the complex. Further analysis by quantum yield measurement is required to better understand this phenomenon. Tb^{3+}-Eu^{3+} ET has been observed in the [Ln_9] complex at a similar composition,[23,36] and Tb^{3+} -Eu^{3+} ET has also been verified in other compositions of the [Ln_1] complex previously in section 4.4.1. The possibility to allow Tb^{3+}-Eu^{3+} ET in the [Ln_1] at different composition and in the [Ln_2] complex will thus be discussed.

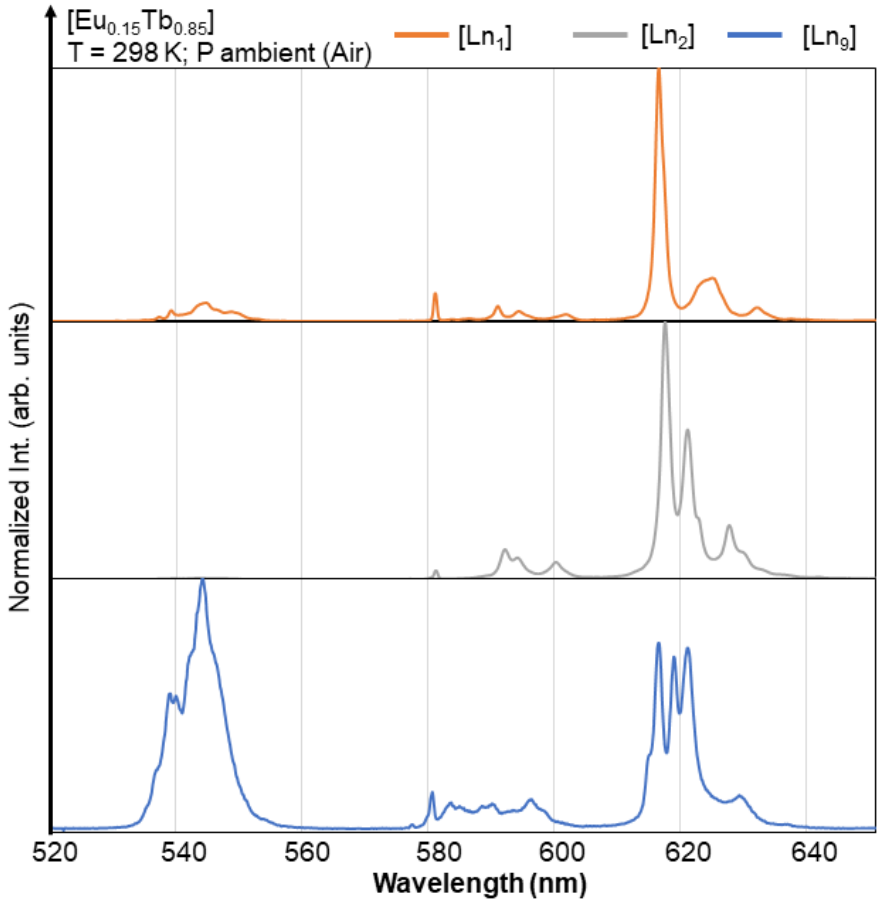

Figure 4.10: Emission spectra of [Ln_1], [Ln_2] and [Ln_9] complexes at composition [$Eu_{0.15}Tb_{0.85}$], shown in orange, grey and blue line respectively (Emission intensity is normalized by the most intense peak).

The structures are presented in Figure 4.11, the nonanuclear complex Ln9, binuclear complex [Ln_2] and mononuclear complex [Ln_1]. The shortest intramolecular distance between two Ln atoms is around 4 Å in multinuclear complex, and the shortest intermolecular distance is around 10 Å in [Ln_9] and [Ln_2], 8 Å in [Ln_1]. More information can be found in Chapter 2, section 2.4.3 and in Table A2.

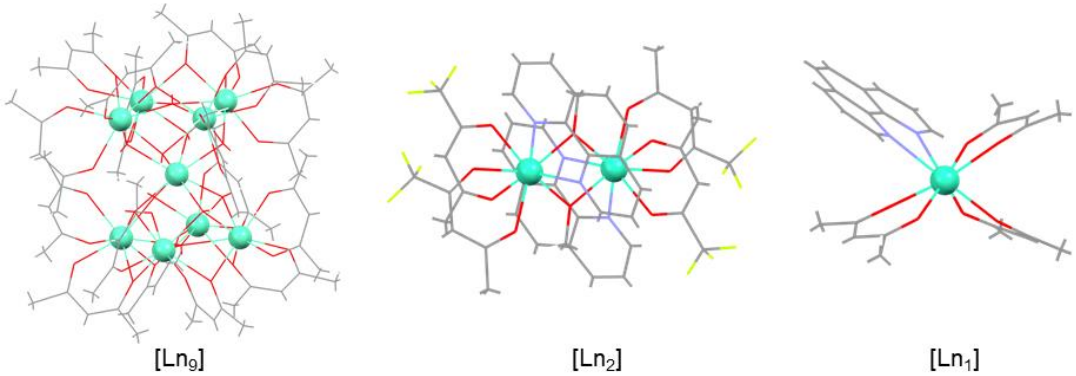

Figure 4.11: Crystal structure of Ln complex [Ln_9], [Ln_2] and [Ln_1], only the Ln atom is shown in ball styles for clarity; The entire structure can be found in Chapter 2.

According to FRET theory, the distance dependence of the ET rate is given by R^6 in a dipole-dipole system.[37,38,47–49] In [Ln_2] and [Ln_9] complexes, the efficiency of Tb^{3+}-Eu^{3+} ET occurring in the intermolecular system is approximately 250 times less than that in the intramolecular system. Consequently, when Tb^{3+}-Eu^{3+} ET is allowed in the complex, intermolecular ET may be negligible compared to intramolecular ET. However, in the mononuclear complex [Ln_1], only intermolecular ET occurs.

Upon excitation at 405 nm, the organic ligands of Ln^{3+} complex are activated, and the electrons from the S_1 state then move to the T_1 state by nonradiative relaxation or IC, for further ET to Ln^{3+} (L-M). However, we assume that the distance between ligands is too great for the π-π interaction to occur, and therefore there is no ET between the ligands in [Ln_1] and [Ln_2] complexes.[39,50] As mentioned earlier in section 4.3.1, both Tb^{3+} and Eu^{3+} accept the transferred energy from the organic ligand to reach their excited state, Tb^{3+} to $^5D_4$ and Eu^{3+} to $^5D_2$, respectively. Furthermore, Eu^{3+} can also be partially excited by laser irradiation at the same wavelength. Subsequently, the excited electrons of Ln^{3+} are deactivated by radiative decay or by ET. The interaction between the ligand and the emitted center, here the Ln^{3+}, enhances the Ln^{3+} emission upon ligand excitation, which is usually called the '*antenna effect*'. As previously observed, with 405 nm irradiation, the absorption from the ligand is intense in the excitation process of Tb^{3+} and Eu^{3+}. Considering the energy transfer between Tb^{3+}-Eu^{3+} in the system, Eu^{3+} could thus be excited by a) direct irradiation with a 405-nm laser, b) ligand-Eu^{3+} ET, or c) Tb^{3+}-Eu^{3+} ET. Furthermore, other nonradiative ET pathways must also be considered.[51]

Studies of the Tb^{3+} -Eu^{3+} ET process are divided into two parts: intramolecular ET in the [Ln_2] complexes, and intermolecular ET in the [Ln_1] complexes. As Tb^{3+} -Eu^{3+} ET has been proven in the [Ln_9] complex, and the Tb^{3+} -Eu^{3+} distance in the [Ln_2] complex is similar to that in the [Ln_9] complex, ET should also be allowed.[37,38,47] Tb^{3+} -Eu^{3+} ET in the [Ln_2] complex will be characterized by excitation spectra. On the other hand, intermolecular ET occurring in the [Ln_1] complex will be strongly impacted by the surrounding environment. The other possible ET process between the ligand and Ln may interfere with the Tb^{3+} -Eu^{3+} ET. Therefore, the discussions of intermolecular ET occurring in [Ln_1] complex address the Tb^{3+}/Eu^{3+} ratio, the dilution by Y^{3+} and the O_2-quenching.

1) Intramolecular ET

Figure 4.12 shows the excitation spectra of the [Ln_2] complex at different compositions. Ligand excitation is observed between 405 and 445 nm in all excitation spectra. The excitation peaks attributed to the $^7F_6$ to $^5D_4$ transition of Tb^{3+} and the $^7F_2$ to $5D_0$ transition of Eu^{3+} are shown in the spectrum of [$Eu_{0.5}Tb_{0.5}$], so Eu^{3+} can be excited by energy transferred from the ligand and Tb^{3+}.

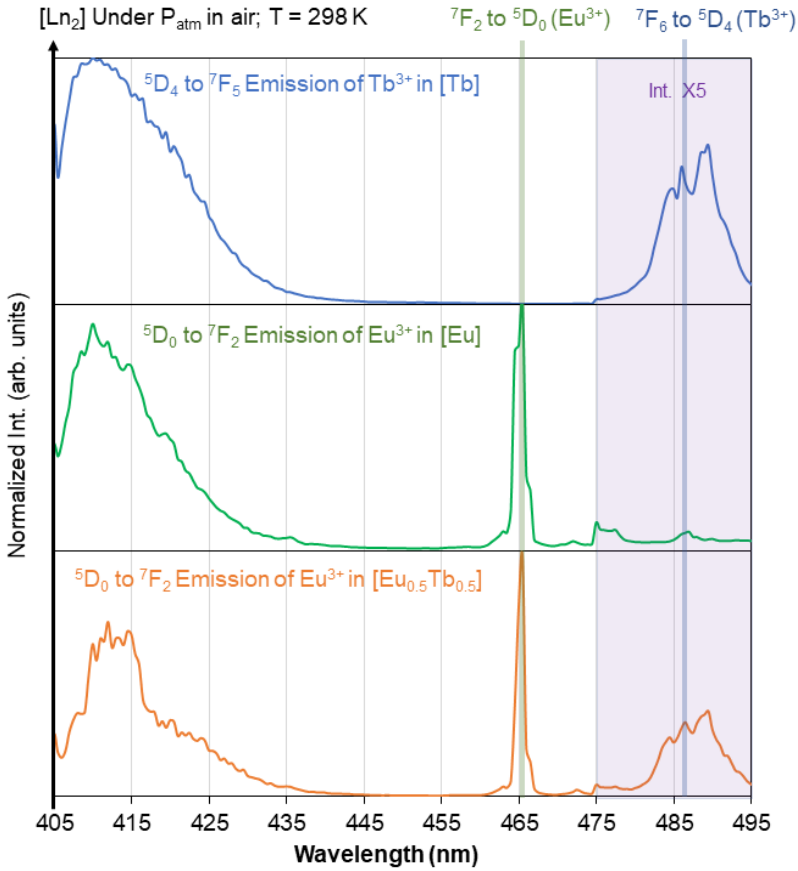

Figure 4.12: Excitation spectra of [Ln_2] complex at [Tb] shown in blue line (emission 550 nm for the transition $^5D_4$ to $^7F_5$), at [Eu] and [$Eu_{0.5}Tb_{0.5}$] shown in green and orange line (emission 612 nm for the transition $^5D_0$ to $^7F_2$) at 298K.

Figure 4.13 shows the emission spectra of [Ln_2] complex at various compositions. The intensity is normalized by the most intense peak. Emission of Eu^{3+} from 610 to 630 nm is intense, whereas the Tb^{3+} peak centered around 550 nm is too weak, only the one at [$Eu_{0.01}Tb_{0.99}$] can be observed. Because the distance between Tb^{3+}-Eu^{3+} is small in [Ln_2] complex, the Tb^{3+}-Eu^{3+} ET is considerably efficient. The presence of Eu^{3+}, even at small concentration, significantly reduces the emission of Tb^{3+}. Considering further applications based on the relative emission intensity of Tb^{3+} and Eu^{3+}, the concentration of Eu^{3+} should be small to optimize the accuracy of measurement, the composition at [$Eu_{0.01}Tb_{0.99}$] is by far the most adapted candidate.

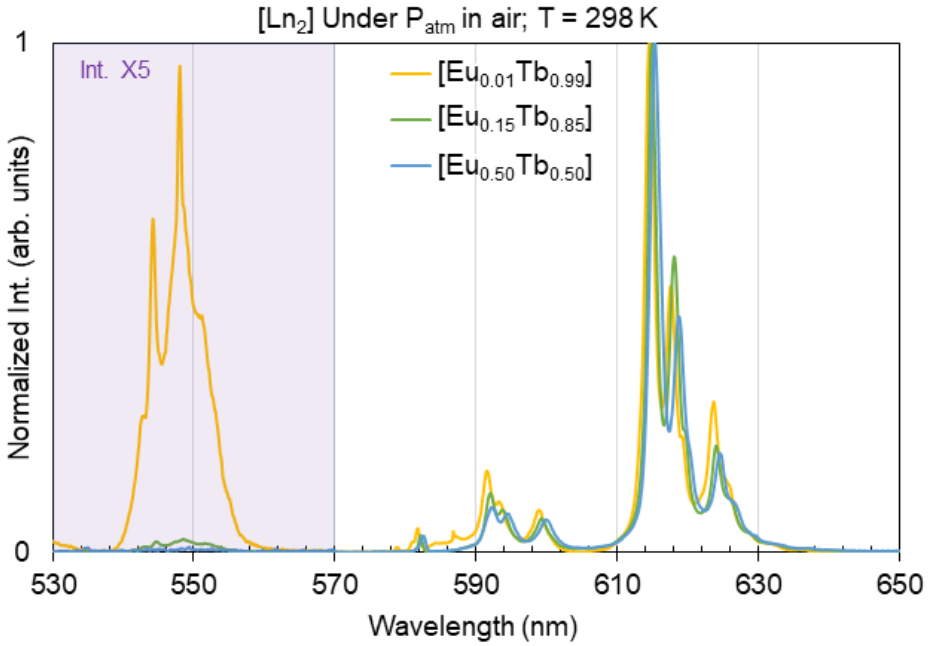

Figure 4.13: Emission spectra of [Ln_2] complexes at [$Eu_{0.01}Tb_{0.99}$], [$Eu_{0.15}Tb_{0.85}$] and [$Eu_{0.50}Tb_{0.50}$] shown in yellow, green, and blue, respectively (Emission intensity is normalized by the most intense peak).

2) Intermolecular ET in [Ln_1] complex

The efficiency of intermolecular ET can be strongly impacted by parameters such as the average distance between Ln^{3+} ions and the interaction between the ligand and Ln^{3+} ions. In this section, the influence of Ln^{3+} compositions on the efficiency of Tb^{3+}-Eu^{3+} ET will be studied. Moreover, the O_2-quenching effect has been reported in the [Ln_1] complex [Tb],[52,53] the influence of the presence of O_2 will also be discussed. However, characterizations by excitation and emission spectra are not optimized to compare ET efficiency, so time-resolved measurements of [Ln_1] complexes are applied in the following.

- **Intermolecular Tb^{3+}-Eu^{3+} ET with different composition [EuTb]**

In Figure 4.14a and 4.14b, the lifetimes of Tb^{3+} and Eu^{3+} are shown for different Eu^{3+} concentrations, respectively. The rise time of Tb^{3+} has not been observed because the ligand-Tb^{3+} ET is too fast (in the nanoseconds range).[39,54] However, a rise time of Eu^{3+} is presented in Figure 4.14b, thus besides the fast ligand-Eu^{3+} ET, the Ln^{3+}-Ln^{3+} ET occurs with Eu^{3+} as an acceptor. At room temperature, interionic ET between Tb^{3+} and Eu^{3+} is an important mechanism when the interionic distance is smaller than the critical distance R_0.[28,29] The considerable reduction in the decay time of the Tb^{3+} emission in complexes with Eu^{3+} indicates the transfer of energy from the $^5D_4$ level of Tb^{3+} to excite Eu^{3+}.[31,50,55] Figure 4.14a shows that the decay time of Tb^{3+} emission decreases with increasing Eu^{3+} concentration, corresponding to the same variation in Eu^{3+} rise time (Figure 4.14b), which can be described by the simplified model equation (Equation 4.1): [30,32,34,56–58]

$$n = \left[n_0 + n_1\left(1 - \exp\left(\frac{-t}{\tau_1}\right)\right)\right]\exp\left(\frac{-t}{\tau_2}\right)$$

Equation 4. 1

Where n and n_0 are the number of electrons in the excited level at time t ant t_0, respectively; τ_2 is the decay time from the upper level; n_1 presents the number of electrons in the feeding level; and τ_1 is the time for feeding this level. This model will be used to fit the decay-time curves; the fitted curve is shown in Figure 4.15 for the complex [$Eu_{0.15}Tb_{0.85}$] as an example (Tb^{3+} decay time τ_1 = 0.2225 ms; Eu^{3+} decay time τ_2 = 0.7434 ms). The fitted decay time of Tb^{3+} (transition $^5D_4 \rightarrow {}^7F_5$ at 550 nm) and Eu^{3+} (transition $^5D_0 \rightarrow {}^7F_2$ at 612 nm) in their pure complex are 0.7143 ms and 0.7131 ms, respectively, which agree well with reported values.[34,59,60]

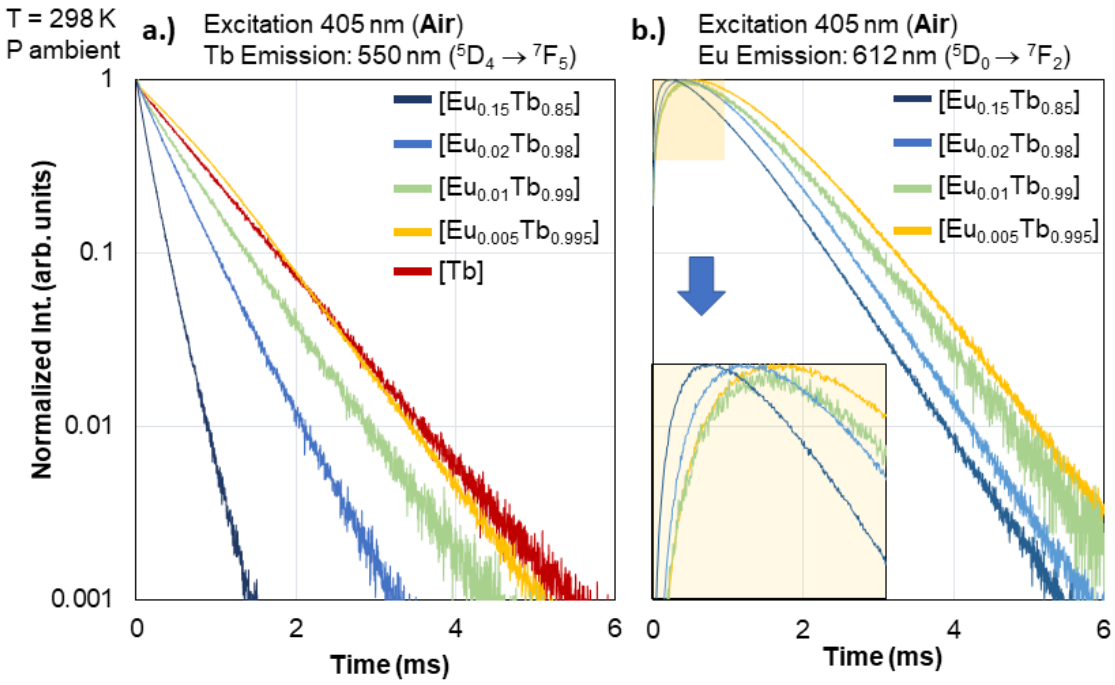

Figure 4.14: Lifetime measurements of a) Tb^{3+} and b) Eu^{3+} in the complex [Ln_1] [$Eu_xTb_{1-x}(acac)_3(phen)$].

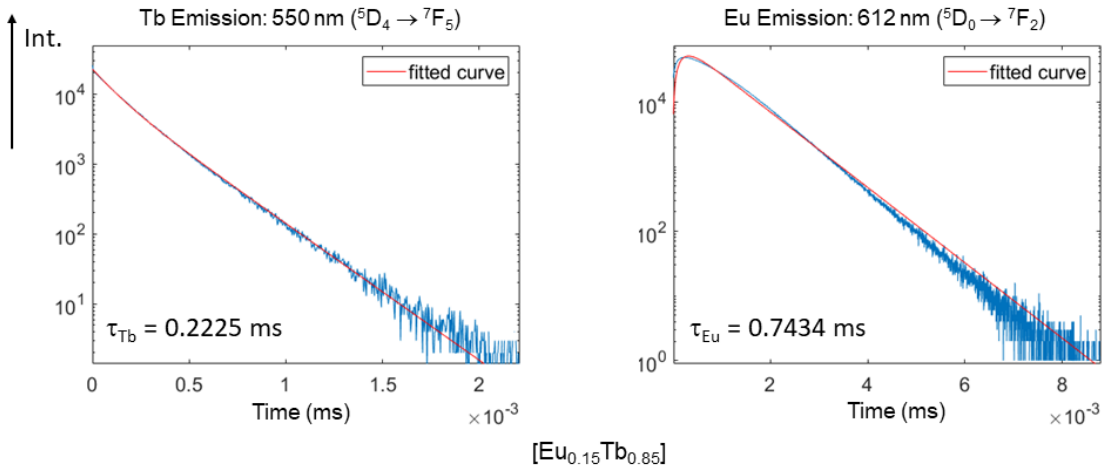

Figure 4.15: Experimental curve and fitted curve of lifetime measurements of a) Tb^{3+} and b) Eu^{3+} in the [$Eu_{0.15}Tb_{0.85}$] complex in air, Tb^{3+} emission at 550 nm and Eu^{3+} emission at 612 nm under 405 nm excitation.

Therefore, in a system with such a high concentration of Tb^{3+} relative to Eu^{3+}, Tb^3-Eu^{3+} ET still occurs even if the concentration of Eu^{3+} is low (0.5 mol%). It can be considered that the doped Eu^{3+} are always surrounded by their sensitizer (Tb^{3+}). Thus, the more Eu^{3+} in the complex, the more Tb^{3+} ions are deactivated by Eu^{3+}, resulting in a decrease in Tb^{3+} decay time with increasing Eu^{3+} concentration. Furthermore, assuming that the proportion of excited Tb^{3+} ions via nonradiative relaxation is negligible, the rise time of Eu^{3+} is equal to the Tb^{3+} decay time, which corresponds to the feeding time of Eu^{3+} by Tb^{3+}. However, the decay time of Eu^{3+} is not significantly influenced by the presence of Tb^{3+}.

- **Addition of yttrium as an optical diluent**

The impact of the Y^{3+} diluent on the Tb^{3+}-Eu^{3+} ET was studied in different compositions. First, lifetime measurements of Tb^{3+} of the complex were performed. As shown in Figure 4.16a, the Tb^{3+}decay time of [Tb] is identical to that of [$Tb_{0.2}Y_{0.8}$], and from 80 mol.% of Y^{3+}, increasing the dilution by Y^{3+} leads to a decrease in the Tb^{3+} decay time. The decrease in Tb^{3+} decay time has also previously been observed due to adding Eu^{3+}, which has been assumed to be an indicator of ET. As there is no ion acceptor in [Tb_xY_{1-x}] complexes, O_2 present in air may be the main cause of the decrease in Tb^{3+} decay time, because the presence of O_2 disrupts the ligand-Ln^{3+} ET because O_2 replaces Ln^{3+} as an energy acceptor. When the O_2 molecule is close enough to the ligand to activate energy quenching, rather than exciting Ln^{3+}, the ligand transfers energy to the triplet state of O_2. This phenomenon is known as O_2 quenching in ligand-excited phosphor.[52,53] Because of O_2 quenching, the highly diluted (> 80 mol%) complex shows significant reductions in the Tb^{3+} decay time. As the Y^{3+} concentration increases, the Tb^{3+} concentration decreases in the [Tb_xY_{1-x}] complex, and under ambient pressure in air, the O_2 quenching effect is greater at lower Tb^{3+} concentrations.

Subsequently, 1 mol% Eu^{3+} was added to the system, and the Tb^{3+} lifetime was measured for the complexes [$Eu_{0.01}Tb_xY_{0.99-x}$], where x = 0.99, 0.20, 0.10, and 0.1. As shown in Figure 4.16b, adding 1 mol% Eu^{3+} in the dilute system further decreases the Tb^{3+} decay time, besides

interfering with O_2 quenching. The reduction in Tb^{3+} decay time is greater with increasing Y^{3+} concentration. The reason may be that the decrease in Tb^{3+} concentration makes the reduction in Tb^{3+} decay time due to the Tb^{3+}-Eu^{3+} ET more visible, or the O_2-quenching effect is more important with decreasing Tb^{3+} concentration, or both. Therefore, to reduce the O_2-quenching effect, the sample was confined in a closed cell for 5 min of N_2 flow to minimize the O_2 concentration in the measurement environment. Lifetime measurements were again performed for the complex at the same compositions under N_2 flow. As shown in Figure 4.16c, in contrast to the previous measurement in air, the Tb^{3+} decay curves under N_2 are all identical regardless of the Tb^{3+} concentration and are identical to the Tb^{3+} decay curve in [Tb] in air. This is because O_2 quenching causes Tb^{3+} decay time to decrease and the N_2 atmosphere has reduced O_2 quenching. Furthermore, when O_2 quenching no longer disrupts the ligand-Tb^{3+} interaction, Eu^{3+}-induced decreases in Tb^{3+} decay times are still observed, but they are slightly lower than measurements in air (Figure 4.16d). Therefore, O_2 quenching does not affect the Tb^{3+}-Eu^{3+} ET in the complex.

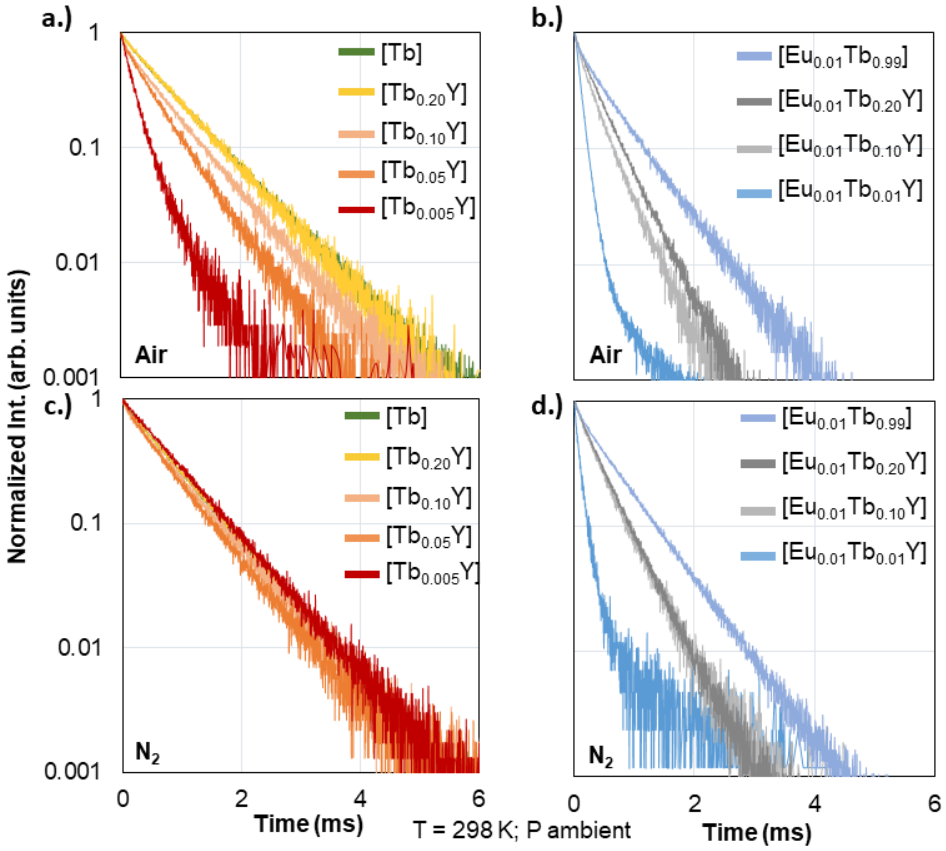

Figure 4.16: Lifetime measurements of Tb^{3+} in the $[Ln_1]$ $[Tb_xY_{1-x}(acac)_3(phen)]$ complex a). in air and c). under 1 atm N_2; lifetime measurements of Tb^{3+} in the $[Eu_{0.01}Tb_xY_{0.99-x}(acac)_3(phen)]$ complex b). in air and d). under 1 atm N_2. (Excitation at 405 nm; Tb emission at 550 nm)

The change in atmosphere will not have a significant impact on the Eu^{3+} decay time regardless of the Eu^{3+} concentration because Eu^{3+} can also be excited by the 405 nm laser (Scheme 1). As shown in Figure 4.17, even the Eu^{3+} decay time in $[Eu_{0.05}Y_{99.5}]$ is identical to

that in [Eu], as expected. Furthermore, we noted in Figure 4.16a and 4.16c that O_2-quenching interference was only significant at low Tb^{3+} concentration (< 20%). To confirm this hypothesis, the measurement of the lifetime of [Eu_xTb_{1-x}], where x = 0.15; 0.02; 0.01; 0.005; and 0, in the N_2 atmosphere was also performed (Figure 4.18) to complement the previous measurement in Figure 4.14, which shows a negligible difference compared to the measurement in the air. As expected, O_2 quenching has no significant effect on the undiluted system [Eu_xTb_{1-x}].

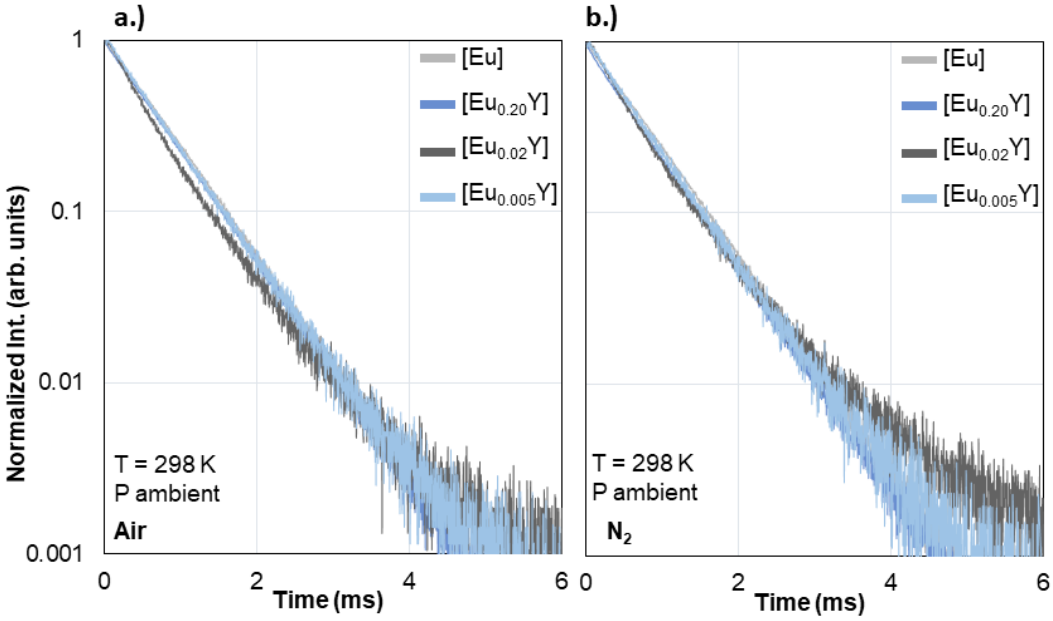

Figure 4.17: Lifetime measurements of Eu^{3+} in the [Ln_1] [Eu_xY_{1-x}] complex a) in air and b) Under 1 atm N_2 to eliminate O_2-quenching, Eu^{3+} emission at 612 nm under 405 nm excitation.

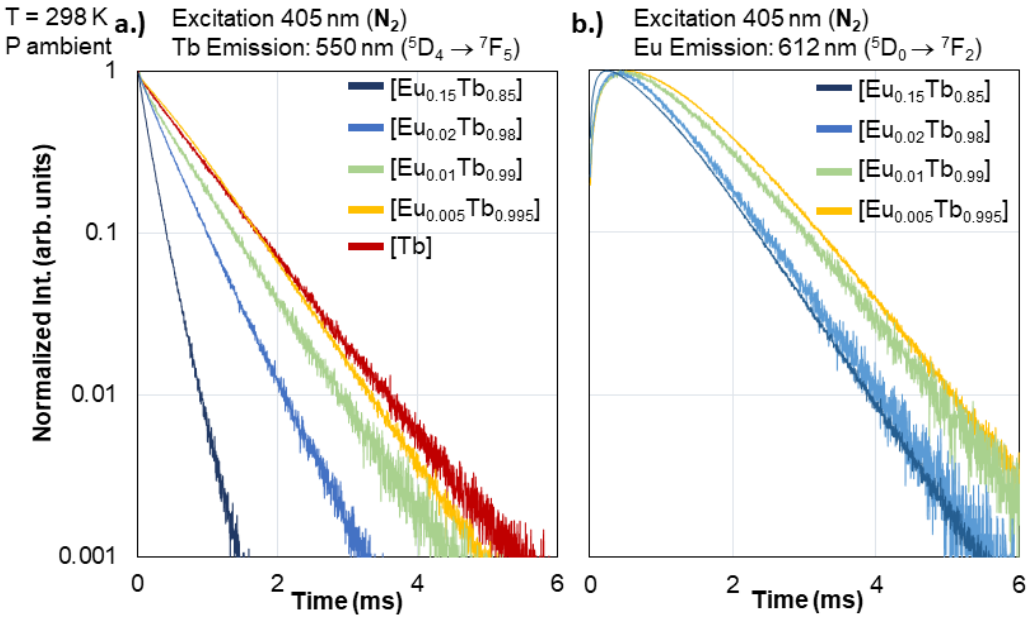

Figure 4.18: Lifetime measurements of a) Tb^{3+} and b) Eu^{3+} in the [Ln_1] [Eu_xTb_{1-x}] complex under 1 atm N_2 to eliminate O_2-quenching.

In the Y^{3+}-diluted system, it was found that Tb^{3+}-Eu^{3+} ET still occurs even at low Tb^{3+} concentration, the reduction of Tb^{3+} decay time, and Eu^{3+} rise time are observed in the $[Eu_{0.01}Tb_{0.01}Y_{0.98}]$ complex (Figure 4.16d and Figure 4.19, respectively). Therefore, Tb^{3+}-Tb^{3+} energy migration may play a critical role in highly dilute systems on the enhancement of Tb^{3+}-Eu^{3+} ET efficiency. Furthermore, increasing the concentration of Y^{3+} decreases the Tb^{3+} decay time (Figure 4.16d) and the Eu^{3+} rise time (Figure 4.19), which theoretically stands for the optimization of Tb^{3+}-Eu^{3+} ET efficiency. However, in this study, increasing the concentration of Y^{3+} leads to a reduction in the absolute emission intensity of Tb^{3+} and Eu^{3+}. This observation was not quantified using an emission intensity reference. Therefore, the decrease in Tb^{3+} decay time and the Eu^{3+} rise time may be caused by other quenching effects, but not the increase in Tb^{3+}-Eu^{3+} ET efficiency.

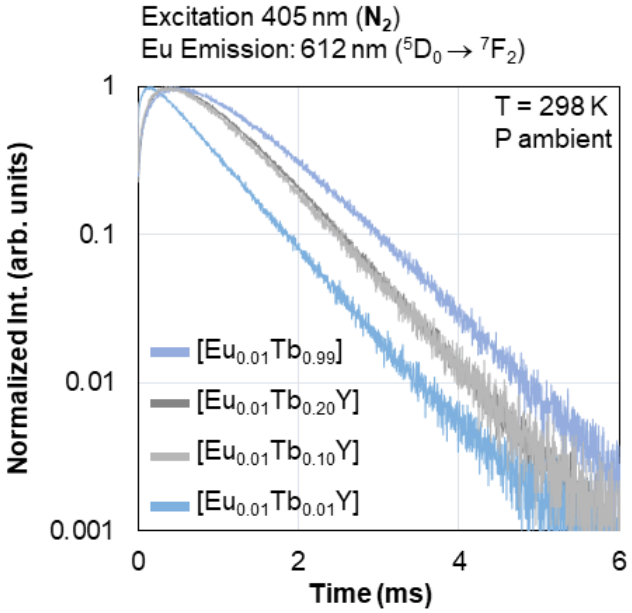

Figure 4.19: Lifetime measurements of Eu^{3+} in the $[Ln_1]$ $[Eu_{0.01}Tb_xY_{0.99-x}]$ complex under 1 atm N_2 to eliminate O_2-quenching.

In conclusion, dilution with Y^{3+} induces a decrease in the Tb^{3+} concentration, which makes the O_2-quenching effect more significant, and leads to a reduction in the emission intensity of Tb^{3+} and Eu^{3+}. To date, dilution by Y^{3+} has only a negative impact on the photoluminescent emission of the complex. However, in such a highly concentrated Tb^{3+} or Eu^{3+} system, the concentration quenching phenomenon must be carefully considered.[40,48,51] Dilution with optically neutral ions such as Y^{3+} can improve the intensity of the emission due to the protection of the emitter from concentration quenching.[61] However, in the current complex, the decay time of Tb^{3+} can be correctly measured even at high Tb^{3+} concentration (Figure 4.14a). Furthermore, dilution with Y^{3+} does not affect the Tb^{3+} decay time when O_2 quenching is eliminated (Figure 4.16c). These results show that Tb^{3+} concentration quenching is not significant enough to be observed in the present system, probably because the samples are well crystallized after synthesis, thus the structural defect may be negligible. Although the Tb^{3+} concentration quenching has not been observed so far, it should be a concern for further

pressure-sensing applications due to the possible pressure-induced structural defect. The structural deformation of the [Tb(acac)$_3$(phen)] complex has been observed under mechanical impact.[62] Therefore, in Section 4.5, Y^{3+}-diluted complexes are studied, but only compositions with a high Tb^{3+} concentration (> 20 mol%) are considered to minimize interference from O_2 quenching.

4.5 Luminescent-intensity-based manometry

The luminescent-intensity-ratio (LIR), or relative emission intensity, is one of the most widely used variables in optics. By calculating the ratio of two distinct emission intensities, the LIR allows us to neglect any impact on the absolute intensity which might be difficult to control in real measurement. If the interaction between two emissive levels can be influenced by the environment, such as temperature, interionic distance, or symmetry of the crystal structure, the LIR reflects their response to environmental variation. Thus, the LIR is considered as a popular variable in many sensing applications.

In the Tb^{3+} and Eu^{3+} complex, the LIR of the Tb^{3+}/Eu^{3+} emission could be calculated by its main peak; the Tb^{3+} peak (at 530-550 nm, zone A) and the Eu^{3+} peak (600-630 nm, zone C) as shown in Figure 4.20 with the emission spectra of [Ln_1] complex [$Eu_{0.02}Tb_{0.98}$] as the example. Assuming that the dispersion of Ln^{3+} is homogenous in the whole crystal, and all the Eu^{3+} are excited by energy from Tb^{3+}-Eu^{3+} ET, the LIR represents the ratio of Tb^{3+} electrons deactivated through radiative relaxation to those deactivated through Tb^{3+}-Eu^{3+} ET. Therefore, at room temperature, in a given complex at a given concentration of Tb^{3+} and Eu^{3+}, the LIR could be a parameter to quantify the amount of energy transferred from Tb^{3+} to Eu^{3+}. To understand the impact of pressure on the Tb-Eu ET process in the complex, the LIR is then used as a reliable variable to quantify the Tb^{3+}-Eu^{3+} ET.

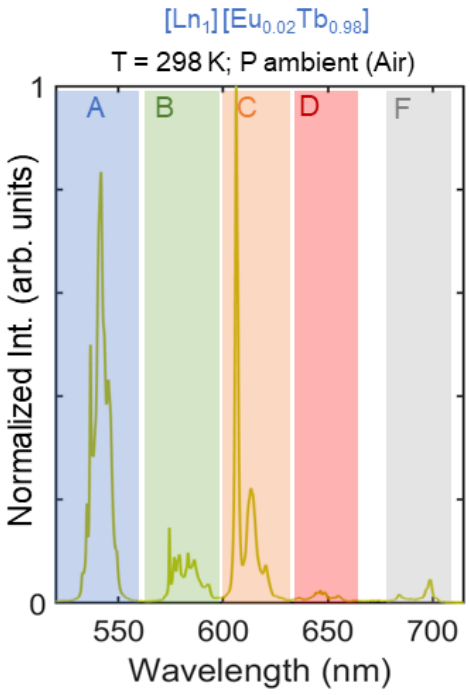

Figure 4.20: Distribution of the emission peak in the complex [$Eu_{0.02}Tb_{0.98}(acac)_3(phen)$]: A for $^5D_4$ to $^7F_5$ (Tb^{3+}), B for $^5D_0$ to $^7F_{0\&1}$ (Eu^{3+}) and $^5D_4$ to $^7F_4$ (Tb^{3+}), C for $^5D_0$ to $^7F_2$ (Eu^{3+}) and $^5D_4$ to $^7F_3$ (Tb^{3+}), D for $^5D_0$ to $^7F_3$ (Eu^{3+}) and $^5D_4$ to $^7F_{2\&1}$ (Tb^{3+}), and F for $^5D_0$ to $^7F_4$ (Eu^{3+}).

This section focuses on the pressure-induced variation on LIR, in order to explore the potential LIR-based pressure sensor among the complexes [Ln_1], [Ln_2] and [Ln_9].

4.5.1 [$Ln(acac)_3(phen)$]

First, to select the adapted composition of [Ln_1] complex, the influence of the Ln^{3+} concentration is studied. The LIR of Tb^{3+}/Eu^{3+} is plotted as a function of the Eu^{3+} concentration at room temperature (298 K), with different concentrations of Y^{3+} as the diluent in Figure 4.21. The LIR strongly depends on the Eu^{3+} concentration: when the Eu^{3+} concentration ranges between 0 and 5 mol%, the LIR decreases rapidly with increasing %Eu. However, compared to the effect of Eu^{3+} concentration, the diluent Y^{3+} concentration has a smaller impact on the LIR value. The conclusion is consistent with the previous results on decay time.

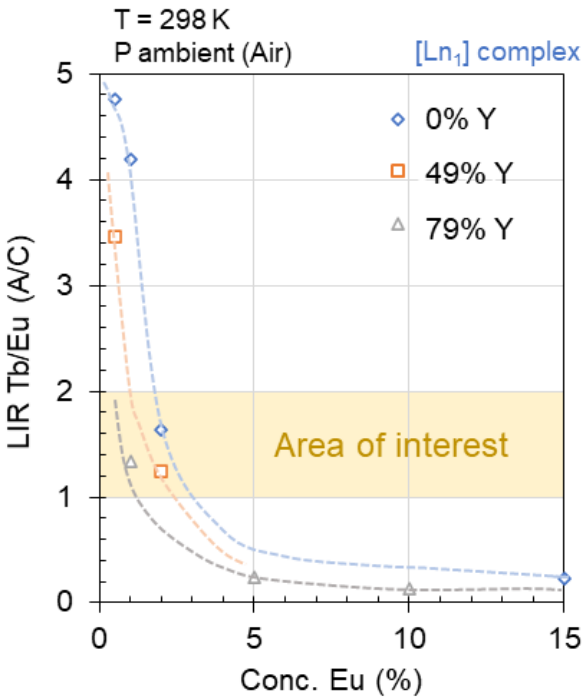

Figure 4.21: Calculated luminescent-intensity-ratio (LIR) at different compositions at 298 K with the estimated trend lines in the dotted line, the area of interest with 1 < LIR < 2.

According to the previous conclusion, at a given temperature, in the same composition as Ln^{3+}, the LIR depends on the efficiency of the Tb^{3+}-Eu^{3+} ET process that occurred in the system. Theoretically, the decrease in the interionic distance of Tb^{3+}-Eu^{3+} leads to a significant increase in the Tb^{3+}-Eu^{3+} ET rate based on the FRET theory,[28,38] and results in a decrease in the LIR Tb/Eu. Here, in the spectrum presenting both the Tb^{3+} and Eu^{3+} emission, the Tb^{3+}-Eu^{3+} ET rate should be reflected by the LIR. For reliability, the Ln^{3+} concentration must be selected according to the suitable LIR value, which cannot be extremely large or

small to avoid the large uncertainty caused by the low emission intensity. Therefore, an area of interest is chosen with a LIR value between 1 and 2 (Figure 4.21). Among the three candidates, the compositions [$Eu_{0.02}Tb_{0.98}$] and [$Eu_{0.01}Tb_{0.2}Y_{0.79}$] were selected for further analysis of structural variation. Crystals are compressed in a DAC, confined by a pure solvent Squalane, under hydrostatic pressure up to 1000 MPa at 20 °C (293 K). The liquid-confined medium of the crystal allows to eliminate the presence of O_2, thus protecting the crystal from luminescence quenching.

As shown in Figure 4.22a and 4.22c, the emission intensity of Tb^{3+} (A for the transition $^5D_4$ to $^7F_5$, at 550 nm) decreases whereas the intensity of Eu^{3+} (C for the transition $^5D_0$ to $^7F_2$, at 612 nm) increases with increasing applied pressure in both complexes. Because the concentration and temperature remain constant during the measurement, the change in structure should be the only reason for the variation in the emission intensity. The cause of the decrease in Tb^{3+} emission intensity with increasing pressure could be that the efficiency of the Tb^{3+}-Eu^{3+} ET is optimized when shortening the Tb^{3+}-Eu^{3+} distance.

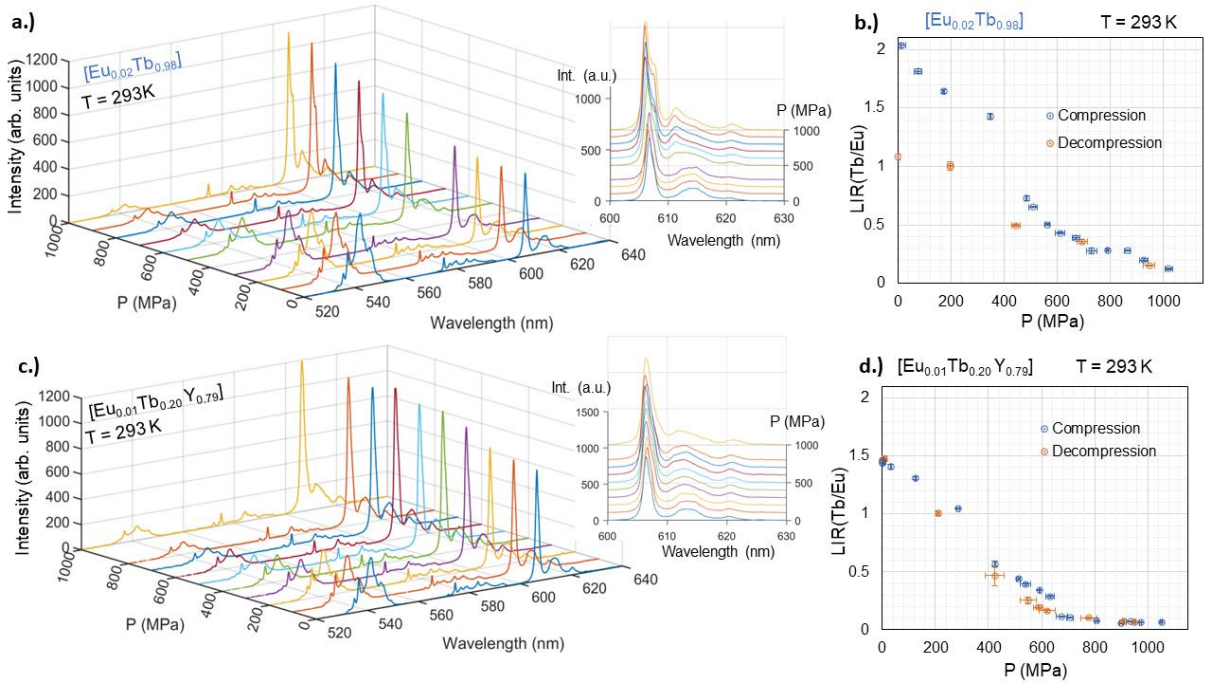

Figure 4.22: Emission spectra under hydrostatic pressure (in DAC) up to 1000 MPa for a) [$Eu_{0.02}Tb_{0.98}(acac)_3(phen)$] and c) [$Eu_{0.01}Tb_{0.2}Y_{0.79}(acac)_3(phen)$] (spectra zoomed in on Eu^{3+} emission 600 – 630 nm), and their calibration curve of calculated LIR as a function of pressure (MPa) in b) and d), respectively. (LIR values are the averages of three subsequent measurements, the error bar is calculated by the standard deviation).

Assuming that the overall crystal lattice is compressed under pressure, the molecular volume should be reduced. This change results in the reduction of the intermolecular and interatomic distance as well as in the modification of structural symmetry, thus in the orientations of ligands (geometry, parallelism). All these structural variations lead to the change in ET processes in the system. The structural impacts on each ET can rarely be

distinguished, due to the complexity of the ET system. Therefore, the same experience was achieved with a physical mixture of pure Tb^{3+} and Eu^{3+} complexes. At 50 wt. % of each complex, the emission spectrum shows both of their own emissions (Figure 4.23a), with LIR = 0.65 at ambient pressure in the DAC. Up to 1000 MPa, no significant changes are observed in the emission spectrum compared to that at ambient pressure, except for slight modifications of the emission peak shape due to structural change in the complex. However, those changes in emission peak can rarely be considered detectable and applicable for pressure sensing in such low pressure ranges. As shown in Figure 4.23b, the LIR varies randomly with pressure due to the inhomogeneity of the mixture. Upon focalized laser excitation, the laser spot is relatively small (~µm) whereas the DAC reduces its confined volume for compression, it is difficult to remain in the same irradiation position during the measurement. Therefore, the homogeneity of the composition has a signific ant impact on the LIR values, which can explain the uncertainty obtained in the LIR calibration under pressure (Figure 4.21 and 4.22d). Furthermore, isolated Tb^{3+} and Eu^{3+} complexes have a negligible response to pressure (<1000 MPa) on the LIR variation. This behavior in a physical mixture of pure Tb^{3+} and Eu^{3+} complexes shows that the decrease of the LIR under increasing pressure comes only from the Tb^{3+}-Eu^{3+} interaction.

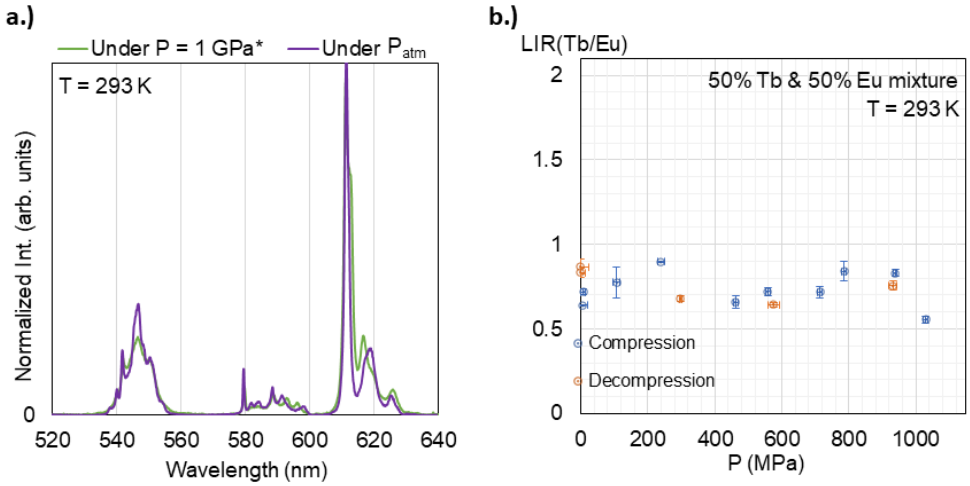

Figure 4.23: a) Emission spectra under hydrostatic pressure (in DAC) up to 1030 MPa* for a physical mixture of [Eu(acac)$_3$(phen)] and [Tb(acac)$_3$(phen)]. b) The calibration curve of the calculated LIR as a function of pressure (MPa). (LIR values are the averages of three subsequent measurements, the error bar is calculated by the standard deviation).

With the [$Eu_{0.02}Tb_{0.98}$] complex, the LIR pressure sensitivity is higher than the [$Eu_{0.01}Tb_{0.2}Y_{0.79}$] complex, resulting in a higher pressure sensitivity. However, the limits of their pressure sensitivity are seen in the disappearance of the Tb^{3+} emission (approximately 700 MPa for both). We assumed this behavior occurs because the original LIR value is different due to the different composition of the complex; and the limit at 700 MPa for pressure sensing should be inherently decided by structural flexibility. Furthermore, in contrast to the complex with Y^{3+} as a diluent, the [$Eu_{0.02}Tb_{0.98}$] complex shows only partial reversibility of the LIR under pressure up to 1000 MPa. This reversibility could be extremely important for pressure measurement applications. Surface defects in the crystal or even slight

cracking of the crystal lattice caused by compression should not be forgotten. Furthermore, structural defects may induce luminescence quenching of the Ln^{3+} emitter. The mechanical impact on the luminescent properties of the complex [Tb(acac)$_3$(phen)] has been reported as triboluminescence.[62] Moreover, the decrease in the intensity of Eu^{3+}-complex under pressure-induced structural contraction has also been observed, the authors assumed that is due to the change in the probability of nonradiative relaxation.[63] Here, the impact of defect quenching is significant at the high Tb^{3+}concentration complex, but not the other. We assume that the Y^{3+} diluents potentially make the Tb^{3+} ions less trapped in structural defects, which would allow for good reversibility of the LIR value under pressure. Therefore, the complex may lose its reversibility after repeated compressions. Unfortunately, DAC experiments are limited to three compressions for the same sample due to the elasticity of its nickel seal, and it is difficult to collect the sample in extremely small quantities after compression. The determination of reproducibility should be further investigated in other compression equipment.

4.5.2 [Ln_2(μ-OMe)(tfa)$_4$(phen)$_2$]

At 293K, the emission spectra of [Ln_2] [$Eu_{0.01}Tb_{0.99}$] under different hydrostatic pressure in Squalane are presented in Figure 4.24a. Even at an extremely high concentration of Tb^{3+}, the Tb^{3+} emission intensity is still low, resulting in a low value of LIR Tb/Eu at ambient pressure. In Figure 4.24b, the pressure calibration curve shows that increasing pressure causes a slight decrease in LIR in the range of 60 – 600 MPa, but that the variation in LIR above 600 MPa becomes random and not reversible. The slight decrease in LIR with increasing pressure is due to structural contraction, which induces a change in the Tb^{3+}-Eu^{3+} ET. However, as the Tb^{3+}-Eu^{3+} ET between two intramolecular ions is already efficient without pressure-induced structural contraction, the variation in LIR is thus small. On the other hand, the ligand [μ-OMe] contending two Ln^{3+} can hardly be modified by the applied pressure, so the distance between them is not easy to shorten.

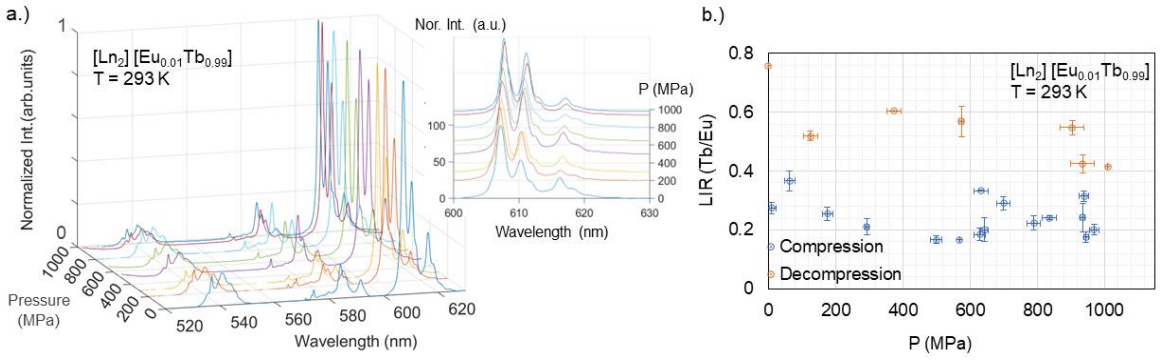

Figure 4.24: a.) Emission spectra of [($Eu_{0.01}Tb_{0.99}$)$_2$(μ-OMe)(tfa)$_4$(phen)$_2$] under hydrostatic pressure in Squalane (Emission intensity is normalized by the most intense peak, spectra zoomed in on Eu^{3+} emission 600 – 630 nm) and b.) the LIR curve as the function of pressure during compression and decompression (Error bars are calculated by the standard deviation of three measurements).

Thus, the [Ln_2] complex studied is by far not suitable for LIR-based pressure sensing due to the highly efficient Tb^{3+}-Eu^{3+} ET in the original structure. Nonetheless, the structure of the binuclear Ln-complex could inspire further applications based on Ln^{3+}-Ln^{3+} energy transfer.

4.5.3 [$Ln_9(acac)_{16}(\mu_3\text{-}OH)_8(\mu_4\text{-}O)(\mu_4\text{-}OH)$]

To optimize the accuracy of the measurement, it is preferable for the original LIR value to be large. Therefore, the [Ln_9] complex of composition [$Eu_{0.05}Tb_{0.95}$] was chosen. The emission spectra of the [Ln_9] complex [$Eu_{0.05}Tb_{0.95}$] are shown in Figure 4.25a as a function of hydrostatic pressure in Squalane. The emission spectra are normalized by the intensity of the Tb^{3+} peak at 550 nm, only the increase in Eu^{3+} emission intensity can be observed with increasing pressure. As a result, the LIR decreases with increasing pressure in Figure 4.25b. In addition, a significant change in the slope of the compression curve is remarked around 550 MPa, and above 600 MPa, the decrease in LIR becomes negligible. Moreover, the variation in LIR is not reversible after compression up to 925 MPa. The significant decrease in LIR at 550 MPa can also be observed in the emission spectra in Figure 4.25a and in the zoomed spectra Figure 4.26. This abrupt variation in LIR arises from the deformation of the Eu^{3+} emission peak, which has been discussed previously in section 4.3. This peak deformation substantially interferes with the LIR calculation, as the integrated surface will be strongly increased. However, peak fitting can solve this LIR uncertainty, but also complicates data processing.

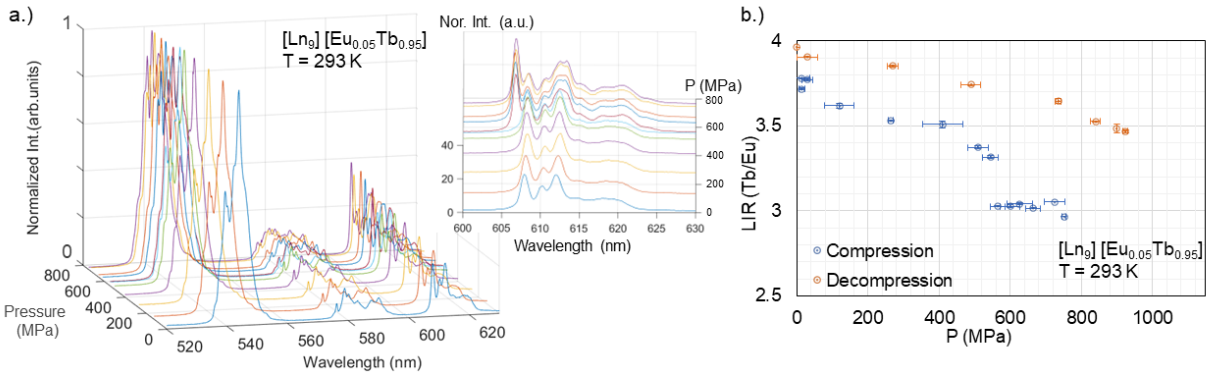

Figure 4.25: a.) Emission spectra of [$(Eu_{0.05}Tb_{0.95})_9(acac)_{16}(\mu_3\text{-}OH)_8(\mu_4\text{-}O)(\mu_4\text{-}OH)$] under hydrostatic pressure in Squalane (Emission intensity is normalized by the most intense peak, spectra zoomed in on Eu^{3+} emission 600 – 630 nm) and b.) the LIR curve as the function of pressure during compression and decompression (Error bars are calculated by the standard deviation of three measurements).

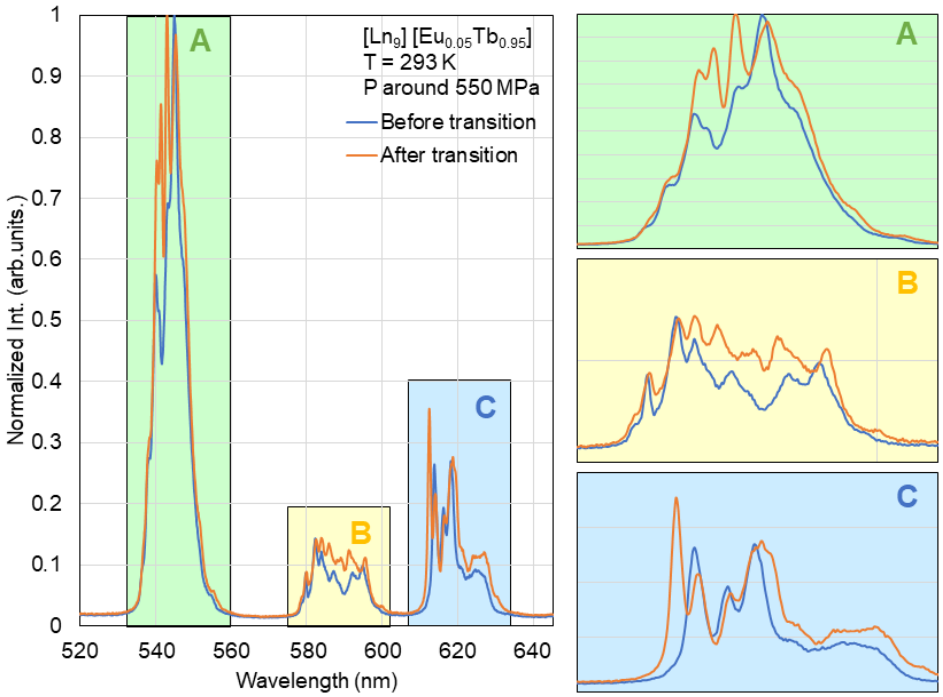

Figure 4.26: Emission spectra of $[(Eu_{0.05}Tb_{0.95})_9(acac)_{16}(\mu_3\text{-}OH)_8(\mu_4\text{-}O)(\mu_4\text{-}OH)]$ at 550 MPa: new transition is shown by the peak at 606 nm and the zoomed spectra (Peak positions are not corrected by the intensity reference).

4.5.4 Novel method for pressure sensing: LIR

Due to the remarkable impact of the compression on the Tb^{3+}-Eu^{3+} ET rate, the Tb^{3+}/Eu^{3+} LIR could be an optical tool to reflect a slight structural variation, which cannot be precisely observed in structural analysis. Using the variation in photoluminescent properties to quantify the slight change in structure at relatively low pressure of the material, the measurement is non-contact, the spatial resolution is thus optimized. Compared with the most applied methods based on the shift of the spectral peak for pressure detection, the LIR method considers the overall transitions among electronic sublevels by integrating the peak area, which simplifies data processing and thus optimizes measurement accuracy.

Among the different complexes, the $[Ln_1]$ complex at $[Eu_{0.01}Tb_{0.20}Y_{0.79}]$ provides excellent sensitivity and reliable reversibility to pressure, making it a potential LIR-based pressure sensor. The applicability of this material in tribological measurements as a pressure sensor will be discussed under varying conditions such as temperature, shear rate.

4.6 Potential pressure sensor in tribology

As LIR will be used as a variable to measure pressure in further tribological tests, the impacts of other parameters on LIR values should be studied. Besides local pressure of contact zone in tribological measurements, local temperature and shear change all the time

with pressure. Thus, the impacts of temperature and shear on the LIR value of the Ln1 complex [$Eu_{0.01}Tb_{0.20}Y_{0.79}$] are studied in this section.

4.6.1 Impact of temperature

At pressures up to 700 MPa, the luminescent-intensity-ratio of Tb^{3+}/Eu^{3+} in the [$Eu_{0.01}Tb_{0.2}Y_{0.79}(acac)_3(phen)$] complex shows a remarkable sensitivity to pressure, and this LIR variation induced by the change of the Tb^{3+}-Eu^{3+} interionic distance is reversible. Therefore, the [$Eu_{0.01}Tb_{0.2}Y_{0.79}(acac)_3(phen)$] complex can be a potential photoluminescent pressure sensor. Given the use of LIR as a variable, pressure detection is independent of the absolute intensity of emission. As the absolute intensity of emission is affected by the sensor concentration and, the equipment parameter (laser density), the pressure detection is thus not affected by them. However, many studies have highlighted the sensitivity of the Tb^{3+}/Eu^{3+} LIR to temperature,[30,32,64,65] usually applied for thermometry sensor research. Furthermore, the impact of temperature can be observed in Figure 4.21 and Figure 4.22d, where the LIR value of [$Eu_{0.01}Tb_{0.2}Y_{0.79}(acac)_3(phen)$] under ambient pressure varies at different temperatures (298 K (Figure 4.21): LIR = 1.32; 293 K (Figure 4.22d): LIR = 1.46). Therefore, the influence of temperature on pressure sensing of the [$Eu_{0.01}Tb_{0.2}Y_{0.79}(acac)_3(phen)$] complex should be carefully studied.

Moreover, the prior condition to allow pressure sensitivity is to occur the Tb^{3+}/Eu^{3+} ET in the system, and the efficiency of Tb^{3+}/Eu^{3+} ET is strongly dependent on temperature in the range below room temperature (293K). The lowest temperature allowed for Tb^{3+}/Eu^{3+} ET should be studied. In this section, the impact of temperature on the LIR value and thus on the pressure sensing mechanism will be studied.

1) T > 293 K

The temperature-induced variation of the Tb^{3+}/Eu^{3+} LIR is often due to the thermal population of Eu^{3+} electrons toward its upper level ($^7F_1$ or $^7F_2$). This results from the Tb^{3+}-Eu^{3+} ET process where the high temperature favors ET from $^7F_2$, which decreases the emission intensity of Tb^{3+} while increasing the emission intensity of Eu^{3+}. Therefore, the Tb^{3+}/Eu^{3+} LIR decreases with increasing temperature. The probability of thermal-populated electrons of Eu^{3+} could be described by Boltzmann's distribution.[31,66–68] However, the Tb^{3+}/Eu^{3+} LIR can also be influenced by the Tb^{3+}-Eu^{3+} ET rate, which can change with temperature, especially at low temperatures. The complex temperature calibration was conducted between 20 and 80 °C to avoid the sample from burning due to the high temperature. A quasi-linear curve is observed up to 60 °C in Figure 4.27, following the Boltzmann's distribution, which agrees the results of other studies,[31,32] showing that Eu^{3+}emission is temperature sensitive up to 60 °C.

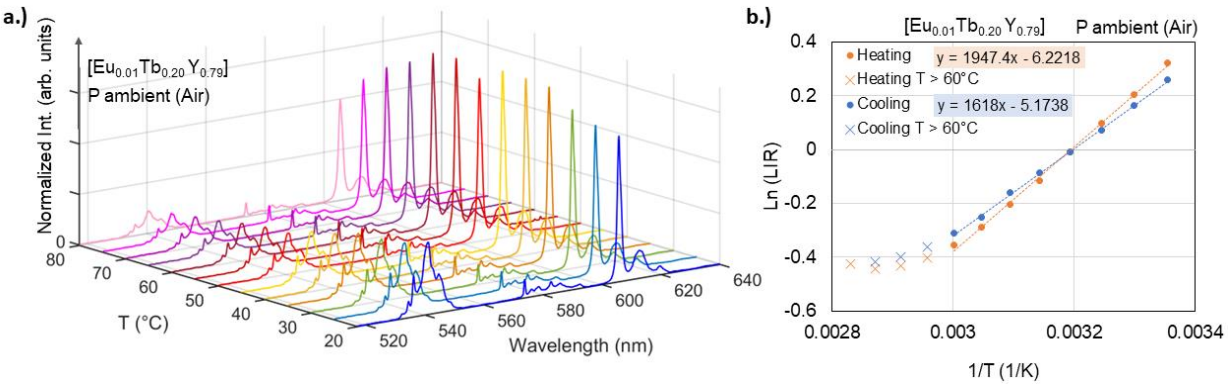

Figure 4.27: The $[Eu_{0.01}Tb_{0.2}Y_{0.79}]$ complex under ambient pressure: a) Emission spectra under 405 nm excitation at different temperatures, b) temperature calibration curve for the luminescent intensity ratio (LIR) Tb/Eu.

Temperature-induced variation of the LIR cannot be overlooked in the pressure detection by the $[Eu_{0.01}Tb_{0.2}Y_{0.79}(acac)_3(phen)]$ complex. The isothermal pressure calibrations at four temperatures are shown in Figure 4.28. The temperature calibration curve under constant ambient pressure performed outside the DAC at the same temperatures was plotted to compare the LIR values. Under ambient pressure, the LIR obtained by the complex measured on a thermal plate for the temperature calibration is the same as those confined in the DAC for the pressure calibration. A coupled effect between pressure and temperature on LIR is observed (Figure 4.28). The LIR decreases with increasing pressure as before, but the slope decreases with temperature. The thermal sensitivity of the LIR disappears after 60 °C, which follows the temperature calibration curves, as shown previously. At increasing temperatures, the limit of pressure sensitivity slightly decreases as the initial LIR decreases significantly under ambient pressure.

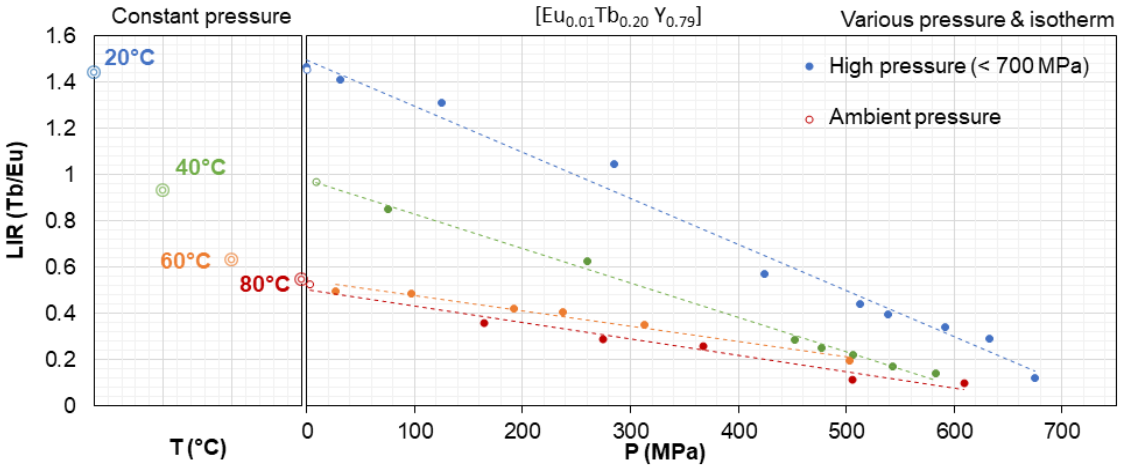

Figure 4.28: The variation of LIR in complex $[Eu_{0.01}Tb_{0.2}Y_{0.79}(acac)_3(phen)]$ under constant pressure (ambient pressure outside DAC) and under various pressures in isotherm medium at 20 °C (293 K) in blue, 40 °C (313 K) in green, 60 °C (333 K) in orange, and 80 °C (353 K) in red (in DAC).

This result shows this material can be applied as a reliable pressure sensor in an isothermal environment. The working temperature range is confirmed up to 80 °C, which is limited by the relatively low stability of the organic complex at high temperatures. The impacts of temperature on LIR values exist, but it can be easily corrected by a pre-calibration of temperature. Although the pressure calibrated curves have not been accurately fitted so far and further studies are required, it can be envisioned that numerous applications of highly accurate pressure sensing by the Ln complex will be inspired by this study. Furthermore, as the pressure sensitivity is more important at lower temperature, the minimum working temperature for a pressure measurement can be low, as long as the temperature allows the Tb^{3+}-Eu^{3+} ET to occur in the system under ambient pressure, which will be discussed in the following.

2) T < 293 K

At a given composition, a low temperature perturbs the Tb^{3+}-Eu^{3+} ET process due to the depopulation of the $^7F_2$ or $^7F_1$ level of Eu^{3+}. To clarify the impact of temperature on the Tb^{3+}-Eu^{3+} ET system, a composition [$Eu_{0.01}Tb_{0.2}Y_{0.79}$] was chosen as an example. As shown in Figure 4.29, the energy transferred from Tb^{3+} to Eu^{3+} decreases considerably from room temperature (298 K) to 93 K; therefore, the rise time of Eu^{3+} disappears as the temperature decreases. This observation correlates with the previous results of the Eu^{3+} excitation spectrum at 93 K. The depopulation of the upper level of Eu^{3+} to the initial state eliminates the Tb^{3+}-Eu^{3+} ET pathway: $^5D_4 \rightarrow {}^7F_6 = {}^7F_2 \rightarrow {}^5D_2$, $^5D_4 \rightarrow {}^7F_5 = {}^7F_1 \rightarrow {}^5D_1$, and $^5D_4 \rightarrow {}^7F_4 = {}^7F_1 \rightarrow {}^5D_0$ (ET A, B, and C_2 in Scheme 4.2, respectively). This causes a significant decrease in the Tb^{3+}-Eu^{3+} ET rate. Furthermore, the impact of temperature on the interaction rate between the ligand and Tb^{3+} has been reported, showing that the rate of the ligand-Tb^{3+} ET decreases with decreasing temperature.[69]

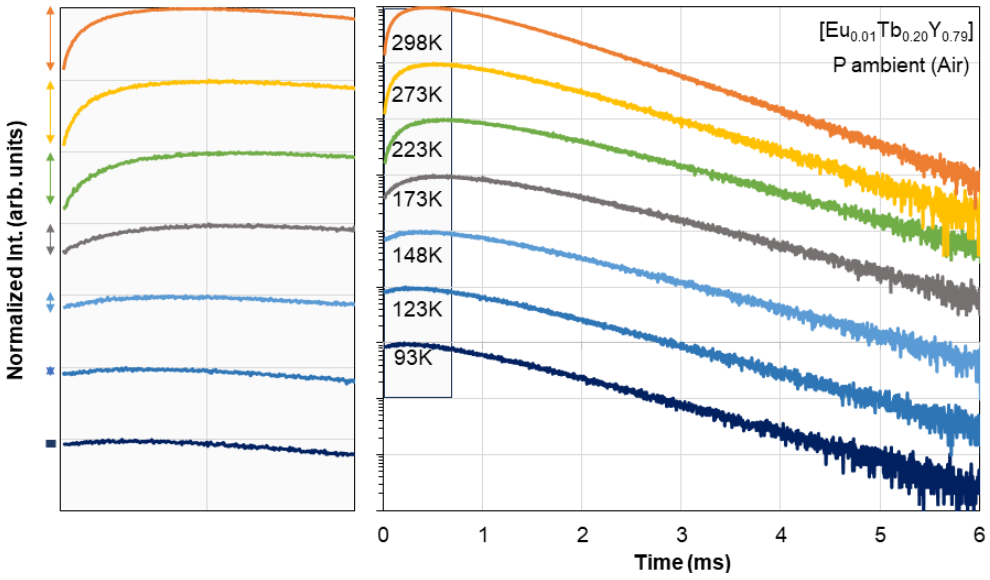

Figure 4.29: Decay time of $^5D_0$ (Eu^{3+}) in [$Eu_{0.01}Tb_{0.2}Y_{0.79}(acac)_3(phen)$] at different temperatures. Insert: zoomed graph in the range of 0–0.5 ms (excitation at 486 nm; Eu^{3+} emission at 612 nm).

In conclusion, the Tb^{3+}-Eu^{3+} ET is only allowed above 173 K in the [Ln_1] complex [$Eu_{0.01}Tb_{0.2}Y_{0.79}$], so as the LIR-based pressure sensing process. Above 273 K, the impact of temperature on Tb^{3+}-Eu^{3+} ET can rarely be observed by the lifetime measurements in Figure 4.29. However, the LIR-based temperature sensitivity has been observed above 175 K in reported results.[32] Combined with the previous results, the temperature-induced variation in LIR can be corrected in the range below 333K. Consequently, the minimum working temperature in pressure sensing is 173 K for [$Eu_{0.01}Tb_{0.2}Y_{0.79}(acac)_3(phen)$] complex.

4.6.2 LIR-based shear rate sensitivity

The triboluminescent properties of [$Tb(acac)_3(phen)$][62] and [$Eu(acac)_3(phen)$][63] complexes have recently been reported. Friction-induced structural variations, including crystal fractures and lattice defects, lead to luminescent emission in non-centrosymmetric solids. Therefore, the variation in photoluminescent properties of [$Eu_{0.01}Tb_{0.20}Y_{0.79}$] under shear can be significant and thus influence the LIR value for further pressure sensing under variable shear. Hence, the complex crystals of [$Eu_{0.01}Tb_{0.20}Y_{0.79}$] are finely ground and dispersed in the lubricant. The lubricant chosen for the first experiments is Nycobase. Photoluminescent emissions from the 1.0 wt.% suspension [$Eu_{0.01}Tb_{0.20}Y_{0.79}$] are collected during and after the shear test, up to 1000 s^{-1} at 293, 313, 333 and 353 K respectively. In the following part, the [$Eu_{0.01}Tb_{0.20}Y_{0.79}$] powder in suspension at 1.0 wt.% will be named as the complex suspension. In Figure 4.30, the normalized emission spectra of the complex suspension at 313 K during the shear test, at a shear rate at 0 s^{-1} and 750 s^{-1}, are shown respectively. Increasing the shear rate induces a significant increase in the emission intensity of the Tb^{3+} peak, at 550 nm.

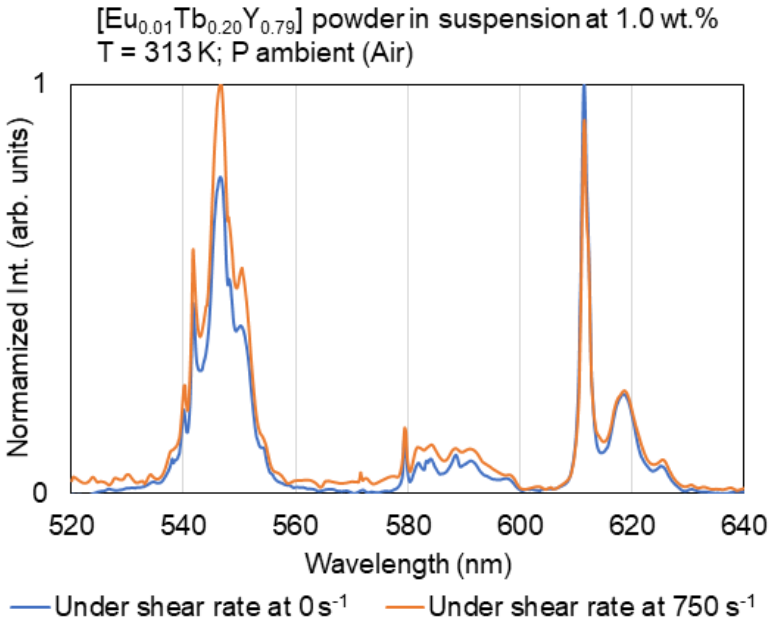

Figure 4.30: Emission spectra of [$Eu_{0.01}Tb_{0.20}Y_{0.79}(acac)_3(phen)$] suspension in Nycobase during shear test (Emission intensity is normalized by the most intense peak).

The Tb/Eu LIR values are then plotted in Figure 4.31 for each temperature at different shear rates. Besides the experiments at 353 K, the increase in LIR can be observed during the high shear rate test (> 500 s^{-1}) for each temperature, and this variation is slightly reduced once the shear test is stopped. The difference in LIR between during and after the shear test under high shear rate is very significant at 293 K and decreases with increasing temperature. A maximum value of LIR for each temperature can still be observed at 750 s^{-1}, and under higher shear rate, the LIR decreases again with increasing shear rate. The experiment at 353 K is different from the others (Figure 4.31d), and the LIR decreases during the shear test at a high shear rate and remains the same after the shear test. The increase in Tb^{3+} emission intensity is clearly observed by the increase in Tb/Eu LIR, the variation in Eu^{3+}emission intensity cannot be determined whereas no intensity reference has been used in the experiments. However, comparison of the absolute emission intensity is quite difficult as the concentration of the complex is difficult to control under the dynamic conditions imposed by the shear test. The increase in LIR can be due to the enhancement of Tb^{3+} emission intensity by shear-induced triboluminescence, or to the decrease in Tb-Eu ET in the system under shear. Preliminary work shows interesting properties in LIR-based shear sensing applications of the [(Y, Tb, Eu)$(acac)_3$(phen)] complex, which may be completed by further studies, opening an avenue for self-calibrated ratiometric photoluminescent shear sensors.

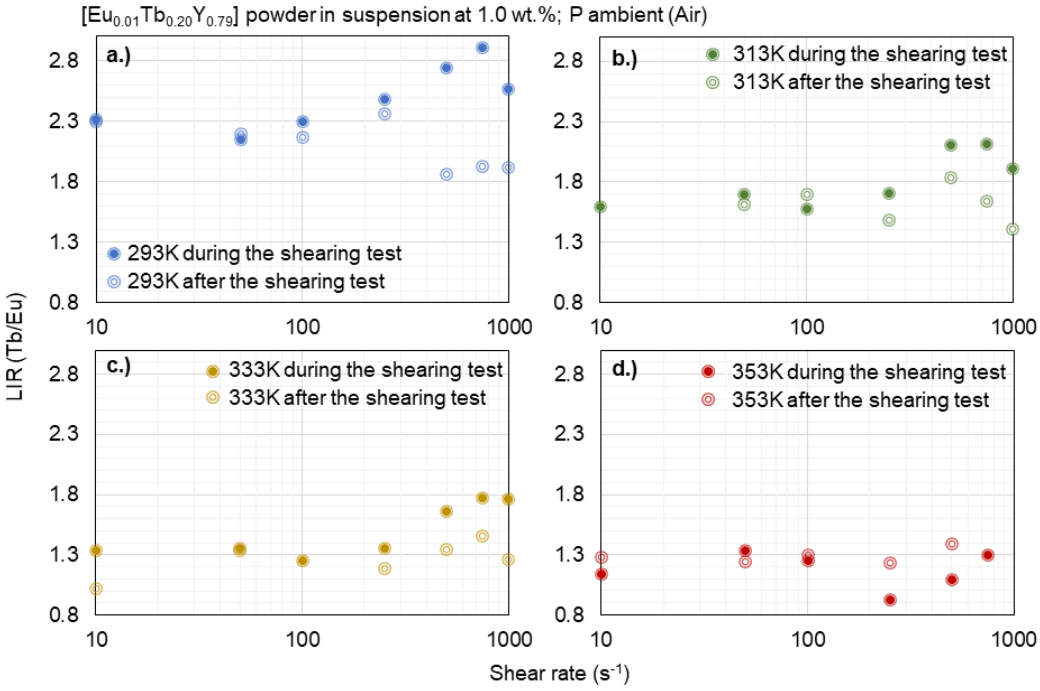

Figure 4.31: LIR of [$Eu_{0.01}Tb_{0.20}Y_{0.79}(acac)_3$(phen)] suspension in Nycobase during and after shearing test at a.) 293K; b.) 313K; c.) 333 K and d.) 353K.

Besides, it should be noted that compared to the LIR value of [$Eu_{0.01}Tb_{0.20}Y_{0.79}$] at ambient pressure and a shear rate of 0 s^{-1}, the LIR at 293 K is larger (Figure 4.31a: 2.3; Figure 4.22d: 1.46). We assumed that the LIR value can be also influenced by the physical environment and the state of dispersion, which will be discussed below.

4.6.3 Impact of physical environment on LIR

A significant difference between the measured LIR values of the [$Eu_{0.01}Tb_{0.20}Y_{0.79}$] complex has been observed depending on the dispersion state of the complex. In order to eliminate the impact of the nature of the solvent, the [$Eu_{0.01}Tb_{0.20}Y_{0.79}$] crystals are dispersed in the same fluid as in the previous results: Nycobase. The emission spectrum of the ground powder [$Eu_{0.01}Tb_{0.20}Y_{0.79}$] in air has also been carried out. Figure 4.32a shows the normalized emission spectra of [$Eu_{0.01}Tb_{0.20}Y_{0.79}$] powder, crystal and 1.0 wt.% Nycobase suspension, respectively. The LIR of the ground powder of [$Eu_{0.01}Tb_{0.20}Y_{0.79}$] is larger than that of the crystal: the crystal size has an impact on the LIR value (Figure 4.32b). At the micrometer scale, large single crystals include less structural defect than small crystals, which means that more Tb^{3+}-Eu^{3+} ET can be allowed, leading to a decrease in the LIR value. Moreover, as shown in Figure 4.32b, the LIR of the [$Eu_{0.01}Tb_{0.20}Y_{0.79}$] crystal decreases slightly in the suspension, while the LIR of the powder increases significantly in the suspension.

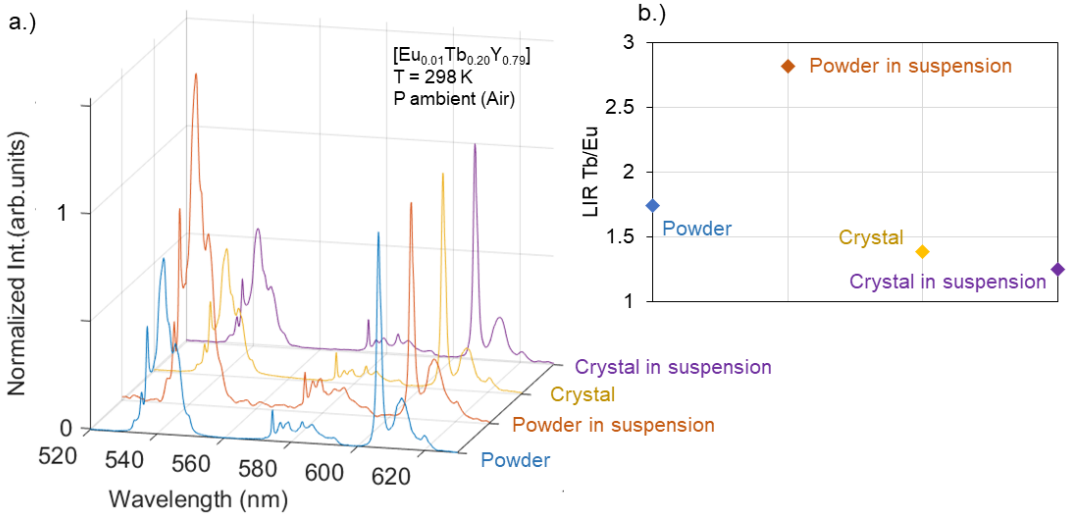

Figure 4.32: a.) Emission spectra of [$Eu_{0.01}Tb_{0.20}Y_{0.79}(acac)_3(phen)$] in different forms at 298 K (Emission intensity is normalized by the peak at 612 nm) and b.) the LIR values.

Assuming that the effect of light reflection and scattering between the dispersed powder and the dispersed crystal is negligible on the LIR value, the significant increase in the LIR of the suspended powder is attributed to the heightened probability of surface quenching of Ln^{3+} emission compared to that of the single crystals in suspension. With increasing surface quenching, the probability of Tb^{3+}-Eu^{3+} ET decreases, leading to an increase in the LIR. In addition, O_2-quenching can also decrease the LIR value. It has been observed that the presence of O_2 affects the Tb^{3+} emission more than that of Eu^{3+}, the reduction in Tb^{3+} emission intensity is more important. Energy transfer from Tb^{3+} to O_2 is more efficient than that from Eu^{3+} as the energy level of Tb^{3+} better matches that of O_2.[70,71] Dispersion in the Nycobase can slightly reduce O_2-quenching, which leads to an increase in the LIR. However, the increase in LIR has not been observed in the suspended crystal, we assume that O_2-quenching is more important in the powder because of the important particle surface. Therefore, particles size has a significant impact on the probability of Tb-Eu ET and thus on the LIR value. Furthermore, the decrease in size can reduce the probability of Tb-Eu ET, leading to a reduction in pressure sensitivity.

4.7 Conclusion and perspectives

This chapter showed the pressure-dependent photoluminescent properties of three types of Ln complexes: mononuclear [Ln_1], binuclear [Ln_2] and nonanuclear [Ln_9]. In order to explore potential pressure sensors for tribological measurement, sensitivity to a relatively low range of pressure [0-1 GPa] has been studied. In a DAC, hydrostatic pressure was applied to the material. At 405 nm excitation, the Ln^{3+} complexes are efficiently excited by the organic ligands. The pressure-induced variation in the crystal structure leads to considerable change in the photoluminescent properties of Tb^{3+} and Eu^{3+} in the complex, making the pressure indirectly measurable by spectral variables.

First, pressure sensitivity based on peak-shift- has been reported by the [Ln_9] complex [$Ln_9(acac)_{16}(\mu_3\text{-}OH)_8(\mu_4\text{-}O)(\mu_4\text{-}OH)$]. Structural variation induces a change in the Eu^{3+} symmetry site, leading to a shift in the emission peak. During the 1st cycle of pressure loading, the structure is changed by compression at 550 MPa, the Eu^{3+} emission peak of the $^5D_0 \rightarrow {}^7F_2$ transition is permanently deformed. The peak centered at 610 nm after the deformation shifts as a function of pressure, with around 0.15 nm/GPa in Nycobase and 0.12 nm/GPa in Squalane. This peak shift is reversible up to 1 GPa in both solvents.

In the second part, the luminescent-intensity-ratio (LIR) based pressure sensitivity of Ln^{3+} complexes is discussed. By adding the Tb^{3+} as the sensitizer in a Eu^{3+} system, the ET process varies with the structural contraction. The impact of structural change on the Tb^{3+}-Eu^{3+} ET was investigated by compressing the complex in a DAC, following by the variation in LIR of Tb^{3+}/Eu^{3+} emission. The Tb^{3+}-Eu^{3+} ET is allowed in all the complexes even at low concentration of Eu^{3+}. The efficiency of Tb^{3+}-Eu^{3+} ET is considerably efficient in the [Ln_2] complex, making the emission of Tb^{3+} difficult to observe. Among three types of complexes, the [Ln_1] [$Eu_{0.01}Tb_{0.2}Y_{0.79}(acac)_3(phen)$] complex shows a significant pressure sensitivity on the Tb^{3+}/Eu^{3+} LIR up to 700 MPa. Dilution by Y^{3+} in the system affects the evolution of Tb^{3+} emission under variation in hydrostatic pressure, so the variation in LIR induced by pressure becomes reversible with dilution by Y^{3+}.

For further application in tribological measurement, the temperature-induced variation on the LIR is verified and can be corrected by temperature calibration for pressure measurement. Moreover, low shear rate (< 500 s^{-1}) has no significant impact on the LIR of the complex suspension. In addition, the physical environment can also influence the LIR, which should be carefully considered in pressure sensing applications. The [Ln_1] [$Ln(acac)_3(phen)$] (Ln^{3+} = Y^{3+}, Tb^{3+}, Eu^{3+}) complex can be a reliable photoluminescent (PL) sensor in pressure-sensing applications in the range 0–700 MPa pressure, which is an important advance in short-range PL pressure sensors.

References

(1) Mao, H. K.; Xu, J.; Bell, P. M. Calibration of the Ruby Pressure Gauge to 800 Kbar under Quasi-Hydrostatic Conditions. *J. Geophys. Res.* **1986**, *91* (B5), 4673. https://doi.org/10.1029/jb091ib05p04673.

(2) Pieprz, M.; Runowski, M.; Ledwa, K.; Carvajal, J. J.; Bednarkiewicz, A.; Marciniak, L. Improving Accuracy and Sensitivity of Lanthanide-Based Luminescent Manometers by Augmented Spectral Shift Method. *ACS Appl. Mater. Interfaces* **2023**. https://doi.org/10.1021/acsaom.2c00198.

(3) Runowski, M.; Woźny, P.; Martín-Benenzuela, I. R. Optical Pressure Sensing in Vacuum and High-Pressure Ranges Using Lanthanide-Based Luminescent Thermometer-Manometer. *J. Mater. Chem. C* **2021**. https://doi.org/10.1039/d1tc00709b.

(4) Runowski, M.; Zheng, T.; Woźny, P.; Du, P. NIR Emission of Lanthanides for Ultrasensitive Luminescence Manometry - Er3+-Activated Optical Sensor of High Pressure. *Dalt. Trans.* **2021**, *50* (41), 14864–14871. https://doi.org/10.1039/d1dt02681j.

(5) Stopikowska, N.; Guo, Q.; Lis, S.; Runowski, M. Optical Pressure Sensor Based on the Emission and Excitation Band Width (Fwhm) and Luminescence Shift of Ce 3+ -Doped Fluorapatite High-Pressure Sensinǵ. *ACS Appl. Mater. Interfaces* **2019**, *11*, 4131–4138. https://doi.org/10.1021/acsami.8b19500.

(6) Runowski, M.; Marciniak, J.; Grzyb, T.; Przybylska, D.; Shyichuk, A.; Barszcz, B.; Katrusiak, A.; Lis, S. Lifetime Nanomanometry-High-Pressure Luminescence of up-Converting Lanthanide Nanocrystals-SrF2:Yb3+,Er3+. *Nanoscale* **2017**, *9* (41), 16030–16037. https://doi.org/10.1039/c7nr04353h.

(7) Casar, J. R.; McLellan, C. A.; Siefe, C.; Dionne, J. A. Lanthanide-Based Nanosensors: Refining Nanoparticle Responsiveness for Single Particle Imaging of Stimuli. *ACS Photonics* **2021**, *8* (1), 3–17. https://doi.org/10.1021/acsphotonics.0c00894.

(8) Lay, A.; Sheppard, O. H.; Siefe, C.; Mclellan, C. A.; Mehlenbacher, R. D.; Fischer, S.; Goodman, M. B.; Dionne, J. A. Optically Robust and Biocompatible Mechanosensitive Upconverting Nanoparticles. *ACS Cent. Sci.* **2019**, *5*, 1211–1222. https://doi.org/10.1021/acscentsci.9b00300.

(9) Lay, A.; Siefe, C.; Fischer, S.; Mehlenbacher, R. D.; Ke, F.; Mao, W. L.; Alivisatos, A. P.; Goodman, M. B.; Dionne, J. A. Bright, Mechanosensitive Upconversion with Cubic-Phase Heteroepitaxial Core − Shell Nanoparticles. *Nano Lett.* **2018**, *18*, 4454–4459. https://doi.org/10.1021/acs.nanolett.8b01535.

(10) Lay, A.; Wang, D. S.; Wisser, M. D.; Mehlenbacher, R. D.; Lin, Y.; Goodman, M. B.; Mao, W. L.; Dionne, J. A. Upconverting Nanoparticles as Optical Sensors of Nano- to Micro- Newton Forces. *Nano Lett.* **2017**, *17*, 4172–4177. https://doi.org/10.1021/acs.nanolett.7b00963.

(11) Runowski, M.; Shyichuk, A.; Tymiński, A.; Grzyb, T.; Lavín, V.; Lis, S. Multifunctional Optical Sensors for Nanomanometry and Nanothermometry: High-Pressure and High-Temperature Upconversion Luminescence of Lanthanide-Doped Phosphates - LaPO4/YPO4:Yb3+-Tm3+. *ACS Appl. Mater. Interfaces* **2018**, *10* (20), 17269–17279. https://doi.org/10.1021/acsami.8b02853.

(12) McLellan, C. A.; Siefe, C.; Casar, J. R.; Peng, C. S.; Fischer, S.; Lay, A.; Parakh, A.; Ke, F.; Gu, X. W.; Mao, W.; Chu, S.; Goodman, M. B.; Dionne, J. A. Engineering Bright and Mechanosensitive Alkaline-Earth Rare-Earth Upconverting Nanoparticles. *J. Phys. Chem. Lett.* **2022**, *13* (6), 1547–1553. https://doi.org/10.1021/acs.jpclett.1c03841.

(13) Vorathin, E.; Hafizi, Z. M.; Ismail, N.; Loman, M. Review of High Sensitivity Fibre-Optic Pressure Sensors for Low Pressure Sensing. *Opt. Laser Technol.* **2020**, *121* (August 2019). https://doi.org/10.1016/j.optlastec.2019.105841.

(14) Mehlenbacher, R. D.; Kolbl, R.; Lay, A.; Dionne, J. A. Nanomaterials for in Vivo Imaging of Mechanical Forces and Electrical Fields. *Nat. Rev. Mater.* **2017**, *3*, 1–17. https://doi.org/10.1038/natrevmats.2017.80.

(15) Seoudi, T.; Philippon, D.; Fillot, N.; Lafarge, L.; Devaux, N.; Mondelin, A.; Vergne, P. CdSe-Based Quantum Dots as In Situ Pressure and Temperature Non-Intrusive Sensors in Elastohydrodynamic Contacts. *Tribol. Lett.* **2020**, *68* (3). https://doi.org/10.1007/s11249-020-01312-x.

(16) Albahrani, S. M. B.; Seoudi, T.; Philippon, D.; Lafarge, L.; Reiss, P.; Hajjaji, H.; Guillot, G.; Querry, M.; Bluet, J. M.; Vergne, P. Quantum Dots to Probe Temperature and Pressure in Highly Confined Liquids.

RSC Adv. **2018**, *8* (41), 22897–22908. https://doi.org/10.1039/C8RA03652G.

(17) Wang, Y.; Seto, T.; Ishigaki, K.; Uwatoko, Y.; Xiao, G.; Zou, B.; Li, G.; Tang, Z.; Li, Z.; Wang, Y. Pressure-Driven Eu2+-Doped BaLi2Al2Si2N6: A New Color Tunable Narrow-Band Emission Phosphor for Spectroscopy and Pressure Sensor Applications. *Adv. Funct. Mater.* **2020**, *30* (34), 1–10. https://doi.org/10.1002/adfm.202001384.

(18) Grasset, O. Calibration of the R Ruby Fluorescence Lines in the Pressure Range [0-1 GPa] and the Temperature Range [250-300 K]. *High Press. Res.* **2001**, *21* (3–4), 139–157. https://doi.org/10.1080/08957950108201020.

(19) Seoudi, T. Non-Intrusive CdSe-Based Quantum Dots for Sensing Pressure and Temperature in Lubricated Contacts, Thesis in Université Claude Bernard Lyon 1, 2020.

(20) Rakov, N.; Maciel, G. S.; Xiao, M. Upconversion Fluorescence and Its Thermometric Sensitivity of Er3+:Yb3+ Co-Doped SrF2 Powders Prepared by Combustion Synthesis. *Electron. Mater. Lett.* **2014**, *10* (5), 985–989. https://doi.org/10.1007/s13391-014-4030-9.

(21) Huber, G.; Syassen, K.; Holzapfel, W. B. Pressure Dependence of 4f Levels in Europium Pentaphosphate up to 400 Kbar. *Phys. Rev. B* **1977**, *15* (11), 5123–5128. https://doi.org/10.1103/PhysRevB.15.5123.

(22) Jovanić, B. R.; Radenković, B.; Zeković, L. D. The Effect of Pressure on the Position and Fluorescence Lifetime for the 5 D 0 → 7 F 2 Transition in Y 1.9 Eu 0.1 O 3. *J. Phys. Condens. Matter* **1996**, *8* (22), 4107–4110. https://doi.org/10.1088/0953-8984/8/22/014.

(23) Tanner, P. A. Some Misconceptions Concerning the Electronic Spectra of Tri-Positive Europium and Cerium. *Chem. Soc. Rev.* **2013**, *42* (12), 5090–5101. https://doi.org/10.1039/c3cs60033e.

(24) Alexander, O. T.; Kroon, R. E.; Brink, A.; Visser, H. G. Symmetry Correlations between Crystallographic and Photoluminescence Study of Ternary β-Diketone Europium(III) Based Complexes Using 1,10-Phenanthroline as the Ancillary Ligand. *Dalt. Trans.* **2019**, 16074–16082. https://doi.org/10.1039/c9dt02580d.

(25) Kuznetsov, A.; Laisaar, A.; Kikas, J. Temperature and Pressure Dependence of Spectral Positions and Widths of 5D0 → 7FJ Emission Lines from Eu3+ Ions in the CaF2 Crystal. *Phys. Scr.* **2013**, *T157*, 0–6. https://doi.org/10.1088/0031-8949/2013/T157/014016.

(26) Zhang, J.; Cui, H.; Zhu, P.; Ma, C.; Wu, X.; Zhu, H.; Ma, Y.; Cui, Q. Photoluminescence Studies of Y2O3:Eu3 under High Pressure. *J. Appl. Phys.* **2014**, *115* (2), 3–8. https://doi.org/10.1063/1.4861386.

(27) Zhang, Q. Y.; Pita, K.; Buddhudu, S.; Kam, C. H. Luminescent Properties of Rare-Earth Ion Doped Yttrium Silicate Thin Film Phosphors for a Full-Colour Display. *J. Phys. D. Appl. Phys.* **2002**, *35* (23), 3085–3090. https://doi.org/10.1088/0022-3727/35/23/308.

(28) Edgar, A. *Luminescent Materials*; 2007. https://doi.org/10.1007/978-0-387-29185-7_40.

(29) Carneiro Neto, A. N.; Moura, R. T.; Shyichuk, A.; Paterlini, V.; Piccinelli, F.; Bettinelli, M.; Malta, O. L. Theoretical and Experimental Investigation of the Tb3+ → Eu3+ Energy Transfer Mechanisms in Cubic A3Tb0.90Eu0.10(PO4)3 (A = Sr, Ba) Materials. *J. Phys. Chem. C* **2020**, *124* (18), 10105–10116. https://doi.org/10.1021/acs.jpcc.0c00759.

(30) Baur, F.; Glocker, F.; Jüstel, T. Photoluminescence and Energy Transfer Rates and Efficiencies in Eu3+ Activated Tb2Mo3O12. *J. Mater. Chem. C* **2015**, *3* (9), 2054–2064. https://doi.org/10.1039/c4tc02588a.

(31) Lin, L.; Li, Z.; Wang, Z.; Feng, Z.; Huang, F.; Dai, Q.; Zheng, Z. Hypersensitive and Color-Tunable Temperature Sensing Properties of (Eu,Tb)(AcAc)3phen via Phonon-Assisted Energy Transfer. *Opt. Mater. (Amst).* **2020**, *110* (August), 110532. https://doi.org/10.1016/j.optmat.2020.110532.

(32) Carneiro Neto, A. N.; Mamontova, E.; Botas, A. M. P.; Brites, C. D. S.; Ferreira, R. A. S.; Rouquette, J.; Guari, Y.; Larionova, J.; Long, J.; Carlos, L. D. Rationalizing the Thermal Response of Dual-Center Molecular Thermometers: The Example of an Eu/Tb Coordination Complex. *Adv. Opt. Mater.* **2022**, *10* (5), 1–12. https://doi.org/10.1002/adom.202101870.

(33) Hasegawa, Y.; Kitagawa, Y. Thermo-Sensitive Luminescence of Lanthanide Complexes, Clusters, Coordination Polymers and Metal–Organic Frameworks with Organic Photosensitizers. *J. Mater. Chem.*

C **2019**, *7*, 7494–7511. https://doi.org/10.1039/c9tc00607a.

(34) Gontcharenko, V. E.; Kiskin, M. A.; Dolzhenko, V. D.; Korshunov, V. M.; Taydakov, I. V; Belousov, Y. A. Mono- and Mixed Metal Complexes of Eu3+, Gd3+, and Tb3+ with a Diketone, Bearing Pyrazole Moiety and CHF2-Group: Structure, Color Tuning, and Kinetics of Energy Transfer between Lanthanide Ions. *Molecules* **2021**, *26* (2655), 1–15.

(35) Blais, C.; Daiguebonne, C.; Suffren, Y.; Bernot, K.; Calvez, G.; Le Pollès, L.; Roiland, C.; Freslon, S.; Guillou, O. Investigation of Intermetallic Energy Transfers in Lanthanide Coordination Polymers Molecular Alloys: Case Study of Trimesate-Based Compounds. *Inorg. Chem.* **2022**, *61* (30), 11897–11915. https://doi.org/10.1021/acs.inorgchem.2c01650.

(36) Guettas, D.; Balogh, C. M.; Sonneville, C.; Malicet, Y.; Lepoivre, F.; Onal, E.; Fateeva, A.; Reber, C.; Luneau, D.; Maury, O.; Pilet, G. Nano-Nonanuclear Mixed-Lanthanide Clusters [Eu9–XTbx] Featuring Tunable Dual Luminescence Properties. *Eur. J. Inorg. Chem.* **2016**, *2016* (24), 3932–3938. https://doi.org/10.1002/ejic.201600412.

(37) Dexter, D. L. A Theory of Sensitized Luminescence in Solids. *J. Chem. Phys.* **1953**, *21* (5), 836–850. https://doi.org/10.1063/1.1699044.

(38) Förster, T. Transfer Mechanisms of Electronic Excitation. *Discuss. Faraday Soc.* **1959**, *27*, 7–17. https://doi.org/10.1039/DF9592700007.

(39) Kleinerman, M. Energy Migration in Lanthanide Chelates. *J. Chem. Phys.* **1969**, *51* (6), 2370–2381. https://doi.org/10.1063/1.1672355.

(40) Fadieiev, Y. M.; Smola, S. S.; Malinka, E. V.; Rusakova, N. V. Study of Association of Eu(III) β-Diketonato-1,10-Phenanthroline Complexes in Silica-Based Hybrid Materials. *J. Lumin.* **2017**, *183*, 121–128. https://doi.org/10.1016/j.jlumin.2016.10.044.

(41) Kitagawa, Y.; Tsurui, M.; Hasegawa, Y. Bright Red Emission with High Color Purity from Eu(Iii) Complexes with π-Conjugated Polycyclic Aromatic Ligands and Their Sensing Applications. *RSC Adv.* **2022**, *12* (2), 810–821. https://doi.org/10.1039/d1ra08233g.

(42) Bao, G.; Wong, K. L.; Jin, D.; Tanner, P. A. A Stoichiometric Terbium-Europium Dyad Molecular Thermometer: Energy Transfer Properties. *Light Sci. Appl.* **2018**, *7* (1). https://doi.org/10.1038/s41377-018-0097-7.

(43) Hasegawa, Y.; Kitagawa, Y.; Nakanishi, T. Effective Photosensitized, Electrosensitized, and Mechanosensitized Luminescence of Lanthanide Complexes /639/638/439/943 /639/638/911 Review-Article. *NPG Asia Mater.* **2018**, *10* (4), 52–70. https://doi.org/10.1038/s41427-018-0012-y.

(44) Peng, X. W.; Liu, Q. Y.; Wang, H. H.; Wang, Y. L. Eu(III)- and Tb(III)-Coordination Polymer Luminescent Thermometers Constructed from a π-Rich Aromatic Ligand Exhibiting a High Sensitivity. *Dye. Pigment.* **2019**, *162* (September 2018), 405–411. https://doi.org/10.1016/j.dyepig.2018.10.055.

(45) Zahariev, T.; Trendafilova, N.; Georgieva, I. Spectroscopic and Photophysical Properties of [Eu (Phen) 2] X 3 3) Complexes , Incorporated into SiO 2 -Based Matrices : Theoretical Study. *Mater. Today Proc.* **2022**, *61*, 1292–1299. https://doi.org/10.1016/j.matpr.2022.05.054.

(46) Zahariev, T.; Shandurkov, D.; Gutzov, S.; Trendafilova, N.; Enseling, D.; Jüstel, T.; Georgieva, I. Phenanthroline Chromophore as Efficient Antenna for Tb 3 + Green Luminescence : A Theoretical Study. *Dye. Pigment.* **2021**, *185* (PA), 108890. https://doi.org/10.1016/j.dyepig.2020.108890.

(47) Förster, T. Zwischenmolekulare Energiewanderung Und Konzentrationsdepolarisation Der Fluoreszenz [German]. *Ann. Phys.* **1948**, *6* (2), 55–75. https://doi.org/10.1002/andp.19614630112.

(48) Dexter, D. L.; Schulman, J. H. Theory of Concentration Quenching in Inorganic Phosphors. *J. Chem. Phys.* **1954**, *22* (6), 1063–1070. https://doi.org/10.1063/1.1740265.

(49) Speiser, S. Photophysics and Mechanisms of Intramolecular Electronic Energy Transfer in Bichromophoric Molecular Systems: Solution and Supersonic Jet Studies. *Chem. Rev.* **1996**, *96* (6), 1953–1976. https://doi.org/10.1021/cr941193+.

(50) Kai, J.; Felinto, M. C. F. C.; Nunes, L. A. O.; Malta, O. L.; Brito, H. F. Intermolecular Energy Transfer and Photostability of Luminescence-Tuneable Multicolour PMMA Films Doped with Lanthanide-β-

Diketonate Complexes. *J. Mater. Chem.* **2011**, *21* (11), 3796–3802. https://doi.org/10.1039/c0jm03474f.

(51) Lustig, W. P.; Li, J. Luminescent Metal–Organic Frameworks and Coordination Polymers as Alternative Phosphors for Energy Efficient Lighting Devices. *Coord. Chem. Rev.* **2018**, *373*, 116–147. https://doi.org/10.1016/j.ccr.2017.09.017.

(52) Kasai, M.; Sugioka, Y.; Yamamoto, M.; Nagata, T.; Nonomura, T.; Asia, K.; Hasegawa, Y. Characteristic Evaluation of Chameleon Luminophore Dispersed in Polymer. *sensors* **2020**, *20* (2623), 1–15. https://doi.org/10.3390/s20092623.

(53) Parker, D.; Kanthi Senanayake, P.; Gareth Williams, J. A. Luminescent Sensors for PH, PO2, Halide and Hydroxide Ions Using Phenanthridine as a Photosensitiser in Macrocyclic Europium and Terbium Complexes. *J. Chem. Soc. Perkin Trans. 2* **1998**, No. 10, 2129–2139. https://doi.org/10.1039/a801270i.

(54) Wu, L.; Fang, Y.; Zuo, W.; Wang, J.; Wang, J.; Wang, S.; Cui, Z.; Fang, W.; Sun, H. L.; Li, Y.; Chen, X. Excited-State Dynamics of Crossing-Controlled Energy Transfer in Europium Complexes. *JACS Au* **2022**, *2* (4), 853–864. https://doi.org/10.1021/jacsau.1c00584.

(55) de Vicente, F. S.; Freddi, P.; Otuka, A. J. G.; Mendonça, C. R.; Brito, H. F.; Nunes, L. A. O.; Vollet, D. R.; Donatti, D. A. Photoluminescence Tuning and Energy Transfer Process from Tb3+ to Eu3+ in GPTMS/TEOS–Derived Organic/Silica Hybrid Films. *J. Lumin.* **2018**, *197* (December 2017), 370–375. https://doi.org/10.1016/j.jlumin.2017.12.048.

(56) Ranson, R. M.; Evangelou, E.; Thomas, C. B. Modeling the Fluorescent Lifetime of Y2O3:Eu. *Appl. Phys. Lett.* **1998**, *72* (21), 2663–2664. https://doi.org/10.1063/1.121091.

(57) Chambers, M. D.; Clarke, D. R. Doped Oxides for High-Temperature Luminescence and Lifetime Thermometry. *Annu. Rev. Mater. Res.* **2009**, *39*, 325–359. https://doi.org/10.1146/annurev-matsci-112408-125237.

(58) Debasu, M. L.; Ananias, D.; Macedo, A. G.; Rocha, J.; Carlos, L. D. Emission-Decay Curves , Energy-Transfer and Effective-Refractive Index in Gd 2 O 3 : Eu 3 + Nanorods. *J. Phys. Chem. C* **2011**, *115*, 15297–15303.

(59) ManjuBala; Kumar, S.; Chahar, S.; Taxak, V. B.; Boora, P.; Khatkar, S. P. Synthesis, NMR and Optical Features of Intense Green Color Terbium(III) Complexes. *Optik (Stuttg).* **2020**, *202* (October 2019), 163636. https://doi.org/10.1016/j.ijleo.2019.163636.

(60) Omagari, S.; Nakanishi, T.; Kitagawa, Y.; Seki, T.; Fushimi, K.; Ito, H.; Meijerink, A.; Hasegawa, Y. Critical Role of Energy Transfer Between Terbium Ions for Suppression of Back Energy Transfer in Nonanuclear Terbium Clusters. *Sci. Rep.* **2016**, *6* (August), 1–11. https://doi.org/10.1038/srep37008.

(61) Dudar, S. S.; Sveshnikova, E. B.; Shablya, A. V; Ermolaev, V. L. Nonradiative Energy Transfer as a Method for Investigation of Self-Assembling Nanostructures of Lanthanide Complexes in Solutions. *High energy Chem.* **2007**, *41* (3), 189–197. https://doi.org/10.1134/S0018143907030034.

(62) Bukvetskii, B. V.; Mirochnik, A. G.; Shishov, A. S. Triboluminescence and Crystal Structure of Centrosymmetric Complex Tb(AcAc)3Phen. *J. Lumin.* **2018**, *195* (October 2017), 44–48. https://doi.org/10.1016/j.jlumin.2017.10.074.

(63) Wong, H. Y.; Zhou, X. Le; Yeung, C. T.; Man, W. L.; Woźny, P.; Półrolniczak, A.; Katrusiak, A.; Runowski, M.; Law, G. L. Stress to Distress: Triboluminescence and Pressure Luminescence of Lanthanide Diketonates. *Chem. Eng. J. Adv.* **2022**, *11* (May). https://doi.org/10.1016/j.ceja.2022.100326.

(64) Marin, R.; Millan, N. C.; Kelly, L.; Liu, N.; Rodrigues, E. M.; Murugesu, M.; Hemmer, E. Luminescence Thermometry Using Sprayed Films of Metal Complexes. *J. Mater. Chem. C* **2022**, *10* (5), 1767–1775. https://doi.org/10.1039/d1tc05484h.

(65) Trannoy, V.; Carneiro Neto, A. N.; Brites, C. D. S.; Carlos, L. D.; Serier-Brault, H. Engineering of Mixed Eu3+/Tb3+ Metal-Organic Frameworks Luminescent Thermometers with Tunable Sensitivity. *Adv. Opt. Mater.* **2021**, *9* (6), 1–12. https://doi.org/10.1002/adom.202001938.

(66) Wade, S. A.; Collins, S. F.; Baxter, G. W. Fluorescence Intensity Ratio Technique for Optical Fiber Point Temperature Sensing. *J. Appl. Phys.* **2003**, *94* (8), 4743–4756. https://doi.org/10.1063/1.1606526.

(67) Bünzli, J.-C. G.; Eliseeva, S. V. *Lanthanide Luminescence*; 2010; Vol. 7.

(68) Brites, C. D. S.; Millán, A.; Carlos, L. D. *Lanthanides in Luminescent Thermometry*; 2016; Vol. 49. https://doi.org/10.1016/bs.hpcre.2016.03.005.

(69) Piguet, C.; Williams, A. F.; Bernardinelli, G.; Moret, E.; Bünzli, J. G. Structural and Photophysical Properties of Lanthanide Nitrate 1:1 Complexes with Planar Tridentate Nitrogen Ligands Analogous to 2,2′:6′,2′-terpyridine. *Helv. Chim. Acta* **1992**, *75* (5), 1697–1717. https://doi.org/10.1002/hlca.19920750523.

(70) Souliø, M.; Latzko, F.; Bourrier, E.; Placide, V.; Butler, S. J.; Pal, R.; Walton, J. W.; Baldeck, P. L.; Guennic, B. Le; Andraud, C.; Zwier, J. M.; Lamarque, L.; Parker, D.; Maury, O. Comparative Analysis of Conjugated Alkynyl Chromophore – Triazacyclononane Ligands for Sensitized Emission of Europium and Terbium. *Chem. - A Eur. J.* **2014**, *20*, 8636–8646. https://doi.org/10.1002/chem.201402415.

(71) Sørensen, T. J.; Kenwright, A. M.; Faulkner, S. Bimetallic Lanthanide Complexes That Display a Ratiometric Response to Oxygen Concentrations. *Chem. Sci.* **2015**, *6* (3), 2054–2059. https://doi.org/10.1039/c4sc03827d.

General Conclusion and Perspectives

This thesis exploits lanthanide-based materials to develop photoluminescent (PL) sensors for the dynamic measurement of local temperature and pressure variations in tribological contacts. Thanks to the long emission lifetimes and sharp emission peaks of the Ln^{3+} 4f-4f transition, the measurements by Ln-based sensors are highly accurate and reliable.

The thesis addressed the need for self-monitoring sensing methods in dynamic measurements for tribological applications, where system parameters change continuously. The Luminescence Intensity Ratio (LIR) method is mainly studied in this work for temperature and pressure sensing by Ln-based materials. Based on the Boltzmann distribution, temperature sensing using PL sensors relies on the population ratios of thermally coupled energy levels (TCLs) within the lanthanide-based material. Upconverting Yb^{3+}/Er^{3+} doped nanoparticles (NPs) are developed as an LIR-based thermometer. The high thermo-sensitivity of Er^{3+} emission from their TCLs ($^2H_{11/2}$ and $^4S_{3/2}$) for the temperature range 293 – 473 K is required for temperature measurements in tribology. In addition, a novel pressure sensitive Tb^{3+}/Eu^{3+} complex based on LIR is presented in this work. This process relies on the pressure-induced variation of the Tb^{3+}-Eu^{3+} energy transfer (ET) rate following the Förster Resonance Energy Transfer (FRET) theory. The ET rate between the Ln^{3+} donor and the Ln^{3+} acceptor is highly sensitive to changes in the distance between them, which can be influenced by pressure-induced structural contraction in the material.

The thesis begins by focusing on the chemical synthesis of PL sensors and their structural characterizations. This includes the study of incorporating PL sensors into fluid or solid matrices. The Yb^{3+}/Er^{3+} doped $GdVO_4$ NPs synthesized exhibit well-defined crystallinity in small sizes (< 50 nm). However, the hydrodynamic size of the NPs in suspension is slightly larger than expected, suggesting the need for further surface functionalization to reduce the dispersed size. Nonetheless, the dispersion of NPs shows good homogeneity and monodispersity in both fluid lubricants and solid matrices. Importantly, the low concentration of NPs in fluid or solid matrices does not affect the physical and mechanical properties of the material, which is crucial for investigating the optical properties of $GdVO_4$ NPs.

In the following chapter, the photoluminescent properties of Yb^{3+}/Er^{3+} doped $GdVO_4$ NPs are presented. These NPs demonstrate accurate and reversible thermometry within a temperature range of 293 to 673 K under excitation by visible blue light and near-infrared (NIR) light. During the upconversion excitation process of $GdVO_4$: Yb^{3+}/Er^{3+} NPs powder, the NIR laser exhibits a heating effect, which becomes more important with increasing laser intensity and temperature. Furthermore, the photoluminescent properties of $GdVO_4$: Yb^{3+}/Er^{3+} NPs in a dispersed medium are investigated, and their thermometry capability remains reliable. We noted that the laser heating effect is typically negligible at low concentrations (e.g., 0.5 wt.% and 5 wt.%), but becomes significant at higher concentrations (50 wt.%). To enhance the temperature measurement accuracy, a laser-induced heating temperature correction method is proposed which was successfully applied to both powder form and solid-dispersed NPs. For temperature sensing in tribological contact, temperature calibration is conducted under hydrostatic pressure up to 1.1 GPa within a diamond anvil cell (DAC) utilizing a suspension of $GdVO_4$: Yb^{3+}/Er^{3+} NPs in suspension of a lubricant (Nycobase 5750). The

outcomes verify the pressure independence of the LIR, and the temperature calibration curve remains consistent under both variable and constant pressure conditions. This observation indicates that incorporating $GdVO_4$: Yb^{3+}/Er^{3+} nanosensors into the lubricant enables temperature measurement using the LIR method, unaffected by changes in pressure.

The thesis also studied the exploration of Ln^{3+} complexes with different nuclearities. By manipulating the ligands, we successfully synthesized Tb^{3+}/Eu^{3+} based β-diketonate complexes with varying nuclearities, namely [Ln_1], [Ln_2], and [Ln_9], exhibiting high purity and homogeneity. These complexes exhibit Ln^{3+}-Ln^{3+} distances ranging from 3 Å to 8 Å, which hold significant relevance in energy transfer investigations among Tb^{3+} and Eu^{3+} ions. The coordination of organic ligands in Ln^{3+} complexes introduce an "*Antenna effect*," resulting in enhanced emission intensity of Ln^{3+} ions within the complex. Additionally, we analyzed the dispersion of Ln^{3+} complexes crystals in fluid lubricants, demonstrating the attainment of favorable hydrodynamic sizes for the complex crystals and desirable rheological properties of the suspensions. These important findings provide a solid foundation for further explorations and investigations into the photoluminescent properties of those complexes.

In Chapter 4, we focused on the pressure-dependent photoluminescent properties of those Tb^{3+}/Eu^{3+} based complexes: mononuclear [Ln_1], binuclear [Ln_2], and nonanuclear [Ln_9]. The aim is to explore their potential as pressure sensors for tribological measurements within a relatively low-pressure range of 0-1 GPa. Hydrostatic pressure is applied to the complexes in a diamond anvil cell (DAC), while excitation at 405 nm efficiently excites the Ln^{3+} complexes through the organic ligands due to the *Antenna effect*. First, in the complex [$Eu_9(acac)_{16}OH_{10}$], pressure sensitivity based on peak-shift was demonstrated. Compression at 550 MPa induces structural changes in the complex, resulting in a permanent deformation of the Eu^{3+} emission peak from the $^5D_0 \rightarrow {}^7F_2$ transition at 610 nm. The peak shift as a function of pressure is approximately 0.15 nm/GPa in Nycobase and 0.12 nm/GPa in Squalane. This peak shift is reversible up to 1 GPa in both solvents.

Then, we introduced Tb^{3+} ions into the system to activate ET from Tb^{3+} to Eu^{3+}. According to FRET theory, pressure-induced variation in the crystal structure of complexes leads to significant changes in the photoluminescent properties of Tb^{3+} and Eu^{3+} ions due to the ET process, enabling indirect measurement of pressure through spectral variables. The study explores the pressure sensitivity of Ln^{3+}-complexes based on LIR. Prior spectral characterizations proved the efficient ET from Tb^{3+} to Eu^{3+} in each complex even at low concentrations of Eu^{3+}. The impact of structural changes on the Tb^{3+}-Eu^{3+} ET is then investigated by compressing the complexes in a DAC, followed by analysis of the LIR variation of the Tb^{3+}/Eu^{3+} emission. The [Ln_2] complex demonstrates a particularly efficient Tb^{3+}-Eu^{3+} ET, making Tb^{3+} emission difficult to observe. Among the three types of complexes, the [$Eu_{0.01}Tb_{0.2}Y_{0.79}(acac)_3phen$] complex exhibits satisfactory pressure sensitivity on the LIR up to 700 MPa. The presence of Y^{3+} in the system influences the evolution of Tb^{3+} emission under varying hydrostatic pressure, resulting in reversible LIR variation when diluted by Y^{3+}. To further enhance its application in tribological measurements, the study verifies the temperature-induced variation of the LIR and proposes a temperature calibration for the pressure measurement. Additionally, low shear rates ($< 500\ s^{-1}$) have no significant impact on the LIR of the complex suspension. However, it is important to consider the influence of the physical environment on the LIR in pressure sensing applications.

This thesis has achieved significant advancements in the development of highly sensitive and reversible PL nanosensors for temperature and pressure measurement. The application of $GdVO_4$: Yb^{3+}/Er^{3+} NPs as pressure-independent sensors has enabled accurate monitoring of temperature variations in tribological contact. Moreover, the $[Ln(acac)_3phen]$ (Ln^{3+} = Y^{3+}, Tb^{3+}, Eu^{3+}) complex has been identified as a reliable PL sensor for pressure-sensing applications within the range of 0-700 MPa, representing a significant breakthrough in short-range PL pressure sensors.

Moving forward, the focus will be on exploring the stability of $GdVO_4$: Yb^{3+}/Er^{3+} NPs as upconversion thermometers under shearing conditions. This will involve conducting temperature calibration while subjecting the NPs to both shearing and temperature variations, particularly at a high shear rate of 10^4 s^{-1} within a confined fluid environment. The next step will be to apply the $GdVO_4$: Yb^{3+}/Er^{3+} NPs for temperature measurement in a tribometer, starting with their use as a suspension in EHL contacts to enable in-situ temperature sensing. Additionally, the pressure-sensing capabilities of the Tb^{3+}/Eu^{3+} complex will be further investigated to enhance its thermal stability and reliability as a pressure sensor. The initial investigation will focus on the pressure sensitivity of the Tb^{3+}/Eu^{3+} complex when incorporated into solid bulk materials, specifically hybrid silica and PDMS, within a low-pressure range of 170 MPa (limited by the properties of the solid matrices).

Annexes

Table A1a: C-O bond lengths (Å) in Ln complexes

Ln1		Ln2		Ln9	
C1-O1	1.268(9)	C3-O2	1.405(7)	C11-O10	1.36(2)
C12-O2	1.26(1)	C33-O4	1.255(8)	C13-O14	1.27(2)
C26-O3	1.266(9)	C7-O6	1.25(1)	C18-O17	1.29(3)
C27-O4	1.271(9)	C9-O10	1.24(1)	C20-O21	1.29(2)
C17-O5	1.27(1)	C35-O36	1.237(8)	C25-O24	1.25(2)
C2-O6	1.27(1)			C27-O28	1.28(2)
				C32-O31	1.24(3)
				C34-O35	1.32(2)

Table A1b: Ln-O bond lengths (Å) in Ln complexes

Ln1		Ln2		Ln9	
Ln1-O1	2.314(5)	Ln1-O2	2.296(3)	Ln1-O3	2.49
Ln1-O2	2.333(5)	Ln1-O4	2.367(4)	Ln1-O4	2.48
Ln1-O3	2.319(6)	Ln1-O6	2.397(4)	Ln2-O2	2.608
Ln1-O4	2.300(5)	Ln1-O36	2.347(4)	Ln2-O4	2.34(1)
Ln1-O5	2.314(5)			Ln2-O10	2.41(1)
Ln1-O6	2.331(5)			Ln2-O14	2.38(1)
				Ln2-O17	2.32(1)
				Ln2-O21	2.39(1)
				Ln3-O1	2.638
				Ln3-O3	2.35(1)
				Ln3-O24	2.36(1)
				Ln3-O28	2.34(1)
				Ln3-O31	2.37(1)
				Ln3-O35	2.48(1)

Table A1c: Ln-N bond lengths (Å) in Ln complexes with ligand 1-10 phenanthroline

Ln1		Ln2	
Ln1-N1	2.565(6)	Ln1-N14	2.602(4)
Ln1-N2	2.534(6)	Ln1-N21	2.588(6)

Table A1d: shortest Ln-Ln distances(Å) in Ln complexes

Ln1		Ln2		Ln9	
Ln1-Ln1	8.003	Ln1-Ln1	3.732	Ln2-Ln2/Ln3-Ln3	3.702
Ln1-Ln1	8.988	Ln1-Ln1	9.294	Ln2/3-Ln1	3.783
Ln1-Ln1	9.414	Ln1-Ln1	9.922	Ln2-Ln2/Ln3-Ln3	5.187
Ln1-Ln1	10.014			Ln2-Ln3	5.799
				Ln2-Ln3	5.849
				Ln2-Ln2/Ln3-Ln3	10.136

Table A2: $[Eu_{0.01}Tb_{0.2}Y_{0.79}(acac)_3(phen)]$: Tb/Y local environment.

SAPR-8	0.39715	**TDD-8**	2.27713	**JBTPR-8**	2.75255
BTPR-8	2.25836	**JSD-8**	5.04488		

SAPR-8 : D4d, square antiprism; TDD-8 : D2d, triangular dodecahedron; JBTPR-8: C2v, biaugmented trigonal prism J50; BTPR-8: C2v, biaugmented trigonal prism; JSD-8: D2d, snub diphenoid J84

Table A3: Definitions of the parameters of crystalline refinements for Ln complexes (cf. Table 2.6 in Chapter 2)

Z	**Number of formula units in the unit cell**
μ (mm^{-1})	Absorption coefficient
R	Residual factor for the reflections judged significantly intense and included in the refinement.
R_w	Residual factor for all reflections
S	The least-squares goodness-of-fit parameter S' for all reflections after the final cycle of least-squares refinement.
$\Delta\rho_{max}$ ($e^-.Å^{-3}$)	The maximum residual electron density
$\Delta\rho_{min}$ ($e^-.Å^{-3}$)	The minimum residual electron density

List of Publications

Published papers:

[1] **Zhou, Y**.; Ledoux, G.; Philippon, D.; Descartes, S.; Martini, M.; He, S.; Desroches, C.; Fournier, D.; Journet, C.; Bois, L. "Laser-Induced Heating in GdVO 4 : Yb^{3+} / Er^{3+} Nanocrystals for Thermometry," *ACS Appl. Nano Mater.*, vol. 5, pp. 16388–16401, 2022, doi: 10.1021/acsanm.2c03466.

[2] **Zhou, Y.;** Ledoux, G.; Bois, L.; Descartes, S.; Bouscharain, N.; Chassagneux, F.; Martini, M.; Bakary, Y. M.; Journet, C.; Philippon, D. "Er^{3+} Doped Nanoparticles as Upconversion Thermometer Probe in confined fluids," *Phys. Chem. Chem. Phys. 2023,* doi: 10.1039/D3CP02218H.

Submitted paper:

[3] **Zhou, Y.**; Ledoux, G.; Bois, L.; Pilet, G.; Colombo, M.; Journet, C.; Descartes, S.; Philippon, D. "Ratiometric Pressure-sensitive Photoluminescent Lanthanide Complex by Energy Transfer between Terbium and Europium," ***Under review*** in *Adv. Opt. Mater (Oct 2023).*

Abstract:

In this study, we present a reversible pressure-sensing material with high sensitivity. Mixed β-diketonate complexes of Tb^{3+} and Eu^{3+} [(Ln)$(acac)_3$phen] are synthesized with phenanthroline as an ancillary ligand. The organic ligands provide the antenna effect to make the Ln^{3+} complex excitable at 405 nm. Eu^{3+} emission results from efficient energy transfer (ET) from Tb^{3+}. At 405 nm excitation, the emission intensity of Tb^{3+} decreases whereas the emission intensity of Eu^{3+} increases with pressure, which makes this complex a potential pressure sensor based on luminescent-intensity-ratio (LIR) up to 700 MPa. This Tb^{3+}/Eu^{3+} complex can be applied for pressure sensing is then discussed in terms of measurement conditions. The addition of the optical neutral ion Y^{3+} to the system can reduce the impact of pressure-induced structural defects on the emission, thus optimizing the reversibility of the LIR variation as a function of pressure. Therefore, here a self-calibrating, reliable, and reversible pressure-sensing material is proposed, with remarkable pressure sensitivity compared to a peak shift-based pressure sensor.

Conferences and Seminaries Contributions

- 2023: Talk, International Conference on Luminescence 2023, Paris, France
- 2023: Talk, European Materials Research Society Spring meeting 2023, Strasbourg, France
- 2022: Talk, International material conference MATÉRIAUX 2022 (in French), Lille, France
- 2022: 3 mins Oral competition, 7th World Tribology Congress, Lyon, France
- 2022: Talk, International Conferences on Modern Materials and Technologies 2022, Perugia, Italy
- 2022: Talk, Journées Internationales Francophones de Tribologie, Metz, France
- 2021: Talk, Auvergne-Rhône-Alpes C'Nano day (in French), remote seminar.